UNIVERSITÀ DI PISA

Department of Physics Enrico Fermi
Doctoral course in Physics, XXXV cycle

Doctoral Thesis

Large-scale structure of the Universe in General Relativity and beyond

Internal Supervisor:

Prof. Giovanni Marozzi

Doctoral candidate:

Tiziano Schiavone

External Supervisors:

Prof. Giovanni Montani
(ENEA and University of Rome Sapienza)

Dr. Giuseppe Fanizza
(Institute of Astrophysics and Space Sciences, Lisbon)

September 2023

UNIVERSITÀ DI PISA

Department of Physics Enrico Fermi
Doctoral course in Physics, XXXV cycle

Large-scale structure of the Universe in General Relativity and beyond

by

Tiziano Schiavone

A thesis submitted in fulfillment of the requirements for the degree of *Doctor Philosophiæ*.
Doctoral program in Physics. Line of research: Theoretical Cosmology and Gravitation.

This thesis has been developed under the supervision of

Prof. Giovanni Marozzi (Università di Pisa)
Prof. Giovanni Montani (ENEA and University of Rome Sapienza)
Dr. Giuseppe Fanizza (Institute of Astrophysics and Space Sciences, Lisbon)

Large-scale structure of the Universe in General Relativity and Beyond
Tiziano Schiavone
tiziano.schiavone@phd.unipi.it
Doctoral thesis in Physics, XXXV cycle

This thesis was written in LyX, a graphical user interface document processor based on the LaTeX digital typesetting system.

List of publications

This thesis is based on the papers listed below.

Published on peer-reviewed journals

[TS1] T. Schiavone, G. Montani, & F. Bombacigno, *$f(R)$ gravity in the Jordan frame as a paradigm for the Hubble tension*, 2023, MNRAS Letters, 522, L72–L77, DOI: 10.1093/mnrasl/slad041, arXiv:2211.16737 [gr-qc]

[TS2] M.G. Dainotti, B. De Simone, T. Schiavone, G. Montani, E. Rinaldi, G. Lambiase, M. Bogdan, & S. Ugale, *On the evolution of the Hubble constant with the SNe Ia Pantheon Sample and Baryon Acoustic Oscillations: a feasibility study for GRB-cosmology in 2030*, 2022, Galaxies, 10(1), 24, DOI: 10.3390/galaxies10010024, arXiv:2201.09848 [astro-ph.CO]

[TS3] M.G. Dainotti, B. De Simone, T. Schiavone, G. Montani, E. Rinaldi, & G. Lambiase, *On the evolution of the Hubble constant in the SNe Ia Pantheon sample*, 2021, ApJ, 912, 150, DOI: 10.3847/1538-4357/abeb73, arXiv:2103.02117 [astro-ph.CO]

Submitted

[TS4] T. Schiavone, & G. Montani, *Signature of $f(R)$ gravity via Lemaître-Tolman-Bondi inhomogeneous perturbations*, submitted to Phys. Rev. D, arXiv:2301.09768 [gr-qc]

[TS5] T. Schiavone, E. Di Dio, & G. Fanizza, *Skewness of the distance-redshift relation in ΛCDM*, submitted to JCAP, arXiv:2307.13455 [astro-ph.CO]

In preparation

[TS6] I. S. Albuquerque, S. Anselmi, T. Anton, [and 35 others, including T. Schiavone], White Paper as the outcome of the workshop *A SHOT IN THE DARK: New Challenges in Cosmology 2022*, Leiden, in preparation

Proceedings

[TS7] M.G. Dainotti, B. De Simone, G. Montani, T. Schiavone, & G. Lambiase, *The Hubble constant tension: current status and future perspectives through new cosmological probes*, 2023, Proceedings of Science 2022, Corfu Summer Institute 2022 "*School and Workshops on Elementary Particle Physics and Gravity*", arXiv:2301.10572 [astro-ph.CO]

[TS8] T. Schiavone, G. Montani, M.G. Dainotti, B. De Simone, E. Rinaldi, & G. Lambiase, *Running Hubble constant from the SNe Ia Pantheon sample?*, Proceedings of the 17th Italian-Korean *Symposium on Relativistic Astrophysics*, arXiv:2205.07033 [astro-ph.CO]

[TS9] T. Schiavone, & G. Montani, *On the evolution of inhomogeneous perturbations in the* ΛCDM *model and* $f\left(R\right)$ *modified gravity theories*, Proceedings of the Sixteenth Marcel Grossmann Meeting on General Relativity, World Scientific, Singapore, 2023, DOI: 10.1142/9789811269776_0154, pp. 1961-1969, arXiv:2111.03197 [astro-ph.CO]

All these papers are referred to in the thesis by their numbers preceded by "TS". These papers are also listed at the beginning of the Bibliography in the back of the thesis.

Contents

Conventions and notations

We adopt the metric signature $(-,+,+,+)$ throughout the thesis, and we use natural units in which the speed of light in vacuum is $c=1$.

We keep explicitly the Newton gravitational coupling G and we denote with $\chi \equiv 8\,\pi\,G$ the Einstein constant.

Throughout, Latin indices $i, j, k, \ldots$ move along the three spatial coordinate labels $1, 2, 3$, while Greek indices $\mu, \nu, \rho, \ldots$ run over the space-time coordinate labels $0, 1, 2, 3$, where $x^0 = t$ is the time coordinate in natural units. Contracted Greek indices are summed according to the Einstein convention. 3-D vectors are indicated with $\vec{v}$.

The components of the gravitational field equations are sometimes denoted with a pair of indices $\mu - \nu$, in which the indices $\mu, \nu = 0, 1, 2, 3$.

The metric tensor components and the Christoffel symbols are denoted with $g_{\mu\nu}$ and $\Gamma^{\rho}_{\mu\nu}$, respectively. The Riemann tensor is defined up to an arbitrary sign, and we use

$$R^{\rho}{}_{\sigma\mu\nu} = \partial_\mu \Gamma^{\rho}_{\nu\sigma} - \partial_\nu \Gamma^{\rho}_{\mu\sigma} - \Gamma^{\rho}_{\nu\epsilon}\,\Gamma^{\epsilon}_{\mu\sigma} + \Gamma^{\rho}_{\mu\epsilon}\,\Gamma^{\epsilon}_{\nu\sigma}\,.$$

We adopt the following convention for the contracted indexes in the Ricci tensor:

$$R_{\mu\nu} = R^{\alpha}{}_{\mu\alpha\nu}\,,$$

where the first index is contracted with the third one.

The symbol ∂_μ indicates the partial derivative with respect to the coordinate x^μ, i.e. $\partial_\mu \equiv \frac{\partial}{\partial x^\mu}$.

The symbol ∇_μ denotes the covariant derivatives with respect to the index μ. The D'Alembert operator in curved spaces is represented by $\Box = g^{\mu\nu}\,\nabla_\mu \nabla_\nu$. The three-dimensional Laplacian is ∇^2, while the angular Laplacian on the two-sphere is denoted with Δ_2.

Referring to a function $g\,(t, r)$ that depend both on the cosmic time t and a radial coordinate r, we adopt the following notations for the derivatives with respect to these variables: $\dot{(g)} \equiv \partial_t g$ and $(g)' \equiv \partial_r g$.

Except for vector or tensor time components, the subscript 0 is usually referred to cosmological quantities evaluated today at the present cosmic time t_0, or equivalently, at the cosmological redshift today $z = 0$. The scale factor today is set to unity: $a_0 = 1$.

In perturbation theory, unless otherwise specified, an overline $\bar{Q}$ is referred to cosmological quantities Q in the homogeneous and isotropic background Universe, and linear perturbations are indicated with δQ. In other context, for the sake of clarity and to avoid ambiguity with the ensamble average, we adopt the notation with the superscripts $Q^{(i)}$ for perturbations, being i the order of each perturbative term.

The ensamble average is also denoted with an overline $\bar{Q}$, while the average on a portion of space-time like the past light-cone is indicated with $\langle Q \rangle$.

Throughout, we adopt the following 3-D Fourier transform convention:

$$f\left(t,\vec{x}\right) = \int \frac{d^3k}{\left(2\pi\right)^3}\, f\left(t,\vec{k}\right)\, e^{-i\vec{x}\cdot\vec{k}} \qquad , \qquad f\left(t,\vec{k}\right) = \int d^3x\, f\left(t,\vec{x}\right)\, e^{i\vec{x}\cdot\vec{k}}\,.$$

The Heaviside step function is defined as

$$\Theta\left(x\right) = \begin{cases} 0 & \text{if } x < 0 \\ \frac{1}{2} & \text{if } x = 0 \\ 1 & \text{if } x > 0\,. \end{cases}$$

We have used a capital letter to distinguish it from the angular coordinate adopted for spherical coordinates (r, θ, ϕ).
The simbol δ alone is used to define the matter density contrast, while a subscript is added to denote the Dirac delta distribution δ_D.
Concerning measurements results, all uncertainties in this thesis are expressed in $1\,\sigma$ ($\sim 68\,\%$ confidence level).

Acronyms and terminology

ΛCDM	Cosmological constant and a cold dark matter component
ΛLTB	Lemaître-Tolman-Bondi inhomogeneous model
$f(R)$	Modified gravity model with a generalized gravitational Lagrangian density
H_0ES	Supernova H_0 for the Equation of State
H_0LiCOW	H_0 Lenses in COSMOGRAIL's Wellspring
wCDM	Varying dark energy equation of state parameter
w_0w_aCDM	Varying dark energy equation of state parameter according to the CLP parametrization
ADM	Arnowitt-Deser-Misner formalism
AGN	Active galactic nuclei
BAO	Baryonic acoustic oscillation
BB	Big Bang
CLASS	Cosmic Linear Anisotropy Solving System
CMB	Cosmic microwave background radiation
COSMOGRAIL	Cosmological monitoring of gravitational lenses
CPL	Chevallier-Polarski-Linder parametrization for the dark energy equation of state parameter
d.o.f.	Degree of freedom
DE	Dark energy
DES	Dark Energy Survey
DM	Dark matter
EDR3	Gaia Early Data Release 3
ESA	European Space Agency
FLRW	Friedmann-Lemaître-Robertson-Walker metric
GLC	Geodesic Light-Cone coordinates
GR	General Relativity

GRB	Gamma-ray burst
GWs	Gravitational waves
GWTC-3	Third LIGO-Virgo-KAGRA Gravitational-Wave Transient
HS	Hu-Sawicki f(R) modified gravity model
HSC	Subaru Hyper Suprime-Cam
HST	Hubble Space Telescope
KAGRA	Kamioka Gravitational Wave Detector
KiDS-450	Kilo Degree Survey
LIGO	Laser Interferometer Gravitational-Wave Observatory
LMC	Large Magellanic Cloud
LSS	Large-scale structure
LTB	Lemaître-Tolman-Bondi inhomogeneous model with a cosmological constant
MCMC	Markov Chain Monte Carlo
MM	Megamaser detector
PDF	Probability distribution function
QFT	Quantum field theory
RSD	Redshift-space distortion
SNe Ia	Type Ia supernovae
WIMPs	Weakly interacting massive particles

List of Figures

List of Tables

Preface

The large-scale structure of the Universe and the nature of dark energy are only just beginning to be comprehensively understood, as we have recently entered the era of precision cosmology. The standard Λ*CDM cosmological model, which includes a cosmological constant* Λ *and a cold dark matter component, successfully explains the evolution and composition of our Universe. However, recent measurements with tighter constraints on cosmological parameters have revealed several serious anomalies and tensions. Such paradoxes and tensions are frequently indications of a possible theoretical model crisis. Therefore, it is necessary to reassess the essential and fundamental pillars of the* Λ*CDM model.*

This thesis aims to address the following questions:

1. *How can cosmological data enable us to distinguish between the* Λ*CDM cosmological model and modified gravity theories?*
2. *What is the impact of local inhomogeneities on cosmological observables?*

The first question pertains to finding alternative theoretical justifications for the cosmological constant. Increasing attention has been paid in recent years to the possibility that the present cosmic acceleration could be explained by extending the present gravitational theory, i.e., General Relativity, within the framework of modified gravity theories. These alternative proposals forecast deviations from the Λ*CDM model and allow us to investigate unresolved cosmological issues, such as the Hubble constant tension.*

The second question concerns the large-scale structure of the Universe and local deviations from spatial homogeneity. As shown by observations and cosmic structures, the real nature of the Universe is inhomogeneous below a specific scale of $\sim 100\,Mpc$*. Consequently, we may expect deviations from a purely homogeneous toy-model, given that the local behavior of structures in the Universe could impact our cosmological measurements.*

Introduction

Humanity has always had many fundamental questions regarding the ultimate nature of the Universe and its structures. According to the ancient Greeks, the Universe was an eternal, imperishable, perfectly ordered system. The term cosmology derives from the ancient Greek word "kosmos," meaning order. The concept involved geometrical harmony and aesthetic beauty.

As a physical science, modern cosmology is based on the scientific method, which employs theories, observations, simulations, and data analysis. It brings together various disciplines, including Physics, Astronomy, Astrophysics, and Particle Physics. Cosmologists study the evolution of the Universe as a whole, in terms of space-time and matter.

We give a summary of some key steps from the early days of modern cosmology to the emergence of cosmological tensions and open debates.

From General Relativity to modified gravity and inhomogeneous cosmological models

The development of modern cosmology has experienced significant and rapid progress since the formulation of General Relativity (GR), which is the present geometrical theory of gravity introduced by Albert Einstein in 1915-1916 [10]. Driven by a unified vision of nature, Einstein was motivated to extend the Special Relativity principle and develop a new formalism that maintains the same form of physical laws under any coordinate transformation. In this regard, he received support from brilliant mathematicians of the last century, such as Grossmann, Levi-Civita, and Ricci, who developed the covariant tensor formalism to ensure the general covariance of the theory. Furthermore, the starting point of GR was the impressive synthesis between inertia and gravitation, the Equivalence Principle, which was summed up in the famous elevator thought experiment [11].

The GR field equations [12, 13] establish a profound connection between the matter and space-time geometry, and this type of theory is also referred to as geometro-dynamics. De facto, the gravitational interaction is removed in GR and becomes a geometric interaction. Sir Isaac Newton's statement regarding the problem of action at a distance is relevant here:

> "*It is inconceivable that inanimate brute matter should, without the mediation of something else which is not material, operate upon and affect other matter without mutual contact*"
>
> [Original letter from Isaac Newton to Richard Bentley, source: 189.R.4.47, ff. 7-8, Trinity College Library, Cambridge, UK].

In GR, through a change of perspective, the presence of matter, i.e., the source of a gravitational field, curves the space in such a way that the trajectories of particles are deviated. Therefore, everything we experience as a gravitational interaction is nothing more than a manifestation of the space-time curvature.

The geometrical properties of a curved space-time can be effectively encapsulated in the well-known quote by the theoretical physicist and cosmologist John Archibald Wheeler:

> "*Space-time tells matter how to move; matter tells space-time how to curve*"
> [14].

This vision of the space-time is completely different from that in classical mechanics, where space-time is regarded as absolute and eternal, independent of the presence of matter.

The first strong confirmation of GR was provided just three years after its publication. Sir Arthur Stanley Eddington observed the gravitational bending of light during the solar eclipse in 1919 [15], as predicted by GR calculations [16]. Another crucial classical test of GR was given by the perihelion precession of Mercury [17], which could not be fully explained using only the Netwonian mechanics. Actually, the anomalous orbit of Mercury was an old problem in celestial mechanics, and the astronomer Urban Le Verrier suggested in 1859 that between the Sun and Mercury there was an elusive planet, called Volcano, which was capable of modifying the orbit of Mercury via gravitational perturbations [18]. Le Verrier had succesfully applied this method in 1846 to discover the existence of Neptune, before observing it directly, by noting irregularities in the orbit of the nearby planet Uranus. Nevertheless, his effort to explain the perihelion precession of Mercury within the Newtonian mechanics was an attempt to save the dominant theory of that time, i.e., the Newtonian gravity. Later, Einstein quantitatively demonstrated that this phenomenon could be addressed in GR [17]. These first two confirmations of GR made Einstein famous worldwide and partially contributed to creating his iconic figure in our culture.

In the present day, GR has been tested with several independent measurements with increasing precision. Recently, in September 14th, 2015, the detection of gravitational waves (GWs) after a century of their prediction has provided yet another powerful validation of GR. These waves were originally predicted by Einstein in 1916 [19–21]. Interestingly, Einstein himself harbored doubts regarding the existence and detectability of GWs. The detection of GWs has been possible as a result of theoretical and technological developments up to design the Laser Interferometer Gravitational-Wave Observatory (LIGO) and the Virgo interferometer [22].

Concerning the building of cosmological models, it was soon realized that Einstein equations were an ideal tool for investigating the dynamics of the Universe once its components had been determined. This realization marked a significant turning point in the field of cosmology. The first attempts to describe the behavior of the Universe on cosmological scales by applying GR were carried out by Einstein himself, resulting in a static model of the Universe [23]. This model was commonly accepted at that time and was motivated by a conservative idea from the late 19th century, whose roots can be traced back to ancient Greek culture. To satisfy the condition of a static Universe within his equations in 1917, Einstein introduced a constant, called the cosmological constant Λ [23], which is charazterized by a repulsive behavior against gravitational attraction.

However, the lack of a strong justification for the cosmological constant and the stability issues of Einstein's model reported by Lemaître [24] had led cosmologists to doubt the real nature of Λ from the beginning. The philosophical conjecture of a static model was soon discarded by observational facts. Although the main evidence for an expanding Universe was provided by Hubble's observations, as we will discuss later, an American astronomer, Vesto Slipher, had already measured in 1912-1915 a redshift in the spiral nebulae in distant galaxies [25]. He concluded that these objects were receding from the Earth, thus providing the first empirical result against the static Universe model, despite the controversial and debated results.

A significant breakthrough was accomplished by the American astronomer Edwin Hubble in 1929, who used cosmological data obtained from Type Ia supernovae (SNe Ia) to demonstrate that the Universe is expanding [26]. The advantage of using these astrophysical objects given by extremely violent explosions for evaluating cosmic distances is that their absolute luminosity can be considered constant since they are generated by the same physical mechanism [27, 28]. Hence, SNe Ia are usually regarded as standard candles. During the peak of brightness, the luminosity of a supernova is greater than that of the whole host galaxy, and it can be observed up to cosmological distances. By measuring the apparent luminosity and bearing in mind the fixed absolute luminosity, the SN Ia distance can be estimated. Hubble discovered a linear relationship between the recession velocity of the observed galaxies and their distance with a proportionality constant H_0, which is called the Hubble constant and represents the current expansion rate of the Universe. Hubble's observations ultimately discredited Einstein's static model. During a cosmological discussion with the Soviet-American physicist George Gamow in 1931, it is believed that Einstein himself declared the cosmological constant as "*the biggest blunder*" of his life [29]. It is probable that Einstein recognized that he had missed a significant opportunity to predict the expansion of the Universe.

Due to the aforementioned observations, there was a need to develop more reliable theoretical models in cosmology. In 1917, Dutch physicist Willem de Sitter developed the first dynamical cosmological model, known as the de Sitter model [30], which was motivated by Slipher's results. In such a framework, the Universe is dominated by the cosmological constant term, leading to an unbalanced repulsion and net expansion in the Universe. In 1922, Russian physicist Alexander Friedmann focused on GR solutions with different values of the spatial curvature and cosmological constant, and concluded that the universe is not static [31, 32]. In 1927, Belgian priest and theoretical physicist Georges Lemaître independently arrived at the same conclusion [24], showing that the Hubble linear relation is just a consequence of a non-static Universe (Hubble's law is also known as the Hubble-Lemaître law). In 1935, American mathematician Howard Percy Robertson and British mathematician Arthur Geoffrey Walker provided geometrical properties of the large-scale Universe [33, 34]. The Friedmann-Lemaître-Robertson-Walker (FLRW) metric is an exact solution of Einstein field equations, describing an expanding, homogeneous, and isotropic Universe [35]. It should be noted that the Hubble-Lemaître law can be derived in the low-redshift limit within the framework of an expanding Universe in the FLRW metric [35]. The full background cosmological dynamics are still essentially based on the field equations in the FLRW metric presented in these papers, under the conditions of spatial homogeneity and isotropy.

In more recent times, a significant discovery has greatly impacted our understanding of the Universe. In 1998, two independent research groups, the Supernova Cosmology Project [36] and the High-z Supernova Search Team [37], obtained an unexpected outcome from SNe Ia observations: the expansion of the universe is accelerating. Luminosity-distance relations have played a pivotal role in determining the accelerating Universe. The cosmic acceleration could be explained by the cosmological constant Λ in Einstein field equations. More generally, the so-called dark energy (DE), which is an exotic fluid characterized by negative pressure, exerts a repulsive force on cosmological scales that counteracts the attractive role of gravity and drives the cosmic accelerated phase in the late Universe [35, 38, 39]. The DE component accounts for roughly 70 % of the present Universe [40], but its true nature remains an open question. In particular, a cosmological constant Λ is a specific type of DE with an equation of state parameter $w = -1$.

Moreover, besides the visible baryonic matter, observational facts on galactic and cosmological scales have suggested the existence of an elusive component known as dark matter. These evidences include the flat profile of galaxy rotation curves, gravitational lensing, and the requirement for additional matter to account for structure formation in the late Universe [41]. Although the exact nature of DM is still a mystery, it is postulated that DM only interacts gravitationally and has a particle origin. Consequently, several experiments [42–44] are underway to search for evidence of new particles, and the most extensively researched DM candidates are weakly interacting massive particles (WIMPs) [45] and axions [46, 47].

At present, our theoretical understanding of the Universe relies significantly on two fundamental pillars:

1. GR serves as the gravitational theory that governs cosmological dynamics.
2. The cosmological principle asserts that the Universe is homogeneous and isotropic on scales greater than $\sim 100\,\mathrm{Mpc}$.

We have discussed the role of GR, and we now turn our attention to the second pillar. One of the principal tenets of the concordance model is the cosmological principle, which is an extension of the Copernican principle, namely there is no preferred location in the Universe. It is reasonable to assume that we live in a homogeneous and isotropic Universe, which appears to be so over distances greater than a characteristic homogeneity scale. The FLRW metric appropriately describes this geometry, and the typical homogeneity scale for the present-day Universe is $\sim 100\,\mathrm{Mpc}$, as indicated by observational evidence from large-scale structures and galaxy surveys [48, 49]. The spatial homogeneity and isotropy of the Universe on large scales are also supported by temperature maps of the cosmic microwave background radiation (CMB), which exhibit typical temperature fluctuations[1] of approximately $\delta T/T \sim 10^{-5}$ from the mean value of $\sim 2.73\,\mathrm{K}$ [40].

As a result of the gradual development of ideas and discoveries made in cosmology since the publication of GR mentioned above, a new cosmological paradigm has been established and is generally accepted as the concordance model. This model, specifically the well-known ΛCDM cosmological model [35], is based on two additional assumptions regarding the dark components in the Universe: a positive cosmological constant $\Lambda > 0$ and a cold dark matter (CDM) component. This self-consistent and robust model provides a good fit to most of the cosmological data and remarkably describes the evolution and structure formation in our Universe.

Undoubtedly, the ΛCDM paradigm is considered by the community of theoretical physicists and cosmologists as one of the most successful cosmological models. Additionally, it is the simplest model from a mathematical point of view and is the concordance model according to Occam's razor. However, it is important to note that the ΛCDM model cannot provide an extensive explanation for the nature of dark components from a fundamental theory. Although several attempts have been made in the last decades to understand the nature of DM and investigate beyond the standard model of particle physics, no dark matter particle has been detected so far.

Furthermore, the cosmological constant poses two significant problems. Firstly, interpreting the cosmological constant as the vacuum energy in quantum field theory (QFT) results in the worst prediction of theoretical physics. Indeed, the theoretical value of the vacuum energy in QFT is $\sim 10^{120}$ times larger than the observed value [51, 52], making difficult to accept a specific value for Λ without a theoretical framework. This is known as the fine-tuning problem. Secondly, we do not fully understand why the densities of DE and DM are of the same order of magnitude today, compared to the cosmic time close to the present, with respect to the age of the Universe. In other words, why has the equivalence between DE and DM densities emerged recently in cosmic time? This is referred to as the coincidence problem.

Due to these issues, it might seem like dark components are ad hoc elements introduced to preserve the present cosmological model, similar to how the elusive planet Volcano was hypothesized by Le Verrier to uphold Newtonian mechanics, as we mentioned before. However, several independent pieces of evidence supporting the existence of dark components due to indirect gravitational effects must be considered. If present and future experiments do not provide any direct and definitive proof of their existence, we must reconsider our hypothesis and revise the robustness of the ΛCDM model.

Regarding possible modifications to the ΛCDM model, a number of approaches have been explored, with the aim of addressing some of the issues discussed earlier. The first minimal approach involves

---

[1] Actually, the observation of a slight temperature dipole [50] in CMB maps has been recently emerged across the sky. CMB anomalies and anisotropies are an open problem, but here we would like to point out that CMB maps have corroborated the idea of a homogeneous and isotropic Universe, despite this recent dipole feature.

altering slightly the composition of the Universe. For example, one might consider a type of DE that leads to late-time cosmic acceleration, in which the equation of state parameter w differs slightly from -1 (the value corresponding to a cosmological constant), or varies with redshift z. Such a model, known as the wCDM model, can be thought of as a time-evolving or "running" cosmological constant. One commonly studied example of this type of model is the Chevallier-Polarski-Linder (CPL) parametrization or $w_0 w_a$CDM model [53, 54]. Another interesting proposal to modify the content of the Universe is given by the popular class of quintessence models [52, 55], which introduces a new cosmic scalar field that mimics the present accelerated phase of the Universe. A further possibility is to consider models in which there is an interaction between DE and DM, the so-called interacting dark energy models [56, 57], which could potentially help to resolve the coincidence problem. However, all of these approaches are essentially phenomenological in nature, as they are not rooted in a fundamental theory, and a reliable scalar field candidate is missing in the late Universe.

Additionally to the unresolved questions concerning the nature of dark components and the cosmological constant problems, other significant anomalies have recently arisen from independent measurements within the framework of the ΛCDM model. Since the discovery of the cosmic acceleration, a growing number of observations and measurements with increasing precision have provided unprecedented cosmological data [40, 58, 59], and also more data will be available in the future [60–66]. As a result, we have gradually had better constraints on cosmological parameters such as the Hubble constant, H_0, and energy densities of Universe components. The era of precision cosmology is upon us.

However, one of the most significant challenges in modern cosmology is the Hubble constant tension [67–70]. This refers to the incompatibility between independent measurements of H_0 from cosmological probes at high and low redshifts. Specifically, there is a significant discrepancy of 4.8 σ at the statistical level between the value of H_0 inferred from CMB data in the early Universe ($H_0^{\mathrm{CMB}} = 67.36 \pm 0.54\,\mathrm{km\ s^{-1}\,Mpc^{-1}}$) [40] and the local value obtained by low-z probes in the late Universe, such as the Cepheid-SN Ia sample ($H_0^{\mathrm{loc}} = 73.04 \pm 1.04\,\mathrm{km\ s^{-1}\,Mpc^{-1}}$) [71]. This tension has become increasingly serious, as new measurements with higher precision have progressively reduced the uncertainty intervals, revealing differences between high- and low-z observations. Various combinations of local probes (see [68] and references therein) suggest that the tension with the CMB data is roughly between 4 and 6 σ. Other local probes, such as SNe Ia and baryonic acoustic oscillations (BAOs) [72, 73], typically considered standard candles and rulers, respectively, are useful for estimating cosmological distances.

The reason for the observed discrepancies in H_0 measurements is unclear. Ever since Hubble's observation in 1929, it has been well-known that galaxies, on average, move away from each other at a present-day expansion rate known as the Hubble constant, H_0, which is defined as the Hubble parameter H evaluated today at redshift $z = 0$ [35]. Thus, H_0 is a constant by definition. The H_0 tension may indicate potential inconsistencies in the high- and/or low-z measurements or systematics.

Another tension between early and late Universe probes pertains to matter clustering data and the growth of cosmic structure. Specifically, measurements based on local probes such as galaxy clustering, weak gravitational lensing, and redshift-space distortion (RSD) [74, 75] indicate reduced matter clustering compared to what is predicted by the ΛCDM model using parameters inferred from CMB data. This discrepancy is quantified by the S_8 parameter [70, 76], which is related to the growth of matter density perturbations and involves the amplitude of weak lensing measurements. This incompatibility between high and low redshift data is called the S_8 tension and is at a level of approximately $\sim 2\,\sigma$. For comprehensive reviews on these tensions and other anomalies within the ΛCDM model, refer to the already mentioned reviews [67–70, 76] and cited sources therein.

These tensions, as well as questions about the nature of DE and DM, and the cosmological constant problem, suggest that the ΛCDM paradigm should be extended. The concordance model is now regarded as a background scenario or an approximation to a more general model. While the vanilla ΛCDM model works adequately for many phenomena concerning the evolution and structure of the Universe, we are naturally inclined to believe that a possible new general model we are looking for should require small deviations from the ΛCDM scenario to explain the aforementioned problems. In recent decades, cosmologists have proposed hundreds of new models close to the ΛCDM paradigm to solve or alleviate these issues. Many of these models have been tested and discarded by observations, but we still lack the constraining power to discriminate between a plethora of theoretical models. Furthermore, having numerous candidates as theoretical models suggests the possible need for an extension of the ΛCDM model. For all these reasons, cosmologists have been motivated to revise the hypotheses and principles that underpin the concordance model.

In the light of the above discussion, we recall that the real strong assumptions made by cosmologists in developing the concordance model (prior to introducing dark components) are the two abovelisted pillars, i.e., GR and the cosmological principle. It is important to stress that these two pillars are uncorrelated, as the cosmological principle is not related to a fundamental theory but rather originated from philosophical reasoning. Because of the critical role played by each pillar, it is necessary to test and verify them in multiple independent ways, particularly now that we are entering the era of precision cosmology. If either of these pillars is incorrect, our models may be drastically flawed.

In regards to deviations from the first pillar of the cosmological concordance model, it is challenging to view GR as the ultimate theory of gravity. Despite the breakthrough discoveries and significant theoretical predictions that successfully describe phenomena in our Universe, the need for unknown and exotic components such as DE and DM, as well as the abovementioned cosmic tensions, may be considered the first signs of a potential breakdown of GR on galactic and cosmological scales.

Among the various possible generalizations of GR and modified gravity theories, the $f(R)$ gravity [77–85] is one of the simplest and most studied classes of extended theories. In this framework, an additional scalar degree of freedom (d.o.f) with respect to GR is introduced in the gravitational field equations, which is represented by a function $f(R)$ in the gravitational Lagrangian density instead of the standard Ricci scalar R in GR.

The $f(R)$ metric gravity can be reformulated in the scalar-tensor theories in which the extra scalar d.o.f. is converted into a scalar field. Specifically, the dynamically equivalent formalism of the $f(R)$ gravity in the so-called Jordan frame [79, 81, 83–86] is similar to the Brans-Dicke theory [87, 88] with a non-vanishing scalar field potential and a zero Brans-Dicke parameter (see also the O'Hanlon model [89]). In particular, in the Jordan frame, the scalar field is non-minimally coupled to the metric.

As in scalar-tensor theories, an equivalent formulation of the $f(R)$ gravity can also be obtained under a conformal transformation in the so-called Einstein frame, which theory in vacuum is equivalent to GR with a self-interacting minimally coupled scalar field. Although the Jordan and Einstein frames are mathematically equivalent, it is still unclear which physical frame should be considered. Indeed, there are ongoing debates about the role of a conformal transformation and energy conditions in modified gravity theories [84, 90–94]. One of the most controversial results is that an accelerating Universe in one frame can be mapped in a decelerating one in the other frame [95, 96]. Also, the difference between the two frames appear more evident when scalar perturbations are considered, since they exhibit different evolutionary patterns. In this thesis, we choose to work in the Jordan frame, because it is only derived by the metric $f(R)$ gravity with a simple redefinition of fields.

However, finding exact solutions in modified gravity is much more challenging than in GR since the presence of additional d.o.f. and the non-linearity of the gravitational field equations lead to a non-trivial cosmological dynamics. For instance, field equations in the $f(R)$ gravity are more complicated than the Einstein equations in GR since they include fourth-order derivatives of the metric. On the other hand, in the equivalent formalism in the Jordan frame, the field equations contain only second derivatives of the metric, like in GR, but at the cost of a non-minimal coupling between the scalar field and the metric.

Despite this, considering the simple case of a homogeneous and isotropic geometry, it is possible to find some cosmological exact solutions in the $f(R)$ gravity [83, 97–100].

The advantage of the $f(R)$ gravity is that the extra d.o.f. may, in principle, alleviate or solve the aforementioned open problems in cosmology. For example, there is no need to introduce ad hoc a cosmological constant or DE in the content of the Universe, but the current cosmic accelerated phase may be provided by specific $f(R)$ functional forms developed by Hu and Sawicki [101, 102], Starobinski [103], and Tsujikawa [104]. Indeed, a different geometrodynamics theory leads to a change in the geometrical side of the Einstein field equations, and this modification can be interpreted as the presence of an effective matter source or fluid: the non-Einsteinian terms play the same role as the DE component. Other proposals of $f(R)$ theories have been investigated, such as alleviating the Hubble constant tension [68, 105, 106]. With the increasing number of new $f(R)$ models and proposals, it is crucial to test gravity in different regimes to highlight possible intrinsic features of a specific model, to discriminate between the ΛCDM scenario and alternative cosmological models based on the $f(R)$ gravity. It should be noted that a viable $f(R)$ model in cosmology should be tested to pass local and cosmological constraints [104, 107]. Moreover, it should mimic a cosmological constant and admit a smooth limit to the ΛCDM model.

Regarding the consequences of the second pillar of the concordance model, it is important to note that the cosmological principle is not spatially invariant at any scale. As previously mentioned, the homogeneity scale is approximately 100 Mpc [48, 49]. Therefore, deviations from the FLRW metric may occur as a result of local inhomogeneities on smaller scales [108, 109]. This thesis focuses on two different approaches to incorporate the impact of local inhomogeneities into cosmological dynamics.

Firstly, a metric approach is employed to describe deviations from a homogeneous Universe. For instance, the Lemaître-Tolman-Bondi (LTB) metric [24, 110–113] can describe a non-static spherically symmetric Universe when the central observer is located in a privileged point. It should be emphasized that the LTB metric only describes an isotropic universe if viewed from a specific preferred point, which is the center that emerges from spherical symmetry. This fact locally breaks the cosmological principle for the preferred point when the LTB model is implemented on spatial scales below ~ 100 Mpc. Nevertheless, the description of a homogeneous Universe and the cosmological principle are recovered asymptotically far enough from that privileged point. The ΛLTB model, which includes a cosmological constant Λ in the LTB metric, can be considered a (simplified) generalization of the ΛCDM paradigm for a locally inhomogeneous Universe.

The LTB solution can be useful for describing the evolution of a cosmological dust when it is regarded locally as a pressureless spherical underdensity compared to the mean matter density of the Universe, according to the so-called local void or Hubble-bubble model [114]. These underdense regions are partially disconnected from the present cosmic accelerating expansion, the Hubble flow, due to local gravitational effects. In such a description of an inhomogeneous Universe, the cosmic expansion rate changes, and the Hubble constant depends on the radial coordinate, where the radius is the distance from the center of the LTB spherical symmetry. Cosmologists have investigated the ΛLTB model not only to study local deviations from a homogeneous Universe [115–120] but also to determine whether and to what extent the Hubble constant tension is affected by local inhomogeneities or voids [121–125]. Indeed, a matter underdensity causes galaxies within it to move away faster from the center of the symmetry than galaxies outside the local void, which instead follow the Hubble flow. These studies have also been motivated by recent observations that have pointed to evidence of a local void around our position in the Universe [126–128].

In terms of the second approach for accounting for deviations from spatial homogeneity in the Universe, the focus is on assessing the impact of local inhomogeneities on cosmological observables, such as the luminosity distance or number counts. The large-scale structure (LSS) must be explored through non-linear physics either via analytical perturbative studies or numerical simulations. Analytical studies improve our understanding of the physics underlying non-linear processes within perturbation theory, while numerical simulations can fully describe non-linearities. The results obtained from these two methods of investigation can be compared within the viable regime of perturbation theory.

Concerning analytical approaches to evaluate fluctuations in galaxy clustering, galaxy density and matter perturbations, the pioneering works with linearized perturbations were presented in [129–132]. Then, a significant development has been provided to extend the relativistic description of LSS to higher orders in perturbation theory [133–138]. On the other hand, concurrently, considerable efforts have been made in full relativistic simulations [139] and also the choice of proper gauges to use Newtonian simulations [140, 141]. In particular, the numerical code *gevolution* [139] is based on N-body numerical relativistic simulations, which provide a valuable arena for the cosmic structure formation.

Furthermore, it should be kept in mind that most of the observations and information inferred from cosmological probes is closely related to photons, which are emitted and detected in a local inhomogeneous Universe. Photons paths are affected by the presence of cosmic structures during their travels on large scales along null geodesics. To describe the propagation of light in a clumpy Universe and the resulting observable features, it is crucial to understand the interplay between photons and cosmic structures.

Consequently, the luminosity distance deviates from a homogeneous and isotropic scenario, leading to the introduction of bias and scatter in the Hubble-Lemaître diagram due to gravitational lensing, peculiar velocities, and selection effects [142–151]. Additionally, non-linear relativistic effects produce non-Gaussian features in the matter distribution, which imply further corrections in the Hubble-Lemaître diagram, also in the form of post-Born effects or bispectrum terms [135, 152–154]. The impact of post-Born corrections were also studied referring to the CMB power spectra [155–161] and shear weak lensing [162–165] .

It should be emphasized that a recent study [166] based on the abovementioned numerical code *gevolution* highlights the presence of non-Gaussian effects in the probability distribution function (PDF) of the luminosity distance through a non-perturbative approach. In other words, the study revealed discrepancies between the luminosity distance in a homogeneous and isotropic model and the reconstructed luminosity distance that accounts for the LSS. Specifically, the normalized PDF of the luminosity distance exhibits non-Gaussian features at low redshifts.

To properly consider the impact of inhomogeneities with a robust theoretical framework and, at the same time, understand the results from numerical simulations, it is advisable to consider the statistical properties of cosmological observables. In this regard, the distribution of cosmic structures across the sky should be considered not only in a geometrical way by performing averages on space-time regions, but also including intrinsic stochastic fluctuations. The averaging formalism in cosmology enables the description of the geometry and dynamics of the Universe on large scales, starting from local small scales through a space-time foliation.

A first study of the averaging formalism on space-like hypersurfaces was introduced by Buchert in the context of the backreaction problem in cosmology [167–169]: after the averaging process, additional contributions appear in the dynamics of the Universe on large scales in comparison to a purely homogeneous scenario. This fact is due to the non-linearity of Einstein gravitational field equations; indeed, the average process and time evolution do not commute. In the original formalism by Buchert, the extra term, i.e., the backreaction parameter, assumes the role of a cosmological constant in the averaged Friedmann equations. However, these initial attempts to find an alternative explanation for Λ through the backreaction are now regarded as unreliable, since the occurrence of extreme inhomogeneities, which are not observed [121, 125], would be necessary.

Nevertheless, the Buchert formalism served as a useful starting point for the development of a more general average prescription. Recently, the authors of papers [170–175] have devised a covariant and gauge-invariant mathematical prescription to average scalar quantities on the past-light cone of the observer. This averaging formalism provides a powerful tool to describe the impact of inhomogeneities on cosmological observables.

Method and outline of the thesis

This thesis aims to discuss the two pillars of the concordance model, i.e. GR and the cosmological principle, by adopting different strategies to investigate the robustness of each pillar. We also explore possible close scenarios with respect to the ΛCDM model, such as modified gravity theories and inhomogeneous cosmologies, considering slight deviations from the two pillars and their consequences.

In this regard, we focus on an open problem in cosmology, such as the Hubble constant tension, since anomalies and irregularities might suggest how to reconsider our theoretical understanding of the Universe. For instance, the discrepancy between high and low redshifts data for measurements of H_0 and the S_8 parameter could point out a possible redshift dependence not considered so far in the vanilla ΛCDM model, which may be detected by using cosmological probes in a given redshift range.

Hence, having in mind the Hubble constant tension, we perform a binned analysis in the redshift space of the Pantheon sample [176], a large compilation of 1048 spectroscopically confirmed SNe Ia, to see if the H_0 tension persists also throughout the Pantheon sample redshift range, $0 < z < 2.26$. The basic idea is to divide the Pantheon sample into redshift bins and check the values of H_0 inferred from statistical analysis for each bin. The idea of a binned analysis of H_0 with redshift was first discussed by [177–179].

Then, we use the Markov Chain Monte Carlo (MCMC) method, assuming a luminosity distance for a flat cosmology both in the ΛCDM and $w_0 w_a$CDM models. The Hubble constant should be obviously constant by definition, and we do not know why independent measurements give us different values of H_0. The advantage of our approach is that we can fit the value of H_0 in each redshift bin, and we show that there is a weak dependence of H_0 on redshift, which is not consistent with zero within more than 1σ. Our results seem to suggest the existence of an effective Hubble constant that may evolves with z, hence changing its value according to the cosmic distance of the sample. Specifically, it should be noted that a slowly decreasing trend of an effective Hubble constant running with the redshift may successfully match the values of H_0 obtained from local probes (low redshifts $z \sim 0-2$) and CMB data (high redshift, $z = 1100$).

The possible time-evolving Hubble constant could be due to astrophysical selection effects or a possible hint of modified gravity theories, a signal of breakdown of the standard cosmology. For instance, the $f(R)$ gravity in the Jordan frame could mimic an effective Hubble constant that evolves with the redshift, as a consequence of the non-minimally coupled scalar field dynamics. Then, we derive the profile of the scalar field potential, associated to the $f(R)$ functional form, able to provide both the present cosmic acceleration, as DE, and also an effective Hubble constant.

Another key point of this thesis is the development of a new method to theoretically discriminate between the ΛCDM model and $f(R)$ modified gravity theories. More specifically, we discuss the evolution of inhomogeneous perturbations implementing the LTB metric within the framework of the ΛLTB scenario and alternative inhomogeneous cosmological models based on the $f(R)$ gravity. We can evaluate the role of a cosmological constant and a scalar field in the Jordan frame, since the evolution of inhomogeneous perturbations in the local Universe strictly depends on the cosmological model considered.

The idea to combine inhomogeneous cosmological models with modified gravity theories in the late Universe to address the Hubble tension is challenging but, perhaps, necessary since local inhomogeneities can only alleviate the tension, as already mentioned. Then, we should consider the combination of more non-standard effects, such as modified gravity and inhomogeneous cosmology. In this regard, it is crucial to find a method to discriminate between $f(R)$ theories and the standard cosmological paradigm within inhomogeneous metric.

Finally, an important result of this thesis concerns the changes in the PDF of cosmological observable due to distribution of matter and local effects in a clumpy Universe. In particular, we will focus on the presence of non-Gaussianities in the LSS and in the Hubble-Lemaître diagram. It should be stressed again that so far only numerical relativistic simulations [166] have provided evidence of non-Gaussianities in the PDF of the luminosity distance, but it is certainly interesting and worthwhile to build concomitantly a theoretical framework to better understand these effects and, then, obtain analytical expressions for a comparison with numerical simulations.

In this regard, bearing in mind the general average prescription in cosmology over the past light-cone [174], we will present a general method to evaluate analytically non-Gaussianities in the Hubble-Lemaître diagram. The key point of this part is the analytical computation of the moments for a generic scalar observable, such as the luminosity distance, averaged over a portion of space-time, following a perturbation approach. In particular, the non-trivial higher-order moments, such as the skewness, related to non-Gaussianities provide essential information about the LSS and signatures of the interplay between photons and cosmic structures.

This thesis is structured in three main parts.

In the Part I, we provide a general overview of the basic elements we need in our main analysis. Specifically, we introduce the standard ΛCDM cosmological model in Chapter 1, focusing on the Universe components, its metric properties, and cosmological dynamical consequences. Also we present the $f(R)$ modified gravity theories, especially in the Jordan frame, to highlight deviations with respect to the ΛCDM model. As a particular application, we present the $f(R)$ Hu-Sawicki (HS) model as an alternative proposal to describe the late-time cosmic acceleration. In Chapter 2, we investigate local inhomogeneities of the Universe. Firstly, we adopt the LTB metric and we derive the cosmological dynamics in such a inhomogeneous scenario. Then, we present the averaging problem in cosmology. We start to present the original concept of the backreaction and we conclude this chapter providing a general prescription to average scalar quantities in the space-time in a gauge-invariant and covariant formulation.

Part II is devoted to the first original investigations of our work concerning the Hubble constant tension. In Chapter 3, we perform a redshift binned analysis of the Pantheon sample of SNe Ia to extract the H_0 values as the only free parameter inside each bin. We show an unexpected slowly decreasing trend of H_0 with the redshift. In Chapter 4, we extend the analysis including BAOs data. In Chapter 5, we explore the possibility to depict an effective GR picture to interpret our previous results theoretically. We build an effective Hubble constant that evolves with the redshift within the $f(R)$ metric gravity in the Jordan frame through the effect of a non-minimally coupled scalar field. Moreover, we infer the shape of the scalar field potential in such a scenario.

In the Part III, we discussed the role of local inhomogeneities of the Universe and their impact on cosmological measurements. In Chapter 6, we characterize the geometry of the Universe by adopting the LTB spherically symmetric solution, and we investigate the evolution of linear perturbations in inhomogeneous cosmological models based on GR or $f(R)$ modified gravity theories. In Chapter 7, we develop a method to predict and compute analytically the skewness of the luminosity distance PDF, which provides useful information about non-Gaussianities in the observable Universe.

Finally, we summarize the main results of this thesis and present the conclusions on page 129.

Part I

General overview

Chapter 1

Cosmological models based on General Relativity and beyond

A gravitational theory is a crucial element in developing a cosmological model since all theoretical predictions and cosmological dynamics are governed by the underlying gravitational laws. In this chapter, we present cosmological models based on GR, such as the ΛCDM model and dark energy models, and those rely on alternative gravitational theories to highlight their differences. We provide an overview of the essential principles and concepts of physical cosmology that are relevant for the ideas covered in the following chapters. We introduce the geometry of a homogeneous and isotropic Universe through the FLRW metric and the main matter and energy constituents to derive in such a scheme all cosmological consequences in the dynamics and in evaluating cosmic distances. We outline how a cosmic distance is evaluated and the main statistical properties in the matter distribution, which are relevant elements not only for formal aspect but also for observational evidence. Indeed, cosmological observables and measurements help to constrain cosmological models. We also address the main open problems associated with the ΛCDM model, such as the Hubble constant and matter fluctuations tensions. Then, we conclude the chapter by exploring alternative models involving $f\,(R)$ modified gravity theories.

1.1 The cosmological concordance model

The cosmological concordance model is based on GR, which is regarded as the gravitational theory able to describe the dynamics of the Universe. In such a framework, the gravitational action is given by the well-known Einstein-Hilbert action with the cosmological constant term Λ:

$$S_g = \frac{1}{2\,\chi} \int d^4x\, \sqrt{-g}\, \left(R - 2\Lambda\right) \,, \tag{1.1}$$

in which R is the Ricci scalar, χ is the Einstein constant, and g is the determinant of the metric tensor with components $g_{\mu\nu}$ (see the list of conventions adopted in this thesis on page vii). Note that $d^4x\,\sqrt{-g}$ is a covariant volume element in the space-time. We have added explictly a constant term related to Λ in the gravitational Lagrangian density.

Including also the matter source with matter fields ψ, which is specified by the matter action $S_M\left(g_{\mu\nu}, \psi\right)$, the total action is given by $S_{\text{tot}} = S_g + S_M$. Then, performing variation of the action $\delta S_{\text{tot}} = 0$ with respect to the metric, we obtain the well-know Einstein-Hilbert gravitational field equations [12, 35]

$$G_{\mu\nu} + \Lambda\, g_{\mu\nu} = \chi\, T_{\mu\nu} \,, \tag{1.2}$$

which includes also the cosmological constant term[1]. The Einstein tensor is denoted with $G_{\mu\nu}$.

The stress-energy tensor $T_{\mu\nu}$ of the matter components on large scales is usually represented as a cosmological perfect fluid, since the dissipative processes are relevant only for short-time transitions in the early Universe. Then, we use the expression of $T_{\mu\nu}$ for a perfect fluid:

$$T_{\mu\nu} = (\rho + p)\; u_\mu \, u_\nu + p\, g_{\mu\nu}\,, \tag{1.3}$$

in which u_μ is the fourth-velocity, p and ρ are the pressure and the energy density of the cosmological fluid, respectively. We adopt a comoving reference frame in which the fourth-velocity is referred to an observer that is moving together with the cosmological fluid.

1.1.1 The Friedmann-Lemaître-Robertson-Walker metric

We recall that the Universe can be considered spatially homogeneous and isotropic on sufficiently large scales, according to the cosmological principle, which we have named the second pillar of the ΛCDM model in the Introduction. As a consequence, GR would imply that the matter distribution in the Universe must also be homogeneous and isotropic. See [35, 52, 180] to derive the form of the metric describing such a geometry. Now we briefly review its main peculiarities.

We consider a set of comoving observers, each of them is moving with the matter flow averaged on sufficiently large scales such as to neglect local deviations from homogeneity. We can select an arbitrary fundamental observer O and the set of all observer O', which are located at a given fixed distance from O at some given local time measured by O. Because of the spatial isotropy, the velocity field does not have any preferred direction, and all the observer O' must remain equidistant from O for any time, hence they must measure the same local value of any physical quantities. Another consequence of the isotropy is that, if all the observer O' use light signals from O, they can in principle synchronize their clocks. Since the choice of the fundamental observer O is arbitrary due to spatial homogeneity, we can repeat this construction of observers in any point of the Universe. As a result, physical quantities and local properties are well-defined on a three-dimensional hypersurface in space-time and evolve over it according to a universal time, the cosmic time t.

In the light of this, it is useful to consider an evolving three-sphere embedded in a four-dimensional space-time, the radius which is denoted with $\mathcal{R}\,(t)$ as a function of the cosmic time t. We now introduce the proper radius $\mathcal{R}_0$, whose value is invariant according to the set of comoving observers, and the scale factor $a\,(t)$, which tells us how a distance evolves with t over cosmological scales. Then, the radius of the three-sphere can be written as $\mathcal{R}\,(t) = a\,(t)\;\mathcal{R}_0$.

Furthermore, the curvature parameter of the three-dimensional surface is defined as

$$k = \frac{1}{\mathcal{R}_0^2}\,, \tag{1.4}$$

which assumes positive, null, or negative values in a spherical, flat, or hyperbolic topology (hypersphere, hyperplane, or hypersaddle), respectively. Concerning the physical dimension[2], we consider a dimensionless scale-factor $a\,(t)$, hence we must have $[\mathcal{R}_0] = [L] = [r]$ and $[k] = [L]^{-2}$.

Since the homogeneous and isotropic three-dimensional surfaces can be regarded as space-like hyper-

---

[1] We recall that in the original proposal of GR there is no a cosmological constant, and Einstein introduced Λ to describe a cosmological static model, as we mentioned in the Introduction. Note that the addition of $\Lambda\, g_{\mu\nu}$ in Einstein field equations is consistent with the general covariance principle. Indeed, if we calculate the covariant derivatives on both sides of (1.2), we end up in a trivial null identity, since geometrical properties, such as the contracted Bianchi identities $\nabla_\mu G^{\mu\nu} = 0$ and Ricci's theorem $\nabla_\mu g^{\mu\nu} = 0$, and the energy-momentum conservation $\nabla_\mu T^{\mu\nu} = 0$ are taken into account.

[2] It is also possible to consider a scale factor with the lenght dimension, but in that case the radial coordinate r must be dimensionless. In this thesis, we decide to work with a dimensionless scale factor.

surfaces labelled by different cosmic times t, it can be shown that the four-dimensional line element of a general curved space-time is written as:

$$ds^2 = -dt^2 + a^2\left(t\right)\left[\frac{1}{1-k\,r^2}dr^2 + r^2\,\left(d\theta^2 + \sin^2\theta\,d\phi^2\right)\right]\,. \tag{1.5}$$

This is the well-known FLRW metric, which provides the solution of the Einstein field equations that describes the geometry of a homogeneous and isotropic Universe[3]. It should be emphasized that the metric (1.5) should be referred to a geometrical description of the Universe on large scales, above $\sim 100\,\mathrm{Mpc}$, where on average local deviations from homogeneity are negligible.

We also stress again that (r,θ,ϕ) are comoving coordinates and the three-dimensional surfaces are comoving, hence these surfaces are expanding following also the evolution of the distribution of matter on average. Thus, except for small local deviations from spatial homogeneity, there is no net outflow of matter through the three-dimensional surfaces. We recall that the curvature parameter k depends on the topology of the Universe: $k=0$ for a flat cosmology, $k>0$ for a closed Universe, and $k<0$ for an open Universe. Note that for $k\neq 0$ it is always possible to rescale the metric (1.5) through $a\left(t\right)\to a\left(t\right)/\sqrt{|k|}$ and $r\to\sqrt{|k|}\,r$ such that we can simply narrow down to $k=+1,-1$ (in units of $\mathcal{R}_0^2$) for a closed and open Universe, respectively.

The FLRW metric can be rewritten in another useful form by adopting the comoving distance instead of the comoving coordinate r. Without any loss of generality, we consider two observers, one located at the origin $r=0$ and the other one at (r,θ,ϕ). The proper (spatial) distance d between them in the FLRW metric (1.5) for any arbitrary cosmic time is

$$d\left(t\right) = a\left(t\right)\int_0^r \frac{dr'}{\sqrt{1-k\,r'^2}} \equiv a\left(t\right)\,D_c\left(r\right)\,. \tag{1.6}$$

In the last equality, we have introduced the comoving distance $D_c\left(r\right)$ as the proper distance in units of $a\left(t\right)$. The proper distance evaluated at the cosmic time t_0 today is exactly equal to the comoving distance, since the standard convention for the present scale factor is adopted: $a_0 = a\left(t_0\right) = 1$. Note the physical dimension $[D_c]$=$[L]$. By solving the integral in (1.6) for different values of k, it is straightforward to obtain the relation between the comoving coordinate r and the comoving distance D_c:

$$r\left(D_c\right) = \begin{cases} \frac{1}{\sqrt{k}}\sin\left(\sqrt{k}\,D_c\right) & k>0 \\ D_c & k=0 \\ \frac{1}{\sqrt{|k|}}\sinh\left(\sqrt{|k|}\,D_c\right) & k<0\,. \end{cases} \tag{1.7}$$

Then, the FLRW metric (1.5) becomes:

$$ds^2 = -dt^2 + a^2\left(t\right)\,\left[dD_c^2 + S_k^2\left(D_c\right)\,\left(d\theta^2 + \sin^2\theta\,d\phi^2\right)\right]\,, \tag{1.8}$$

where the function $S_k\left(D_c\right)\equiv r\left(D_c\right)$. Considering Eq. (1.7), we get

$$S_k\left(D_c\right) = \frac{1}{\sqrt{k}}\sin\left(\sqrt{k}\,D_c\right) \tag{1.9}$$

whatever the value of k (including $k<0$ with the sine of a complex number).

---

[3] Note that the metric (1.5) is written in the synchronous gauge [35], where $g_{00}=-1$, and this fact enables us to define a universally agreed cosmic time, as we mentioned above. In addition, the requirement for the metric tensor components $g_{0i}=0$ is perfectly consistent with the cosmological principle, otherwise a preferred direction would be introduced. In other words, the scale factor $a\left(t\right)$ evolves in the same way along any spatial directions and is only a function of the cosmic time t in a homogeneous and isotropic scenario, due to spatial isotropy.

Understanding the evolution of the scale factor in terms of the Universe components in GR is one of the main purpose of cosmology, but before moving on cosmological dynamics we focus on some kinematic properties of the Universe on large scales, which can be derived directly from the form of the FLRW metric and are based only on the cosmological principle. In the following section, we discuss these kinematic properties.

1.1.2 The cosmological redshift and the Hubble law

Mostly astronomical observations rely on detecting light signals, hence it is crucial to investigate how photons travel in a homogeneous and isotropic Universe. We adopt the FLRW metric (1.5), and we consider, for simplicity, a photon travelling radially from a source to an observer located in the origin. We recall that photons travel along null geodesic with $ds^2 = 0$, hence we obtain from Eq. (1.5)

$$ds^2 = -dt^2 + a^2\left(t\right)\,\frac{dr^2}{1 - k\,r^2} = 0\,. \tag{1.10}$$

Furthermore, since the photon is approaching the observer, its proper distance decreases with time. Hence, we must choose a minus sign after taking the square root of Eq. (1.10), i.e.,

$$dt = -a\left(t\right)\,\frac{dr}{\sqrt{1 - k\,r}}\,. \tag{1.11}$$

We can rewrite the comoving distance $D_c\left(r_e\right)$, defined implictly in in Eq. (1.6), between an observer in the origin and a source located in $\left(r_e, \theta, \phi\right)$ as

$$D_c\left(r_e\right) = \int_0^{r_e} \frac{dr}{\sqrt{1 - k\,r}} = \int_{t_e}^{t_0} \frac{dt}{a\left(t\right)}\,. \tag{1.12}$$

We denote with r_e the radial coordinate of the source that produces light signals at the emission time t_e, which are revealed by the observer today at the time t_0. Since D_c does not depend on the cosmic time, we can adopt (1.12) for referring to a successive light signal emitted from the same source at the time $t_e + \delta t_e$ and revealed by the observer in the origin at the time $t_0 + \delta t_0$, with $\delta t_e \ll t_e$ and $\delta t_0 \ll t_0$. In particular, we can consider two light signals as succesive wave crests. Thus, it is straightforward to obtain that the observed and emitted frequencies or wavelengths are related to the change of the scale factor:

$$\frac{\nu_0}{\nu_e} = \frac{\lambda_e}{\lambda_0} = \frac{a\left(t_e\right)}{a\left(t_0\right)}\,, \tag{1.13}$$

where $\nu_0 = 1/\delta t_0$ and $\nu_e = 1/\delta t_e$. In particular, note that if $a\left(t\right)$ is increasing, i.e., an expanding Universe, then $a\left(t_0\right) > a\left(t_e\right)$, and we obtain a redshifted signal: $\nu_0 < \nu_e$. It should be also emphasized that a redshift implies a time dilation between the observed and emitted signals.

The cosmological redshift parameter z is a dimensionless quantity defined as the relative change of wavelength:

$$z \equiv \frac{\lambda_0 - \lambda_e}{\lambda_e}\,. \tag{1.14}$$

Then, we obtain the well-known relation between the cosmological redshift z and the scale factor

$$\frac{a_0}{a\left(t\right)} = 1 + z\,, \tag{1.15}$$

where the subscript 0 denotes the cosmic time today t_0 at the redshift $z = 0$, and we have referred to a generic emitted time t. Note that $z > 0$ in an expanding Universe for $t < t_0$, by definition. Observable quantities, like the redshift, are related to the ratio between different values of $a\left(t\right)$ measured at different times. Moreover, a cosmological observable that depends on t could be equivalently rewritten as a function of a or z.

For nearby sources characterized by $z \ll 1$ and $t \lesssim t_0$, we can expand $a\left(t\right)$ in a power series as

$$a\left(t\right) \approx a\left(t_0\right) + \dot{a}\left(t_0\right)\,\left(t - t_0\right) + \ldots\,, \tag{1.16}$$

which also leads to

$$z \approx H_0\,\left(t_0 - t\right) + \ldots \approx H_0\,d_L + \ldots\,. \tag{1.17}$$

An over-dot denotes the derivative with respect to the cosmic time t, and we have used Eq. (1.15). The coefficient H_0 is known as the Hubble constant:

$$H_0 \equiv \frac{\dot{a}\left(t_0\right)}{a\left(t_0\right)}\,. \tag{1.18}$$

More generally, the Hubble parameter $H\left(t\right)$ is defined as

$$H\left(t\right) \equiv \frac{\dot{a}\left(t\right)}{a\left(t\right)} = \frac{d}{dt}\left[\ln a\left(t\right)\right]\,, \tag{1.19}$$

and gives us information about the logarithmic evolution of the scale factor with t. The Hubble constant H_0 is nothing more than the Hubble parameter evaluated today at $t = t_0$ or $z = 0$.

In the last step of Eq. (1.17), we wrote the luminosity distance $d_L \approx t_0 - t$ for $t \approx t_0$ (see Sect. 1.1.5). We interpret the cosmological redshift as the Doppler effect, in which the sources are galaxies moving with (non-relativistic) velocities v_{G} with respect to the observer in the origin and signals are photons, thus z is also given by the ratio between the relative velocity and the speed of light, i.e., $z = v_{\mathrm{G}}$. Finally, we obtain the well-known Hubble-Lemaître law [26] from Eq. (1.17):

$$v_{\mathrm{G}} = H_0\,d_L\,, \tag{1.20}$$

which was originally formulated from empirical evidences, but it could be predicted for an expanding Universe in the FLRW metric. The Hubble constant H_0 has the dimensions of a frequency, $\left[H_0\right] = \left[T\right]^{-1}$, but is is usually expressed in units of km $\mathrm{s}^{-1}\mathrm{Mpc}^{-1}$ according to the units of galaxies velocities and distances used in the Hubble-Lemaître law (1.20). Conventionally, quantities related to H_0 are often indicated in terms of the following dimensionless parameter:

$$h = \frac{H_0}{100\,\mathrm{km\ s^{-1}Mpc^{-1}}}\,.$$

The standard value of H_0 is commonly set to $\sim 70\,\mathrm{km\ s^{-1}Mpc^{-1}}$. However, inferring an unanimous value of H_0 from cosmological probes is a challenging effort since discrepancies have recently emerged from different measurements, as we discuss in Sect. 1.1.7.

It should be emphasized that a change in the photon wavelength is similar to the Doppler effect, which naturally implies a redshift or blueshift, if sources are receding from the observer or approaching, respectively. However, the cosmological redshift is not due to a simple relative motion between the source and the observer, but it is a geometrical effect as a result of the Universe expansion, the Hubble flow. Indeed, galaxies coordinates are fixed for a comoving observer (radial coordinates and comoving distances are fixed in time in the FLRW metric), but their mutual distances change because the space-time geometry evolve with time.

Similarly, expanding Eq. (1.16) up to the second order in z, we obtain

$$d_L\left(z\right) \simeq \frac{1}{H_0}\left[z+\frac{1}{2}\left(1-q_0\right)z^2\right]+\dots\,, \tag{1.21}$$

where q_0 is called the deceleration parameter:

$$q_0 \equiv -\frac{\ddot{a}}{a\,H^2}\bigg|_{t=t_0} = -\frac{\ddot{a}\,a}{\dot{a}^2}\bigg|_{t=t_0}\,. \tag{1.22}$$

This quantity was originally defined with a minus sign for historical reasons. Indeed, it was commonly believed that the Universe was expanding in a decelerated phase today, hence $\ddot{a} < 0$ and $q_0 > 0$. Actually, the breakthrough discovery of the accelerated expansion of the Universe [36, 37] has provided the opposite result: $\ddot{a} > 0$ and $q_0 < 0$.

1.1.3 Cosmological dynamics of the homogeneous and isotropic Universe

The Einstein-Hilbert gravitational field equations (1.2) employed on the FLRW metric (1.5) provide two independent equations, i.e. the Friedmann equations [35]:

$$H^2\left(t\right) \equiv \left(\frac{\dot{a}\left(t\right)}{a\left(t\right)}\right)^2 = \frac{\chi\,\rho_{\mathrm{tot}}\left(t\right)}{3} - \frac{k}{a^2\left(t\right)} \tag{1.23}$$

$$\frac{\ddot{a}\left(t\right)}{a\left(t\right)} = -\frac{\chi}{6}\left(\rho_{\mathrm{tot}}+3\,p_{\mathrm{tot}}\right)\,, \tag{1.24}$$

in which $p_{\mathrm{tot}}\left(t\right)$ and $\rho_{\mathrm{tot}}\left(t\right)$ are the total pressure and energy density of the cosmic source. In particular, the first Friedmann equation (1.23) was obtained from the $0-0$ component of the Einstein field equations (1.2), while the second Friedmann equation (1.24), also commonly named the cosmic acceleration equation, was derived from the $1-1$ component of (1.2) combined with Eq. (1.23). It should be emphasized that $p_{\mathrm{tot}}\left(t\right)$ and $\rho_{\mathrm{tot}}\left(t\right)$ depend only on the cosmic time t, due to spatial isotropy. For the sake of brevity, note that in the Friedmann equations (1.23) and (1.24) we have implicitly redefined the cosmological constant term as a fluid[4] with energy density $\rho_\Lambda = \Lambda/\chi$ and pressure $p_\Lambda = -\rho_\Lambda$. Then, the total energy density $\rho_{\mathrm{tot}} = \rho_{\mathrm{m}} + \rho_{\mathrm{r}} + \rho_\Lambda$ is provided by different components: matter (m), radiation (r), and the cosmological constant Λ.

Moreover, the energy conservation law results from the continuity equation

$$\dot{\rho}_{\mathrm{tot}} + 3\,H\,\left(\rho_{\mathrm{tot}} + p_{\mathrm{tot}}\right) = 0\,, \tag{1.25}$$

or the divergenceless law of the stress-energy tensor $\nabla_\mu T^{\mu\nu} = 0$ for $\nu = 0$ in the FLRW metric. Alternatively, Eq. (1.25) could be also derived from the laws of thermodynamics, considering the Universe as a closed system [181]. The continuity equation (1.25) allows us to describe the evolution of the matter-energy sources. Actually, this equation is not independent of the two Friedmann equations (1.23) and (1.24), since it can be obtained by combining them, specifically after taking the time derivative of both sides of Eq. (1.23).

Furthermore, the equation of state outlines the relation between p_i and ρ_i for various species, which for a barotropic fluid is simply written as $p_i\left(\rho\right) = w\,\rho_i$. The equation of state parameter w_i takes different values according to the component considered: $w_{\mathrm{m}} = 0$, $w_{\mathrm{r}} = 1/3$, and $w_\Lambda = -1$.

---

[4] Adopting this choice, the gravitational action in Eq. (1.1) and the Einstein-Hilbert equations (1.2) can be rewritten without an explicit cosmological constant Λ in the geometrical part, but including an additional cosmological fluid in the source.

Once the equation of state is taken into account separately for different components, it is possible to solve the cosmological dynamics in the FLRW metric with two quantities to be determined: $a\,(t)$ and $\rho_{\text{tot}}\,(t)$. In particular, the matter component evolves according to the following well-known relation

$$\rho_m\,(a) = \frac{\rho_{m0}}{a^3}\,, \qquad \rho_m\,(z) = \rho_{m0}\,\left(1+z\right)^3\,, \tag{1.26}$$

while the radiation component follows a different power-law dependence

$$\rho_r\,(a) = \frac{\rho_{r0}}{a^4}\,, \qquad \rho_r\,(z) = \rho_{r0}\,\left(1+z\right)^4\,, \tag{1.27}$$

as it can be easily checked by solving the continuity equation (1.25) for each component. Differently, if $w_\Lambda = -1$, the energy density ρ_Λ is a constant:

$$\rho_\Lambda = \rho_{\Lambda 0}\,. \tag{1.28}$$

By solving the Friedmann equation (1.23) for a flat cosmology taking into account the different evolution of components, it is straightforward to obtain the following solution

$$a\,(t) \propto t^{2/3} \tag{1.29}$$

for a matter dominated Universe (Einstein-de Sitter model), while we get

$$a\,(t) \propto t^{1/2} \tag{1.30}$$

for a radiation dominated Universe. Note that for both these cases $\rho_i \propto t^{-2}$, where we used Eqs. (1.26) and (1.27). Instead, if the Universe is dominated by the cosmological constant term, the scale factor evolves exponentially with the cosmic time according to de-Sitter solution [30, 35]:

$$a\,(t) = a_0\,e^{\sqrt{\frac{\Lambda}{3}}\,(t-t_0)}\,. \tag{1.31}$$

Note that the cosmological constant provides a cosmic accelerated expansion from Eq. (1.24). This fact can also be explictly pointed out from the expression of the deceleration parameter (1.22) in the cosmological constant dominated Universe

$$q_0 = \left.\frac{\chi\,\left(\rho_{\text{tot}} + 3\,p_{\text{tot}}\right)}{2\,\chi\,\rho_{\text{tot}} - 6\,\frac{k}{a^2}}\right|_{t=t_0} \approx \left.\frac{1}{2}\,\left(1+3\,w_\Lambda\right)\right|_{t=t_0} = -1\,, \tag{1.32}$$

where we used Eqs. (1.23) and (1.24) for a flat cosmology. All these asymptotic functions (1.29), (1.30), and (1.31) of the scale factor might be regarded as useful approximate solutions in different cosmic epochs since dominant and subdominant components changed throughout the cosmic history.

We focus now briefly on the impact of the value of the curvature parameter on the cosmological dynamics in the FLRW metric. It should be noted from Eq. (1.23) that $\dot{a}\,(t) > 0$ and $a\,(t) \neq 0$ for any cosmic time t in the cases of a flat or open Universes. Thus, considering these topologies, the Universe is expected to expand indefinitely. If instead the Universe is closed, there will be a specific cosmic time t_{TP} when the scale factor reaches a turning point and the Universe expansion stops. More specifically, this could happen for $a\,(t_{\text{TP}}) = \sqrt{3/\chi\rho_{\text{tot}}}$, for which $H\,(t_{\text{TP}}) = 0$ and $\ddot{a}\,(t_{\text{TP}}) < 0$. Hence, in this scenario, the Universe expansion achieves a maximum for $t = t_{\text{TP}}$, then the cosmic evolution is reversed. To understand the ultimate fate of the Universe, it is crucial to determine the Universe topology and have better measurements of the curvature parameter k.

Now, we show how to rewrite the Friedmann equation (1.23) in an alternative form. We recall the definition of the dimensionless cosmological density parameters

$$\Omega_i\left(t\right) \equiv \frac{\rho_i\left(t\right)}{\rho_c\left(t\right)} \tag{1.33}$$

for different components i, in which

$$\rho_c\left(t\right) \equiv \frac{3\,H^2\left(t\right)}{\chi} \tag{1.34}$$

is the critical energy density of the Universe.

Therefore, by dividing all terms in both of sides of Eq. (1.23) by H^2, we can rewrite the dimensionless first Friedmann equation:

$$\Omega_{\text{tot}}\left(t\right) + \Omega_k\left(t\right) = 1\,, \tag{1.35}$$

where $\Omega_{\text{tot}}\left(t\right) = \Omega_m\left(t\right) + \Omega_r\left(t\right) + \Omega_\Lambda\left(t\right)$ and the curvature density parameter is

$$\Omega_k\left(t\right) \equiv -\frac{k}{a^2\left(t\right)H^2\left(t\right)}\,. \tag{1.36}$$

In the light of the above discussion about the topology of the Universe, we can distinguish three different cases:

$$\begin{cases} k > 0 \quad \text{if } \Omega_{\text{tot}} > 1 \quad \Longleftrightarrow \quad \rho_{\text{tot}} > \rho_c \quad \text{[overcritical Universe]} \\ k = 0 \quad \text{if } \Omega_{\text{tot}} = 1 \quad \Longleftrightarrow \quad \rho_{\text{tot}} = \rho_c \quad \text{[critical Universe]} \\ k < 0 \quad \text{if } \Omega_{\text{tot}} < 1 \quad \Longleftrightarrow \quad \rho_{\text{tot}} < \rho_c \quad \text{[undercritical Universe]}\,. \end{cases}$$

Now we can understand the physical meaning of ρ_c, which is the total energy density for a flat Universe. Only if the Universe is overcritical, which happens in a closed Universe, the present expansion of the Universe might stop with a turning point. The value of the critical energy density today is $\rho_{c0} \approx 1.05\,\times 10^4\,h^2\,\text{eV cm}^{-3}$ which corresponds to a mass density of $\approx 1.88 \times 10^{-29}\,h^2\,\text{g cm}^{-3}$ [182].

Finally, the Friedmann equation (1.23) can be recast to express the Hubble parameter $H\left(z\right)$ as a function of the redshift z. The general formula is usually written as

$$H\left(z\right) = H_0\,E\left(z\right)\,, \tag{1.37}$$

where $E\left(z\right)$, often called the reduced Hubble parameter, strictly depends on the evolution of the Universe components and incorporates all cosmological parameters within the model considered. For instance, the functional form of $E\left(z\right)$ in the ΛCDM model is given by

$$E\left(z\right) = \sqrt{\Omega_{m0}\,\left(1+z\right)^3 + \Omega_{r0}\,\left(1+z\right)^4 + \Omega_{\Lambda 0} + \Omega_{k0}\,\left(1+z\right)^2}\,. \tag{1.38}$$

We divided both sides of Eq. (1.23) by H_0^2, we wrote explicitly the evolution with the redshift for each component from Eqs. (1.26), (1.27), and (1.28), and we used the definition of ρ_c and Ω_i from Eqs. (1.34), (1.33), and (1.36). Furthermore, the cosmological density parameters evolve with z differently for each component as

$$\Omega_m\left(z\right) = \Omega_{m0}\,\frac{\left(1+z\right)^3}{E^2\left(z\right)}\,, \qquad \Omega_r\left(z\right) = \Omega_{r0}\,\frac{\left(1+z\right)^4}{E^2\left(z\right)}\,, \qquad \Omega_\Lambda\left(z\right) = \frac{\Omega_{\Lambda 0}}{E^2\left(z\right)}\,. \tag{1.39}$$

As we mentioned above for the Friedmann asymptotic solutions, a specific component might be dominant in the cosmic past since the density parameters associated to matter, radiation, and the cosmological constant evolve differently with z. Comparing these functional forms from Eq. (1.39), it is straightforward to obtain the redshift $z_{\rm eq}$ of the matter-radiation equality

$$1+z_{\rm eq}=\frac{\Omega_{m0}}{\Omega_{r0}}\,, \tag{1.40}$$

and the redshift z^* for which the density parameters of matter and the cosmological constant are equal, i.e.,

$$\left(1+z^*\right)^3=\frac{\Omega_{\Lambda 0}}{\Omega_{m0}}\,. \tag{1.41}$$

Note that these redshifts are related only to the present cosmological density parameters. The fractions of matter, radiation, and cosmological constant of the Universe today ($z=0$) are inferred from Planck by using CMB power spectra and CMB lensing reconstruction (see Table 2 from [40]), assuming a flat ΛCDM cosmological model:

$$\Omega_{m0}=0.3153\pm 0.0073\,,\qquad \Omega_{\Lambda 0}=0.6847\pm 0.0073\,,\qquad \Omega_{r0}=(9.27\pm 0.23)\cdot 10^{-5}\,. \tag{1.42}$$

Considering these values, the abovementioned redshifts in Eqs. (1.40) and (1.41) are $z_{\rm eq}=3402\pm 26$ and $z^*=0.295\pm 0.011$, respectively. Thus, the Universe may be regarded as cosmological constant dominated for $z\lesssim z^*$, while it is matter dominated for $z^*\lll z\lll z_{\rm eq}$. Although the current radiation density could be considered negligible, the effects of this component must be taken into account for $z\gtrsim z_{\rm eq}$. It should be emphasized that the matter-radiation equality occurred in the early Universe in a past cosmic epoch before the decoupling of CMB photons from baryons at $z_d=1089.92\pm 0.25$.

1.1.4 Age of the Universe

Determining the values of cosmological parameters allows to estimate the age of the Universe, which is strongly related to the evolution of the Hubble parameter $H\left(z\right)$ and cosmological dynamics. Note that the definition (1.19) introduces a time scale $t_H=H^{-1}$,which is called the Hubble time. The spatial distance covered by a photon in t_H is obtained by extrapolating the linear recession law in Eq. (1.20) to the speed of light, which defines the Hubble length $L_H=t_H$. This typical spatial scale is useful to determine wheter a phenomenon is affected by the cosmic expansion. Note also that $t_0\approx H_0^{-1}=9.785\,h^{-1}$ Gyears is an approximation for the age of the Universe, as we show below.

From the asymptotic solutions (1.29) and (1.30), it is straightfoward to obtain the following relations between the age of the Universe t_0 and the Hubble constant H_0:

$$t_0=\frac{2}{3\,H_0}=6.523\,h^{-1}\,\text{Gyears}\,,\qquad\qquad t_0=\frac{1}{2\,H_0}=4.892\,h^{-1}\,\text{Gyears}\,, \tag{1.43}$$

for matter- and radiation-dominated Universe, respectively. However, to have a better estimate of t_0, we should consider all the components of the Universe in the general case.

Starting from the definitions of redshift (1.15) and the Hubble parameter (1.19), the time derivative of the redshift is written as

$$\frac{dz}{dt}=-\left(1+z\right)\,H\left(z\right)\,. \tag{1.44}$$

Then, we can compute the cosmic time for a given redshift:

$$t\left(z\right)=\int_z^{+\infty}\frac{dz'}{\left(1+z'\right)\,H\left(z'\right)}=\frac{1}{H_0}\int_z^{+\infty}\frac{dz'}{\left(1+z'\right)\,E\left(z'\right)}\,. \tag{1.45}$$

We have assumed that when we approach the initial cosmic time (Big Bang), the Universe expansion began with $a\to 0$ for $t\to 0$, hence $z\to+\infty$. Once $H\left(z\right)$, or equivalently $E\left(z\right)$, is specified within a cosmological model, it is possible to determine $t\,(z)$. For instance, in a ΛCDM model we get

$$t\,(z) = \frac{1}{H_0} \int_0^{\frac{1}{1+z}} \frac{dx}{x\,\sqrt{\Omega_{m0}\,x^{-3} + \Omega_{r0}\,x^{-4} + \Omega_{\Lambda 0} + \Omega_{k0}\,x^{-2}}}\,, \tag{1.46}$$

where we have used Eq. (1.38) and the change of variable, $x = (1+z)^{-1}$. Finally, we obtain the expression of the age of the Universe t_0 for $z = 0$. As we mentioned above, $t_0 \approx H_0^{-1}$ is only an approximation. Note also that the relations (1.43) are recovered for a matter- and radiation-dominated Universe in a flat cosmology. In the general case, t_0 must be computed numerically. Considering the values in Eq. (1.42) inferred by Planck [40], the present estimate for the age of the Universe is $t_0 = 13.797 \pm 0.023\,\text{Gyears}$.

1.1.5 Luminosity distance and angular diameter distance

In this section, we define distances as we consider the luminous flux emitted by a far source at large redshifts $z \gtrsim 0.1$, for which the impact of the cosmic expansion must be taken into account.

Astrophysical objects such as SNe Ia are characterized by a fixed absolute luminosity, hence measuring the apparent luminosity it is possible to determine the distance of the source. The absolute luminosity L is the power emitted by a light source, i.e., the energy emitted per unit of time, while the apparent luminosity l is the luminous flux seen from Earth, i.e., the energy received per unit of time and receiving area.

If we consider an isotropic Universe in Euclidean geometry (no cosmic expansion), then the emitted energy equally redistributes through a spherical source towards the observer located at a distance d from the source. Thus, the relation between L and l is given by

$$l = \frac{L}{4\,\pi\,d^2}\,. \tag{1.47}$$

For an expanding Universe, this relation between luminosities mediated by a distance has to be generalized at large distances by considering three modifications. Firstly, the distance d should be replaced by the effective radial distance measured today $a\,(t_0)\;r$, where r is the radial coordinate of the Earth in the FLRW metric (1.5) as seen from the source, and t_0 is the observing time today. Secondly, the signal is redshifted and the photon frequencies are described by Eqs. (1.13) and (1.15): $\nu_0 = \nu_e\;(1+z)^{-1}$. Also the energy $h\,\nu_0$ of a single photon received on Earth is smaller than the respective energy $h\,\nu_e$ emitted from the source. Finally, a cosmological redshift also leads to a time dilation between the observed and emitted signals: $dt_0 = dt_e\;(1+z)$. As a consequence, from the definition of L as the energy per unit of time, we see that, for an expanding Universe, Eq. (1.47) is rewritten as

$$l = \frac{L}{4\,\pi\,a_0^2\,r^2\;(1+z)^2} \equiv \frac{L}{4\,\pi\,d_L^2}\,, \tag{1.48}$$

in which, in the last equality, we have defined the luminosity distance

$$d_L\,(z) \equiv a_0\,r\;(1+z)\;, \tag{1.49}$$

Note that d_L relates L and l in an expanding Universe and is defined in such a way to rewrite Eq. (1.47) similarly to the concept presented in Euclidean geometry.

Another useful distance is obtained by comparing angular sizes with spatial distances in an expanding Universe. It should be recalled that stars within a galaxy are held together by gravity and they do not follow the Hubble flow. If a galaxy source is characterized by a typical transverse proper distance s, which subtends a small angle θ, as seen from the line of sight of the observer, then θ is given by

$$\theta = \frac{s}{r\,a\left(t_e\right)} \equiv \frac{s}{d_A}\,. \tag{1.50}$$

We have defined the so-called angular diameter distance

$$d_A = r\,a\left(t_e\right)\,, \tag{1.51}$$

which generalizes for an expanding Universe the usual relation between the angle subtended and the radius valid in Euclidean geometry. Then, combining Eqs. (1.15), (1.49), and (1.51), it is straightforward to obtain the well-known Etherington distance-duality equation [35]

$$d_L\left(z\right) = \left(1+z\right)^2\, d_A\left(z\right)\,, \tag{1.52}$$

which establishes a relationship between the luminosity distance and the angular diameter distance.

So far, we have discussed the luminosity distance only from the geometry of an expanding Universe, but we can write d_L from the dynamics in terms of cosmological parameters. It should be emphasized that Eq. (1.49) is consistent with the power series (1.21) for $z \ll 1$ and the definition of redshift (1.15). However, for larger redshifts, it is not useful this expansion. Concerning the causal path of photons, we recall the comoving distance $D_c\left(r\right)$ in Eq. (1.12) and we rewrite it in terms of z

$$D_c\left(r\right) = \int_0^z \frac{dz'}{\left(1+z'\right)\,H\left(z'\right)\,a\left(z'\right)} = \frac{1}{H_0\,a_0}\int_0^z \frac{dz'}{E\left(z'\right)}\,, \tag{1.53}$$

in which we have used Eqs. (1.15), (1.44), and (1.37). Then, combining this equation (1.53) with Eqs. (1.7) and (1.49), we can write d_L as

$$d_L\left(z\right) = \left(1+z\right)\,S_k\left(\frac{1}{H_0}\int_0^z \frac{dz'}{E\left(z'\right)}\right) = \frac{\left(1+z\right)}{H_0\sqrt{k}}\,\sinh\left(\sqrt{k}\int_0^z \frac{dz'}{E\left(z'\right)}\right)\,, \tag{1.54}$$

where the function S_k was defined in Eq. (1.9) whatever the value of k. This is the most general expression for the luminosity distance, but in many applications we can confine our attention to a flat geometry ($k = 0$), hence Eq. (1.54) reduces to

$$d_L\left(z\right) = \frac{\left(1+z\right)}{H_0}\int_0^z \frac{dz'}{E\left(z'\right)}\,. \tag{1.55}$$

Furthermore, once the function $E\left(z\right)$ is clearly defined for a given cosmological model, the luminosity distance can be computed. If we replace $E\left(z\right)$ within the ΛCDM model from Eq. (1.38), then Eq.(1.54) becomes

$$d_L\left(z\right) = \frac{\left(1+z\right)}{H_0\sqrt{\Omega_{k0}}}\,\sinh\left(\sqrt{\Omega_{k0}}\int_0^z \frac{dz'}{\sqrt{\Omega_{m0}\,\left(1+z'\right)^3 + \Omega_{r0}\,\left(1+z'\right)^4 + \Omega_{\Lambda 0} + \Omega_{k0}\,\left(1+z'\right)^2}}\right) \tag{1.56}$$

for a generic curvature scalar, which reduces to

$$d_L\left(z\right) = \frac{\left(1+z\right)}{H_0}\int_0^z \frac{dz'}{\sqrt{\Omega_{m0}\,\left(1+z'\right)^3 + \Omega_{r0}\,\left(1+z'\right)^4 + \Omega_{\Lambda 0}}} \tag{1.57}$$

in a flat geometry.

1.1.5.1 Estimating cosmic distances

Cosmological probes characterized by fixed and constant properties across the Universe can be very useful to estimate cosmological distances, since they can be used as reference points with well-known features. Standard candles exhibit a constant inherent luminosity, whereas standard rulers are other cosmological probes characterized by a typical spatial scale at a given redshift. This feature enables the estimation of their distances based on measurement of the apparent luminosity and the apparent angular size for standard candles and rulers, respectively. In other words, once the Universe evolution is considered, we can determine distances by measuring the luminous flux on Earth from an object of known absolute luminosity or observing the angle subtended by an object of known size.

Standard candles SNe Ia are astrophysical objects characterized by a fixed absolute luminosity. This peculiar property is the result of the same physical mechanism by which all SNe Ia are generated [27, 28]. A SN Ia is originated from the violent explosion of a compact object, a carbon-oxigen white dwarf. In a binary system, a white dwarf gradually accumulate mass by stealing matter from the nearby star until it reaches a critical mass, the so-called Chandrasekhar limit of $\sim 1.44\,M_{\odot}$. This limit is dictated by the opposition between gravity and the electron degeneracy pressure inside the star. As soon as the white dwarf mass exceeds this threshold, the star becomes unstable and begins to collapse. This process leads to a significant increase in temperature causing the reaction that converts ^{12}C and ^{16}O into ^{56}Ni. Eventually, a thermonuclear explosion occurs with the violent ejection of external layers of the white dwarf. These violent explosions are what we called SNe, which can be more brilliant than the whole host galaxy as seen from Earth. Thus, SNe are very useful cosmological probes since they can be observed from very long distances. However, these extreme events are relatively rare happening only a few times per century in a galaxy. Since this phenomenon occurs when the mass of the unstable white dwarf is typically close to the Chandrasekhar limit, the absolute luminosity of a SN Ia can be reliably determined a priori. These strict conditions allows SNe explosions to be used as reference points and promoted to a well-defined class of standard candles to estimate cosmic distances, since the apparent luminosity of a SN Ia is strongly related to its distance from Earth.

Actually, astronomers prefer to adopt apparent and absolute magnitude from a traditional and historical notation rather than apparent and absolute luminosity. In this regard, the theoretical distance modulus of a SN is defined as

$$\mu_{\rm th} = m_{th} - M = 5\ \log_{10}\ d_L\,(z) + 25\,, \tag{1.58}$$

where m_{th} and M are the apparent and absolute magnitude of a SN, respectively, and d_L is the luminosity distance (1.54) expressed in Mpc. All detailed information about a specific cosmological model are incapsulated in $d_L\,(z)$, more specifically in the expression of the function $E\,(z)$ contained within. It should be emphasized that M is degenerate with H_0, as it can be proved by combining Eqs. (1.58), (1.54) and (1.38).

The theoretical definition of the distance modulus (1.58) must be compared against the observed distance modulus $\mu_{\rm obs}$, which can be written as

$$\mu_{\rm obs} = m_B - M + \alpha\, x_1 - \beta\, c + \Delta M + \Delta B\,. \tag{1.59}$$

This quantity depends on SNe astrophysical parameters, such as the color c and the stretch x_1 via the coefficients α and β, respectively [27, 176]. In Eq. (1.59), m_B is the B band (blue) apparent magnitude, and M is the B band absolute magnitude for a reference SN with $c = 0 = x_1$. Furthermore, ΔM denotes a distance correction related to the host-galaxy mass, and ΔB is a bias correction [176]. Identifying the value of M poses a challenge when determining cosmological parameters, as various factors such as selection biases, Milky Way extinction, and microlensing effects introduce sources of systematics and statistical errors into the process, as detailed in [176]. We remark that SNe explosions are observed in different wavelenght bands, but they are brighter in the B band. Furthermore, to be properly standardized, SNe must be observed during their peak in luminosity. Before the peak, the SNe intensity increases with time in a period of ~ 20 days, whereas it slowly decreases in ~ 2 months after the peak in which ^{56}Ni decays into ^{56}Co and then ^{56}Fe. The time evolution of the intensity of a SN is the so-called light curve, which are crucial to calibrate SNe and use them as standard candles (see e.g. Spectral Adaptive Lightcurve Template or SALT [183] as a method to standardize SNe Ia).

The original Hubble diagram plotted galaxy velocities against distance according to Eq. (1.20), but nowadays when we say Hubble diagram we refer to a plot of the luminosity distance (or the distance modulus or the apparent luminous flux) versus redshift.

To test a cosmological model with SNe data, it is helpful the comparison between $\mu_{\rm th}$ in Eq. (1.58) and the $\mu_{\rm obs}$ in Eq. (1.59). The distance residual

$$\Delta\mu = \mu_{\rm obs} - \mu_{\rm th} \tag{1.60}$$

is defined as the difference between the distance moduli. To perform statistical analysis, the $\chi^2_{\rm SNe}$ for SNe data can be built as

$$\chi^2_{\rm SNe} = \Delta\mu^T\, C^{-1}\, \Delta\mu\,. \tag{1.61}$$

The full covariance matrix

$$C = C_{\rm sys} + D_{\rm stat} \tag{1.62}$$

includes both systematic errors in the matrix $C_{\rm sys}$ and also statistical errors for each SN in the diagonal matrix $D_{\rm stat}$. The latter matrix takes into account the effects due to photometry, peculiar velocities, biases, stochastic gravitational lensing, mass step correction, and intrinsic scatter [176].

Standard rulers Baryon acoustic oscillations (BAOs) are a mixture of bubbles and wrinkles in the density distribution of matter imprinted today in galaxy clusters, as a result of a phenomenon occured in the early Universe. Now we briefly explain why BAOs are the most studied standard rulers and we describe their formation in early times, which requires only cosmological perturbations and linear physics with a good approximation.

Before decoupling, the Universe consisted of a highly ionized hot and dense plasma of photons, baryons, electrons, and DM particles. Energetic photons were trapped in the primordial plasma, because of recurring interactions with matter. Indeed, due to high temperatures in the early Universe, photons could scatter baryons preventing the formation of neutral atoms. In other words, radiation was in thermal equilibrium with hot matter. Considering these significant interactions, baryons and photons were tightly coupled and moved together in the primordial plasma as a single fluid.

BAOs were originated just in the photon-baryon fluid as a consequence of a competition between gravity and pressure forces in the plasma. We further explain about these processes. Small perturbations in the primordial plasma could create an overdense region containing photons, baryons, and dark matter. While gravity tends to attract and gather more matter in this overdensity, the fluid pressure due to photon-baryon interactions provides the opposite effect. Thus, these competing effects resulted in oscillations of the photon-matter fluid, analogous to spherical sound waves. During this process, DM remained at the center of the overdensity since it interacts only gravitationally, while photons and baryons were pushed together outwards along acoustic waves creating bubbles in the primordial plasma. The distance reached by the propagation of acoustic wave in the plasma is known as the sound horizon, which is defined as

$$r_s\left(z\right)=\frac{1}{H_0}\int_z^{\infty}\frac{c_s\,dz'}{E\left(z'\right)}\,, \tag{1.63}$$

where $c_s=c\left[3\left(1+\frac{3}{4}\,\eta\right)\right]^{-1/2}$ is the speed of sound in the baryon-photon fluid, being η the baryon-photon ratio.

The processes in the plasma could not last forever. Indeed, as the Universe expanded, the plasma cooled and reached the temperature of $\sim 3000\,\mathrm{K}$ approximately 288000 years after the Big Bang at the beginning of the recombination epoch for $z_r\sim 1300$. Then, photons were no longer energetic enough to interact with baryons, hence electrons and protons could begin to combine to form neutral hydrogen atoms. Actually, a significant fraction of photons continued to interact with baryons also after the beginning of the recombination until the last scattering surface. After that, photons diffused away and the Universe became transparent at the decoupling epoch for $z_d\sim 1100$, approximately when the Universe was 380000 old. As a consequence, there were no longer pressure forces and the system interacted only gravitationally. The propagation of the acoustic waves stopped definitively at decoupling. The relic photons emitted after decoupling led to a snapshot of the early Universe at the last scattering surface, the CMB radiation, which is observed today as an almost completely uniform background radiation. Concerning matter overdensities, instead, baryons formed structures as spherical shells, where DM remained located in the center.

We remark that the baryonic matter perturbations reached a maximum sound horizon given by the redshift of decoupling, then they are frozen in the CMB. The radius of the baryonic shells at the decoupling is a typical length scale, which can be well determined. In other words, the maximum distance covered by an acoustic wave in the plasma before the epoch of decoupling established the length of a cosmological standard ruler: the size of the sound horizon at decoupling, i.e., $r_d\equiv r_s\left(z_d\right)$. Then, these shells imprinted on LSS have evolved by following the Universe expansion. BAOs provide information about the cosmic history independently of SNe data. Since the Universe evolution is characterized by spatial isotropy on large scales, it is expected that galaxies were formed within primordial overdensities and that a large number of galaxies are separated today by a typical scale, as a result of the evolution of the standard ruler, which was fixed equally at the last scattering. For these reasons, BAO matter clustering is considered as a standard ruler in cosmology, since galaxies might cluster on a specific scale.

However, it is challenging to find a regular pattern in the matter distribution today due to the superposition of several matter shells. Therefore, statistical methods should be considered to extract a spatial scale from galaxy clusters. In this regard, the two-point correlation function (see Sect. 1.1.6) gives the probability to find a galaxy located at a given distance from another one. BAO signal is related to a net peak in the correlation function and oscillations in its power spectrum. Analyzing clustering of galaxies, surveys such as the Sloan Digital Sky Survey (SDSS) [184] showed that the radius of spherical shells is $\sim 150\,\mathrm{Mpc}$. Moreover, the size of the sound horizon at decoupling is well constrained by CMB maps [40].

Measurements of the BAO spatial scale along the radial direction or the line of sight are related to the Hubble parameter $H\left(z\right)$, while we can obtain information about the angular diameter distance $d_A\left(z\right)$ from the standard ruler in the trasverse direction. A distance often used for BAOs measurements is a combination of the latter two quantities, and is defined as [73, 185, 186]

$$D_V\left(z\right)=\left[z\,\left(1+z\right)^2\frac{d_A^2\left(z\right)}{H\left(z\right)}\right]^{1/3}\,, \tag{1.64}$$

which is called the volume averaged distance or dilation scale. The BAO estimator d_z gives the comoving size of the sound horizon at decoupling (1.65) in unit of D_V, i.e.,

$$d_z\left(z\right)=\frac{r_d}{D_V\left(z\right)}\,.$$

When BAO signal is detected, we are determining how r_d has evolved since the decoupling, namely we are measuring today the combination $H_0\,r_d$ (or $h\,r_d$). Thus, H_0 and r_d are fully degenerate. Assuming a fiducial flat ΛCDM model, the best fit for this combination is $(r_d\cdot h)_{\text{fid}}=(104.57\pm1.44)$ Mpc [187]. A method to estimate r_d is given by a simple fitting formula [187]

$$r_d=\frac{\left(r_d\cdot h\right)_{\text{fid}}}{h}\,. \tag{1.65}$$

Alternatively, to quantify r_d, the linear perturbation code CAMB [188] provides a numerical calibrated approximation with the following formula [189]:

$$r_d\approx\frac{55.154\cdot e^{-72.3(\omega_\nu+0.0006)^2}}{\omega_m^{0.25351}\omega_b^{0.12807}}\,\text{Mpc}, \tag{1.66}$$

where $\omega_i=\Omega_i\cdot h^2$ are the reduced density parameters and $i=m,\nu,b$ represent (total) matter, neutrino and baryons.

For BAOs data analysis, the comparison between the observed $d_z^{\text{obs}}(z)$ and theoretical $d_z^{\text{th}}(z)$ are useful to define the following statistical parameter:

$$\chi^2_{\text{BAO}}=\Delta d^T\cdot\mathcal{M}^{-1}\cdot\Delta d\,, \tag{1.67}$$

where $\Delta d=d_z^{\text{obs}}\left(z\right)-d_z^{\text{th}}\left(z\right)$ and $\mathcal{M}$ is the covariance matrix given in [186]. Note that if ω_ν and ω_b are fixed, then using Eqs. (1.64), (1.66), and (1.67), it is possible, for instance, to constrain H_0 and Ω_{m0}. In the analysis performed in Chapter 4, we assume $\omega_\nu=0.00064$ [190] and $\omega_b=0.02237$ [40].

1.1.6 Statistical properties in the large-scale structure

1.1.6.1 The density contrast and the power spectrum

The structures we observe today, such as galaxies and the clusters of galaxies, are related to local deviations from spatial homogeneity and were generated from small perturbations in the early Universe. The small temperature fluctuations in the CMB maps can be considered the seeds for the structure formation or initial conditions for the physical cosmology. Hence, these perturbations grew in an expanding Universe due to gravity.

To describe deviations from a homogeneous background Universe in the matter distribution today, it is useful to define the matter density contrast (or density perturbation field, or density fluctuation)[5]

$$\delta\left(t,\vec{x}\right)\equiv\frac{\delta\rho_m\left(t,\vec{x}\right)}{\bar{\rho}_m\left(t\right)}\equiv\frac{\rho_m\left(t,\vec{x}\right)-\bar{\rho}_m\left(t\right)}{\bar{\rho}_m\left(t\right)}\,, \tag{1.68}$$

where $\rho_m\left(t,\vec{x}\right)$ is the mass density field and $\bar{\rho}_m\left(t\right)$ denotes the respective background quantity.

In principle, the cosmic field $\delta\left(t,\vec{x}\right)$ should be specified at every point in space at a given time to accurately consider matter fluctuactions in the Universe. However, this procedure is impractical and a statistical approach has to be employed[6]. In this regard, imagine to divide the Universe into N cells

---

[5] See [72, 180, 182] for details about the topics covered in the present section.

[6] Similarly, in statistical mechanics, it is unconceivable to associate positions and velocities to each single particle, but macroscopic and global properties of a gas are described statistically.

located at $\vec{x}_1,\, \vec{x}_2,\, \dots \vec{x}_N$. Each cell is associated with the density contrast $\delta_i \equiv \delta\left(\vec{x}_i\right)$ with $i = 1, 2, \dots N$. The latter quantity δ_i is treated as a random perturbation field with a PDF $\mathscr{F}_x\left(\delta_1, \delta_2, \dots, \delta_N\right)$. The general expression for the moments of such a distribution can be written as

$$\overline{\delta_1^{A_1}\delta_2^{A_2}\dots\delta_N^{A_N}} = \int \delta_1^{A_1}\delta_2^{A_2}\dots\delta_N^{A_N}\, \mathscr{F}_x\left(\delta_1, \delta_2, \dots, \delta_N\right)\, d\delta_1 d\delta_2 \dots d\delta_N\,, \tag{1.69}$$

in which the exponents $A_i \in \mathbb{Z}_0^+$ and the overline denotes the stochastic or ensamble average[7]. The first moment $\overline{\delta\left(\vec{x}\right)}$ is vanishing trivially from the definition of a random perturbation field. The second moments, instead, are the variance of the perturbation field

$$\sigma^2 \equiv \overline{\delta_1^2\delta_2^0\dots\delta_N^0}\,, \tag{1.70}$$

and the two-point correlation function

$$\xi\left(x\right) \equiv \overline{\delta_1\delta_2} \equiv \overline{\delta_1^1\delta_2^1\delta_3^0\dots\delta_N^0}\,. \tag{1.71}$$

It should be emphasized that a cosmic field must be statistically homogeneous and isotropic due to the cosmological principle, hence its moments must be invariant under spatial translation and rotation. As a consequence, $\xi\left(x\right)$ depends only on the mutual distance $x = \left|\vec{x}_2 - \vec{x}_1\right|$ between two cells (we referred to the two first cells, but it can be generalized for any cells pair). The two-point correlation function gives the probability to have a peak in the density contrast at a given distance from another one. Furthermore, note that $\xi\left(0\right) \equiv \sigma^2$ and $\xi\left(x\right)$ is also called autocorrelation function.

The equivalent representation in the Fourier space is convenient especially for the linear regime. A cell in the real space is now replaced by a volume with periodic boundary conditions. The random field $\delta\left(\vec{x}\right)$ and its Fourier transform are related according to the following convention

$$\delta\left(\vec{x}\right) = \int \frac{d^3k}{\left(2\pi\right)^3}\, \delta_{\vec{k}}\, e^{-i\,\vec{k}\cdot\vec{x}}\,, \tag{1.72}$$

where $\delta_{\vec{k}}$ are the spectral functions, which are generally characterized by an amplitude and a phase. Similarly to the real space, it is possible to figure out a distribution function to describe the statistical properties of $\delta_{\vec{k}}$ in the Fourier space, which provides the probability to find a mode $\delta_{\vec{k}}$ with given amplitude and phase. The second moment in Fourier is related to the well-known power spectrum $P\left(\vec{k}\right)$ of the perturbation field:

$$\overline{\delta_{\vec{k}}\delta^*_{\vec{k}'}} = \left(2\pi\right)^3\, \delta_D\left(\vec{k} - \vec{k}'\right)\, P\left(\vec{k}\right)\,, \tag{1.73}$$

in which δ_D denotes the three-dimensional Dirac delta. Considering Eqs. (1.71) and (1.73), it is straightforward to see that the power spectrum is nothing more than the two-point correlation function in the Fourier representation:

$$P\left(\vec{k}\right) = \int d^3x\, \xi\left(\vec{x}\right)\, e^{i\,\vec{k}\cdot\vec{x}}\,, \tag{1.74}$$

which can be rewritten for a isotropic random perturbation field

$$P\left(k\right) = 4\pi \int_0^\infty dr\, r^2\, \xi\left(r\right)\, \frac{\sin\left(k\,r\right)}{k\,r} = 4\pi \int_0^\infty dr\, r^2\, \xi\left(r\right)\, j_0\left(k\,r\right) \tag{1.75}$$

by adopting spherical coordinates. j_0 is the spherical Bessel function of order 0. Note that the inverse

---

[7] In many papers and textbooks, the stochastic average is commonly denoted with $\langle\dots\rangle$. In this thesis, we use this notation for averages on a region of space-time, while we adopt an overline for the stochastic average, not to be confused with an overline denoting background quantities for a homogeneous and isotropic Universe.

relation of Eq. (1.75), i.e.,

$$\xi\left(r\right)=\frac{1}{2\pi^{2}}\int_{0}^{\infty}dk\,k^{2}\,P\left(k\right)\,\frac{\sin\left(k\,r\right)}{k\,r}=\frac{1}{2\pi^{2}}\int_{0}^{\infty}dk\,k^{2}\,P\left(k\right)\,j_{0}\left(k\,r\right)\tag{1.76}$$

is consistent for $r\to 0$ with the definition of variance (1.70), according to Eq. (1.69). Furthermore, now it can be appreciated from Eq. (1.75) that a bump in the correlation function corresponds to oscillations in the power spectrum, as previously mentioned in the BAO physics (see Sect. 1.1.5).

If the moments of the distribution are known at any order, then the PDF is fully determined. However, if the random field $\delta\left(\vec{x}\right)$ is Gaussian, namely if the field values $\left(\delta_{1},\ldots,\delta_{N}\right)$ follow a Gaussian distribution, only first two moments are enough to characterize statistical properties. The advantage of a Gaussian random field is that different Fourier modes evolve independently in the linear regime. Moreover, a Gaussian random field remains so during linear evolution. The initial conditions at the end of the inflation era seem to suggest that the cosmic density field is well described by a Gaussian random field, which is also homogeneous and isotropic. There are mainly three reasons to consider a Gaussian random field. The first one is of theoretical nature: quantum fluctuations in the early Universe generated during inflation are considered Gaussian and led to the cosmic perturbation field, which remain Gaussian at least up to late times, whereas non linear processes must be taken into account. The second reason arises from statistics. According to the central limit theorem, the distribution of a sufficiently large random sample is approximately normally distributed. Moreover, a linear combination of Gaussian variates also follows a Gaussian distribution. This is our case, since the cosmic density field involves different Fourier modes. Actually, this is true up to when non linearities become significant at low redshifts. Finally, the third one is an observational reason: so far, there is no clear evidence to prefer non-Gaussian distribution. Thus, the two-point correlation function, as well as the power spectrum, play a crucial role for a homogeneous and isotropic Gaussian random field, since they are the only quantities that have to be specified.

So far, we have introduced the two-point correlation function and the related power spectrum referring to matter fluctuations as a variate. We can also consider the gravitational potential as a random variable in space and define consequently statistical estimators. We recall that the gravitational (Bardeen) potential [35] is governed by the Poisson equation[8]

$$\nabla^{2}\psi\left(t,\vec{x}\right)=4\pi G\,\rho\left(t,\vec{x}\right)\,a^{2}=4\pi G\,\overline{\rho}_{m}\left(t\right)\,\delta\left(\vec{x}\right)\,a^{2},\tag{1.77}$$

where in the last equality we have used the definition (1.68) and neglected radiation perturbations. Considering the Fourier transform, we can also write the single spectral function $\psi_{\vec{k}}$ associated to the Bardeen potential

$$\psi_{\vec{k}}=-\frac{3}{2}\,\frac{\Omega_{m0}\,\mathcal{H}_{0}^{2}}{a\,k^{2}}\,\delta_{\vec{k}}\tag{1.78}$$

in terms of the spectral function $\delta_{\vec{k}}$, where $\mathcal{H}_0$ is the conformal Hubble constant[9]. Therefore, we can also define moments of the PDF such as the two-point correlation function in real space $\overline{\psi\left(t,\vec{x}_{1}\right)\,\psi\left(t,\vec{x}_{2}\right)}$, or in momentum space $\overline{\psi_{\vec{k}_{1}}\,\psi_{\vec{k}_{2}}}$, and their respective power spectra, which provides amplitudes of the gravitational potential fluctuations.

---

[8] For the sake of clarity, here we write explicitly the Einstein constant χ in terms of the Newtonian coupling G.

[9] We recall the definition of the conformal Hubble parameter: $\mathcal{H}\equiv a\left(\eta\right)'/a\left(\eta\right)\,H=a\,H$, being η the conformal time such that $d\eta=dt\,/\,a\left(t\right)$

1.1.6.2 Amplitude of matter fluctuations

The initial power spectrum $P_i\,(k)$ predicted by inflation models is usually written as a power law [35, 180]

$$P_i\,(k) = A\,k^n\,, \tag{1.79}$$

where n is called the spectral index and A is the amplitude. In particular, the Harrison–Zel'dovich's power spectrum is obtained for $n = 1$. The spectral index was measured by Planck and its value is $n = 0.965 \pm 0.004$. Observations and galaxy surveys provide constraints on the amplitude of the power spectrum. For historical reasons, the variance of the galaxy distribution is used to normalize a theoretical power spectrum by evaluating the variance over different spherical regions with radius R (the value of R is set by the experimental resolution). It can be shown [180] that the predicted variance is written as

$$\sigma_R^2 = \frac{1}{2\pi^2}\int dk\,k^2\,P\,(k)\,\hat{W}_R^2\,(k)\,, \tag{1.80}$$

in which the window function

$$\hat{W}_R\,(k) = \frac{3}{(k\,R)^3}\,\left[\sin\left(k\,R\right) - k\,R\,\cos\left(k\,R\right)\right] = \frac{3\,j_1\,(k\,R)}{k\,R} \tag{1.81}$$

acts like a filter for the power spectrum and j_1 in Eq. (1.81) is the spherical Bessel function of order 1. The window function $\hat{W}_R\,(k)$ is obtained as the Fourier transform of the most commonly used spherical top-hat window function in real space:

$$W_R\,(r) = \begin{cases} \frac{3}{4\pi R^3} & \text{if } r \leq R \\ 0 & \text{otherwise}\,. \end{cases} \tag{1.82}$$

Eq. (1.80) provides the variance of mass fluctuations smoothed over spatial scale R. The motivation to use a window function is to introduce a characteristic smoothing scale, since the real density perturbation field is grainy.

The value of the standard deviation σ_R can be obtained empirically from galaxy surveys and is ~ 1 for $R = 8\,h^{-1}\,\text{Mpc}$. Hence, the idea was to set σ_R from the distribution of galaxies for this value of R to normalize the power spectrum. However, a complete description should require the non linear regime, in which the Fourier modes are coupled. Furthermore, the assumption that the galaxy distribution is an accurate probe of the total mass distribution is only an approximation, and a bias parameter b should be considered:

$$\delta_{\text{gal}} = b\,\delta\,. \tag{1.83}$$

Indeed, when we observe galaxies to probe the galaxy distribution, we receive photons from our past lightcone (no cold dark matter particles). The link bewteen the mass and galaxy distribution is not fully understood. Although these important clarifications, traditionally, a power spectrum is normalized by the following cosmological parameter:

$$\sigma_8 \equiv \sigma_R\left(R = 8\,h^{-1}\,\text{Mpc}\right)\,. \tag{1.84}$$

It should be emphasized that σ_R is evaluated today at $z = 0$ by observing the LSS, hence it depends on the present-day linear power spectrum evolved from the primordial one. It is often used the S_8 parameter, a weighted amplitude of matter fluctuations, which is related to σ_8 through the simple relation

$$S_8 \equiv \sigma_8 \sqrt{\frac{\Omega_{m0}}{0.3}}\,.$$

The value of S_8 is object of studies and we will discuss it later in Sect. 1.1.7.

1.1.6.3 Growing perturbations in the linear regime

So far, we discuss statistical properties of the matter density contrast in space. To examine the time evolution of fluctuations in an expanding Universe, the theory of cosmological perturbations [35, 72, 191–193] is required. Considering a fluid description with linear perturbations, it can be obtained that $\delta\,(t,\vec{x})$ evolves according to the following second-order differential equation [180]:

$$\ddot{\delta} + 2\,H\,\dot{\delta} = 4\pi G\,\overline{\rho}_m\,\delta + \frac{c_s^2}{a^2}\,\nabla^2\delta\,, \tag{1.85}$$

where c_s is the adiabatic speed of sound for isentropic initial perturbations. This equation is similar to the one that describes a damped oscillator. Note that the second term on the left-hand side acts as a friction term for the growth of perturbations, since the cosmic expansion tends to remove them. On the other hand, the first term on the right-hand side is a source term due to gravity, which tends to amplify perturbations. The last term is due to spatial changes of δ and can be regarded as a pressure contribution. Eq. (1.85) can be rewritten equivalently in Fourier as

$$\ddot{\delta}_{\vec{k}} + 2\,H\,\dot{\delta}_{\vec{k}} = \left(4\pi G\,\overline{\rho}_m - \frac{k^2\,c_s^2}{a^2}\right)\delta_{\vec{k}}\,, \tag{1.86}$$

and it is valid for any single Fourier mode in linear regime. This evolution equation can be employed to analyze the growth of perturbations up to gravitational instability [180, 194].

In particular, referring to an expandind background Universe within the Einstein-de Sitter model for isentropic perturbations in a pressureless fluid, it can be shown that Eq. (1.86) admits two solutions

$$\delta_{\vec{k}}^{(+)} \propto t^{2/3}\,, \qquad \delta_{\vec{k}}^{(-)} \propto t^{-1}\,, \tag{1.87}$$

where we have used Eq. (1.29). We are interested in growing modes like $\delta_{\vec{k}}^{(+)}$ since they led to structure formation and gravitational collapse up to non-linear regime. Indeed, the amplitudes of decaying solutions become negligible after some times compared to those of growing modes. If we focus, instead, on non-interacting matter fluctuations in Eq. (1.86), it is straightforward to obtain that $\delta_{\vec{k}}^{(+)} \propto \ln t$,which shows that dark matter perturbations in the linear regime grow slowly and are almost frozen. This phenomenon is called "stagspansion" or stagnated expansion (Mészàros effect [195]). On the other hand, in the non-linear regime, dark matter perturbations become dominant (see [180, 182] for the non linear collapse of dark matter halos).

We define the linear growth function as

$$D_1\,(a) \equiv \frac{\delta\,(a)}{\delta\,(1)}\,, \tag{1.88}$$

which is associated to growing solutions. Moreover, another important quantity is the so-called linear growth rate of clustering $f\,(a)$, which is defined via a logarithmic derivative as

$$f\,(a) \equiv \frac{d\ln D_1}{d\ln a} \equiv \frac{a}{D_1}\,\frac{dD_1}{da}\,. \tag{1.89}$$

When cosmological perturbations are considered in the Fourier representation, during the linear evolution, different Fourier modes can be amplified or damped. In other words, the power spectrum is modified with respect to the primordial one in the early Universe, because the evolutionary process acts as a filter of the initial fluctuations. In this regard, we recall that the amplitude of a sub-horizon Fourier mode for different redshifts in the post-recombination era is related to the transfer function $T\left(k\right)$ in the linear regime. It is oftern convenient to rewrite any linear power spectrum in terms of the primordial power spectrum as

$$P\left(k\right) = P_i\left(k\right)\, T^2\left(k\right) \, . \tag{1.90}$$

The linear transfer function $T\left(k\right)$ quantifies the evolution of the perturbation amplitude and allows us to compute the linear power spectrum for any k and later times. This concept underlying Eq. (1.90) can be referred to both matter and gravitational potential fluctuations. More specifically, the linear transfer function in the post-recombination Universe related to matter perturbations in the distribution of galaxies is written as [72, 154]

$$T_\delta = b\, D_1 \, , \tag{1.91}$$

while the relation for the gravitational potential is

$$T_\psi = -\frac{3}{2}\, \frac{\Omega_{m0}\, \mathcal{H}_0^2}{a\, k^2}\, D_1 \, , \tag{1.92}$$

in which we have used Eqs. (1.83) and (1.78), respectively.

1.1.6.4 Higher-point correlation functions and the bispectrum

We focused so far on the two-point correlation function and the power spectrum, which are the fundamental ingredients to characterize a homogeneous and isotropic Gaussian random field. More in general, for a purely Gaussian distribution, all correlation functions of odd order vanish, while higher order correlators of even order can be decomposed into a sum of products of two-point correlation functions according to Wick's theorem. We emphasize that even if the primordial fluctuations followed a pure normal distribution, non-linear effects of gravity and gravitational instabilities might play a role in the evolution into non-Gaussian perturbations. Alternatively, the presence of non-Gaussianities also in the primordial power spectrum has been investigated [193].

For non-Gaussian distributions, the first non-trivial higher-order correlator is the three-point function $\zeta\left(\vec{x}_1, \vec{x}_2, \vec{x}_3\right)$, which now we write in term of the variate $\delta\left(\vec{x}\right)$ in real space as

$$\zeta\left(\vec{x}_1, \vec{x}_2, \vec{x}_3\right) \equiv \overline{\delta_1\, \delta_2\, \delta_3} \equiv \overline{\delta_1^1 \delta_2^1 \delta_3^1 \ldots \delta_N^0} \, , \tag{1.93}$$

according to Eq. (1.69). The respective quantity in Fourier space is the so-called bispectrum $B\left(\vec{k}_1, \vec{k}_2, \vec{k}_3\right)$, which is related to $\zeta\left(\vec{x}_1, \vec{x}_2, \vec{x}_3\right)$ through the following relation:

$$\overline{\delta_{\vec{k}_1} \delta_{\vec{k}_2} \delta_{\vec{k}_3}} = \left(2\pi\right)^3\, \delta_D^{(3)}\left(\vec{k}_1 - \vec{k}_2 - \vec{k}_3\right)\, B\left(\vec{k}_1, \vec{k}_2, \vec{k}_3\right) \, . \tag{1.94}$$

This equation is a generalization of Eq. (1.73). Note that the bispectrum depends on three wavenumbers and in this case the Dirac delta selects only non-vanishing triangular configurations, namely those that form a specific shape of a closed triangle in Fourier space.

Similarly, all these concepts can be also referred to the gravitational Bardeen potentials. We will see an application of the bispectrum contribution in the cosmological perturbation theory in Chapter 7.

1.1.7 The Hubble constant and matter fluctuations tensions

Despite the outstanding results and predictions, the ΛCDM model must deal with open problems of a theoretical and observational nature. One of the biggest challenges in modern cosmology is the Hubble constant tension: there is a persistent and serious discrepancy between the measurement of H_0 obtained from the CMB radiation and other independent measurements inferred from local probes in the late Universe. More precisely, the Planck data of the CMB radiation (TTTEEE+lowE+lensing) provides $H_0^{\mathrm{CMB}} = (67.36 \pm 0.54)$ km s^{-1} Mpc^{-1} [40], while the local values of H_0 obtained by the Supernova H0 for the Equation of State (SH0ES) team are inconsistent with H_0^{CMB}. Measurements of Cepheids in the Large Magellanic Cloud (LMC) from Hubble Space Telescope (HST) gives $H_0 = (74.03 \pm 1.42)$ km s^{-1} Mpc^{-1} [196], pointing out a discrepancy[10] of 4.4 σ with H_0^{CMB}. Furthermore, parallax measurements based on Milky Way Cepheids with HST photometry and the ESA Gaia mission Early Data Release 3 (EDR3) [197] provides $H_0 = (73.2 \pm 1.3)$ km s^{-1} Mpc^{-1} with an incompatibility of $4.2\,\sigma$ with CMB data. More recently, the SH0ES team from a Cepheid-SN sample [71] obtained $H_0^{\mathrm{loc}} = (73.04 \pm 1.04)$ km s^{-1} Mpc^{-1} , which is in tension at 4.8 σ with the Planck value.

Actually, the discrepancy ranges from 4.4 σ to more than 6σ depending on the combination of local data used. The collaboration H_0 Lenses in COSMOGRAIL Wellspring (H0LiCOW) report a value of $H_0 = \left(73.3^{+1.7}_{-1.8}\right)$ km s^{-1} Mpc^{-1} [198] by using gravitational lensed quasars. Independent measurements of cosmic chronometers (based on models of evolving galaxy star luminosity) report the best-fit value of $H_0 = (67.06 \pm 1.68)$ km s^{-1} Mpc^{-1} [199]. Estimates of H_0 based on a combination of cosmological data, including calibration of the tip of the red giant branch on SNe Ia [200], quasars [201], time-delay measurements, cosmic chronometers, and gamma-ray bursts (GRBs) [202–204], report a value of H_0 that is between the CMB, BAO, and local measurements. Furthermore, the use of type 1 Active Galactic Nuclei (AGN) represents another promising cosmological probe given the peculiarity of their spectral emission [205]. Recent results on the measurements of the Hubble parameter and constant through the Third LIGO-Virgo-KAGRA Gravitational-Wave Transient Catalog (GWTC-3) can be found in [206], and the employement of cosmological measurements from gravitational waves turns out to be really promising in the next decades. The status of some of these discrepancies is summarized in Fig. 1.1, where the values of H_0 among different probes are shown. Another similar but more detailed plot is reported in Fig 1.2. See [67, 68] and references therein for an exhaustive summary of recent Hubble constant measurements and theoretical proposals to deal with the H_0 tension.

To date, the H_0 tension is really puzzling and the reason for this discrepancy requires absolutely further investigation. This open problem might be explained by internal inconsistencies in Planck data and/or SNe Ia systematics in the local determination of H_0, or considering a different content of matter in our Universe, or also with a new physics that lies beyond the standard cosmological model.

In addition to the abovementioned problem, another cosmological tension afflict the ΛCDM model, despite it is less worrisome than the first one. Indeed, there is another discrepancy between CMB data and local cosmological probes concerning the S_8 parameter. Considering the data Planck 2018 [40], the value of this parameter is $S_8^{\mathrm{CMB}} = 0.832 \pm 0.013$, whereas other research teams report different values from the weak gravitational lensing of galaxies, such as the Kilo Degree Survey (KiDS-450) [207] with $S_8 = 0.745 \pm 0.039$, and the Subaru Hyper Suprime-Cam (HSC) survey [208] with $S_8 = 0.780^{+0.030}_{-0.033}$. Moreover, the Dark Energy Survey (DES) [209] provides the value of $S_8 = 0.777^{+0.036}_{-0.038}$ from analysis of the cosmic shear. These latter three values are in tension with S_8^{CMB} at a level of 2.1, 1.5, and $1.4\,\sigma$. As it

---

[10] To quantify the incompatibility between two measurements of the same quantity, the following procedure is usually implicitly considered. We consider two measurements, namely $A \pm \sigma_A$ and $B \pm \sigma_B$ in which A and B are the mean values with their respective standard errors. The new variable $A - B$ is usually built and its error is provided by the usual propagation of errors: $\sigma_{A-B} = \sqrt{\sigma_A^2 + \sigma_B^2}$. Then, the deviation of A from B in terms of deviation standards is simply: $|A - B|\, \sigma_{A-B}^{-1}$.

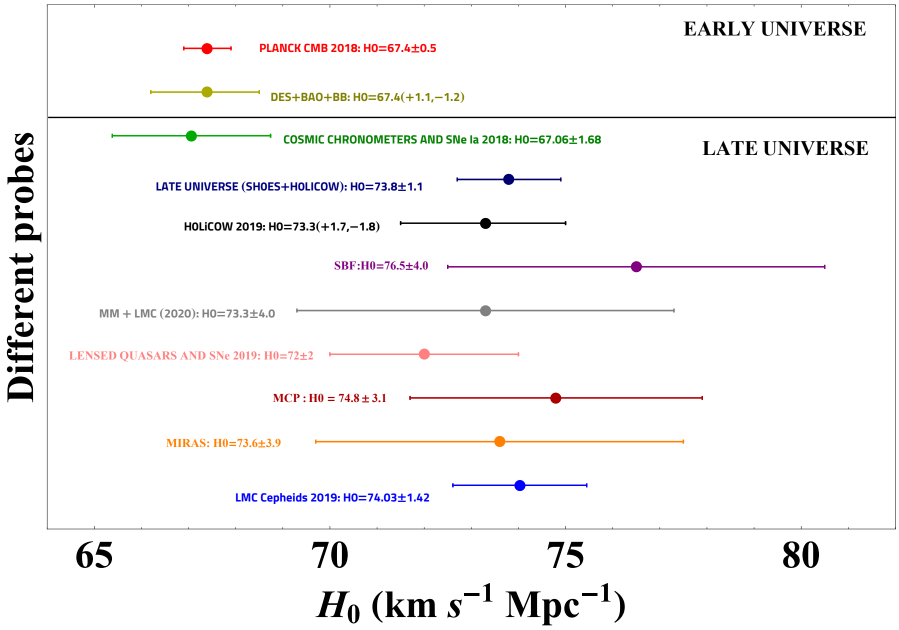

Figure 1.1: Value of H_0 from different probes starting from the early universe: Planck 2018 measurements of CMB from the last scattering surface in the Planck Collaboration [40] are shown in bright red; Dark Energy Survey (DES) + BAO + Big Bang (BB) Nucleosynthesis is shown in light green; cosmic chronometers and SNe Ia in are shown in bright green; a late universe combination of Supernovae-H0 for the Equation of State of Dark energy (SH0ES) and H_0 Lenses in COSmological MOnitoring of GRAvItational Lenses (COSMOGRAIL) Wellspring is shown in dark blue; H0LiCOW alone is shown in black; the Cepheids surface brightness fluctuations method is shown in purple; Megamaser (MM) + LMC is shown in gray; lensed quasars together with SNe Ia in are shown in pink; the Maser Cosmology Project is shown in dark red; Mira variables are shown in orange; Cepheids in the LMC are shown in bright blue. Figure extracted from [TS 3]. See references therein for details.

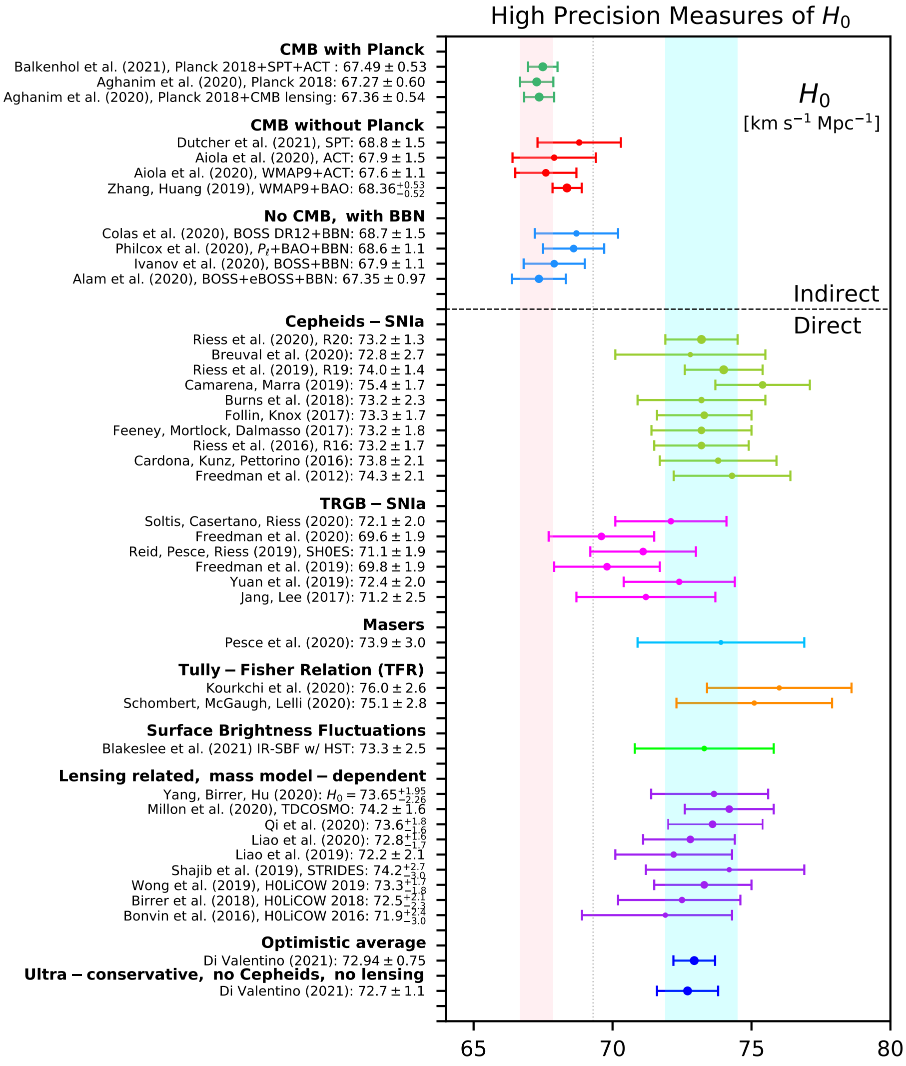

Figure 1.2: Direct and indirect recent measurements of the Hubble constant H_0 obtained by different teams. The light pink vertical band matches the value $H_0^{\rm CMB} = (67.36 \pm 0.54)$ km s^{-1} Mpc^{-1} inferred by CMB data [40], while the light blue band denotes the value $H_0 = (73.2 \pm 1.3)$ km s^{-1} Mpc^{-1} from SH0ES Team [197]. To realize this figure, only direct and indirect measurements of H_0 with error bars less than 3.0 and 1.5 km s^{-1} Mpc^{-1} are considered, respectively. It is quite immediate to see the H_0 tension between CMB data and local probes. In addition, the dotted line for 69.3 km s^{-1} Mpc^{-1} draws a distinction between direct and indirect measurements since this value is given by the central value from SH0ES Team reduced by three respective σs. The original figure is plotted in [68], and see references therein for details.

can be seen, the S_8 tension does not reach the critical level like the Hubble tension, but it is nevertheless an open problem, which cannot be explained within the ΛCDM model.

Although in our analysis we focus specifically on the Hubble tension, it should be also kept in mind that it is not the only open problem in the standard cosmological model. See references [67–70, 76] for details about tensions and anomalies within the ΛCDM model.

1.2 Dark energy models as a minimal extension of the standard paradigm

In this section, we generalize the results obtained in the ΛCDM model (Sect. 1.1) since we consider a dark energy component in the content of the Universe with an equation of state parameter $w_{\mathrm{DE}} < -1/3$. Note that the dark energy component ensures the present cosmic acceleration, as it can be checked from Eq. (1.24). We recall that a cosmological constant Λ is nothing more than a particular form of dark energy with $w_\Lambda = -1$. Then, the wCDM model can be regarded as a minimal extension from the ΛCDM paradigm, but with interesting consequences concerning the cosmological dynamics.

In the wCDM model, the total energy density is given by $\rho_{\mathrm{tot}} = \rho_m + \rho_r + \rho_{\mathrm{DE}}$, where we have simply replaced ρ_Λ with the energy density of the DE component ρ_{DE} with respect to the ΛCDM scenario. Hence, the dimensionless first Friedmann equation (1.35) is now referred to $\Omega_{\mathrm{tot}}(t) = \Omega_m(t) + \Omega_r(t) + \Omega_{\mathrm{DE}}(t)$. Considering the continuity equation (1.25) associated with a dark energy component in which w evolves with the redshift z, i.e. $w_{\mathrm{DE}} = w_{\mathrm{DE}}(z)$, we generalize the expression of the reduced Hubble parameter (1.38) as [35]

$$E(z) = \sqrt{\Omega_{m0}(1+z)^3 + \Omega_{r0}(1+z)^4 + \Omega_{\mathrm{DE}\,0}\exp\left[3\int_0^z \left[1 + w_{\mathrm{DE}}(z')\right]\frac{dz'}{1+z'}\right] + \Omega_{k0}(1+z)^2}\,. \qquad (1.95)$$

It is straightforward to check that, if $w_{\mathrm{DE}} = -1$ for the dark energy component, a cosmological constant Λ is reproduced and the standard Hubble function (1.38) for the ΛCDM model is recovered. Therefore, we can substitute $E(z)$ given by Eq. (1.95) in the general expression (1.54) of the luminosity distance to obtain the corrected version for the wCDM model.

Finally, notice that for a simple linear model $w(z) = w_0 + w_1\,(1+z)$, with constant parameters w_0 and w_1, the exponential term in Eq. (1.95) would grow increasingly unsuitable at redshift $z \gg 1$, leading to large deviations from the ΛCDM model, which is not expected from CMB data. Thus, this kind of $w(z)$ model must be discarded. For high z, instead, although many models have been proposed, we will focus on the CPL parameterization [53, 54] or w_0w_aCDM model:

$$w(z) = w_0 + w_a\,\left[1 - a(z)\right] = w_0 + w_a\,\frac{z}{(1+z)}\,. \qquad (1.96)$$

The advantage of this model is that it works well also for early times. As a consequence, the reduced Hubble function in Eq. (1.95) becomes specifically:

$$E(z) = \sqrt{\Omega_{m0}(1+z)^3 + \Omega_{r0}(1+z)^4 + \Omega_{\mathrm{DE}\,0}(1+z)^{3(1+w_0+w_a)}\,e^{-3\,\frac{w_a\,z}{1+z}} + \Omega_{k0}(1+z)^2}\,. \qquad (1.97)$$

The CPL parametrization leads us to a slowly evolving dark energy scenario slightly different from a cosmological constant. To have a slight deviation from the cosmological constant and a slow evolution with redshift, the values for the parameters are usually $w_0 \sim -1$ and $w_a \sim 0$. These modifications in the cosmological dynamics affect not only the propagation of photons or the luminosity distance, but all phenomena occurred in the past cosmic history and the estimation of the age of the Universe[11]. It can be seen that modifying cosmological dynamics is challenging since we would have only slight modifications with respect to the ΛCDM model to avoid disrupting all predictions and successes derived from the standard paradigm.

1.3 $f\,(R)$ modified gravity theories

There is no a priori motivation to consider a linear gravitational Lagrangian density with respect to the Ricci scalar R, apart from obtaining a second-order partial differential system for the field equations. We recall that the gravitational Lagrangian density contained in the Einstein-Hilbert action (1.1) in GR has a basic form and is given by the simplest curvature invariant (except for a constant). In the context of $f\,(R)$ theories, the gravitational Lagrangian density is generalized as a function f of R, i.e. an extra d.o.f. In addition, considering a matter term S_M, the total action of $f\,(R)$ gravity is given by [79, 81, 83, 84]

$$S_{\text{tot}} = \frac{1}{2\,\chi} \int d^4x\,\sqrt{-g}\,f\,(R) + S_M\,(g_{\mu\nu}, \psi)\ , \tag{1.98}$$

where we have generalized the action (1.1).

Then, varying the total action with respect to the metric, we can write the generalized gravitational field equations in the $f\,(R)$ gravity:

$$f_R\,(R)\ R_{\mu\nu} - \frac{1}{2}\,g_{\mu\nu}\,f\,(R) + g_{\mu\nu}\ \Box\,f_R\,(R) - \nabla_\mu\nabla_\nu f_R\,(R) = \chi\,T_{\mu\nu}\,, \tag{1.99}$$

where $f_R\,(R) = df/dR$, while ∇_μ is the covariant derivative associated with the Levi-Civita connection of the metric, and $\Box = g^{\rho\sigma}\,\nabla_\rho\nabla_\sigma$. Note that Eqs. (1.99) represent a system of ten independent fourth-order partial differential equations in the metric. If $f\,(R) = R$, specifically, the fourth-order terms vanish, and field equations reproduce exactly the Einstein field equations in GR (1.2).

If we calculate the trace of Eqs. (1.99), we end up in

$$f_R\,(R)\ R - 2\,f\,(R)\ + 3\ \Box\,f_R\,(R) = \chi\,T\,, \tag{1.100}$$

in which T is the trace of $T_{\mu\nu}$. Note that R are related to T via a differential equation, while in GR a simple algebraic relation $R = -\chi\,T$ emerges from the trace of the Einstein field equations (1.2). Therefore, once a specific matter is given, we could expect a large number of possible solutions for the metric in the $f\,(R)$ gravity rather than in GR.

It is sometimes useful to refer to the deviation $F\,(R)$ from the gravitational Lagrangian density in GR, i.e.

$$f\,(R) = R + F\,(R)\ . \tag{1.101}$$

In this way, it is straightforward to show that the extended field equations (1.99) can be rewritten in an effective GR-picture as

$$G_{\mu\nu} = \chi\,\left(T_{\mu\nu} + T^{[F]}_{\mu\nu}\right)\ , \tag{1.102}$$

where we have introduced an effective stress-energy tensor related to $F\,(R)$ and its derivatives, i.e.

$$T^{[F]}_{\mu\nu} = -\frac{1}{\chi}\,\left[F_R\,(R)\ R_{\mu\nu} - \frac{1}{2}\,g_{\mu\nu}\,F\,(R) + g_{\mu\nu}\ \Box\,F_R\,(R) - \nabla_\mu\nabla_\nu F_R\,(R)\right]\ . \tag{1.103}$$

---

[11] Other interesting alternative dark energy models involve the presence of an external scalar field (e.g. the quintessence models [52, 55]), but we do not consider them in this thesis.

Also in this form, it is easy to verify that Eqs. (1.102) coincide with the Einstein field equations in GR (1.2) if $f(R) = R$. The idea that the non-Einsteinian term may play a role as a new exotic cosmological fluid emerges from this effective GR-picture given by Eqs (1.102).

Now, we rewrite the extended field equations in the $f(R)$ gravity in another way to emphasize the Newtonian coupling in these theories. Indeed, Eqs. (1.99) can be reformulated as

$$G_{\mu\nu} = \frac{\chi}{f_R(R)} \left(T_{\mu\nu} + T^{[\mathrm{eff}]}_{\mu\nu} \right) , \tag{1.104}$$

in which $T^{[\mathrm{eff}]}_{\mu\nu}$ is another effective stress-energy tensor associated to $f(R)$ and its derivatives:

$$T^{[\mathrm{eff}]}_{\mu\nu} = \frac{1}{\chi} \left\{ \frac{1}{2} g_{\mu\nu} \left[f(R) - f_R(R)\, R \right] + \nabla_\mu \nabla_\nu f_R(R) - g_{\mu\nu} \,\Box\, f_R(R) \right\} . \tag{1.105}$$

In addition to simulate the presence of an extra cosmological fluid, this formulation of the generalized field equations in the $f(R)$ gravity allows us to see that $G_{\mathrm{eff}} = G/f_R(R)$ may be regarded as an effective gravitational coupling, related to geometrical modification of the theory, where we recall that the Newtonian coupling constant G is included in the definition of the Einstein constant χ.

Finally, we finish this subsection by showing the generalized Friedmann equations within the $f(R)$ gravity in a flat FLRW metric:

$$H^2 = \frac{\chi \rho}{3 f_R} + \frac{1}{f_R} \left[\frac{R f_R - f}{6} - f_{RR}\, H\, \dot{R} \right] \tag{1.106}$$

$$\frac{\ddot{a}}{a} = -\frac{\chi}{6 f_R} (\rho + 3 p) - \frac{1}{2 f_R} \left[\dot{R}^2 f_{RRR} + \left(H \dot{R} + \ddot{R} \right) f_{RR} + \frac{1}{6} (f - R f_R) \right] . \tag{1.107}$$

The former is obtained by the component $0-0$ of the field equations (1.99), while the latter is the modified acceleration equation given by a combination of the $1-1$ component of Eqs. (1.99) and Eq. (1.106). These modified equations can be recast in terms of an effective cosmological fluid [81]. It should be noted the presence of extra terms in the right-hand side of Eq. (1.107) with respect to the usual acceleration equation (1.24), as well as an effective Einstein constant χf_R^{-1}. These additional contributions in the modified acceleration equation might mimic a cosmological constant and predict deviations from the ΛCDM model. In this regard, three interesting $f(R)$ models are mostly studied to account for the late time cosmic acceleration without a true cosmological constant [101, 103, 104]. In Sect. 1.3.2 we present one of these models proposed by Hu and Sawicki [101, 102].

1.3.1 The dynamically equivalent formalism in the Jordan frame

We investigate the equivalence between $f(R)$ theories of gravity and the scalar-tensor representation in the Jordan frame [79, 81, 83]. It should be noted that it is usually difficult to manage field equations (1.99) in the metric $f(R)$ gravity, since we have seen specifically they constitute a system of fourth-order partial differential equations in the metric.

To bring field equations to a form that is easier to handle, the $f(R)$ gravity can be restated in the scalar-tensor formalism. It can be checked that the following action

$$S = \frac{1}{2\chi} \int_\Omega d^4x \sqrt{-g} \left[B\, (A - R) + f(A) \right] + S_M (g_{\mu\nu}, \psi) , \tag{1.108}$$

containing two auxiliary fields A and B, is dynamically equivalent to the $f(R)$ action. Indeed, variation with respect to B leads to the equation $A = R$, and then Eq. (1.108) gives the action (1.98) for $f(R)$ gravity.

Furthermore, by performing a variation of the action (1.108) with respect to A, we can solve the d.o.f. for the auxiliary field, i.e. $B = -f_A(A)$, where $f_A(A) = df/dA$. Then, Eq. (1.108) becomes

$$S = \frac{1}{2\chi} \int_\Omega d^4x \sqrt{-g}\, \left[f_A(A)\, (R - A) + f(A)\right] + S_M(g_{\mu\nu}, \psi)\,. \tag{1.109}$$

This action is again dynamically equivalent to that given in Eq. (1.98), since we obtain from variation with respect to A

$$f_{AA}(A)\, (R - A) = 0\,,$$

and eventually $A = R$, if $f_{AA}(A) \neq 0$.

Reformulating the $f(R)$ modified gravity in the scalar-tensor representation, the field A is usually restated in terms of a scalar field

$$\phi = f_A(A)\,. \tag{1.110}$$

On the other hand, if $f_A(A)$ is invertible, this relation implies also $A = A(\phi)$. Moreover, the scalar field potential is defined as

$$V(\phi) = \phi\, A(\phi) - f\left[A(\phi)\right]\,, \tag{1.111}$$

and the action (1.109) becomes

$$S_J = \frac{1}{2\chi} \int_\Omega d^4x \sqrt{-g}\, \left[\phi\, R - V(\phi)\right] + S_M(g_{\mu\nu}, \psi)\,. \tag{1.112}$$

This dynamically equivalent action for the $f(R)$ modified gravity is written in the so-called Jordan frame. It is quite similar to the prototype of extended gravitational theories, the Brans-Dicke formulation [87, 88] with a non-zero potential and a null Brans-Dicke parameter or the O'Hanlon proposal [89]. It should be noted that the extra d.o.f. given by the $f(R)$ function turns into a scalar field ϕ, which is non-minimally coupled to the metric. Conversely, there is only a minimal coupling for the matter.

Actually, as shown in [80], the relation $f_{RR}(R) \neq 0$ is actually a redundant requirement for the dynamic equivalence between an $f(R)$ theory and a scalar-tensor formulation in the Jordan frame. Indeed, it is sufficient to require that $f_R(R)$ be invertible (continuous and one-to-one in a given interval), i.e. the existence of $R = R(f_R)$. In this way, it is possible to build a scalar field potential $V(\phi)$.

Variations of the action (1.112) with respect to the metric and scalar field lead to field equations in the Jordan frame

$$G_{\mu\nu} = \frac{\chi}{\phi}\, T_{\mu\nu} - \frac{1}{2\,\phi}\, g_{\mu\nu}\, V(\phi) + \frac{1}{\phi}\, \left(\nabla_\mu \nabla_\nu \phi - g_{\mu\nu}\, \Box\, \phi\right) \tag{1.113a}$$

$$R = \frac{dV}{d\phi}, \tag{1.113b}$$

respectively.

Furthermore, by taking the trace of Eq. (1.113a) and using Eq. (1.113b), a dynamical equation for the scalar field is obtained

$$3\, \Box\, \phi + 2\, V(\phi) - \phi\, \frac{dV}{d\phi} = \chi\, T \tag{1.114}$$

for a given matter source, where T is the trace of the matter stress-energy tensor.

Although the presence of a non-minimally coupled scalar field implies non-trivial dynamics in the Jordan frame, it is often convenient to adopt the Jordan frame of the $f(R)$ gravity, since the field equations (1.113a), (1.113b), and (1.114) are now second-order differential equations.

Finally, one can see that the gravitational coupling constant is redefined also in the Jordan frame, similarly to the $f(R)$ metric formalism. More specifically, looking at Eq. (1.113a), $G_{\text{eff}} = {}^{G}\!/_{\phi}$ may be considered as an effective gravitational coupling.

Looking at the action given in Eq. (1.112), the extra d.o.f. provided by $f\,(R)$ does not affect the matter action even in the Jordan frame. Therefore, the stress-energy tensor of ordinary matter must be divergence-free as in GR: $\nabla_\nu T^{\mu\nu} = 0$. Since Bianchi identities are kept in modified gravity, the Einstein tensor is also covariant divergence-free: $\nabla_\nu G^{\mu\nu} = 0$. Here, we define an effective stress-energy tensor related to the scalar field

$$T^{[\phi]}_{\mu\nu} = -\frac{1}{2\,\phi}\,g_{\mu\nu}\,V\,(\phi) + \frac{1}{\phi}\,\left(\nabla_\mu\nabla_\nu\phi - g_{\mu\nu}\,\Box\,\phi\right) \tag{1.115}$$

to rewrite the field equations (1.113a) in the Jordan frame as

$$G_{\mu\nu} = \frac{\chi}{\phi}\,T_{\mu\nu} + T^{[\phi]}_{\mu\nu}\,.$$

Then, considering the divergence-free relations above, it is trivial to show that

$$\nabla_\nu T^{[\phi]\,\mu\nu} = \frac{\chi}{\phi^2}\,T^{\mu\nu}\,\nabla_\nu\phi\,. \tag{1.116}$$

The effective stress-energy tensor $T^{[\phi]}_{\mu\nu}$ does not satisfy the usual law of the ordinary matter [210–213], unless in vacuum ($T_{\mu\nu} = 0$). The extra scalar d.o.f. in the Jordan frame is quite different from a matter field; actually, ϕ is an effective scalar field originating from a scalar mode intrinsically due to a modification in the gravitational action. Note that the laws (1.116) describing the dynamics of $T^{[\phi]}_{\mu\nu}$, as well as the continuity equation related to $T_{\mu\nu}$, are not independent of the field Eqs. (1.113a) and (1.114). However, Eqs. (1.116) can be employed as auxiliary equations to rewrite field equations in a different equivalent form.

Finally, we present the non-vanishing field equations in the Jordan frame of $f\,(R)$ gravity in a flat FLRW geometry:

$$H^2 = \frac{\chi\,\rho}{3\,\phi} - H\,\frac{\dot{\phi}}{\phi} + \frac{V\,(\phi)}{6\,\phi}\,, \tag{1.117a}$$

$$\frac{\ddot{a}}{a} = -\frac{\chi\,\rho}{6\,\phi} - \frac{H}{2}\,\frac{\dot{\phi}}{\phi} - \frac{1}{2}\,\frac{\ddot{\phi}}{\phi} + \frac{V\,(\phi)}{6\,\phi}\,, \tag{1.117b}$$

$$3\ddot{\phi} - 2\,V\,(\phi) + \phi\,\frac{dV}{d\phi} + 9\,H\,\dot{\phi} = \chi\,\rho\,. \tag{1.117c}$$

The modified Friedmann equations (1.117a) and (1.117b), which was obtained from field equations (1.113a), correspond to Eqs. (1.106) and (1.107) in the $f\,(R)$ metric formalism. Note the presence of extra terms in the right-hand side with respect to the usual acceleration equation (1.24) in GR, as well as the presence of the non-minimally coupling. Lastly, Eq. (1.117c) has been derived from Eq. (1.114) and concerns the scalar field evolution in the Jordan frame.

1.3.2 The Hu-Sawicki model

Among several proposals for the functional form of the $f\,(R)$, one of the most studied dark energy models is provided by Hu and Sawicki [101, 102].

The deviation $F\,(R)$, related to $f\,(R)$ through Eq. (1.101), for the HS model is

$$F\,(R) = -m^2\,\frac{c_1\,\left({}^{R}\!/_{m^2}\right)^n}{c_2\,\left({}^{R}\!/_{m^2}\right)^n + 1}\,, \tag{1.118}$$

where n is a positive integer, c_1 and c_2 are the HS dimensionless parameters, and $m^2 \equiv \chi\, \rho_{m0}/3$ with ρ_{m0} matter density today.

Note that for $R \gg m^2$ the limiting case with an effective cosmological constant $\Lambda_{\text{eff}} = c_1\, m^2/2\, c_2$ is recovered [101]. Approximating the cosmic accelerated phase of a flat ΛCDM model with an effective cosmological constant, we obtain the first constraint on the parameters c_1 and c_2:

$$\frac{c_1}{c_2} \approx 6\, \frac{\Omega_{\Lambda 0}}{\Omega_{m0}}\,, \tag{1.119}$$

in which we have used the definitions of cosmological density parameters Ω_{m0} and $\Omega_{\Lambda 0}$. Furthermore, Hu and Sawicki [101] have shown that today $R_0 \gg m^2$, and also the approximation $R \gg m^2$ is viable for the entire past cosmic expansion.

Hereinafter, we set $n = 1$ for simplicity, focusing on the most extensively studied scenario in the HS gravity. In that case, the derivative $F_R \equiv dF/dR$ for $R \gg m^2$ is approximately

$$F_R \approx -\frac{c_1}{c_2^2} \left(\frac{m^2}{R}\right)^2 . \tag{1.120}$$

In particular, for a flat ΛCDM model

$$\frac{R}{m^2} = 3 \left(\frac{1}{a^3} + 4\, \frac{\Omega_{\Lambda 0}}{\Omega_{m0}}\right) , \tag{1.121}$$

where we have used Eqs. (1.23) and (1.24) and the definition of the Ricci scalar R in a flat FLRW metric (1.5).

We can rewrite Eq. (1.120) evaluated today in the limiting case for $R \gg m^2$:

$$F_{R0} \approx -\frac{c_1}{c_2^2} \left[3 \left(1 + 4\, \frac{\Omega_{\Lambda 0}}{\Omega_{m0}}\right)\right]^{-2} , \tag{1.122}$$

in which we have implicitly assumed that the value of Λ_{eff} to be the same as Λ in the ΛCDM limit. Hence, by setting a reference value for F_{R0}, we can obtain the second constraint on c_1 and c_2. Note that, according to Eqs. (1.110) and (1.101), we have in the Jordan frame:

$$\phi = 1 - F_R\,. \tag{1.123}$$

It should be noted that F_R quantifies the deviation from the GR scenario, where $\phi = 1$.

The scalar field potential $V(\phi)$ in the Jordan frame for the HS model assumes the following form:

$$V(\phi) = \frac{m^2}{c_2} \left[c_1 + 1 - \phi - 2\sqrt{c_1\,(1 - \phi)}\right] , \tag{1.124}$$

where we used the definitions given in Eqs. (1.110) and (1.111) referred to the $F(R)$ function in Eq. (1.118). Moreover, we have selected the branch for the potential related to a minus sign just before the square root in Eq. (1.124) to converge to an asymptotically stable De Sitter Universe [214, 215].

Finally, we show two reasonable values for the HS dimensionless parameters c_1 and c_2. More precisely, we fix $\Omega_{m0} = 0.3111$, and $\Omega_{\Lambda 0} = 0.6889$ from the Planck measurements [40]; we set the value of the derivative of the field at the present cosmic time $|F_{R0}| = 1.0 \cdot 10^{-7}$, considering the strongest bound between solar system [101] and cosmological constraints [107, 216], including strong gravitational lensing [217], galaxy clusters [218, 219], CMB data [220–223], redshift-space distortion [224], and binary pulsars [225]. Then, using the conditions (1.119) and (1.122) for the ΛCDM limit, we obtain $c_1 = 2.0 \cdot 10^6$ and

$c_2 = 1.5 \cdot 10^5$. Considering these values for c_1 and c_2, in Fig. 1.3 we show the profile of the HS scalar field potential in the Jordan frame, noting a slow evolution of $V(\phi)$.

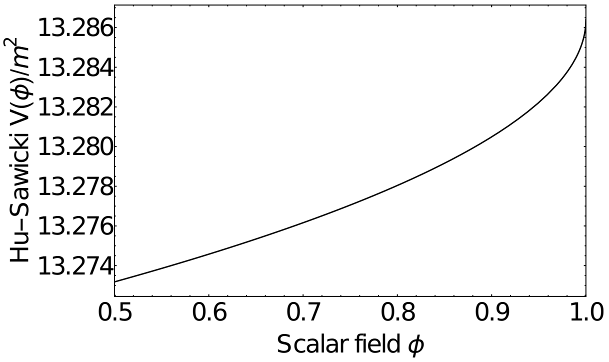

Figure 1.3: Behavior of the HS scalar field potential in the Jordan frame, according to Eq. (1.124), with dimensionless parameters $c_1 = 2.0 \cdot 10^6$ and $c_2 = 1.5 \cdot 10^5$. It should be noted that $V(\phi)/m^2$ is dimensionless. Plot reported from [TS 4].

1.3.3 Modified luminosity distance

In this section, we derive the correction for the distance luminosity in the late Universe within the framework of the $f(R)$ metric formalism. Let us start with the Ricci scalar R in a flat FLRW metric (1.5) ($k = 0$), which can be recast in the form

$$R = 12\,H^2 + 6H\,\frac{dH}{d\gamma}, \tag{1.125}$$

where in this section the Hubble parameter H is expressed as a function of $\gamma \equiv \ln(a)$.
Now, following the HS formalism [101], we introduce two auxiliary variables, y_H and y_R, that are useful to write the luminosity distance in the $f(R)$ gravity. We write the Hubble parameter and Ricci scalar as

$$H^2 = m^2\left[(1+z)^3 + y_H\right], \qquad R = m^2\left[3\,(1+z)^3 + y_R\right], \tag{1.126}$$

where the two dimensionless variables y_H and y_R encompass extra contributions with respect to the matter component in the ΛCDM model. We remind the definition: $m^2 = \chi\,\rho_{m0}/3 = H_0^2/\Omega_{m0}$. Note that if y_H is simply a constant, the first relation is nothing more the Friedmann equation (1.23) in a spatially flat ΛCDM model. In the context of $f(R)$ gravity, instead, y_H and y_R evolve and their dynamics strongly depend on the form of the $f(R)$ function or, equivalently, the scalar field potential $V(\phi)$.
We rewrite the modified Friedmann equation (1.106) and the Ricci scalar relation (1.125) in terms of y_H and y_R. Then, we have a set of coupled ordinary differential equations:

$$\frac{dy_H}{d\gamma} = \frac{1}{3}y_R - 4y_H \tag{1.127}$$

$$\frac{dy_R}{d\gamma} = \frac{9}{a^3} - \frac{1}{y_H + a^{-3}}\frac{1}{m^2 F_{RR}}\left[y_H - F_R\left(\frac{1}{6}y_R - y_H - \frac{a^{-3}}{2}\right) + \frac{1}{6}\frac{F}{m^2}\right]. \tag{1.128}$$

We have used the definition of the deviation $F(R)$ given by Eq. (1.101). The solution of this coupled first-order differential equations system above can not be obtained analytically, but can be numerically calculated. We need initial conditions such that this scenario mimics the ΛCDM model in the matter dominated universe at initial redshift $z_i \gg 1$. Hence, we impose the following conditions for y_H and y_R

at the redshift z_i:

$$y_H(z_i) = \frac{\Omega_{\Lambda 0}}{\Omega_{m0}} \tag{1.129}$$

$$y_R(z_i) = 12\frac{\Omega_{\Lambda 0}}{\Omega_{m0}}. \tag{1.130}$$

The standard ΛCDM model is reached for $z = z_i$ or asymptotically, and we consider a flat geometry, neglecting the radiation contribution, such that $\Omega_{\Lambda 0} = 1 - \Omega_{m0}$ from Eq. (1.35). Finally, the luminosity distance (1.55) can be written as

$$d_L(z) = \frac{(1+z)}{H_0}\int_0^z \frac{dz'}{\sqrt{\Omega_{m0}\Big(y_H(z') + (1+z')^3\Big)}}\,, \tag{1.131}$$

including the solution $y_H(z)$ from Eq. (1.126).

Chapter 2

Inhomogeneous cosmology

The cosmological principle was a fundamental element in developing the ΛCDM model. The assumption of spatial homogeneity and isotropy, such that space-time is exactly described by the FLRW metric, facilitates our mathematical description of the Universe and seems to be a successful approach. However, the real Universe appears far from homogeneity and isotropy on local scales and deviations become significant at late times: galaxy clustering, cosmic structures, and the existence of huge voids point out that the cosmological principle is only valid on large scales. Thus, although the ΛCDM model is based on a exact homogeneous and isotropic scenario and is supported by successful cosmological evidence, our picture might be an approximate or simplified description of the Universe. The basic assumption is that, in practice, the average of local inhomogeneities over large scales are ruled out such that the properties of homogeneity and isotropy are recovered, at least statistically, on scales large enough. Note that an exact homogeneous and isotropic scenario is conceptually different from a description that turns out to be so only statistically. In the latter case, a typical scale for spatial homogeneity ($\sim 100\,\mathrm{Mpc}$) and an averaging procedure on such a scale are implicitly defined.

In this Chapter, we introduce the LTB metric to describe an inhomogeneous Universe and discuss its impact on the dynamics and cosmological consequences. We derive the gravitational field equations, highlighting differences with respect to the ΛCDM model. In particular, we do so within the framework of GR (for a more general discussion of inhomogeneous models within $f\left(R\right)$ modified gravity theories, see the Chapter 6). Instead of considering a metric that is tailored for inhomogeneous models and contains intrinsically deviations from a smooth scenario, another useful approach is to investigate the impact of clumpy matter distribution on the global cosmological dynamics. In this regard, we introduce the averaging procedure in cosmology to predict the effects of local structures on cosmological observable. Firstly, we briefly show the basic ideas of averaging *à la* Buchert, and then we report a generalized mathematical prescription, which is covariant and gauge-invariant and can be applied, for instance, to average a scalar quantity on the past-light cone of the observer.

2.1 The Lemaître-Tolman-Bondi spherically symmetric solution

The LTB spherical solution [24, 52, 110, 111, 113] describes the geometry of an inhomogeneous but isotropic Universe, generalizing the FLRW line element (1.5). The LTB model is an exact solution of Einstein-Hilbert equations to describe a spherical symmetric void. In the LTB model, the space is isotropic only observing the Universe from a specific preferred point, i.e. the center that is singled out by adopting a spherical symmetry, where an observer is supposed to be located. A useful choice is to adopt spherical spatial coordinates in such a scheme. Differently, observers placed in other positions with respect to the central observer incur anisotropies, specifically along the direction connecting the center of the coordinates and the observer considered. Thus, the LTB model violates the Copernican principle by considering a special position in the Universe. As a possible application, the evolution of a dust cosmological model resulting in a spherical mass overdensity (or underdensity) with vanishing pressure can be formulated in the LTB formalism.

The LTB spherically symmetric line element in the synchronous gauge is written as

$$ds^2 = -dt^2 + e^{2\alpha} dr^2 + e^{2\beta} \left(d\theta^2 + \sin^2\theta \, d\phi^2\right) \,, \tag{2.1}$$

in which r is the radial coordinate indicating the spatial distance from the preferred point. There are two metric functions, $\alpha = \alpha\,(t,\, r)$ and $\beta = \beta\,(t,\, r)$, which do not depend on angular directions.

The ΛLTB model is a cosmological scenario based on GR with the assumption of a cosmological constant Λ, considering the LTB metric (2.1). In this section, we separate explicitly the cosmological constant and matter term. Moreover, we are interested in the late Universe, hence we recall that we neglect relativistic species, since they are subdominant today. As a consequence, the total energy density of the Universe $\rho_{\rm tot}$ has only contributions from the matter component and the cosmological constant. Here, we neglect the subscript m in ρ for the energy density of the matter component for brevity.

2.1.1 Dynamics of the LTB inhomogeneous Universe

The three independent Einstein field equations (1.2) in the ΛLTB model with a pressure-less dust ($p = 0$) are provided by the $0-1$, $0-0$ and $1-1$ components, which rewrite as

$$\frac{\dot\beta'}{\beta'} - \dot\alpha + \dot\beta = 0 \,, \tag{2.2a}$$

$$\dot\beta^2 + 2\,\dot\alpha\,\dot\beta + e^{-2\beta} - e^{-2\alpha}\left[2\,\beta'' + 3\,\beta'^2 - 2\,\alpha'\,\beta'\right] = \chi\,\rho + \Lambda \,, \tag{2.2b}$$

$$2\,\ddot\beta + 3\,\dot\beta^2 + e^{-2\beta} - \beta'^2\,e^{-2\alpha} = \Lambda \,, \tag{2.2c}$$

respectively, where $\dot{()} = d/dt$ and $()\,' = d/dr$. The other non-null field equations in the LTB metric are related to the previous equations system due to the spherical symmetry. More precisely, it is straightforward to show the following relations between the Einstein tensor components in the LTB metric:

$$G^2_{\ 2} = G^1_{\ 1} + \frac{\left(G^1_{\ 1}\right)'}{2\,\beta'} \,, \tag{2.3}$$

and also $G^3_{\ 3} = G^2_{\ 2}$.

It should be noted that the two metric functions α and β can be related in GR, by exploiting the $0-1$ component (2.2a) of the Einstein field equations, in order to rewrite the LTB line element (2.1) in a simpler form [112]. Indeed, Eq. (2.2a) rewrites as

$$\frac{\dot\beta'}{\beta'} = \partial_t\left[\ln\left(\beta'\right)\right] = \dot\alpha - \dot\beta \,, \tag{2.4}$$

which admits the solution

$$\beta' = g\,(r)\; e^{\alpha-\beta} \,, \tag{2.5}$$

where $g\,(r)$ is an arbitrary function of the radial coordinate r. In particular, note that

$$e^{\alpha} = \frac{\beta'\,e^{\beta}}{g\,(r)} = \frac{\left(e^{\beta}\right)'}{g\,(r)} \,. \tag{2.6}$$

Then, the LTB line element (2.1) can be rewritten as

$$ds^2 = -dt^2 + \frac{[(a\,r)\,']^{\,2}}{1 - r^2\,K^2} dr^2 + (a\,r)^{\,2}\,\left(d\theta^2 + sin^2\theta\,d\phi^2\right)\,, \tag{2.7}$$

in which the following parametrization has been adopted

$$g\,(r) \equiv \left(1 - r^2\,K^2\right)^{\,1/2} \tag{2.8}$$

with $K = K\,(r)$, and $a\,(t, r) \equiv e^{\beta}\,r^{-1}$ has been defined as the generalization of the scale factor in an inhomogeneous Universe.

By using the LTB metric, the remaining Einstein field equations (2.2b) and (2.2c) become

$$3\,\left[\dot{a}^2\,a\,r^3 + a\,r^3\,K^2\right]' = (\chi\,\rho + \Lambda)\,\left[(a\,r)^{\,3}\right]'\,, \tag{2.9a}$$

$$\frac{2\,\ddot{a}}{a} + \frac{\dot{a}^2}{a^2} + \frac{K^2}{a^2} = \Lambda\,, \tag{2.9b}$$

respectively.

It may be observed that the form of the LTB metric given by Eq. (2.7) reminds the FLRW line element (1.5). More specifically, if $a\,(t, r)$ and $K\,(r)$ do not depend on the radial coordinate r, the FLRW geometry is exactly recovered to describe a homogeneous and isotropic Universe. Furthermore, it is straightforward to show in that limit that Eq. (2.9a) turns into the Friedmann equation (1.23), which combined with Eq. (2.9b), also provides the cosmic acceleration equation (1.24) in the FLRW metric. Differently from the homogeneous and isotropic scenario, in the ΛLTB model the generalized scale factor depends also on both time and the radial comoving coordinate. This implies, for instance, that also the Hubble expansion rate is spatially inhomogeneous [226], and the presence of local inhomogeneities affects the redshift-luminosity distance relation.

Finally, the continuity equation (the energy-momentum conservation law $\nabla_\mu T^{\mu\nu} = 0$ with $\nu = 0$) for a pressure-less perfect fluid in the LTB metric (2.1) can be written as

$$\dot{\rho} + \left(\dot{\alpha} + 2\,\dot{\beta}\right)\,\rho = 0\,, \tag{2.10}$$

or equivalently

$$\dot{\rho} + \left(\frac{\dot{a} + r\,\dot{a}'}{a + r\,a'} + 2\,\frac{\dot{a}}{a}\right)\,\rho = 0\,, \tag{2.11}$$

if the LTB metric in the form given by Eq. (2.7) is considered.

Note that if we had considered a more general barotropic fluid with non-vanishing pressure p (the equation of state parameter is $w \neq 0$), the component of $\nabla_\mu T^{\mu\nu} = 0$ with $\nu = 1$ would provide $p'\,(t, r) = 0$ and also implies $\rho'\,(t, r) = 0$. As a consequence, in that case, the pressure and the energy density associated to this fluid must be homogeneous, they cannot depend on r. Therefore, we can admit the existence of radial inhomogeneities in the LTB metric only for a pressureless matter. This is the reason why a dust is usually considered in the ΛLTB model.

2.2 Averaging formalism in cosmology

The implicit assumption in the standard ΛCDM model is that matter fluctuations are randomly distributed on large scales, hence deviations from homogeneity are discarded after an averaging procedure. The averaging problem in cosmology consists in describing the large-scale geometry and dynamics, averaging cosmological quantities on small scales [167–169]. This procedure might be employed to test the assumption of a homogeneous and isotropic Universe. Finding the appropriate and well-defined averaging prescription is a significant challenge not only for theoretical cosmology but also for observational reasons. For instance, what is the effect of (local) inhomogeneities of the Universe on (global) cosmological measurements? Many observational facts and phenomena in our Universe are based on information supplied by photons, which can be regarded as probes of local inhomogeneities. Indeed, along their journey in the Universe, photons interact with several structures and might be influenced by the matter distribution. Hence, we could expect deviations in the redshift-distance relation with respect to a pure homogeneous scenario due to effects on local scales, which are usually neglected in the standard paradigm. A natural choice for the region of the averaging procedure is to perform such a process on the past-light cone of the observer. Several proposals have been recently investigated to average cosmological observables on space-like and null hypersurfaces. To generalize the averaging procedure for any observer and any choice of region in which averages are performed, the mathematical prescription should be covariant and gauge-invariant [170–174]. If it had not been, we would have had misinterpreted effects that occurred only in a specific gauge and not in other ones, or we would have lose some physical effects because of the choice of the gauge. Furthermore, the advantage of a gauge-invariant formalism is to allows us to simplify the description, choosing a proper gauge[1] .

2.2.1 The backreaction problem

When we move from a local description of the Universe with coarse-grained structures to a picture on large scales through an averaging procedure, we might have modifications in the global geometry and consequences in the cosmological dynamics.

Let us consider physical phenomena that occur on two different cosmological scales (we refer to a local and a large scale). Suppose we know exactly the metric $g_{\mu\nu}^{[\mathrm{loc}]}$ and the stress-energy tensor $T_{\mu\nu}^{[\mathrm{loc}]}$ at a given local scale, where the Universe does not appear homogeneous. We assume the validity of Einstein equations at such scale:

$$G_{\mu\nu}^{[\mathrm{loc}]} = \chi\, T_{\mu\nu}^{[\mathrm{loc}]} \,. \tag{2.12}$$

On the other hand, if we focus on large scales, we should perform averages on several regions. In the standard cosmology, the geometry of the Universe appears to be homogeneous on large scales, as well as the cosmological fluid. In such a framework after the averaging process, inhomogeneities are negligible. In particular, averages are implicitly performed on the metric and cosmological fluid (naively, the scale factor, pressure and density of the cosmological fluid in the ΛCDM model do not depend on space). Therefore, we can write

$$G_{\mu\nu}\left(\langle g_{\mu\nu}\rangle\right) = \chi\, \langle T_{\mu\nu}\rangle \,, \tag{2.13}$$

where $\langle\ldots\rangle$ denotes an average defined on a spatial domain. We recall that the Einstein tensor $G_{\mu\nu}$ depends on second derivatives of the metric tensor components $g_{\mu\nu}$ (it contains also time derivatives). However, a meticolous average of the Einstein field equations should be

$$\langle G_{\mu\nu}\left(g_{\mu\nu}\right)\rangle = \chi\, \langle T_{\mu\nu}\rangle \,. \tag{2.14}$$

It should be emphasized that time evolution and averaging processes do not commute, i.e.,

$$\langle G_{\mu\nu}\left(g_{\mu\nu}\right)\rangle \neq G_{\mu\nu}\left(\langle g_{\mu\nu}\rangle\right) \,, \tag{2.15}$$

---

[1] The Geodesic Light-Cone (GLC) coordinates [227] are particularly suitable for the light-cone averaging. GLC are observational coordinates that simplify the geometrical description of a four-dimensional space-time in terms of a light-cone foliation to conveniently write the expressions of redshift, luminosity distance and their averages on the past light-cone [172].

because of the non-linearity of Einstein field equations. As a consequence, the correct field equations (2.14) should contain an extra contribution $E_{\mu\nu}$ on large scales as compared with Eq. (2.13), and they rewrite as

$$G_{\mu\nu}\left(\langle g_{\mu\nu}\rangle\right) = \chi\,\langle T_{\mu\nu}\rangle + E_{\mu\nu}\,. \tag{2.16}$$

Note that this field equations are different from Eqs. (2.12) used at local scales, since an extra term emerges from the non-commutation between the averaging procedure and time evolution. If we apply an average procedure on a lumpy distribution and then compute the time progression of the smoothed values using the Einstein equation, the outcome would differ from what we would get by evolving the original inhomogeneous distribution and averaging it only at the very end. Hence, starting from a local point of view, we end up in a large-scale description: the Universe might appear homogeneous after the averaging process, but the extra term $E_{\mu\nu}$ could affect the cosmological dynamics. This fact is the so-called backreaction problem in cosmology, namely the backreaction of local inhomogeneities on the global cosmological dynamics of an averaged background. The extra contribution is regarded as a correction (backreaction) term.

The backreaction mechanism was investigated by T. Buchert [167–169] to try to explain, or partially explain, the accelerated expansion of the present-day Universe through an additional source in the Einstein field equations provided by the backreaction term. Buchert used the synchronous gauge and chose a foliation of space-time with space-like hypersurfaces; he applied the averaging procedure specifically for a set of comoving observers, starting from field equations in the Arnowitt-Deser-Misner (ADM) formalism [113, 228, 229]. Following Buchert's approach, the averaged Friedmann equations include an extra contribution, which may play the role of a cosmological constant.

In this thesis, we are not interested in this approach to provide an explanation for the dark energy component, but we remark that Buchert's formalism was the starting point and a powerful tool to develop a more general average prescription with the idea of analyzing the effect of inhomogeneities on cosmological observables, as we discuss in Chapter 7. In particular, Buchert defined the average of a scalar quantity $S\left(t,\vec{x}\right)$ on a three-dimensional compact and simply connected domain $\mathcal{D}$ as

$$\langle S\left(t,\vec{x}\right)\rangle_{\mathcal{D}}\left(t\right) \equiv \frac{1}{V_{\mathcal{D}}}\int d^3x\,\sqrt{g^{(3)}}\,S\left(t,\vec{x}\right)\,, \tag{2.17}$$

where $V_{\mathcal{D}} \equiv \int d^3x\,\sqrt{g^{(3)}}$ is the volume of $\mathcal{D}$, and the integration measure is weighted with the determinant $g^{(3)}$ of the three-metric induced on space-like hypersurfaces.

Finally, we stress the fact that we will focus on average only scalar quantities on a portion of space-time in GR. We have to mention that there is no currently well-defined procedures to average vectors and tensors[2].

2.2.2 Light-cone averaging prescriptions

Since astronomical and astrophysical observations are based on receiving light signals from a space-time region associated with null hypersurfaces, the past light-cone of the observer, it is crucial to perform the light-cone averaging for a given scalar quantity $\mathcal{S}\left(x\right)$, for instance the luminosity distance. The Buchert's averaging prescription in Eq. (2.17) depends on the choice of space-like hypersurfaces used to foliate the space-time, and consequently on the integration domain $\mathcal{D}$. The average in Eq. (2.17) is not gauge invariant, since if we change gauge the averaging procedure is performed on a different hypersurface. Therefore, it can be shown that this problem of gauge invariance can be overcome by introducing a proper window function, which is intendended to select a specific region of the space-time for averaging,

---

[2] An interesting general formalism is the so-called Macroscopic Gravity [230], which was developed by R. Zalaletdinov to try to average tensors on general manifolds. The final purpose is to average the Einstein-Hilbert field equations.

and most importantly, it regulates domain deformations due to gauge transformations such that the new average prescription is gauge-invariant [172, 174]. To this end, the window function should contain only scalar quantities. Let us see more in detail how to define a proper averaging prescription on the past-light cone.

We consider a foliation of the space-time $\mathcal{M}_4$ given by space-like hypersurfaces $\Sigma\left(A\right)$, each of which is labelled with a constant value of a scalar function $A\left(x\right)$ with $x = (t, \vec{x})$. We recall that for space-like hypersurfaces the function $A\left(x\right)$ has time-like gradient: $\partial_\mu A\, \partial^\mu A < 0$. The normal vectors of $\Sigma\left(A\right)$ are written as

$$n_\mu = -\frac{\partial_\mu A}{\sqrt{-\partial_\nu A\, \partial^\nu A}}\,, \tag{2.18}$$

which satisfies also $n_\mu\, n^\mu = -1$ and can be identified in the four-velocity of a comoving observer along the flow lines of n_μ. Moreover, $V\left(x\right)$ is a scalar field associated with null hypersurfaces, such that $\partial_\mu V\, \partial^\mu V = 0$. In this region, the photons momenta are $k_\mu = \partial_\mu V$. For a given observer, the past light-cone is the four-dimensional region Ω bounded by two hypersurfaces, one space-like, $A\left(x\right) = A_0 = \text{const.}$, and the other one null, $V\left(x\right) = V_0 = \text{const.}$

The average of a scalar quantity $\mathcal{S}\left(x\right)$ in the past light-cone [172] is defined as

$$\langle \mathcal{S}\left(x\right)\rangle \equiv \frac{I\left(S; W_\Omega\right)}{I\left(1; W_\Omega\right)}\,, \tag{2.19}$$

where the integral is given by

$$I\left(\mathcal{S}; W_\Omega\right) = \int_{\mathcal{M}_4} d^4x\, \sqrt{-g\left(x\right)}\, W_\Omega\left(x\right)\, \mathcal{S}\left(x\right) \tag{2.20}$$

in terms of a window function $W_\Omega\left(x\right)$. Note that $I\left(1; W_\Omega\right)$ provides the volume of Ω.

Now, we can build several averaging prescriptions using different window functions, which select only a specific region of the past light-cone, depending on cosmological observables or different physical applications. For instance, the intersection of $\Sigma\left(A_0\right)$ with the light-cone $V\left(x\right) = V_0$ represents a compact, two-dimensional region Ω embedded in the past light-cone. This is the region from which a source could emit light signals, and the averaging procedure can be applied to scalar observables, such as the luminosity distance or redshift. In this case, the window function is can be written as

$$\begin{aligned} W_\Omega\left(x\right) &= -n^\mu\, \nabla_\mu \Theta\left[\left(A\left(x\right) - A_0\right)\right]\, n^\nu\, \nabla_\nu \Theta\left[V_0 - V\left(x\right)\right] \\ &= \left|\partial_\mu V\left(x\right)\, \partial^\mu A\left(x\right)\right|\, \delta_D\left[A\left(x\right) - A_0\right]\, \delta_D\left[V_0 - V\left(x\right)\right]\,, \end{aligned} \tag{2.21}$$

where Θ denotes the Heaviside step function, and we have used Eq. (2.18) and the property that the distributional derivative of Θ gives the Dirac delta function δ_D.

We can have different prescriptions of average, according to the choice of the window function. If we are receiving signals though massive messengers from internal region Ω of the past light-cone of the observer, it is convenient to consider space-time regions that are causally connected with us. Then, we perform averages with the following window function are

$$\begin{aligned} W_\Omega\left(x\right) &= n^\mu\, \nabla_\mu \Theta\left(A - A_0\right)\, \Theta\left[V_0 - V\right] \\ &= \sqrt{-\partial_\mu A\, \partial^\mu A}\, \delta_D\left(A - A_0\right)\, \Theta\left(V_0 - V\right)\,, \end{aligned} \tag{2.22}$$

which is useful to select the causally connected sections of the fixed hypersurface $\Sigma\left(A_0\right)$, spanned by the variation of the null hypersurfaces $V\left(x\right)$.

Finally, another interesting possibility is to average a scalar quantity on different regions of a fixed light-cone V_0, spanned by the variation of $\Sigma(A)$, if photons are arriving from sources located a different redshifts. Then, the window function becomes

$$\begin{aligned} W_\Omega(x) &= -\Theta(A - A_0)\, n^\mu\, \nabla_\mu \Theta(V_0 - V) \\ &= \frac{|\partial_\mu V\, \partial^\mu A|}{\sqrt{-\partial_\nu A\, \partial^\nu A}}\, \Theta(A - A_0)\, \delta_D(V_0 - V)\ . \end{aligned} \tag{2.23}$$

The resulting integration region Ω is a truncated light-cone. The different light-cone averaging prescriptions from Eq. (2.19) with integration regions selected by the window functions (2.21), (2.22), and (2.23) are summarized in Fig. 2.1.

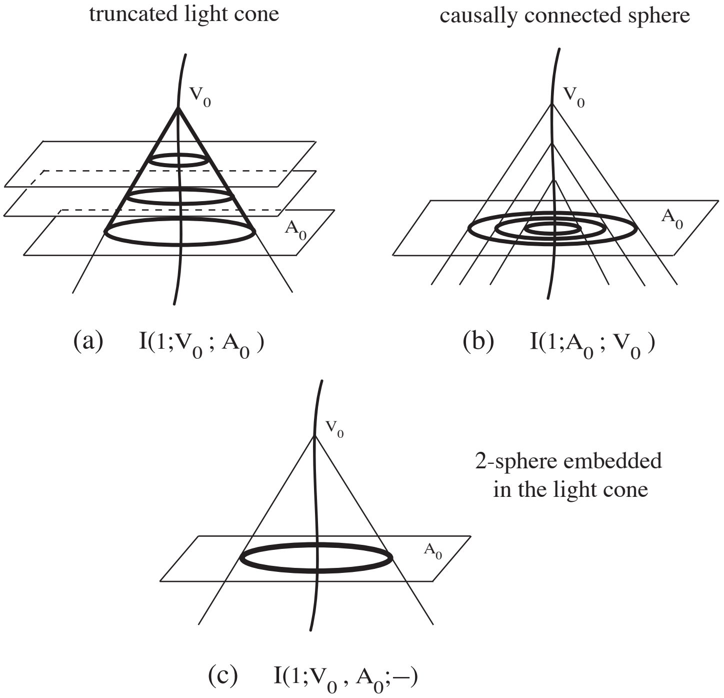

(a) $I(1;V_0;A_0)$ (b) $I(1;A_0;V_0)$

(c) $I(1;V_0,A_0;-)$

Figure 2.1: The light-cone averaging can be performed on different regions related to the past-light cone of the observer. The covariant and gauge-invariant average prescritpion from Eq. (2.19) is adapted by using three different window functions (2.21), (2.22), and (2.23) (see the panels (c), (b), (a), respectively). This plot is reported in [172].

2.2.3 Generalized formulation to average cosmological observables

Before generalizing the previous averaging prescriptions, we remark here that it is crucial to know what the basic elements which shoud be considered to define a well-posed prescription, such as the physical observables we are interested in, the location of the source, the types of signals emitted from the source to us, and the nature of the observer. Furthermore, we could be interested in introducing an extra weight factor in the integral for averaging, such as the matter density or galaxy number counts.

Bearing in mind these various aspects, we present an extension of the averaging procedure reported in the previous section, following the approach developed in [174]. In this regard, in addition to specify obviously the cosmological observable $\mathcal{S}(x)$ to be averaged (i.e., the luminosity distance), we have to define a set of other five different scalar fields $\Gamma \equiv (A, B, C, V, \rho)$:

- $A(x)$ is related to a free-falling observer with its four-velocity n_μ in the form of Eq. (2.18), and has time-like gradient, i.e., $\partial_\mu A\, \partial^\mu A < 0$;

- $B\left(x\right)$ labels the space-like hypersurfaces, where the sources are placed, such that $\partial_\mu B\, \partial^\mu B < 0$;
- $C\left(x\right)$ allows to define the four-vector

  $$m_\mu = -\frac{\partial_\mu C}{\sqrt{\left|\partial_\nu C\, \partial^\nu C\right|}} \,, \tag{2.24}$$

  whose flow lines are considered to evaluate the span of the volume integral over a fixed hypersurface B;
- $V\left(x\right)$ identifies the past-light cone of the observer, as shown in the averaging prescriptions in the previous section;
- $\rho\left(x\right)$ is the eventual extra weight we mentioned above.

First of all, note that if $A = B = C$ and $\rho = 1$, we recover the averaging procedure in Sect. 2.2.2. On the contrary, we remark here that while the scalar field A relies on the state of motion of the observer, the two fields B and C depends on the geometry and the conditions under which observations are obtained. For instance, if we aim to investigate light signals emitted from sources at a given redshift, it is convenient to select $C = A$, which implies $m_\mu \equiv n_\mu$, and also set $B = k^\mu\, n_\mu$, which identifies the redshift z of photons emitted from the source with respect to the observer. Furthermore, we stress that if the signal messengers are massive, then the scalar field V must have time-like gradient.

As a specific application, now we focus on averaging $\mathcal{S}\left(x\right)$ on the compact, two-dimensional region Ω embedded in the past light-cone, given by the intersection of the hypersurface $\Sigma\left(B_s\right)$, where B_s identifies the source, with a fixed past light-cone of the observer $V = V_0$. Hence, we can set $\Gamma = \left[A\left(x\right), B_s, C\left(x\right), V_0, \rho\left(x\right)\right]$ and this light-cone average is defined as

$$\left\langle \mathcal{S}\right\rangle_{\Sigma(B_s)} \equiv \frac{I\left(\mathcal{S},\Gamma\right)}{I\left(1,\Gamma\right)} \,, \tag{2.25}$$

where the integral $I\left(\mathcal{S},\Gamma\right)$ is written as in Eq. (2.20), but it contains a window function $W_\Omega\left(x\right)$ more general and different from those given in Eqs. (2.21), (2.22), and (2.23). In this case, we write

$$\begin{aligned} W_\Omega\left(x\right) &= \rho\, n^\mu\, \nabla_\mu \Theta\left(V_o - V\right)\, m^\mu\, \nabla_\mu \Theta\left(B_s - B\right) \\ &= \rho\, \delta_D\left(V_o - V\right)\, \delta_D\left(B_s - B\right)\, \frac{\partial^\mu A\, \partial_\mu V}{\sqrt{\left|\partial_\alpha A\, \partial^\alpha A\right|}}\, \frac{\partial^\nu C\, \partial_\nu B}{\sqrt{\left|\partial_\beta C\, \partial^\beta C\right|}} \,, \end{aligned} \tag{2.26}$$

where we have used again the distributional derivative of Θ and the definitions of the four-vectors n^μ and m^μ. It is straightforward to check that the window function (2.21) is recovered if $A = B = C$ and $\rho = 1$, as we mentioned above.

We would like to stress that, actually, we will not adopt a specific averaging prescription in this thesis, since the method presented in Chapter 7 is completely general and valid for any prescription. Our intention in this chapter was to present the averaging problem and some useful prescriptions to average scalar observables on the past-ligh cone, in order to have a clear picture of how a well-posed averaging prescription should be defined, when we will discuss it in Chapter 7.

Part II

The evolution of the Hubble constant with the redshift

Chapter 3

Redshift binned analysis using standard candles

The Hubble constant tension is one of the biggest open problems of modern cosmology, as we discussed in Sect. 1.1.7. Having in mind that this discrepancy is given by independent measurements of the Hubble constant H_0 referred to different redshifts (local measurements versus CMB data), in this chapter we investigate the possibility of a hidden evolutionary effect that could imply a running Hubble constant with the redshift [177–179, 231–234]. We focus on the data analysis of the Pantheon sample [176], a compilation of 1048 spectroscopically confirmed SNe Ia that gathers different surveys with a redshift range $0 < z < 2.26$. SNe Ia are observed up to a low redshift range: the farthest so far discovered is at $z = 2.26$ [235]. The basic idea of the analysis developed in this chapter is to divide the sample into redshift bins to check whether H_0 assumes constant values inside each bin or evolves along the redshift range of the Pantheon sample. In this regard, we follow a binned analysis of the Pantheon sample in three, four, twenty, and fourthy redshift bins to extract the values of H_0 in each bin. Then, if data points suggest a possible evolution, we want to fit them with a function of the redshift. Note that, in principle, a possible evolution of an effective Hubble constant with the redshift might address the H_0 tension, since the fitting function arising from the phenomenology of SNe Ia could match incompatible measurements of the Hubble constant obtained from probes at different redshifts. The Part II of this thesis is devoted to investigate a possible and unexpected evolution of the Hubble constant. In this and the next chapter we perform analysis on local sample, while in Chapter 5 we will provide a theoretical interpretation of an effective Hubble constant. The content of this chapter is mainly based on the original works from [TS 3, 6, 8].

3.1 Methodology

We compare the theoretical distance modulus $\mu_{\rm th}$ of each SN given by Eq. (1.58) with the observed distance modulus $\mu_{\rm obs}$ in Eq. (1.59). We remind that $\mu_{\rm th}$ depends on the luminosity distance d_L, hence is referred to a specific cosmological model. In this chapter, the analysis is perfomed by considering spatially flat ΛCDM and $w_0 w_a$CDM cosmological models in the late Universe, for which the Hubble function, contained in the luminosity distance through the general expression (1.55), is provided by Eqs. (1.38) and (1.97), respectively, with $\Omega_{k0} = 0$, and $\Omega_{r0} = 0$. Also note that $\Omega_{\Lambda 0} = 1 - \Omega_{m0}$ and $\Omega_{\rm DE\ 0} = 1 - \Omega_{m0}$ for the flat ΛCDM and $w_0 w_a$CDM models, respectively.

It should be emphasized that the Hubble constant H_0 is degenerate with the absolute magnitude M of a SN, as we mentioned in Sect. 1.1.5, and as it can be checked by combining Eqs. (1.58), (1.55) and

(1.38). Specifically, M is calibrated to -19.35 in the Pantheon sample such that $H_0 = 70.0\,\mathrm{km\ s^{-1}\ Mpc^{-1}}$ [176].

We now introduce a slight modification for the computation of luminosity distance (1.55), which in the case of SNe Ia is more precise according to [121]:

$$d_L\left(z_{\text{hel}}, z_{\text{HD}}\right) = \left(1 + z_{hel}\right) \int_0^{z_{HD}} \frac{dz'}{H\left(z'\right)}\,, \tag{3.1}$$

where z_{hel} is the heliocentric redshift, and z_{HD} is the corrected CMB redshift, or “Hubble-diagram” redshift, which takes into account the peculiar velocity corrections.

To perform a statistical analysis, we consider the difference $\Delta\mu = \mu_{\text{obs}} - \mu_{\text{th}}$ and the χ^2_{SNe} defined in Eq. (1.61), which we rewrite here for the sake of convenience:

$$\chi^2_{\text{SNe}} = \Delta\mu^T\, C^{-1}\, \Delta\mu\,, \tag{3.2}$$

where

$$C = C_{sys} + D_{stat} \tag{3.3}$$

is the full covariance matrix. The C_{sys} matrix involves systematic errors, while D_{stat} is a diagonal matrix that contains statistical errors for each SN, due to peculiar velocities, photometry, bias, stochastic gravitational lensing, mass step correction, and intrinsic scatter [176]. Referring to the Pantheon sample, $\Delta\mu$ represents a vector with 1048 components, while C, C_{sys} and D_{stat} are 1048×1048 square matrices. The Pantheon sample data is available in the repository by Scolnic et al. (2018) [176] (https://github.com/dscolnic/Pantheon).

Since we are interested in checking the values of H_0 along the redshift range of the Pantheon sample, we follow a binning approach. Therefore, we split the Pantheon sample in different redshift bins each having the same number N of SNe Ia. More precisely, we have considered 1048 SNe Ia, ordered them by redshift, and then divided into different redshift bins (three, four, twenty, and fourthy) with equally populated subsamples of SNe Ia. The choice of three bins is motivated by a relatively high number of SNe to still provide statistical representative subsamples. For instance, if we have three bins, $N \approx 349$ SNe for each bin, and the redshift ranges are $0.01 < z < 0.18$, $0.18 < z < 0.34$, and $0.34 < z < 2.26$. In the case of four bins, instead, $N = 262$ in each bin and the redshift ranges are: $0.01 < z < 0.13$, $0.13 < z < 0.25$, $0.25 < z < 0.42$, and $0.42 < z < 2.26$. Moreover, if we consider twenty and fourthy bins, the redshift ranges for their first bins are $0.010 < z < 0.021$, and $0.010 < z < 0.016$, respectively.

Then, we build the subvectors $\Delta\mu$ containing data from N SNe, according to the binning division and redshift order. We also divide the full covariance matrix C into $N \times N$ submatrices for each redshift bin. In this regard, concerning simply the statistical contribution D_{stat} in C, each diagonal element of the D_{stat} matrix is related to a single SN, hence we can quickly build the submatrices starting from D_{stat}. However, if we include the systematic errors, we need to consider also C_{sys}, which is not a diagonal matrix. Thus, we used a customized code to select C_{sys} elements involved only with the SNe within the redshift bin taken into account. Hence, we build properly the submatrices, considering both statistical and systematic errors related to the SNe for each bin.

3.2 Preliminary analysis

To focus only on H_0 as a nuisance parameter in a one-dimensional analysis and constrain it in each bin, we need to fix the values of the other cosmological parameters. Thus, in each bin we assume the fiducial value $\Omega_{m0} = 0.298$ for a flat ΛCDM model, and $\Omega_{m0} = 0.308$ with $w_0 = -1.009$ and $w_a = -0.129$ for a flat w_0w_aCDM model in all the redshift ranges. These fiducial values are chosen according to the results in [176] combining the SNe and CMB analysis. Moreover, we need to fix the absolute magnitude M of SNe Ia in each bin. Bearing in mind the degeneracy between M and H_0, we calibrate M to obtain a value of $H_0 = 73.5\,\mathrm{km\ s^{-1}\,Mpc^{-1}}$ in the first redshift bins, according to a nominal value from measurements of the local probes at low redshifts.

Thus, we perform a preliminary analysis for both ΛCDM and w_0w_aCDM models to obtain the respective value of M for each binning division in the first redshift bin, which is characterized by a mean redshift $z \ll 1$. To do this, we minimize the χ^2_{SNe} in Eq. (1.61) with the *Cobaya* package available in Python [236]. Then, we use the MCMC methods to sample a posterior distribution and obtain the confidence intervals of the parameter at the 68 % level. Finally, M is obtained for each binning division (see Table 3.1). The results for M are summarized in Fig. 3.1 and Table 3.1. Note that the values of M are all compatible with each other in 1 σ. After this preliminary analysis, we fix M in all the other bins. One might expect that also H_0 assumes the same values in all the redshift bins, due to its degeneracy with M.

However, one might argue that this approach does not always guarantee that the value of Ω_{m0}, which we fix as a fiducial, remains consistent within 1 σ or 2 σ with the values obtained by applying the same analysis to the total Pantheon sample (no bins). To this end, we perform the binned analysis with three and four bins by varying Ω_{m0} and H_0 contemporaneously for a flat ΛCDM model. The results obtained for Ω_{m0} are consistent in 1 σ for three bins and in 2 σ for four bins with the values obtained when we employ the total Pantheon sample. Our derived value of $\Omega_{m0} = 0.298 \pm 0.016$ from the total Pantheon sample is consistent within 1 σ with the value obtained in [176] from the Pantheon sample itself, thus validating our approach. Then, this method guarantees us that the precompiled covariance matrix C, given by [176], can be reliably used.

We here clarify the selection criteria for the choice of the binning division: the contours for the parameters H_0 and Ω_{m0} should constrain these parameters, so that Ω_{m0} for every single bin in the groups of three and four bins must be compatible at least within 2 σ with the value of Ω_{m0} relative to the full Pantheon sample. The results are summarized in Fig. 3.2. Looking at three bins (see the left panel of Fig. 3.2), we have the most favored framework: all three bins show closed contours in these intervals: $0 < \Omega_{m0} < 1$, $60\ \mathrm{km\ s^{-1}\,Mpc^{-1}} < H_0 < 80\ \mathrm{km\ s^{-1}\,Mpc^{-1}}$. Furthermore, in this case the value of Ω_{m0} is consistent within 1 σ with the value of Ω_{m0} related to the full sample, shown in red. The four-bin scenario (see the right panel of Figure 3.2) has been introduced to mimic the bin division of [178], and the results are quite satisfactory, but not all bins are compatible within 1 σ with the reference value of the total Pantheon, rather reaching compatibility only in 2 σ, as shown in the red contours. We performed an additional analysis that has demonstrated that the division of the Pantheon sample into more than four bins leads to incompatible values of Ω_{m0} with the fiducial value of the total Pantheon sample in 2 σ. Thus, this analysis leads us to conclude that with the cosmological parameters here adopted ($\Omega_{m0} = 0.298, H_0 = 73.5\,\mathrm{km\ s^{-1}\,Mpc^{-1}}$), the optimal number of bins in which we can divide the Pantheon sample is at most four, thus strongly disfavoring the possibility of subsequent divisions in bins. Nevertheless, we show what the results of our analysis would look like in the cases of twenty and fourthy bins, here considered very extreme cases of binning.

3.3 Main analysis

Now, we can approach the main part to check the values of H_0 after a binned analysis of the Pantheon Sample for both the ΛCDM and w_0w_aCDM models, i.e. adopting the expression of the luminosity distance within these theoretical frameworks. We use again the minimization of χ^2_{SNe}, and in the MCMC we set the priors: $60\ \mathrm{km\ s^{-1}\,Mpc^{-1}} < H_0 < 80\ \mathrm{km\ s^{-1}\,Mpc^{-1}}$. Finally, we extract and obtain the value

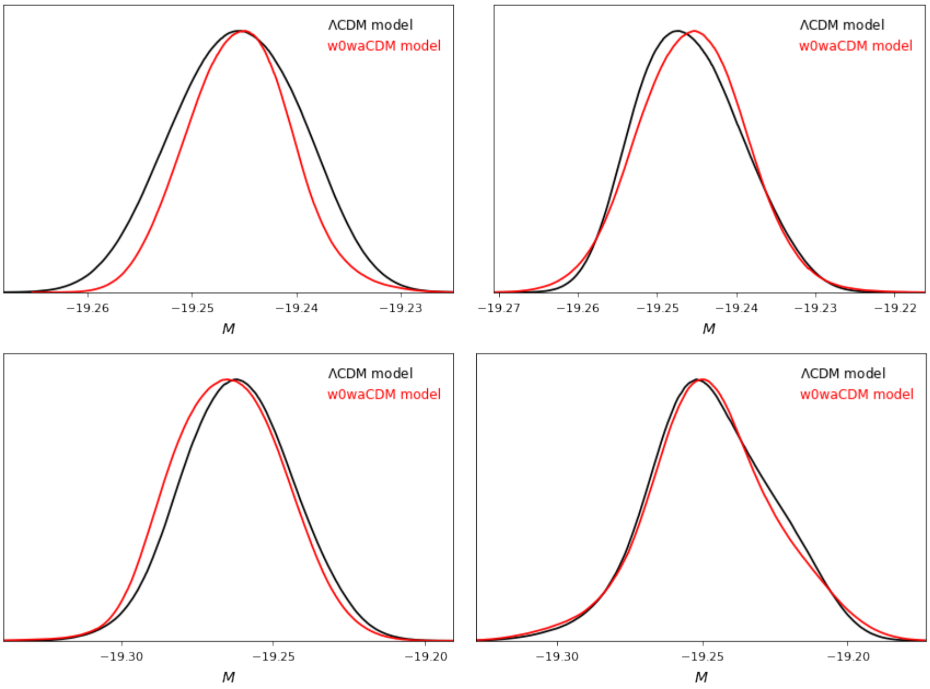

Figure 3.1: Posterior distributions for M after minimizing χ^2_{SNe} and performing the MCMC for the first bin in each binning division: bin 1 of 3 (upper left panel), bin 1 of 4 (upper right panel), bin 1 of 20 (lower left panel), and bin 1 of 40 (lower right panel). In this analysis, H_0 is set to the value of $73.5\,\mathrm{km\ s^{-1}\,Mpc^{-1}}$. This figure is extracted from [TS 3].

of H_0 in each redshift bin. To investigate an evolution of H_0 with the redshift z, we apply a non-linear fit [TS 3] written as

$$H_0^{\mathrm{fit}}\left(z\right) = \frac{\tilde{H}_0}{\left(1+z\right)^{\,\alpha}}\,, \tag{3.4}$$

with two fitting parameters, $\tilde{H}_0$ and α. Note that $\tilde{H}_0 = H_0^{\mathrm{fit}}\left(z=0\right)$. Moreover, the α coefficient indicates the evolutionary trend: if $\alpha \neq 0$, we have a redshift evolution, otherwise H_0^{fit} is simply a constant. We here remark that the choice of the functional form of $H_0^{\mathrm{fit}}\left(z\right)$ as a power law is standard for characterizing the evolution of many astrophysical sources or cosmological quantities.

In Figs. 3.3 and 3.4, we can observe a slowly and unexpected decreasing trend [TS 3] for $H_0^{\mathrm{fit}}\left(z\right)$ in the ΛCDM model and also in the w_0w_aCDM model. The fitting parameters and their respective errors in 1 σ are listed in Table 3.1. Note that, for instance, the α parameter is consistent with zero, namely no evolution, in 2.0 σ in the ΛCDM model using three bins, while for four bins α is consistent with zero only at 1.5 σ. Similarly, for the case of w_0w_aCDM model, α is consistent with zero only at the level of 1.9 σ for three bins and only in 1.2 σ for four bins, thus showing an evolution of $H_0^{\mathrm{fit}}\left(z\right)$ with redshift.

Note that the α parameters are steeper in the case of twenty and fourty bins, because we have a smaller number of SNe inside each bin. Hence, deviations of data from the fitting function $H_0^{\mathrm{fit}}\left(z\right)$ become more evident. On the contrary, if we consider bins with hundreds of SNe, these small deviations are averaged, thus resulting in a flatter trend. Nevertheless, the α coefficients in the four cases are mutually compatible in 1 σ, thus highlighting a persistent decreasing trend in the data. These results seem to suggest that the Hubble constant may evolve with z, hence changing its value according to the cosmic distance of the sample.

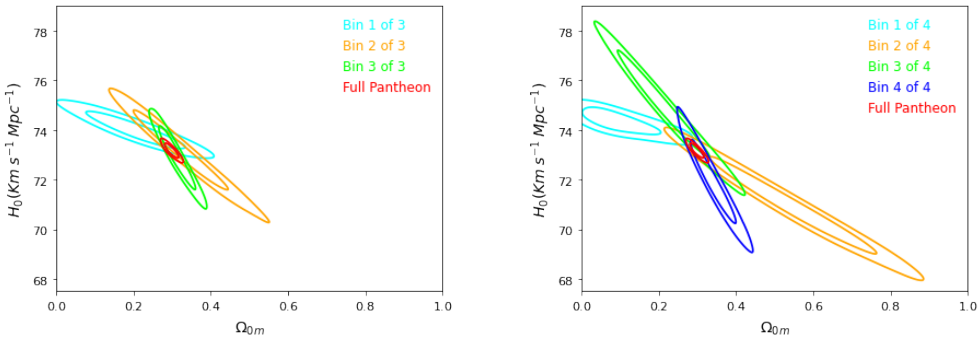

Figure 3.2: Contours for the cosmological parameters Ω_{m0} and H_0 within the framework of a flat ΛCDM model. Left panel: The contours are shown considering three bins, where the color code is used for contours related to the first (light blue), second (orange), and third (green) redshift bin. Right panel: The same analysis is performed using four bins, adopting the same color code with the addition of the fourth bin in dark blue. In both of these figures, shown with the same axis scale for better comparison, the red contour denotes the analysis computed considering the total Pantheon sample. To plot the contours, we assume the local values of M as presented in Table 3.1 (upper part) considering three and four bins within the ΛCDM framework. This figure is extracted from [TS 3].

Flat ΛCDM model, fixed $\Omega_{m0} = 0.298$						
Bins	$\tilde{H}_0$ (km s^{-1} Mpc^{-1})	α	$\frac{\alpha}{\sigma_\alpha}$	M	$H_0^{\rm fit}$ ($z = 11.09$) (km s^{-1} Mpc^{-1})	$H_0^{\rm fit}$ ($z = 1100$) (km s^{-1} Mpc^{-1})
3	73.577 ± 0.106	0.009 ± 0.004	2.0	-19.245 ± 0.006	72.000 ± 0.805	69.219 ± 2.159
4	73.493 ± 0.144	0.008 ± 0.006	1.5	-19.246 ± 0.008	71.962 ± 1.049	69.271 ± 2.815
20	73.222 ± 0.262	0.014 ± 0.010	1.3	-19.262 ± 0.014	70.712 ± 1.851	66.386 ± 4.843
40	73.669 ± 0.223	0.016 ± 0.009	1.8	-19.250 ± 0.021	70.778 ± 1.609	65.830 ± 4.170

Flat w_0w_aCDM Model, fixed $\Omega_{m0} = 0.308$, $w_0 = -1.009$, and $w_a = -0.129$						
Bins	$\tilde{H}_0$ (km s^{-1} Mpc^{-1})	α	$\frac{\alpha}{\sigma_\alpha}$	M	$H_0^{\rm fit}$ ($z = 11.09$) (km s^{-1} Mpc^{-1})	$H_0^{\rm fit}$ ($z = 1100$) (km s^{-1} Mpc^{-1})
3	73.576 ± 0.105	0.008 ± 0.004	1.9	-19.244 ± 0.005	72.104 ± 0.766	69.516 ± 2.060
4	73.513 ± 0.142	0.008 ± 0.006	1.2	-19.246 ± 0.004	71.975 ± 1.020	69.272 ± 2.737
20	73.192 ± 0.265	0.013 ± 0.011	1.9	-19.262 ± 0.018	70.852 ± 1.937	66.804 ± 5.093
40	73.678 ± 0.223	0.015 ± 0.009	1.7	-19.250 ± 0.022	70.887 ± 1.595	66.103 ± 4.148

Table 3.1: Fitting parameters ($\tilde{H}_0$ and α) of $H_0^{\rm fit}(z)$ (Eq. (3.4) and extrapolated values at high redshifts, after a binned analysis of the Pantheon sample, focusing on a flat ΛCDM model (upper part) and a flat w_0w_aCDM model (lower part). The first column indicates the number of bins, the second and the third columns denote the fitting parameters, $\tilde{H}_0$ and α, contained in the $H_0^{\rm fit}(z)$ function, according to Eq. (3.4). The compatibility of α with zero (no evolution) is expressed in terms of 1 σ in the fourth column. The new absolute magnitude M, which provides $H_0 = 73.5\,\text{km s}^{-1}\,\text{Mpc}^{-1}$ in the first bins, is listed in the fifth column. In the last two columns, we show the extrapolated values of $H_0^{\rm fit}(z)$ and the corresponding errors at the redshift of the most distant galaxies, $z = 11.09$, and the last scattering surface, $z = 1100$. All the uncertainties are given in 1σ.

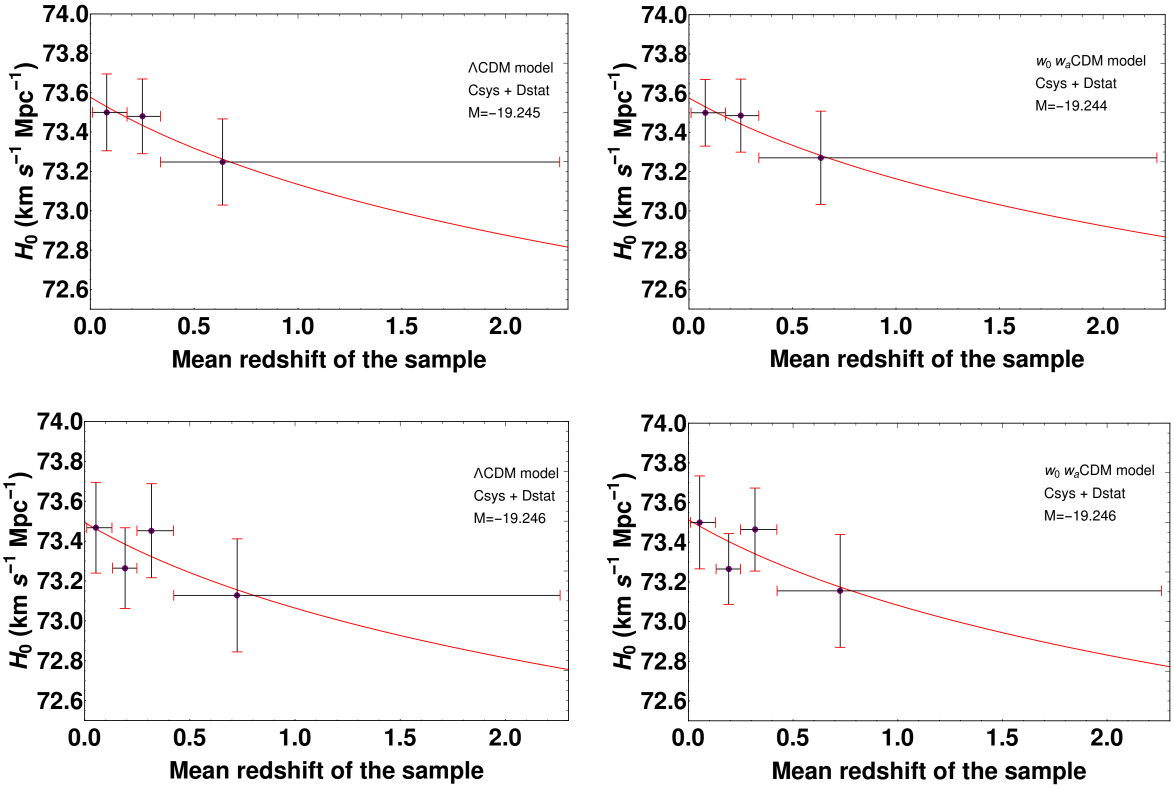

Figure 3.3: Evolution of $H_0(z)$ with redshift according to Eq. (3.4) as a result of a binned analysis of the Pantheon sample in three and four redshift bins for a flat ΛCDM model (left panels) with fixed density parameter $\Omega_{m0} = 0.298$, and a flat $w_0 w_a$CDM model (right panels) with fixed parameters $w_0 = -1.009$, $w_a = -0.129$, and $\Omega_{m0} = 0.308$. These panels are extracted from [TS 3].

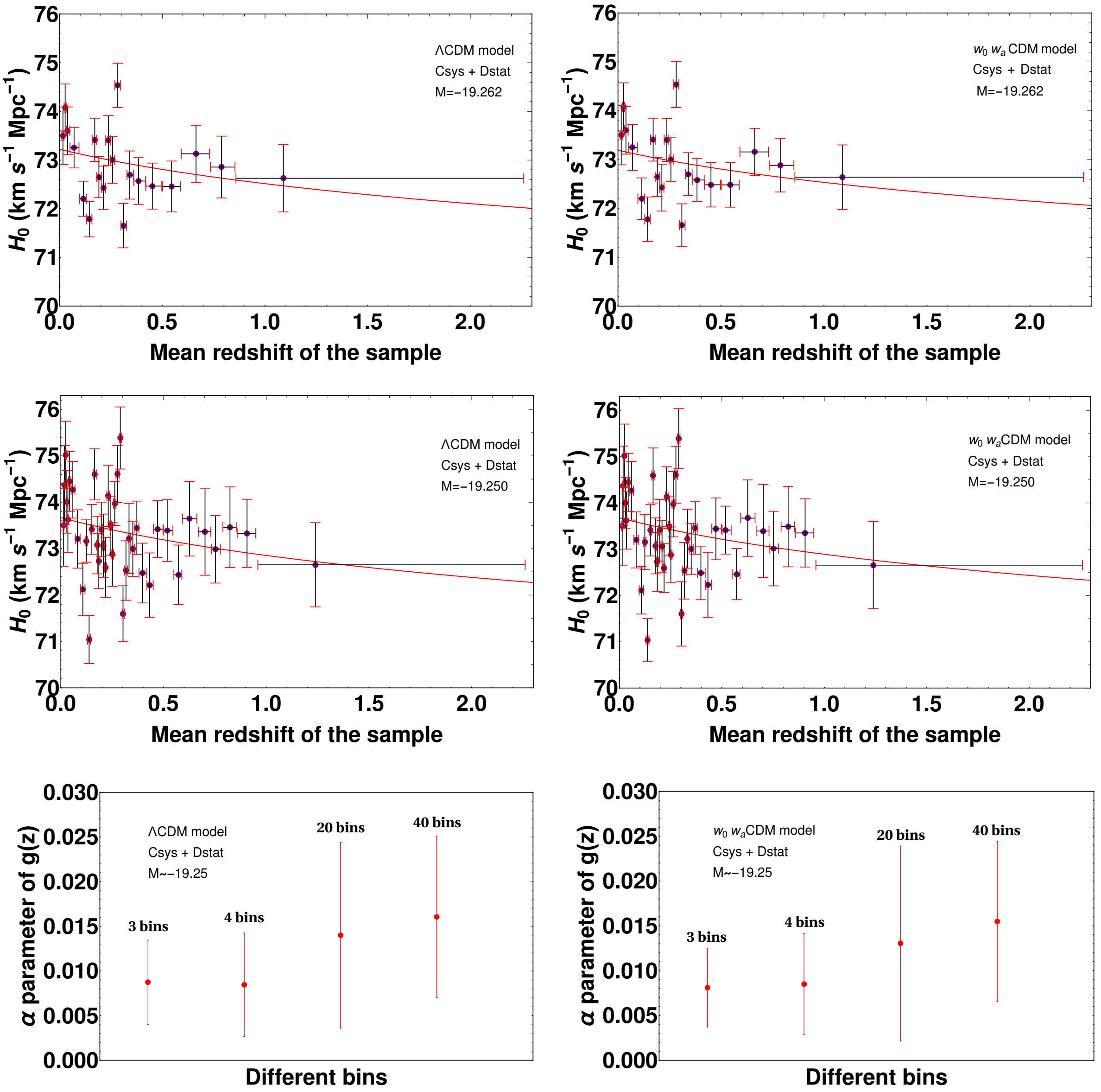

Figure 3.4: The left panels show an evolving trend of $H_0^{\rm fit}(z)$, by starting from $H_0 = 73.5\,\mathrm{km\ s^{-1}\,Mpc^{-1}}$ and with the corresponding associated fiducial value for M, indicated inside each plot, for the ΛCDM model. The upper and the middle left panels show twenty and fourthy bins, respectively, similarly to Fig. 3.3. The lower left panel shows the α parameter as a function of the different bins (3, 4, 20, 40), as a results of the fitting procedure summarized in Table 3.1. The right panels show the same pattern referred the $w_0 w_a$CDM model. This figure is reported from [TS 3].

3.4 Final results

It should be emphasized that we have investigated this evolutionary trend of $H_0^{\mathrm{fit}}(z)$ also within the framework of the $w_0 w_a$CDM model to verify the hypothesis of whether this trend disappears when considering a modified equation-of-state parameter for the dark energy. Our results point out that $H_0^{\mathrm{fit}}(z)$ exhibits a redshift evolution also in the $w_0 w_a$CDM model, thus $w_{\mathrm{DE}}\,(z)$ for the dark energy is not enough to explain the observed trend. In other words, we should have had a flat profile of $H_0^{\mathrm{fit}}(z)$, after a binned analysis of the Pantheon sample, using the luminosity distance and the Hubble function (1.97) within the framework of the $w_0 w_a$CDM model, to claim that the evolution of $H_0^{\mathrm{fit}}(z)$ observed in the ΛCDM model could be explained by a dark energy parameter $w_{\mathrm{DE}}\,(z)$, but this is not the case. Hence, the observed evolution of $H_0^{\mathrm{fit}}(z)$ is not due to the $w_{\mathrm{DE}}(z)$.

A possible evolutionary trend of the Hubble constant implies interesting consequences. If the observed trend of $H_0^{\mathrm{fit}}(z)$ is intrinsic and does not depend on a specific sample, one may ask what happens with other local probes or in the early Universe at very high redshifts. Hence, we extrapolate the fitting function of $H_0^{\mathrm{fit}}(z)$ to the redshift of the most distant galaxies, $z = 11.09$ [237], assuming that this trend could be observed in principle also in other high-redshift probes. Furthermore, we extrapolate $H_0^{\mathrm{fit}}(z)$ also to the redshift of the last scattering surface, $z = 1100$, to compare the latter values of $H_0^{\mathrm{fit}}(z)$ with the one inferred from Planck measurements for the CMB. We find that the extrapolated values to $z = 1100$ in Table 3.1 are consistent within 1 σ with the value of H_0^{CMB}, obtained from the Planck measurements for both the ΛCDM and $w_0 w_a$CDM models regardless the number of bins. We here stress that the error bars on the extrapolated values are large essentially because we propagate the errors on both $\tilde{H}_0$ and α.

It should be emphasized that the decreasing trend $H_0^{\mathrm{fit}}(z)$ not only reduces the tension but provides a new way to approach the problem. Indeed, there could be no more a tension between independent measurements of H_0, but an intrinsic evolution of $H_0^{\mathrm{fit}}(z)$ may match the observations obtained from different probes located at different redshifts.

Besides, we would need to account for this new definition of $H_0^{\mathrm{fit}}(z)$ in the luminosity distance for an effective flat ΛCDM picture in the following way:

$$d_L(z) = \frac{1+z}{\tilde{H}_0} \int_0^z \frac{(1+z')^{\,\alpha}\, dz'}{\sqrt{\Omega_{m0}\,(1+z')^3 + \Omega_{\Lambda 0}}}. \tag{3.5}$$

In Fig. 3.5 we show how the corrected luminosity distance (blue line for three bins, green line for four bins), which takes into account the dependence of $H_0^{\mathrm{fit}}(z)$, deviates from the standard luminosity distance (red line) defined in Eq. (1.55) in the flat ΛCDM model. It is visible that at high z ($z = 11.09$), there is an overestimation of 2.2% and 2% of the corrected luminosity distance computed in the ΛCDM model from Eq. (3.5) compared to the standard luminosity distance in Eq. (1.55) for three and four bins, respectively.

We conclude this chapter by postponing the theoretical discussions of our results, which will be properly addressed in Chapter 5. Before doing that, we show an extension of the current analysis in the next chapter.

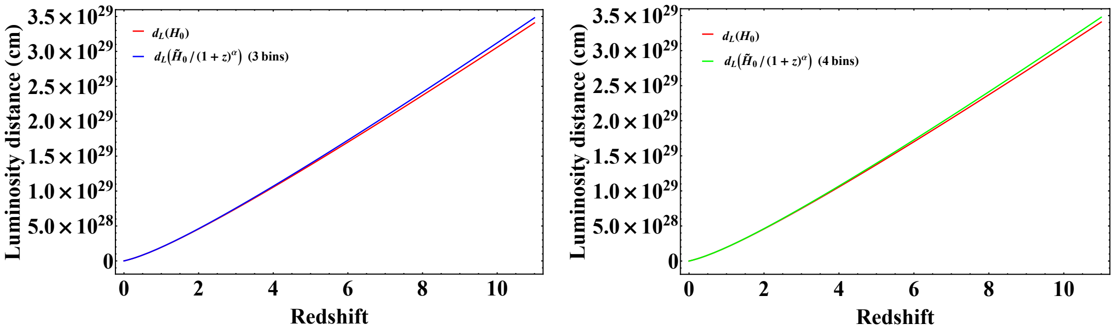

Figure 3.5: Luminosity distance in linear scale (cm) for the flat model Equation (3.5) vs. the luminosity distance corrected by using Eq. (3.4) for both three (left panel) and four bins (right panel). This figure is extracted from [TS 3].

Chapter 4

Redshift binned analysis using standard candles and rulers

The analysis in the previous chapter has shown a slow evolution of the Hubble constant throughout the redshift range of the SNe Ia Pantheon sample. Once we have established if the Hubble constant undergoes redshift evolution, the Pantheon sample can safely be combined with other probes. In this chapter, we investigate if this evolution still holds by using other local probes. In addition to standard candles, namely the SNe Ia gathered in the Pantheon sample, we also consider standard rulers, i.e. BAOs (see Sect. 1.1.5). Here, we start with the local value of $H_0 = 70.0$ km s^{-1} Mpc^{-1} and divide the Pantheon sample into three bins ordered in increasing values of redshift. We extend our previous analysis performed in Chapter 3, by varying not only one single cosmological parameter but two contemporaneously (H_0, Ω_{m0} in the ΛCDM model and H_0, w_a in the $w_0 w_a$CDM model). Then, we implement a MCMC analysis obtaining the value of H_0 for each bin. In order to discuss the possibility that an effective redshift evolution of the Hubble constant could be due to a modified gravity scenario, we perform a similar binning analysis within the $f\left(R\right)$ HS model, which was introduced in Sect. 1.3.2. Our approach has a two-fold advantage: on the one hand, it is relatively simple, and on the other hand, it may be able to highlight a residual dependence on the SNe Ia parameters with redshift. We here point out that this analysis is focused to study the reliability of the trend of an effective Hubble constant as a function of the redshift. Finally, we will conclude this chapter by discussing some reasons to explain our results, but a more fulfilling theoretical interpretation will be provided in Chapter 5. The analysis performed in this chapter is presented in [TS 2, 6, 8].

4.1 Binning approach within General Relativity

4.1.1 Methodology

We follow a redshift binning approach similar to the one adopted in Chapter 3 to investigate the Hubble constant tension through low-redshift probes, specifically the SNe Ia and BAOs data. We combine Eqs. (3.2) and (1.67) to obtain the total χ^2

$$\chi^2 = \frac{1}{2}\chi^2_{\mathrm{SNe}} + \frac{1}{2}\chi^2_{\mathrm{BAO}}. \tag{4.1}$$

In this chapter, we combine each SNe bin with only one BAO data point, which has a redshift value within the SNe bin: this approach of using one BAO comes from [238]. More specifically, we consider a subset of the BAO dataset available in [186]. Through Eq. (4.1), we investigate if a redshift evolution of $H_0^{\rm fit}\,(z)$ is present, firstly from the binning of SNe Ia+BAOs with simple dark energy models, namely the ΛCDM and w_0w_aCDM models (see Sects. 1.1 and 1.2).

In our binned analysis, we focus on the optimal values of H_0 to minimize the χ^2 in Eq. (4.1). We recall that the Hubble constant is contained in the expression of the luminosity distance in Eq. (1.55) and H_0 is regarded as a nuisance parameter, which is free to vary, to better analyze a possible redshift evolution. Here, we adopt a starting value for $H_0 = 70.0$ km s^{-1} Mpc^{-1}, which is different from the one adopted in the in Chapter 3, that was $H_0 = 73.5$ km s^{-1} Mpc^{-1}. If a trend with redshift exists, it should be independent on the initial value of H_0. Then, we follow the assumptions on the fiducial value of $M = -19.35$ and we consider the conventional value of the Pantheon sample release. The systematic contributions for the Pantheon sample are calibrated through a reference ΛCDM cosmological model, where H_0 is 70.0 km s^{-1} Mpc^{-1}.

Concerning the number of bins in our analysis, we decide to divide our sample in three redshift bins. This choice is is justified by the high number of SNe Ia (around hundreds of SNe per bin) that can still constitute statistically illustrative subsamples of the Pantheon sample and that can properly consider the contribution of systematic uncertainties. Indeed, a feasibility study done in Chapter 3 performed with different bins selections has highlighted how the maximum number of bins in which the Pantheon sample should be divided is three (see Fig 3.2), otherwise the statistical fluctuations would dominate on a multi-dimensional analysis, leading to relatively large uncertainties which would mask any evolving trend, if present.

Furthermore, for the same reason, it is not advisable to leave free to vary more than two parameters at the same time, thus in the current chapter, we will analyze the behavior of H_0 in three bins, when it is varied together with a second cosmological parameter. This fact makes necessary the choice of more tight priors since we are basing the current analysis on the prior knowledge, avoiding the degeneracies among the parameter space, and letting the priors have more weight in the process of posteriors estimation. We let the parameters H_0 and Ω_{m0} vary simultaneously for the ΛCDM model, while in the w_0w_aCDM model the varying parameters are H_0 and w_a. We decid to leave w_a free to vary since, according to the CPL parametrization in Eq. (1.96), w_a gives direct information about the evolution of the $w(z)$ while w_0 is considered a constant in the same model.

Concerning the fiducial values for the ΛCDM model and the priors assignment for the MCMC computations, we apply Gaussian priors with mean equal to the central values of $\Omega_{m0} = 0.298 \pm 0.022$ and $H_0 = 70.393 \pm 1.079$ from [176], and with $1\ \sigma = 2 \times 0.022$ and $1\ \sigma = 2 \times 1.079$ for Ω_{m0} and H_0, respectively. In summary, to draw the Gaussian priors, we consider the mean value of the parameters as the expected one of the Gaussian distribution and we double the σ value which is then considered the new standard deviation for the distribution. Concerning the w_0w_aCDM model, we fix $w_0 = -0.905$ and we consider the priors on w_a with the mean $= -0.129$ taken from Table 13 of [176], while $1\ \sigma =$ is the 20% of its central value. Such an assumption with small priors is needed since we are avoiding phantom dark energy models with $w\,(z) < -1$.

4.1.2 Analysis

After the minimization of χ^2 in Eq. (4.1), we extract the H_0 value and its uncertainty in each redshift bin, via the *Cobaya* code [236]. To this end, we execute an MCMC using the D'Agostini method to obtain the confidence intervals for H_0 at the 68% and 95% levels, in three redshift bins.

Once H_0 is obtained for each bin, we perform a fit of H_0 using the same fitting function in Eq. (3.4), adopted in the previous analysis in Chapter 3. Our Results are presented in the panels of Table 4.1. We here stress that the fiducial absolute magnitude value is assumed to be $M = -19.35$ for each SNe bin, thus it will not be mentioned in the same Table. All the uncertainties in the tables are in 1 σ. As reported in the upper half of Table 4.1, namely with the ΛCDM model, if we do not include the BAOs then the α coefficient is compatible with 0 (no evolution) in 2.0 σ for the three bins case. When we introduce the BAOs within the ΛCDM model, we observe again a reduction of the α/σ_α ratio for three bins down to 1.2. Concerning the lower half of Table 4.1 with the w_0w_aCDM model, when BAOs are not included we have α non compatible with 0 in 5.7 σ and, including the BAOs, the compatibility with 0 is given in 5.8 σ. The increasing of the ratio α/σ_α is observed when BAOs are added in the case of w_0w_aCDM model in three bins. The results can be visualized in Fig. 4.1. Comparing the α/σ_α ratios reported in Table (3.1) with Table 4.1, we have that for the ΛCDM model the current α values are compatible in 1 σ with the αs reported in Table (3.1), while the α estimated in the w_0w_aCDM model are compatible in 3 σ with the α values in the same reference paper.

Table 4.1: Upper half: fitting parameters of $H_0^{\rm fit}(z)$ for three bins (flat ΛCDM model, varying H_0 and Ω_{m0}) in the cases with SNe only and with the SNe + BAOs contribution. In the columns the fitting parameters $\tilde{H}_0$ and α are reported, and the last column denotes how many σs the evolutionary parameter α is compatible with zero (namely, α/σ_α). Lower half: similarly, fit parameters of $H_0^{\rm fit}(z)$ (flat w_0w_aCDM model, varying H_0 and w_a) without and with the BAOs.

Flat ΛCDM model, varying H_0 and Ω_{m0}			
Probes	$\tilde{H}_0$ (km s^{-1} Mpc^{-1})	α	$\frac{\alpha}{\sigma_\alpha}$
SNe	70.093 ± 0.102	0.009 ± 0.004	2.0
SNe+BAOs	70.084 ± 0.148	0.008 ± 0.006	1.2

Flat w_0w_aCDM model, varying H_0 and w_a			
Probes	$\tilde{H}_0$ (km s^{-1} Mpc^{-1})	α	$\frac{\alpha}{\sigma_\alpha}$
SNe	69.847 ± 0.119	0.034 ± 0.006	5.7
SNe+BAOs	69.821 ± 0.126	0.033 ± 0.005	5.8

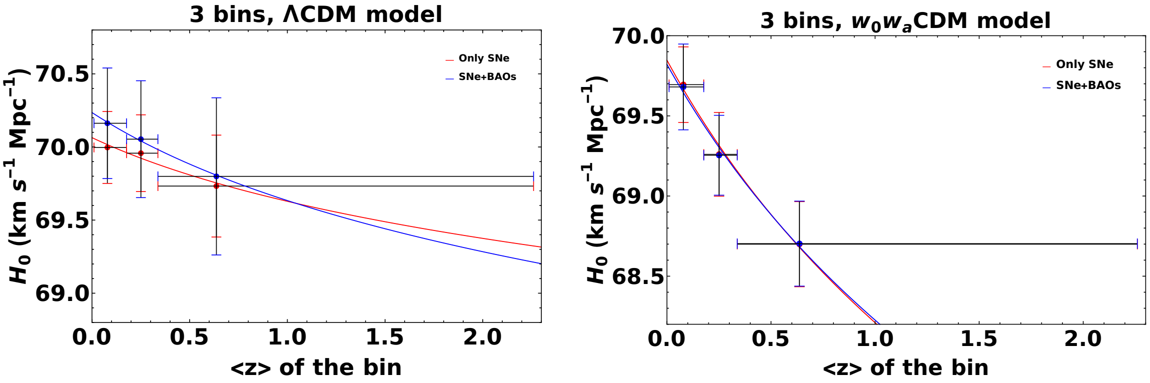

Figure 4.1: Left panel: the $H_0(z)$ vs. z by varying also Ω_{m0}. The red color indicates the case with only SNe Ia as probes, while the blue refers to the case of SNe + 1 BAO per bin. This color-coded will be applied also in the right panel. Right panel: the same plot for the w_0w_aCDM model, considering the local fiducial value $H_0 = 70.0\,\mathrm{km\ s^{-1}\,Mpc^{-1}}$, where both H_0 and w_a are left free to vary. These panels are extracted from [TS 2].

4.2 Binning approach within the $f(R)$ Hu-Sawicki model

In order to investigate possible theoretical explanations for a decreasing trend of $H_0^{\mathrm{fit}}(z)$, we now focus on modified gravity models, testing the $f(R)$ HS model.

4.2.1 Methodology

We repeat a similar binning approach as in the previous section, but here we adopt the luminosity distance given in Eq. (1.131) in the $f(R)$ gravity, specifically the HS model (see Sects. 1.3.2 and 1.3.3). We recall that $d_L(z)$ can be computed in this formalism only after solving the set of coupled ordinary differential equations (1.127), (1.128), where y_H denote the deviation of H^2 with respect to the matter contribution in the ΛCDM model.

We have introduced the HS model in Sect. 1.3.2, but we rewrite here the functional form of its $f(R)$ for convenience:

$$f(R) = R + F(R) = R - m^2 \frac{c_1 \left(R/m^2\right)^n}{c_2 \left(R/m^2\right)^n + 1}, \tag{4.2}$$

In particular, in this section we focus on the HS model with $n = 1$ in a flat geometry for simplicity, and because this is the most studied case. We also recall that the parameters c_1 and c_2 are fixed by the following conditions (see Eqs. (1.119) and (1.122)):

$$\frac{c_1}{c_2} \approx 6\frac{\Omega_{\Lambda 0}}{\Omega_{m0}} \tag{4.3}$$

$$F_{R0} \approx -\frac{c_1}{c_2^2}\left(\frac{12}{\Omega_{m0}} - 9\right)^{-2}, \tag{4.4}$$

where F_{R0} is the value of the field $F_R \equiv dF/dR$ at the present time, and $F(R)$ is the deviation from the Einstein–Hilbert Lagrangian density. Cosmological constraints provide $|F_{R0}| \leq 10^{-7}$ from gravitational lensing and $|F_{R0}| \leq 10^{-3}$ from Solar system [107, 216, 225]. We explore several choices of F_{R0}.

To simplify the numerical integration of the modified luminosity distance (1.131), we approximate the numerical solution y_H, obtained from the system (1.127), (1.128), by a polynomial of order 8. This function is an accurate representation of y_H when we restrict the solution to the range of Pantheon sample (see Fig. 4.2). As a consequence, we obtain constraints on c_1 and c_2, according to Equations (4.3) and (4.4).

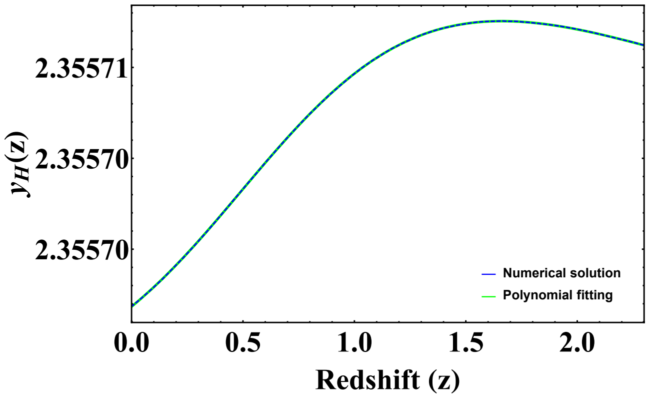

Figure 4.2: The numerical solution for Eqs. (1.127) and (1.128) (blue dashed curve) plotted together with its polynomial fitting (green continuous curve) in the case of $F_{R0} = -10^{-7}$. The assumption of a function of redshift in the form of a order-8 polynomial allows an accurate fit for the numerical values. The same fitting procedure has been used in the $F_{R0} = -10^{-4}$ case. This figure is included in [TS 2].

4.2.2 Analysis

We here run the analysis in three redshift bins both for the case of Ω_{m0} fixed to a fiducial value of 0.298 and for several values of $F_{R0} = -10^{-7}, -10^{-6}, -10^{-5}, -10^{-4}$ (see Table 4.2 and Fig. 4.3) or we let Ω_{m0} vary with the two values of $F_{R0} = -10^{-7}, -10^{-4}$ (see Table 4.4 and Fig. 4.4) for the SNe alone and with SNe + BAOs.

Note also that the α parameters are all consistent for the several values of F_{R0} in 1 σ, as you can see in Table 4.2, for both SNe Ia and SNe Ia + BAOs. Moreover, the values of α are consistent in 1 σ with the ones obtained from the analysis of the ΛCDM model (see also Table 4.1). We consider the cases $F_{R0} = -10^{-7}$, $F_{R0} = -10^{-4}$ and, to study how these results may vary according to the different values of Ω_{m0} chosen, we tested the model with four values of $\Omega_{m0} = (0.301, 0.303, 0.305)$ taken from the 1 σ from a Gaussian distribution centred around the most probable value of 0.298 (see [176]).

We show in Fig. 4.4 the comparison between the different applications of the Hu–Sawicki model: in the left panels (upper and lower), we consider SNe Ia only, while in the right panels (upper and lower) we combine SNe Ia + BAOs.

Table 4.2: Fitting parameters of $H_0^{\rm fit}(z)$ for three bins within the Hu–Sawicki model, with SNe only and SNe + BAOs with a fixed value of $\Omega_{m0} = 0.298$ and with several values of F_{R0} : $-10^{-4}, -10^{-5}, -10^{-6}, -10^{-7}$. The columns contains: (1) the sample used, (2) F_{R0} values, (3) $\tilde{H}_0$, (4) α, according to Eq. (3.4); (5) how many σs α is compatible with zero (namely, the ratio α/σ_α). .

$f(R)$ Hu-Sawicki model, results of the redshift binned analysis				
Sample	F_{R0}	$\tilde{H}_0$ (km s^{-1} Mpc^{-1})	α	$\frac{\alpha}{\sigma_\alpha}$
SNe	-10^{-4}	70.089 ± 0.144	0.008 ± 0.006	1.2
SNe+BAOs	-10^{-4}	70.127 ± 0.128	0.008 ± 0.006	1.4
SNe	-10^{-5}	70.045 ± 0.052	0.007 ± 0.002	3.0
SNe+BAOs	-10^{-5}	70.062 ± 0.132	0.007 ± 0.005	1.3
SNe	-10^{-6}	70.125 ± 0.046	0.010 ± 0.002	5.4
SNe+BAOs	-10^{-6}	70.115 ± 0.153	0.008 ± 0.007	12.1
SNe	-10^{-7}	70.118 ± 0.131	0.011 ± 0.006	1.9
SNe+BAOs	-10^{-7}	70.053 ± 0.150	0.007 ± 0.007	1.1

Thus, the existence of this trend is, once again, confirmed, and it remains unexplained also in the modified gravity scenario. Indeed, a suitable modified gravity model which would be able to predict the observed trend of H_0, would allow observing a flat profile of $H_0^{\rm fit}(z)$ after a binned analysis.

Table 4.4: Fitting parameters of $H_0^{\rm fit}(z)$ for three bins within the Hu–Sawicki model, with SNe and SNe + BAOs by fixing several values of $\Omega_{m0} = 0.298, 0.303, 0.301, 0.305$ and values of $F_{R0} = -10^{-4}$ and $F_{R0} = -10^{-7}$. The columns are as follows: (1) the sample used; (2) the Ω_{m0} value; (3) F_{R0}; the fitting paramenters (4) $\tilde{H}_0$, (5) α, according to Eq. (3.4); (6) how many σs the evolutionary parameter α is compatible with zero (namely, α/σ_α).

$f(R)$ Hu-Sawicki model, results of the redshift binned analysis					
Sample	Ω_{m0}	F_{R0}	$\tilde{H}_0$ $\left(\text{km s}^{-1}\,\text{Mpc}^{-1}\right)$	α	$\frac{\alpha}{\sigma_\alpha}$
SNe	0.298	-10^{-7}	70.140 ± 0.045	0.011 ± 0.002	5.1
SNe+BAOs	0.298	-10^{-7}	70.050 ± 0.126	0.007 ± 0.006	1.2
SNe	0.303	-10^{-7}	70.088 ± 0.075	0.012 ± 0.004	3.0
SNe+BAOs	0.303	-10^{-7}	70.004 ± 0.139	0.009 ± 0.007	1.3
SNe	0.301	-10^{-7}	70.054 ± 0.056	0.009 ± 0.003	3.0
SNe+BAOs	0.301	-10^{-7}	70.072 ± 0.170	0.010 ± 0.008	1.2
SNe	0.305	-10^{-7}	70.048 ± 0.034	0.012 ± 0.002	6.0
SNe+BAOs	0.305	-10^{-7}	70.004 ± 0.140	0.010 ± 0.007	1.4
SNe	0.298	-10^{-4}	70.135 ± 0.080	0.009 ± 0.004	2.2
SNe+BAOs	0.298	-10^{-4}	70.087 ± 0.155	0.009 ± 0.007	1.2
SNe	0.303	-10^{-4}	70.096 ± 0.146	0.012 ± 0.007	1.7
SNe+BAOs	0.303	-10^{-4}	70.044 ± 0.129	0.009 ± 0.006	1.5
SNe	0.301	-10^{-4}	70.111 ± 0.158	0.012 ± 0.008	1.5
SNe+BAOs	0.301	-10^{-4}	70.038 ± 0.170	0.009 ± 0.008	1.1
SNe	0.305	-10^{-4}	70.074 ± 0.026	0.016 ± 0.001	16.0
SNe+BAOs	0.305	-10^{-4}	70.028 ± 0.090	0.011 ± 0.004	2.4

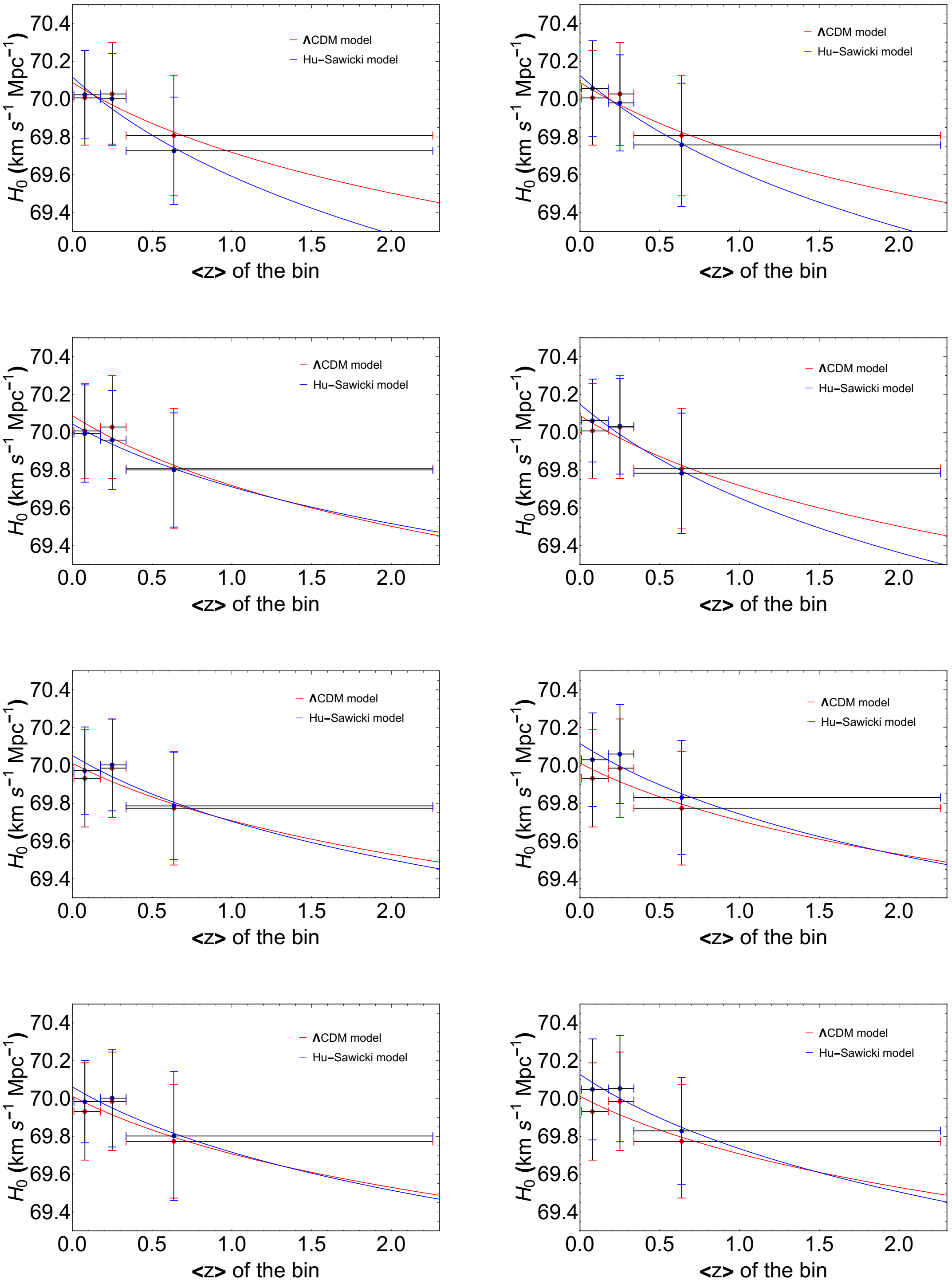

Figure 4.3: The first four panels deal with H_0 vs. z for SNe, the four bottom panels include BAO measurements for the HS model. The upper 4 panels show from the left to the right $F_{R0} = -10^{-7}, -10^{-6}, -10^{-5}, -10^{-4}$, respectively. The standard ΛCDM cosmology is shown in red and the HS model in blue. Analogously, the bottom panels have the same notation about the values of F_{R0}. These panels are extracted from [TS 2].

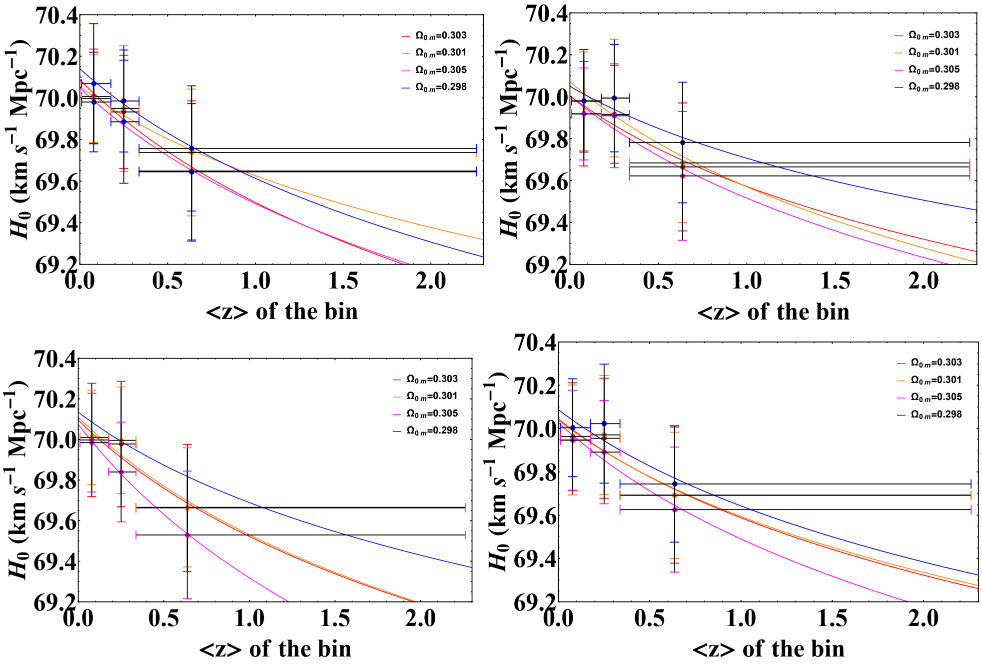

Figure 4.4: The Hubble constant versus redshift plots for the three bins of SNe Ia only, considering the Hu–Sawicki model. **Upper left panel.** The condition of $F_{R0} = -10^{-7}$ is applied to the case of SNe only, with the different values of $\Omega_{m0} = 0.301, 0.303, 0.305$. **Upper right panel.** The same of the upper left, but with the contribution of BAOs. **Lower left panel.** The SNe only case with the $F_{R0} = -10^{-4}$ condition, considering the different values of $\Omega_{m0} = 0.301, 0.303, 0.305$. **Lower right panel.** The same as the lower left, but with the contribution of BAOs. These figures are plotted in [TS 2].

4.3 Discussion of the results

In the following subsections, we discuss the role of selection biases in the Pantheon sample and possible theoretical interpretations related to our results.

4.3.1 Possible astrophysical reasons

We here consider several effects that can play a role to have a running Hubble constant with the redshift. One of them is the presence of metallicity in SNe Ia. The average stellar ages and metallicities evolve with redshift, so it may happen that the average corrected SN Ia brightness at higher redshift will be fainter than the one at lower redshift, if the observed bias is caused by the progenitor age or metallicity [239]. This bias could affect in a non-negligible way the estimation of cosmological parameters. Many authors have suggested different methods to encompass this problem. The authors of [240] have suggested using host-galaxy mass as a third SN Ia brightness-correction parameter (after stretch and color), and this is done in [176]: many of the associated systematic uncertainties of these effects are on the 1% level. This tactic might improve any effects of luminosity caused by the SNe progenitor, while the possible intrinsic color discrepancy between SNe Ia in hosts of different metallicities may explain the observed bias of corrected SN Ia luminosity with host mass (and metallicity). Even if a strong correction for color–luminosity factor is applied ($\beta \sim 3$), a considerable Hubble residual step, ΔM, is still observed (see Eq. (1.59)) between high- and low-metallicity hosted SNe. This could mean that other effects are contributing to biases [239].

According to the stretch and the color evolution in [239], it was concluded that the stretch-corrected and color-corrected SN Ia Hubble residuals of SNe Ia in high-mass and low-mass host galaxies differ by 0.077 ± 0.014 mag, a result compatible with the one determined by [176]. The physical reason for that behavior may be linked to the interstellar dust, age, and metallicity of SNe: while the first cannot contribute alone to the observed bias, the last two can produce the Hubble residual trends compatible with the ones observed in [239]. The most important concept that must be considered regarding the evolution of color and stretch factor concerns the changes of SNe Ia in the Pantheon sample. In [176], to account for the stretch and color parameter evolution, both α and β are parameterized as a function of redshift in the following ways: $\alpha(z) = \alpha_0 + \alpha_1 \times z$ and $\beta(z) = \beta_0 + \beta_1 \times z$. This parameterization is not included in the μ_{obs} from Eq. (1.59) because there is no explicit evolutionary trend for $\alpha(z)$ and $\beta(z)$, so $\alpha_1 = 0$ and $\beta_1 = 0$. The only exception is that $\beta(z)$ shows different trends for high and low-z SNe subsamples, and this is due to selection effects on SNe. Hence, in [176], this uncertainty was included in the value of β_1 as an additional statistical uncertainty.

Regarding the properties of the host galaxies and the selection effects associated with these, several tests include probing the relations between luminosity and the properties of the host galaxies of the SNe [240–242] and analysis of the light-curve fit parameters of SNe and how these parameters relate to luminosity [243]. Thus, in our analysis following the treatment in [176], we can state that the color evolution is included, while the stretch evolution is not included because it turns out to be negligible. In previous studies [244], the effect of considering or neglecting the evolution of SN parameters has been investigated, showing that the impact on cosmological parameters and models is not negligible. Recent studies on the SALT2.4 light-curve stretch in [245] show that the basic SN stretch distribution evolves with redshift.

Differently from [176], another functional form for the stretch population was suggested in [245]:

$$x_1(z) = \delta(z)\mathcal{N}(\mu_1, \sigma_1^2) + (1 - \delta(z))[a\mathcal{N}(\mu_1, \sigma_1^2) + (1 - a)\mathcal{N}(\mu_2, \sigma_2^2)] \tag{4.5}$$

where $a = 0.51$, $\mu_1 = 0.37$, $\mu_2 = -1.22$, $\sigma_1 = 0.61$, $\sigma_2 = 0.56$ and $\delta(z) = (K^{-1}(1 + z)^{-2.8} + 1)^{-1}$ with $K = 0.87$. Nevertheless, the authors of [245] state that for cosmological purposes a great number of d.o.f. for a given model can still be accepted in a sample that contains a large number of SNe Ia, like the Pantheon, but this choice does not allow us to successfully extract the SNe property distribution from a Malmquist-biased sample [246]. The Malmquist bias effect is indeed an astrophysical effect that deals with all sources that are at a cosmological redshift. According to this effect, we cannot detect faint sources at high redshift, so there is a larger population of brighter sources at lower redshift. We point out that this effect could enter our results especially when we consider the highest redshift bin because the distances derived from SN are affected by selection effects, and at higher redshift, this selection weighs more. The simulations performed by [176] for investigating the redshift evolution are limited up to $z = 0.7$. This redshift corresponds to the 18th bin out of 20 and the 36th bin out of 40, respectively. Thus, the remaining effect from $0.7 \leq z \leq 2.26$ still needs to be investigated.

In conclusion, many factors may cause the observed evolutionary trend for $H_0^{\text{fit}}(z)$ in our binning analysis: the drift of the stretch parameter with redshift is an excellent candidate given that the power law function of $H_0^{\text{fit}}(z)$ that we use here for the evolution is a general function that can be used for any astrophysical source. The analysis we have performed is a way indeed to switch the evolution from the stretch to H_0, although surely the function $\delta(z)$ is different from $H_0^{\text{fit}}(z)$. With the current binned analysis, we have investigated the impact of the redshift evolution of the SN Ia population's intrinsic properties on cosmology. In particular, we have focused on H_0, thus adding more information and insights to the open discussion initiated by [245]. This scenario seems to be the most favorable, but it is not the only possible one. Our results might suggest to check systematic uncertainties for the Pantheon sample and a careful analysis of the astrophysical parameters of local probes, but we would like to allow additional theoretical explanations that will be discussed in the next chapter.

4.3.2 Theoretical interpretations

The evolution of the Hubble constant with the redshift needs a physical interpretation. The Hubble constant must be a constant by definition, and its observed evolution could be a signal of a wrong framework, for instance, a possible hidden function of the redshift, which has not been taken into account so far. In this subsection, we mainly explore the modified gravity scenario with some preliminary attempts, but a more complete theoretical interpretation will be presented in Chapter 5. Before that, we just mention the effects of local inhomogeneities of the Universe.

4.3.2.1 Local matter underdensity

From a theoretical point of view, the existing tension between the Planck observations and the SNe Ia data could suggest an effect associated with local inhomogeneities of the Universe. Since the observer measurements of cosmological observables are potentially sensitive to the local spacetime around the observer, the presence of inhomogeneities in the local Universe could affect the cosmological parameters. For instance, the so-called void models place the observer inside a local underdensity of radius about $z < 0.15$, and this fact implies a locally measured Hubble constant that is larger than the global expansion rate: a perturbation in density causes a perturbation in the expansion rate, as shown in [181]. We could infer that the local universe may be underdense on spatial scales of several hundreds of megaparsec if we consider that the matter underdensity is defined as underdense compared to the universe average density. In [126–128] there are shreds of evidence for a local matter underdensity on scales of roughly $\sim 300\,\mathrm{Mpc}$ with a density contrast $\delta\rho_0/\rho_0 \sim -0.2$.

A similar approach consists of adopting the spherically symmetric LTB inhomogeneous model [24, 110–113] to outline a possible dependence of the Hubble function also on the radial coordinate, in principle able to theoretically account for the presented behavior of $H_0(z)$. See, for instance, the analysis in [118], where inhomogeneities are inferred to explain the whole universe acceleration phenomenon. Such a scenario, when applied to the H_0 measurement tension, is expected to be associated with a typical spatial scale on which the weak underdensity must manifest itself. Moreover, we have to recover the ΛCDM model and the homogeneous value of H_0 at greater spatial scales, according to the Planck observations.

However, the local underdensity requires the assumption of our unlikely special reference system inside the underdense region. Besides, using low-redshift distance estimators such as SNe Ia, the existence of a local matter underdensity would certainly reduce the H_0 tension, but it would not remove it [121, 125]. Then, we are observing a phenomenon whose origin does not seem to be associated with an intrinsic weak universe inhomogeneity, but it could be due to a different physical reason. If the H_0 tension will still persist, a new cosmology beyond the ΛCDM model may be necessary, since not even the void models can reconcile such a difference.

4.3.2.2 Modified gravity scenario

Since a proportionality in the Friedmann equation (1.23) exists between the Hubble function $H(z)$ and the ΛCDM model density sources, mediated by the Einstein constant χ, a possible dependence of H_0 on the redshift can be naturally restated in terms of a dependence of χ on this same variable, that is, $H_0(z) \propto \sqrt{\chi(z)}$. Namely, we see that the value of the constant H_0 is decaying when measured by astrophysical sources at increasing z values, because the Einstein constant might decay with increasing redshift, and this effect is not accounted for in the ΛCDM model. The possible evolution of H_0 could point out an evolution of the Einstein constant χ. A similar scenario has also been inferred in [178], but by analyzing SN Ia data with the scope of obtaining the evolution on $\mathcal{M}$ rather than H_0.

Given this possible theoretical explanation, we investigate which modified gravity theory can mimic such a behavior of the Einstein constant with redshift. According to the performed fitting, we note that we are predicting a very slow decay, as shown in Table 3.1, since we would have $\chi \propto (1+z)^{-2\,\alpha}$ with $\alpha \sim 10^{-2}$.

A theoretical framework able to justify an effective dependence of the Einstein constant on time and, hence, on the redshift, is provided by the $f(R)$ model in the Jordan frame (see Sect. 1.3). The formulation of the $f(R)$ theories in an equivalent scalar-tensor paradigm turns out to be particularly intriguing for our purposes: we recall that the function $f(R)$ is restated as a real scalar field ϕ, which is non-minimally coupled to the metric in the Jordan frame. Note that in the Jordan frame the quantity χ affects only the gravitational part of the action in Eq. (1.112). It should be emphasized that the standard gravity interaction with a matter source is mediated via the scalar field $\phi(x)$, which implies an Einstein constant as a function of the coordinates, that is, $\chi \to \chi_{\text{eff}} = \chi\,/\,\phi$. Indeed, a varying Einstein constant χ_{eff} may in principle lead to an evolution of $H_0\,(z)$. If we look at the function of $H_0^{\text{fit}}\,(z)$ in Eq. (3.4), we require an effective Einstein constant $\chi \sim (1+z)^{-2\,\alpha}$ to preserve constant the present critical density $\rho_{c0} = 3\,H_0^2/\chi$. However, in addition to the rescaling of the Einstein constant, the non-minimally coupled scalar field in this scheme has its intrinsic evolution characterized by second-order derivatives entering the field equations (1.113a) and (1.113b).

We suggest that this scenario can interpret our results, because the possibility of dealing with a significant universe acceleration requires a slow dynamics of the field, allowing that its potential term mimics a cosmological constant. This situation is naturally reached when the potential term is sufficiently slow-varying in a given time interval. We see that the hypothesis of a near-frozen scalar field evolution is a possible assumption, as far as the potential term should provide a dynamical impact, sufficiently close to a cosmological constant term.

Motivated by the discussion so far, we have already investigated in Sect. 4.2 if one of the most reliable models for reproducing the dark energy effect with modified gravity, i.e., the Hu–Sawicki proposal, was able to induce the requested luminosity distance to somehow remove the observed effect, thus accounting for its physical nature. However, the Hu–Sawicki model seems to be inadequate to account for the observed phenomenon of the decaying $H_0^{\text{fit}}(z)$ since also within this framework the unexpected effect of a running Hubble constant was not removed. The non-positive result of this investigation leads us to explore theoretically the question of reproducing simultaneously the dark energy contribution and the observed $H_0^{\text{fit}}(z)$ effect, by a single $f(R)$ model of gravity in the Jordan frame. Then, we need to look for a new $f\,(R)$ model. Indeed, the HS model predicts deviations from GR and the ΛCDM model only in the late Universe, but it is crucial to build a new $f(R)$ model to study the H_0 tension able to describe properly the cosmological dynamics along different cosmic epochs from today to the recombination at $z = 1100$, by linking also the CMB observations.

Scalar field potential in the Jordan frame inferred from our results Then, in order to infer the functional form of a new $f\,(R)$ model from the results of our binned analysis, we study the cosmological dynamics in the Jordan frame, considering a scalar-field near-frozen dynamics. More specifically, we require the following ansatz

$$\phi\,(z) = (1+z)^{2\,\alpha} \tag{4.6}$$

to account for $H_0^{\text{fit}}\,(z)$ in Eq. (3.4). These concepts suggest that an extra d.o.f. with respect to GR might imply the unexpected trend of $H_0^{\text{fit}}\,(z)$.

We do not mention so far which scalar field potential we should have in the Jordan frame, mimicking a cosmological constant in a slow-roll and at the same time providing an effective Hubble constant. As a preliminary approach, we try to understand which profile we could expect for the scalar field potential, inferred from the behavior of $H_0^{\text{fit}}\,(z)$. This is quite different from a standard analysis of $f(R)$ models.

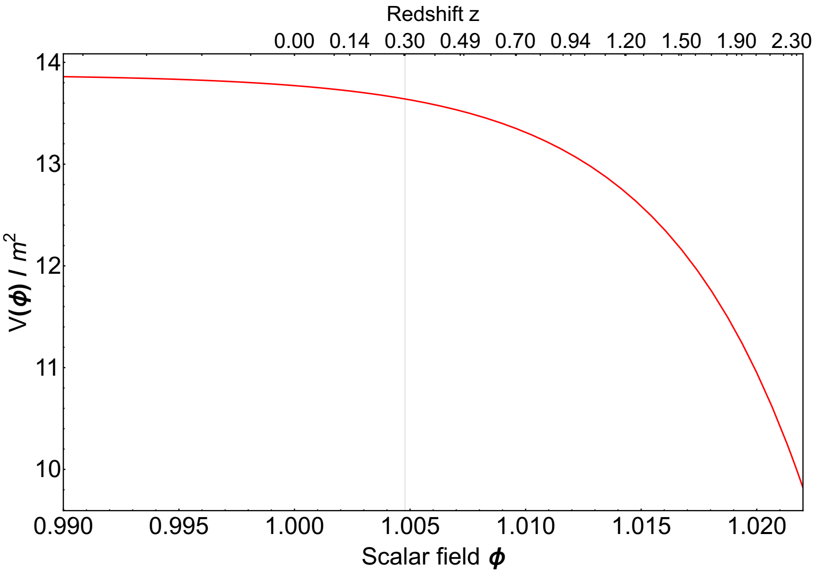

Figure 4.5: Scalar field potential $V(\phi)$ in the Jordan frame given by Eq. (4.10) and inferred from the evolution of $H_0^{\text{fit}}(z)$ with the redshift (3.4). The quantity $V(\phi)/m^2$ is dimensionless. Note the presence of a flat region of the potential for $0 < z \lesssim 0.3$ or $\phi \lesssim 1.005$. This figure is extracted from [TS 2, 8].

Generally, a specific $f(R)$ function is defined a priori, and then the dynamical equations are studied to obtain constraints on the free parameters. Here, instead, starting from the observed decreasing trend of $H_0^{\text{fit}}(z)$ and assuming $\phi(z)$ from Eq. (4.6), we wonder what the scalar field potential would be in a scalar-tensor dynamics. Therefore, we can infer $V(\phi)$ [TS 2, 8] by starting from the modified Friedmann equation ((1.117a)), which allows us to write $V(\phi)$ as

$$V(\phi) = 6(1-2\alpha)\left(\frac{dz}{dt}\right)^2 \phi^{1-1/\alpha} - 6m^2\,\phi^{3/2\alpha}\,, \tag{4.7}$$

where we have used the standard definition of redshift (1.15), and $\rho \sim (1+z)^3$ for a matter component (1.26). Now, we need to specify the term dz/dt, which is given by

$$\frac{dz}{dt} = -(1+z)\,H(z). \tag{4.8}$$

Here, we can not simply use the extended Friedmann equation to replace $H(z)$. In principle, we would need to compute the Hubble parameter $H(z)$ from the field equations, and then replace $H(z)$ in the term $\frac{dz}{dt}$. However, this procedure is not viable, since we need to fix a well-defined $V(\phi)$ to solve the field equations. Then, we decide to impose the Hubble parameter

$$H(z) = \frac{\tilde{H}_0}{(1+z)^\alpha}\sqrt{\Omega_{m0}\,(1+z)^3 + 1 - \Omega_{m0}}\,, \tag{4.9}$$

as suggested from our binned analysis, although its analytical form is different from the Hubble parameter obtained using the modified Friedmann equation. In other words, to obtain $V(\phi)$, we impose in the Jordan frame dynamics the same physical effect observed from the redshift binned analysis of the Pantheon sample and BAOs. We have simply replace H_0 with $H_0^{\text{fit}}(z)$ given by Eq. (3.4) in the standard Friedmann equation (1.38) in the ΛCDM model.

Hence, combining Eqs. (4.7), (4.8) and (4.9), we obtain the final expression of the potential [TS 2, 8]:

$$\frac{V(\phi)}{m^2} = 6\,(1-2\alpha)\,\frac{1-\Omega_{m0}}{\Omega_{m0}} - 12\,\alpha\,\phi^{\frac{3}{2\alpha}}\,, \tag{4.10}$$

where we have considered the relation $\Omega_{m0} = m^2/\tilde{H}_0^2$. As it has been built, the potential (4.10) might provide an effective Hubble constant that evolves with redshift. You can see the form of the scalar field potential in Fig. 4.5, where we fixed $\alpha = 0.009$ (see Table 3.1) and $\Omega_{m0} = 0.298$ for plotting $V(\phi)/m^2$. We stress that the flatness of the potential does not emerge throughout the Pantheon sample redshift range, $0 < z < 2.3$, but it appears only in a narrow region for $0 < z \lesssim z^*$, where $z^* = 0.3$ is the redshift at the dark energy and matter components equivalence of the universe. Thus, the potential mimics a cosmological constant in the era dominated by dark energy, thus validating our approach.

Furthermore, we can obtain the $f(R)$ function related to $V(\phi)$ in Eq. (4.10). Using the field equation (1.113b) $R = dV/d\phi$ in the Jordan frame, and also the relation $f(R) = R\,\phi(R) - V(\phi(R))$ from Eq. (1.111), we write:

$$f(R) = -6\,m^2\left[(3-2\alpha)\left(-\frac{R}{18\,m^2}\right)^{\frac{3}{3-2\alpha}} + (1-2\alpha)\,\frac{1-\Omega_{0m}}{\Omega_{0m}}\right]. \tag{4.11}$$

Expanding this expression for $\alpha \sim 0$, according to the values of α from the binned analysis (see Table 3.1), we obtain [TS 2, 8]:

$$f(R) \approx \left(R - 6\,m^2\,\frac{1-\Omega_{m0}}{\Omega_{m0}}\right) + \frac{2}{3}\alpha\left[R\,\ln\left(-\frac{R}{m^2}\right) - (1+\ln 18)\;R + 18m^2\,\frac{1-\Omega_{m0}}{\Omega_{m0}}\right] + O\left(\alpha^2\right)\,. \tag{4.12}$$

It should be emphasized that the first term above is precisely the gravitational Lagrangian density in GR with a cosmological constant $\Lambda = 3m^2\,(1-\Omega_{m0})\,/\,\Omega_{m0}$, where we used $m^2 = \tilde{H}_0^2\,\Omega_{m0}$. Moreover, it is clear that the first-order term in α in Eq. (4.12) gives the deviation from GR. Hence, the α coefficient stresses corrections to GR.

It is worthwhile to remark that the expression above may not be the final form of the underlying modified theory of gravity, associated with the global universe dynamics, but only its asymptotic form in the late Universe, i.e., as the scalar of curvature approaches the value corresponding to the cosmological constant in the ΛCDM model. In all these computations we do not consider relativistic or radiation components at very high redshifts, but it may be interesting to test this model with other local probes in the late Universe.

The proposed discussions above show a possible interpretation of our results coming from the binned analysis, and we suggest a candidate for $V(\phi)$, assuming the evolution of $H_0^{\mathrm{fit}}(z)$. Further investigations about a reliable $f(R)$ model able to explain both the the cosmic accelerated phase in the late Universe and an effective Hubble constant that evolves with the redshift are presented in the next chapter.

Requirements for a suitable $f(R)$ model Now we follow an alternative approach to provide some general properties that an $f(R)$ model in the Jordan frame must possess to induce the necessary scenario of a slowly varying Einstein constant. We consider again the dynamical impact of the scalar field ϕ, related to the $f(R)$ function. Let us observe that the following relation holds

$$\frac{d\phi}{dz} = -\frac{1}{1+z}\,\frac{\dot{\phi}}{H} \tag{4.13}$$

from the definitions of the redshift (1.15) and the Hubble parameter (1.19). In order to get the desired behavior $\phi \propto (1+z)^{2\alpha}$, we must deal with a dynamical regime where the following request is satisfied:

$$\frac{\dot{\phi}}{H} = -2\,\alpha\,\phi\,. \tag{4.14}$$

We consider a slow-rolling evolution of the scalar field ϕ in the late universe, near enough to $\phi \simeq 1$. Then, focusing on the dark energy dominated phase, we neglect the contribution of the matter density in the modified Friedmann equation. (1.117a). For the sake of simplicity, we regard the potential term $V(\phi \simeq 1)$ as the dominant contribution, and we neglect the other terms $H_0\,\dot{\phi}$ and $\ddot{\phi}$. Under these conditions, Eqs. (1.117a) and (1.117c) become

$$H^2 = \frac{V}{6\phi} \tag{4.15}$$

and

$$\frac{\dot{\phi}}{H} = \frac{1}{9H^2}\left(2V - \phi\frac{dV}{d\phi}\right)\,, \tag{4.16}$$

respectively.

Referring to Eq. (4.15) at $z \sim 0$, we make the identification $H_0^2 \equiv V(\phi \simeq 1)/6$. Hence, in order to reproduce Eq. (4.14), we must require that for $\phi \to 1$, the following relation holds:

$$\alpha = \frac{1}{3V}\left(\phi\,\frac{dV}{d\phi} - 2V\right)\,. \tag{4.17}$$

Note that α must be positive to obtain a decreasing trend of the Hubble constant. The analysis above states the general features that a $f(R)$ model in the Jordan frame has to exhibit to provide a viable candidate to reproduce the observed decay behavior of $H_0^{\rm fit}(z)$.

An Example for low redshifts As an extra viable example for the dark energy dominated Universe (slightly different from the traced above), we consider a potential term similar to the one adopted in the so-called chaotic inflation [192, 247], i.e.,:

$$V(\phi) = Q + 6H_0^2\phi^2\,, \tag{4.18}$$

where Q is a positive constant, such that $Q \ll 6H_0^2$. From Eq. (4.15), we immediately get

$$H^2 \simeq H_0^2\phi \sim H_0^2\,, \tag{4.19}$$

where we recall that we are considering $\phi \approx 1$. Analogously, from Eq. (4.17), we obtain:

$$\alpha \sim -\frac{Q}{9H_0^2}\,. \tag{4.20}$$

The negative value of α is coherent with the behavior $H^2 \propto \phi$. Hence, we can reproduce the requested behavior of $\phi(z)$ by properly fixing the value of Q to get α as it comes out from the data analysis of Sect. 4.1. Specifically, we get $Q \sim 10^{-3}H_0^2$ to have $\alpha \sim 10^{-2}$.
Furthermore, it is easy to check that, for $\phi \to 1$, Eq. (4.14) and Eq. (4.19), we find the relation

$$\ddot{\phi} \sim \mid \alpha \mid H_0\dot{\phi} \ll 3H_0\dot{\phi}\,, \tag{4.21}$$

which ensures that we are dealing with a slow-rolling phase.
Finally, we compute the $f(R)$ function corresponding to the potential in Eq. (4.18), recalling the relation

(1.111):

$$f(R) = \frac{R^2}{24H_0^2} - Q\,. \tag{4.22}$$

It should be emphasized that this specific model is reliable only as far the universe matter component is negligible, $z \ll 0.3$.

We summarize our theoretical discussions in modified gravity. Our preliminary attempts of modified gravity models showed that the $f(R)$ gravity in the Jordan frame is a possible candidate to account for the observed effect of $H_0^{\mathrm{fit}}(z)$. Firstly, we inferred the scalar field potential and the functional form of $f\,(R)$ from our results by imposing an ansatz on the scalar field dynamics. Secondly, we focused on an alternative example in the late Universe, considering another specific scalar field potential to check the requirement of a slow-rolling phase. Furthermore, in the former case, we imposed a phenomenological behavior of the Hubble parameter $H\,(z)$ in Eq. (4.9), as if the Hubble constant evolves with the redshift according to our data analysis, but we did not fully explain how it is possible to define an effective Hubble constant within the $f\,(R)$ metric formalism. The next chapter aims to clarify this point. We conclude this chapter by noting that the accomplishment of a satisfactory model requires a significant effort in further investigation, especially accounting for the constraints that observations in the local universe provided for modified gravity.

Chapter 5

An effective Hubble constant in the Jordan frame of $f\,(R)$ gravity

The analysis pursued by the SNe Ia community, mainly represented by the data of the Pantheon [176] and Pantheon+ [71] samples, seem to exclude the existence of a redshift evolution of these objects and show a reliable control of all the main sources of errors. However, some recent studies report a possible redshift dependence of the marginalized absolute magnitude of SNe Ia, or the Hubble constant itself [177–179, 231–234], as we have also seen in Chapters 3 and 4. In particular, we have discussed about the possibility that the observed dependence of an effective Hubble constant $H_0^{\mathrm{eff}}(z)$, predicted by the binning analysis of the Pantheon sample, can be interpreted as a variation of the Einstein constant, naturally achieved for example by $f(R)$ gravity in the Jordan frame. However, in the previous chapter, it was shown how one of the most reliable $f(R)$ models, the HS proposal, is inappropriate to reproduce the desired effect. This negative result suggested the necessity to consider an alternative dark energy $f(R)$ model, able to account both for the Universe acceleration and a variable $H_0^{\mathrm{eff}}(z)$ parameter. In the previous chapter, we discussed some preliminary proposals of $f\,(R)$ models. The present chapter is dedicated to the formulation of a model satisfying such requirements, following the prescriptions of a decreasing trend for $H_0^{\mathrm{eff}}(z)$. We are interested in providing a theoretical framework able to mimic a running Hubble constant with the redshift. Then, we derive the profile of the potential term for the scalar field, which in turn allows us to reconstruct the underlying $f(R)$ model.

The analysis is divided into two parts: the first one is characterized by an analytical approach, while the second one relies on a pure numerical study. The analytical formulation starts with the hypothesis that the potential can be satisfactorily described by a dynamical deviation from a flat region. Unlike the analysis performed in previous chapters, we do not fix a priori the form of $\phi(z)$, but we obtain it from the dynamics in the Jordan frame. In the numerical analysis, we assume again the evolution of $H_0^{\mathrm{eff}}(z)$, but we relax the request of a constant potential term in a given region. The theoretical framework developed in this chapter is based on [TS 1, 7].

5.1 Analytic solution for the scalar field potential

In order to build the profile of the scalar field potential $V\,(\phi)$, we assume the presence of an effective Hubble constant $H_0^{\mathrm{eff}}(z)$ evolving with the redshift. We recall that the results of the analysis performed in Chapters 3 and 4 suggested the parametrization for $H_0^{\mathrm{fit}}\,(z)$ given in Eq. (3.4). Note that a decreasing trend with the redshift may address the Hubble tension, since the extrapolation of the fitting function $H_0^{\mathrm{fit}}(z)$ from $z = 0$ to the recombination redshift $z = 1100$ might succesfully match

$H_0^{\rm loc} = (73.04 \pm 1.04)$ km s^{-1} Mpc^{-1} and $H_0^{\rm CMB} = (67.36 \pm 0.54)$ km s^{-1} Mpc^{-1}. Then, we build the Hubble function $H(z)$ as:

$$H\left(z\right) = H_0^{\rm eff}(z)\,\sqrt{\Omega_{m0}\left(1+z\right)^3 + 1 - \Omega_{m0}}\,, \tag{5.1}$$

where Ω_{m0} is the cosmological density parameter for the matter component. Moreover, we focus on a cosmological dust in the late Universe, for which we recall that $\rho = \rho_0\left(1+z\right)^3$ according to Eq. (1.26).

To reconstruct the evolution of $H_0^{\rm eff}(z)$, we compare the phenomenological Hubble function $H(z)$ given by Eq. (5.1) and the generalized Friedmann equation (1.117a). Considering that in a homogeneous Universe we have $\phi = \phi\left(z\right)$, Eq. (1.117a) rewrites

$$H^2 = \frac{1}{\phi - \left(1+z\right)\,\phi'}\,\frac{\chi}{3}\left(\rho + \frac{V\left(\phi\right)}{2\,\chi}\right)\,, \tag{5.2}$$

where in this chapter $\phi' \equiv d\phi/dz$. We used the definition of redshift (1.15) and also the fact that $dz/dt = -\left(1+z\right)\,H\left(z\right)$.

We define the potential as

$$V\left(\phi\right) \equiv 2\chi\rho_\Lambda + g\left(\phi\right)\,, \tag{5.3}$$

where we recall that ρ_Λ is the present value of the Universe dark energy density, and $g\left(\phi\right)$ is the deviation from a cosmological constant scenario. To rewrite Eq. (5.2) in a form similar to Eq. (5.1) and discuss the ΛCDM limit, we assume the existence of a region in which $g\left(\phi\right) \ll 2\chi\rho_\Lambda$ for $0 < z \lesssim z^*$, where we recall that $z^* \sim 0.3$ is the redshift of matter-dark energy equality, defined in Eq. (1.41). Hence, considering only the constant term in $V\left(\phi\right)$, we rewrite Eq. (5.2) as

$$H^2 = \frac{H_0^2}{\phi - \left(1+z\right)\,\phi'}\left[\Omega_{m0}\left(1+z\right)^3 + 1 - \Omega_{m0}\right]\,, \tag{5.4}$$

where we used the definitions of the critical energy density of the Universe (1.34) and also the cosmological density parameters (1.33) for $z = 0$. Moreover, we recall that $\Omega_{\Lambda 0} = 1 - \Omega_{m0}$ in a flat Universe. From Eq. (5.4), one can recognize the usual terms in the Friedmann equation (1.23) in the ΛCDM scenario, up to a factor related to the scalar field ϕ. Indeed, comparing Eqs. (5.1) and (5.4), we can define the effective Hubble constant

$$H_0^{\rm eff}(z) = \frac{H_0}{\sqrt{\phi - \left(1+z\right)\,\phi'}}\,, \tag{5.5}$$

which is related to the scalar field dynamics $\phi(z)$.

Let us now take into account the scalar field equation (1.114). Using the relation $\phi = \phi\left(z\right)$ and the approximation for the scalar field potential $V\left[\phi\left(z\right)\right] \approx 2\chi\rho_\Lambda$, we obtain:

$$3\,H^2\left(1+z\right)\,\left[\left(1+z\right)\,\phi'' - \phi'\right] - 3\,\left(1+z\right)\,\frac{\ddot{a}}{a}\,\phi' + \phi\,\frac{dV}{d\phi} = \chi\,\left(\rho + 4\rho_\Lambda\right)\,. \tag{5.6}$$

It should be emphasized that we do not neglect the term $dV/d\phi = dg/d\phi$, since we want to check *a posteriori* the viability of the approximation for the scalar field potential at low redshifts.

Furthermore, by substituting the term $\ddot{\phi}$ from Eq. (1.114) in Eq. (1.117b), we have

$$\frac{\ddot{a}}{a} = -\frac{\chi}{3\,\phi}\,\left(\rho + \rho_\Lambda\right) + \frac{1}{6}\frac{dV}{d\phi} - H^2\,\left(1+z\right)\frac{\phi'}{\phi}\,. \tag{5.7}$$

Then, we combine Eqs. (5.1), (5.6), and (5.7), and we obtain

$$\begin{aligned}\frac{d\tilde{V}}{dz} = \frac{1}{\frac{\phi}{\phi'} - \frac{1+z}{2}} \Bigg\{ 3 \left[(1+z)^3 + \frac{1-\Omega_{m0}}{\Omega_{m0}} \right] \Bigg[1 - (1+z)\, \frac{\phi'}{\phi} + \\ - (1+z)\, \frac{H_0^{\mathrm{eff}\,2}(z)}{H_0^2} \left((1+z) \left(\phi'' + \frac{\phi'^2}{\phi} \right) - \phi' \right) \Bigg] + 9 \frac{1-\Omega_{m0}}{\Omega_{m0}} \Bigg\}, \end{aligned} \tag{5.8}$$

where we rescaled the potential as a dimensionless quantity $\tilde{V} \equiv V/m^2$ with the constant $m^2 \equiv \chi\rho_0/3 = H_0^2\Omega_{m0}$. To reproduce a decreasing trend for $H_0^{\mathrm{eff}}(z)$ similar to $H_0^{\mathrm{fit}}(z)$ in Eq. (3.4), we require the following condition

$$\phi(z) - (1+z)\, \phi'(z) = (1-2\alpha)\, \phi(z)\,, \tag{5.9}$$

which admits the solution:

$$\phi\,(z) = K\, (1+z)^{2\alpha}\,. \tag{5.10}$$

We fixed the initial condition $\phi\,(0) = K$ at $z = 0$, where $K = 1 - 10^{-7}$ [101] denotes the deviation from a pure GR scenario ($\phi = 1$).

As a consequence of Eq. (5.5), the effective Hubble constant becomes

$$H_0^{\mathrm{eff}}(z) = \frac{H_0}{\sqrt{K\,(1-2\alpha)}\,(1+z)^{\alpha}}\,, \tag{5.11}$$

which is a decreasing function, as requested to match the values of H_0^{loc} and H_0^{CMB} for $z = 0$ and 1100, respectively. In this regard, we set $\alpha = 1.1 \cdot 10^{-2}$ and $H_0 = 72.2\,\mathrm{km\ s^{-1}\,Mpc^{-1}}$. Note, in particular, that the value of α is consistent in 1 σ with the fitting parameters $\alpha = 0.009 \pm 0.004$ used in the analysis of three redshift bins in Table 3.1.

Finally, by substituting $\phi(z)$ from Eq. (5.10) and $H_0^{\mathrm{eff}}(z)$ from Eq. (5.11) into Eq. (5.8), we can easily integrate to obtain $g(z)$ and reconstruct analytically the scalar field potential. After long but straightforward calculations, we obtain:

$$\tilde{V}\,(z) = \tilde{V}\,(0) + \frac{6\alpha}{1-\alpha} \left\{ 2\,(2+\alpha)\, \frac{1-\Omega_{m0}}{\Omega_{m0}} \ln(1+z) + \frac{1+2\alpha}{3} \left[(1+z)^3 - 1 \right] \right\}, \tag{5.12}$$

where we set the integration constant $\tilde{V}(0) = 6\,(1-\Omega_{m0})\,/\Omega_{m0}$, coming from $V\,[\phi\,(z=0)] = 2\chi\rho_\Lambda$. After solving relation (5.10) for $z = z\,(\phi)$, we rewrite the potential as

$$\tilde{V}\,(\phi) = \tilde{V}\,(\phi = K) + \frac{6\alpha}{1-\alpha} \left\{ \frac{2+\alpha}{\alpha} \frac{1-\Omega_{m0}}{\Omega_{m0}} \ln\left(\frac{\phi}{K}\right) + \frac{1+2\alpha}{3} \left[\left(\frac{\phi}{K}\right)^{\frac{3}{2\alpha}} - 1 \right] \right\}. \tag{5.13}$$

Such a procedure it can be demonstrated to be consistent with the method outlined in [248], which adapted to our scalar-tensor reformulation amounts to directly integrate in ϕ the equation $\frac{dV}{d\phi} = R$, once the equality $R = 6\dot{H} + 12H^2$ and the expressions for $\phi(z)$ and $H(z)$ in (5.10) - (5.11) are taken into account. An explicit calculation shows that the two results coincide up to the numerical factor $\frac{1-2\alpha}{1-\alpha} \sim 1$, since $\alpha \sim 10^{-2}$, guaranteeing the consistency of the two approaches. This very small discrepancy is due to the approximation we considered in constructing the analytical model (we disregarded the small term $g(z)$ in the modified Friedmann equation (5.2)). The numerical treatment, which follows in the next section, is clearly consistent to the method in [248] up to the desired order of approximation. In particular, a numerical approach is clearly needed to get the function $N(R)$, being N the e-folding variable introduced in [248], which is not analytically solvable.

The profile of $\tilde{V}$ can be appreciated in Fig. 5.2 (we fixed the value $\Omega_{m0} = 0.298$ [176]), and it can be considered nearly flat for $0 < z \lesssim z^*$, where the percentage variation of $\tilde{V}$ is about 1.6%, which validates our hypothesis on a dark-energy-dominated era. We conclude this section by noting that in general for $f(R)$ theories the stability of scalar perturbations, i.e. the absence of tachyonic modes in the Jordan frame ([249]), implies on a Minkowski background that $\frac{d^2V}{d\phi^2} > 0$ when evaluated in ϕ_{min}, with ϕ_{min} defined by $\frac{dV}{d\phi} = R_{min} = 0$. In our case, however, since (5.13) is reliable only for a cosmological setting, we can simply look at the behavior with the redshift of the ratio between the square root of the second potential derivative and the Hubble function, as suggested by [250]. As illustrated in Fig. 5.3, this ratio is indeed greater than unity for $z = 0$, and increases with increasing values of z, implying, in agreement with the conclusions of [250], that our model is coherent with the requirements of the chameleon mechanism [107].

5.2 Numerical analysis of the model

We now relax the assumption on the existence of a flat region of the scalar field potential for $0 < z \lesssim z^*$, but we continue to consider the presence of an effective Hubble constant $H_{0,\mathrm{eff}}(z)$. Let us proceed with a complete numerical analysis of the system (1.117a)-(1.114), which we want to solve in terms of $\phi(z)$ and $V[\phi(z)]$.

Firstly, we rewrite the generalized Friedmann equation (1.117a) in the variable z, isolating the dimensionless scalar field potential

$$\tilde{V}(z) = 6\left\{\frac{H_0^{\mathrm{eff}\,2}(z)}{H_0^2}\left[(1+z)^3 + \frac{1-\Omega_{m0}}{\Omega_{m0}}\right]\left[\phi(z) - (1+z)\,\phi'(z)\right] - (1+z)^3\right\}\,, \tag{5.14}$$

where we used Eq. (5.1) and the fact that $\rho \sim (1+z)^3$.

Secondly, we rewrite the scalar field equation (1.114) as:

$$\begin{aligned}&\left[(1+z)^3 + \frac{1-\Omega_{m0}}{\Omega_{m0}}\right]\left\{\frac{H_0^{\mathrm{eff}\,2}(z)}{H_0^2}\left[(1+z)^2\,\phi''(z) - 2\,(1+z)\,\phi'(z)\right]\right.\\ &\left.+\frac{H_0^{\mathrm{eff}}(z)}{H_0^2}\frac{dH_0^{\mathrm{eff}}(z)}{dz}\,(1+z)^2\,\phi'(z)\right\} + \frac{3}{2}\frac{H_0^{\mathrm{eff}\,2}(z)}{H_0^2}\phi'(z)\,(1+z)^4 - \frac{2}{3}\tilde{V}\left[\phi(z)\right] + \frac{\phi(z)}{3\phi'(z)}\frac{d\tilde{V}}{dz} = (1+z)^3\,.\end{aligned} \tag{5.15}$$

Then, by substituting $\tilde{V}(z)$ from Eq. (5.14) into Eq. (5.15) and imposing an effective Hubble constant like in Eq. (5.11), we obtain a second-order differential equation in $\phi(z)$. We solve numerically this equation with the following initial conditions for $z = 0$: $\phi(0) = K$, and $d\phi/dz\,(0) = 2\alpha K$. We fixed the same values for α, Ω_{m0}, and K adopted in Sect. 5.1.

In Fig. 5.1 we show the evolution of ϕ with z using a red line, while in Fig. 5.2 we plot the profile of $\tilde{V}$ in terms of z and ϕ. In all these figures, we also compare our numerical results with the respective profiles obtained from the analytical solution based on the assumption of a flat potential at low redshifts in Sect. 5.1, noting that corresponding solutions mostly overlap for $z \ll 1$. It should be stressed that the potential $\tilde{V}$ exhibits a nearly flat profile for $0 < z \lesssim z^*$ also for the numerical solution with a percentage variation of about 1.3%.

5.3 The low-redshift f(R) profile

We are interested in obtaining an analytical expression for the $f(R)$ function, reproducing both the late-time cosmic acceleration and a running Hubble constant with the redshift, according to Eq. (3.4). To this end, we expand the solution for $\phi(z)$ and $\tilde{V}[\phi(z)]$ in the limit of low redshifts for $z \ll 1$.

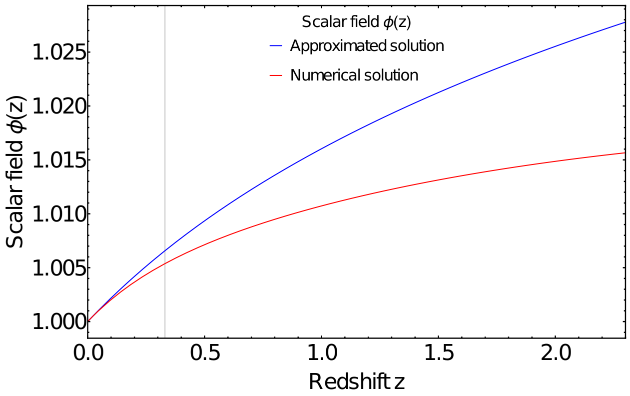

Figure 5.1: Behavior of the scalar field ϕ VS redshift z in the Jordan frame, assuming an effective Hubble constant $H_0^{\text{eff}}(z)$ in Eq. (5.11). The blue line is referred to the approximated solution developed in Sect. 5.1, while the red line is obtained from the numerical analysis discussed in Sect. 5.2, after solving Eqs. (5.14) and (5.15). The gray vertical line denote $z = z^*$. This figure is reported in [TS 1].

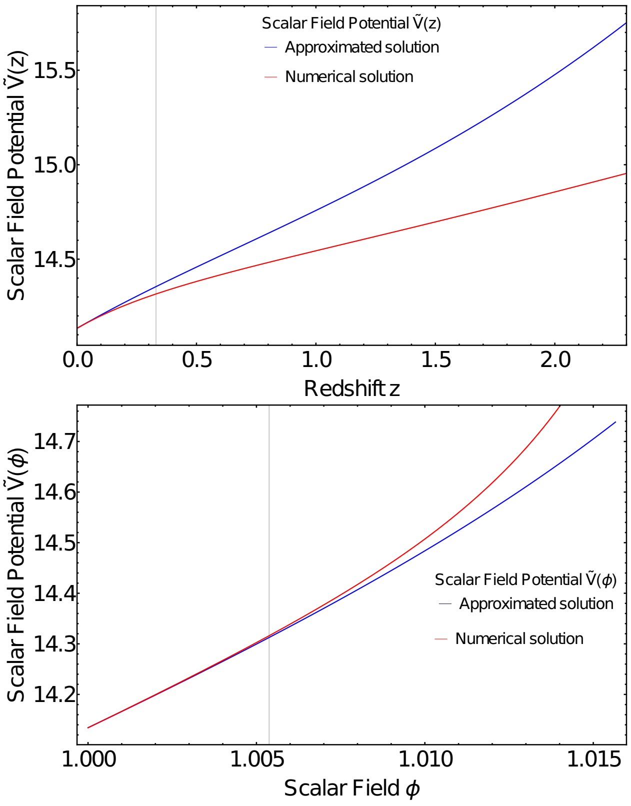

Figure 5.2: Profile of the scalar field potential in terms of the redshift z (top panel) and the scalar field ϕ (bottom panel) in the Jordan frame, inferred from the assumption of a running Hubble constant $H_0^{\text{eff}}(z)$, according to Eq. (5.11). Note that $\tilde{V} = V(\phi)/m^2$ is a dimensionless potential. The blue and red lines are referred to the approximated solution (Sect. 5.1) and numerical results (Sect. 5.2), respectively. The gray vertical lines denote $z = z^*$ in the top panel and $\phi = \phi(z^*)$ in the bottom one. These panels are extracted from [TS 1].

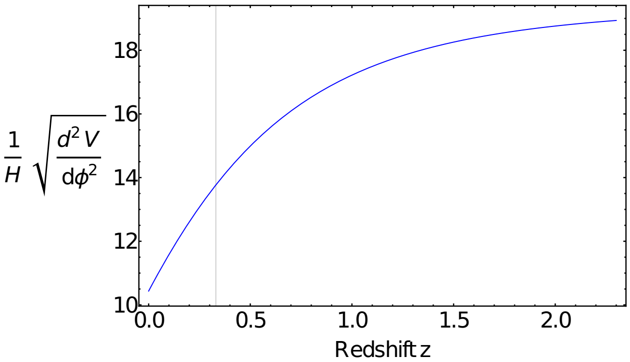

Figure 5.3: Ratio between the square root of the second derivative of the potential $V = m^2\tilde{V}$ and the Hubble function in terms of the redshift. We have used Eqs. (5.1), (5.10), (5.11), and (5.13). This figure is obtained in [TS 1].

More specifically, starting from Eq. (5.10) for $z \ll 1$, we get up to the second order:

$$\phi(z) \approx K\left[1 + 2\alpha z - \alpha\left(1 - 2\alpha\right) z^2\right] + O\left(z^3\right) . \tag{5.16}$$

Note that the low-redshift limit $z \ll 1$ is equivalent to an expansion for ϕ around K. Then, we expand $\tilde{V}\left[\phi(z)\right]$ given by Eq. (5.13) for $\phi \approx K$:

$$\tilde{V}(\phi) \approx \tilde{V}(K) + A_1\,(\phi - K) + A_2\,(\phi - K)^2 + O\left[(\phi - K)^3\right] , \tag{5.17}$$

where the dimensionless constants A_1 and A_2 are defined as

$$A_1 = \frac{6}{K\,(1-\alpha)}\left[\frac{1+2\alpha}{2} + (\alpha+2)\,\frac{1-\Omega_{m0}}{\Omega_{m0}}\right] , \tag{5.18}$$

$$A_2 = \frac{3}{K^2\,(1-\alpha)}\left[\frac{1+2\alpha}{2}\left(\frac{3}{2\alpha} - 1\right) - (\alpha+2)\,\frac{1-\Omega_{m0}}{\Omega_{m0}}\right] . \tag{5.19}$$

Once we have the expression for $\tilde{V}\left(\phi\right)$, we use Eq. (1.113b), i.e., $R = dV/d\phi$, for solving in $\phi = \phi\left(R\right)$. Then, inverting the relation (1.111), i.e., $f\left(R\right) = R\,\phi\left(R\right) - V\left[\phi\left(R\right)\right]$, we obtain

$$f\left(R\right) \approx m^2 B_0 + B_1\,R + B_2\,\frac{R^2}{m^2} , \tag{5.20}$$

where we have defined the constants

$$B_0 = \frac{A_1^2}{4A_2} - \tilde{V}\left(K\right) , \qquad B_1 = K - \frac{A_1}{2A_2} , \qquad B_2 = \frac{1}{4A_2} . \tag{5.21}$$

It should be stressed that Eq. (5.20) provides an approximated solution of the $f\left(R\right)$ function for $z \ll 1$, which contains constant, linear, and quadratic terms in R, with the ΛCDM model recovered for $K \to 1$ and $\alpha \to 0$. Clearly, the function $f(R)$ has been constructed on a cosmological setting and its parameters are not directly suitable for a comparison in the Solar system framework. Nonetheless, the absence of a tachyonic mode, as ensured by the positive coefficient in front of the R^2 term, is a reliable consistency check for the theory.

5.4 Summary

We started our analysis from the results obtained in Chapters 3 and 4, which outlined a dependence of the value of H_0 with the redshift via a binned data analysis of the SNe Ia Pantheon sample within $2\ \sigma$. The specific form of the decaying $H_0^{\rm fit}(z)$ given in Eq. (3.4) was the phenomenological input of our theoretical study.

The idea proposed above consists in setting up a dark energy model that is able to account for a variation with z of the H_0 value. More specifically, we adopted the theoretical paradigm of $f(R)$ gravity, as viewed in the Jordan frame, where we used the non-minimally coupled scalar field for describing the variation of the effective Einstein constant.

Starting from the equations of motion for an isotropic Universe, we assumed the scalar field as a function of the redshift, and we determined the behavior of Eq. (5.10) by imposing the desired decaying of $H_0^{\rm eff}(z)$. Then, by means of the scalar field dynamics, we were able to recover the corresponding potential term, which fixed in turn the $f(R)$ model.

The investigation was performed both analytically and numerically: in the former case, in Sect. 5.1 we assumed the existence of a flat region of the scalar field potential, approximated by a constant value, and then we explicitly determined the potential derivative in Eq. (5.8); in the latter case, the scheme was implemented directly on the two basic equations (1.117a) and (1.114), without any assumption on the potential form. It was rather remarkable that, in both analyses, the potential term singled out a nearly flat region for $z \lesssim 0.3$ (Fig. 5.2), which is exactly when the dark energy contribution of the Universe dominates on the matter content.

The low-redshift limit of our model in Sect. 5.3 allowed an analytical determination of the potential term, and hence of the underlying $f(R)$ model. The resulting expression (5.20) for the modified Lagrangian contains a cosmological constant, as well as linear and quadratic contributions in the Ricci scalar. In particular, this result is consistent with other $f(R)$ gravity models proposed to describe deviations from GR in the ΛCDM cosmological scenario, without introducing dark energy [81, 251–253]. It is very remarkable for the robustness of our model that this modified scheme approaches the ΛCDM scenario only when $\alpha \to 0$ and $df/dR \to 1$. In other words, even if we reduce the function $H_0^{\rm eff}(z)$ to a fixed constant value, our model can still contain a small deviation from the ΛCDM Universe.

Thus, we can claim that our study is able to simultaneously address two key points: on one hand, we get a modified gravity model as a suitable dark energy candidate; on the other hand, we provided a natural interpretation for the profile of $H_0^{\rm fit}(z)$ obtained in Chapters 3 and 4. The study presented in this chapter calls attention to further investigations as the redshift increases towards the CMB observations, in order to understand if it can satisfactorily solve the Hubble tension.

Part III

Inhomogeneities and non-Gaussianities in the large-scale structure of the Universe

Chapter 6

The evolution of local inhomogeneities of the Universe in different cosmological models

While the Part II of this thesis was devoted to discuss possible deviations from the first pillar of the ΛCDM model, i.e. GR as the underlying gravitational theory in cosmology, in the Part III we are interested in the second pillar, i.e., the cosmological principle. In particular, in the present chapter, we analyze inhomogeneous cosmological models in the local Universe, based on the LTB metric and developed using linear perturbation theory on a homogeneous and isotropic Universe background. Focusing on the different evolution of spherical symmetric inhomogeneities, we want to compare the ΛLTB model, in which we recall that the cosmological constant Λ is included in the LTB formalism, with inhomogeneous cosmological models based on $f(R)$ modified gravity theories viewed in the Jordan frame. In particular, we adopt the HS $f(R)$ model in the Jordan frame to describe the cosmic accelerated phase for the background Universe. We will note that the key difference between the ΛLTB model and the $f(R)$ gravity in an inhomogeneous cosmology is outlined by the 0-1 component of the gravitational field equations since it intrinsically links the metric tensor components to the non-minimally coupled scalar field, present in the Jordan frame. Investigations about local inhomogeneities in the late Universe not only are interesting to test the spatial scale of homogeneity, but our method presented in [TS 4, 9] may allow us to discriminate if the present cosmic acceleration is caused by a cosmological constant term or a modified gravity effect. The idea to combine the modified metric $f(R)$ gravity with local inhomogeneities of the late Universe could be also particularly intriguing to solve the Hubble constant tension. Indeed, the combination of more than one non-standard physical effect may be needed since the ΛLTB model separately can only alleviate the tension, as already mentioned in the Introduction. Here, we focus on a prodromic question to distinguish a standard paradigm from an alternative cosmology in the LTB metric. Local inhomogeneities incorporated in a modified gravitational scenario might become a predictive tool to search for some specific markers of the matter distribution.

6.1 The Lemaître-Tolman-Bondi model in the Jordan frame of $f(R)$ gravity

We extend the content of Sect. 2.1.1, which was referred to the LTB model in GR, and in this section we study the cosmological dynamics in the LTB metric (2.1) within the framework of the $f(R)$ gravity in the Jordan frame. The 0-1, 0-0, 1-1 components of the gravitational field equations (1.113a) are written as

$$\frac{\dot{\beta}'}{\beta'} - \dot{\alpha} + \dot{\beta} = -\frac{1}{2\,\phi\,\beta'}\left(\dot{\phi}' - \dot{\alpha}\,\phi'\right)\,, \tag{6.1a}$$

$$\begin{aligned}&\dot{\beta}^2 + 2\,\dot{\alpha}\,\dot{\beta} + e^{-2\,\beta} - e^{-2\,\alpha}\left[2\,\beta'' + 3\,\left(\beta'\right)^2 - 2\,\alpha'\,\beta'\right] = \\ &\quad -\frac{1}{\phi}\left\{\left(\dot{\alpha} + 2\,\dot{\beta}\right)\,\dot{\phi} - e^{-2\,\alpha}\,\left[\phi'' - \phi'\,\left(\alpha' - 2\,\beta'\right)\right]\right\} + \frac{\chi\,\rho}{\phi} + \frac{V\left(\phi\right)}{2\,\phi}\,,\end{aligned} \tag{6.1b}$$

$$2\,\ddot{\beta} + 3\,\dot{\beta}^2 + e^{-2\,\beta} - e^{-2\,\alpha}\,\left(\beta'\right)^2 = \frac{V\left(\phi\right)}{2\,\phi} - \frac{1}{\phi}\left[\ddot{\phi} + 2\,\dot{\beta}\,\dot{\phi} - 2\,e^{-2\,\alpha}\,\beta'\,\phi'\right]\,, \tag{6.1c}$$

respectively, where we have put a cosmological pressure-less dust as a source. In the Appendix on page 133, it is shown that the other non-vanishing gravitational field equations, i.e. 2-2 and 3-3 components, depend on the previous set of equations, as it must be, basically due to the spherical symmetry in the LTB geometry.

Moreover, the scalar field equation (1.114) rewrites as

$$\ddot{\phi} + \left(\dot{\alpha} + 2\,\dot{\beta}\right)\,\dot{\phi} - e^{-2\,\alpha}\,\left[\phi'' - \phi'\,\left(\alpha' - 2\,\beta'\right)\right] - \frac{2}{3}\,V\left(\phi\right) + \frac{\phi}{3}\,\frac{dV}{d\phi} = \frac{\chi\,\rho}{3}\,. \tag{6.2}$$

Note that in an inhomogeneous cosmology all the quantities ϕ, ρ, α, and β depend on both t and r.

It should be emphasized the occurrence of extra contributions in field equations (6.1) and (6.2) with respect to the ΛLTB model, due to the coupling between the scalar field ϕ and the metric functions α, β, as well as the presence of the scalar field potential. For instance, it is quite clear to recognize an extra coupling term by comparing the 0-1 field Eq. (6.1a) with the respective Eq. (2.2a) in GR. As a consequence, this coupling in the Jordan frame does not allow us to find a relation between α and β, and then rewrite the LTB metric in a simpler form, unlike the ΛLTB model in GR (see Sect. 2.1.1). For all these reasons, the cosmological dynamics in the Jordan frame is really different from the GR scenario.

On the opposite, the continuity equation related to the ordinary stress-energy tensor $T_{\mu\nu}$ for a dust in the LTB metric exactly exhibits the same form provided in Eq. (2.10) both in GR and $f\left(R\right)$ gravity. In the latter theory, other additional equations are those related to the effective stress-energy tensor $T^{[\phi]}_{\mu\nu}$, defined in Eq. (1.115), for the scalar field in the Jordan frame. More specifically, Eqs. (1.116) in the LTB metric become

$$\frac{1}{2}\,\frac{dV}{d\phi} - \frac{V\left(\phi\right)}{2\,\phi} - \ddot{\alpha} - 2\,\ddot{\beta} - \dot{\alpha}^2 - 2\,\dot{\beta}^2 + \frac{1}{\phi}\left\{\left(\dot{\alpha} + 2\,\dot{\beta}\right)\,\dot{\phi} - e^{-2\,\alpha}\,\left[\phi'' - \phi'\left(\alpha' - 2\,\beta'\right)\right]\right\} = \frac{\chi}{\phi}\,\rho\,, \tag{6.3a}$$

$$\ddot{\alpha} + \dot{\alpha}\,\left(\dot{\alpha} + 2\,\dot{\beta}\right) + 2\,e^{-2\,\alpha}\,\left[\beta'\,\left(\alpha' - \beta'\right) - \beta''\right] - \frac{1}{\phi}\,\left[\ddot{\phi} + 2\,\dot{\beta}\,\dot{\phi} - 2\,e^{-2\,\alpha}\,\beta'\,\phi'\right] + \frac{V\left(\phi\right)}{2\,\phi} - \frac{1}{2}\,\frac{dV}{d\phi} = 0 \tag{6.3b}$$

for $\mu = 0$, 1, respectively.

It should be recalled that these laws for $T^{[\phi]}_{\mu\nu}$ are not independent of the field equations (6.1) and (6.2), because these laws basically come from field equations using Bianchi identities. Nevertheless, these additional equations (6.3) can be useful to rewrite field equations in a different form. For instance, Eq. (6.3b) has been employed to find the dependence between the 1-1 and 2-2 components of the gravitational field equations (6.1c) and (A.2), which implies spatial isotropy in the LTB geometry, as it has been shown in the Appendix on page 133.

To sum up, within the Jordan frame of $f\left(R\right)$ gravity in the LTB metric, we have obtained a system of four partial differential equations (6.1) and (6.2) with four unknown functions: $\alpha\left(t,r\right)$, $\beta\left(t,r\right)$, $\rho\left(t,r\right)$, and $\phi\left(t,r\right)$. Note that the scalar field potential $V\left(\phi\right)$ provides a d.o.f. in the theory. Furthermore, other supplementary equations are provided by Eqs. (2.10) and (6.3).

6.2 Perturbation approach for the Lemaître-Tolman-Bondi model in General Relativity

In this section, we consider local inhomogeneities of the Universe as small spherically symmetric perturbations over a flat background FLRW geometry. We follow a linear perturbation approach, so that we have the FLRW geometry at the zeroth-order perturbation theory, while we build a lumpy Universe described by the LTB metric at the first-order perturbation [254]. Thus, we can write the LTB metric tensor components as

$$g_{\mu\nu}^{\mathrm{LTB}} = \bar{g}_{\mu\nu}^{\mathrm{FLRW}} + \delta g_{\mu\nu}\,, \tag{6.4}$$

in which an overbar denotes the background FLRW metric and the symbol δ is related to linear perturbation terms. We emphasize that, choosing this decomposition, we require spherically symmetric perturbations.

Moreover, we adopt the synchronous gauge for the LTB metric, which intrinsically includes two degrees of freedom in the perturbed metric. Indeed, two independent metric functions, i.e., $\alpha\left(t,r\right)$ and $\beta\left(t,r\right)$, are contained in the original LTB line element (2.1) or, equivalently, $a\left(t,r\right)$ and $K^2\left(r\right)$ in GR, according to Eq. (2.7). Actually, $K^2\left(r\right)$ is not exactly a dynamical d.o.f. but an arbitrary parametric function, as a result of the LTB cosmological dynamics. To be more specific, we recall that, in Sect. 2.1.1, the 0-1 component (2.2a) of the Einstein field equations has allowed us to find a relation between the metric functions $\alpha\left(t,r\right)$ and $\beta\left(t,r\right)$ in GR, hence to reduce one d.o.f., and the LTB metric in GR assumes the form given in Eq. (2.7) in terms of $a\left(t,r\right)$ and $K^2\left(r\right)$.

Since the background FLRW and the perturbed LTB metrics are both locally rotationally symmetric and are given in the same normal geodesic frame, we only need to focus on scalar functions, as shown in [255, 256]. Hence, the scale factor $a\left(t,r\right)$ and the energy density of the matter component $\rho\left(t,r\right)$, contained in the field equations (2.9a) and (2.9b), are defined as:

$$a\left(t,r\right) = \bar{a}\left(t\right) + \delta a\left(t,r\right) \tag{6.5a}$$

$$\rho\left(t,r\right) = \bar{\rho}\left(t\right) + \delta\rho\left(t,r\right)\,. \tag{6.5b}$$

Note that the curvature function $K^2\left(r\right)$ in the LTB metric (2.7) involves radial inhomogeneities, so it can be regarded as a perturbative contribution. In other words, even if the background metric is flat ($\bar{k}=0$), it is possible to define a linear curvature pertubation, which is exactly given by the curvature function $K^2\left(r\right)$ in the LTB metric, according to the metric decomposition in Eq. (6.4). Thus, in addition to the metric perturbation δa, we have another perturbed quantity with respect to the background FLRW metric, which is $K^2\left(r\right)$.

We also require that background terms dominate over the linear perturbations

$$\delta a\left(t,r\right) \ll \bar{a}\left(t\right) \qquad\qquad \delta\rho\left(t,r\right) \ll \bar{\rho}\left(t\right) \tag{6.6}$$

at any time t, or redshift z, in the late Universe. This condition is dictated by the cosmological principle.

Once the decomposition has been defined in Eqs. (6.5a) and (6.5b), the evolution in time and space of the physical quantities can be obtained by studying the gravitational field equations (2.9a) and (2.9b) at background and linear levels. We recall that in GR the 0-1 component (2.2a) of the Einstein field equations allows us to find a relation between the metric functions $\alpha\left(t,r\right)$ and $\beta\left(t,r\right)$, hence the LTB metric assumes the form given in Eq. (2.7) in GR.

6.2.1 Background solution

If we consider only background terms, it is straightforward to show that Eq. (2.9a) turns into the standard Friedmann equation (1.23), which for a flat FLRW geometry (1.5) becomes

$$H^2(t) \equiv \left[\frac{\dot{\bar{a}}(t)}{\bar{a}(t)}\right]^2 = \frac{\chi\,\bar{\rho}(t)}{3} + \frac{\Lambda}{3}\,. \tag{6.7}$$

We have used the fact that $\bar{a}$ and $\bar{\rho}$ do not depend on the radial coordinate r.

Furthermore, the other Eq. (2.9b) can be rewritten at the background level as

$$2\,\frac{\ddot{\bar{a}}(t)}{\bar{a}(t)} + \left[\frac{\dot{\bar{a}}(t)}{\bar{a}(t)}\right]^2 = \Lambda\,, \tag{6.8}$$

which combined with Eq. (6.7), provides the second Friedmann equation (1.24) in a flat FLRW geometry:

$$\frac{\ddot{\bar{a}}(t)}{\bar{a}(t)} = -\frac{\chi\,\bar{\rho}}{6} + \frac{\Lambda}{3}\,. \tag{6.9}$$

We define a dimensionless time variable

$$\tau = \frac{t}{t_0}\,, \tag{6.10}$$

in which t_0 is the present cosmic time in the synchronous gauge (today $\tau = 1$). Note that τ is the cosmic time in units of the present Hubble time since t_0 can be approximately written in terms of the Hubble constant as $t_0 \approx 1/H_0$.

Then, we rewrite the Friedmann equation (6.7) as

$$\left[\frac{1}{\bar{a}(\tau)}\,\frac{d\bar{a}(\tau)}{d\tau}\right]^2 = \frac{\Omega_{m0}}{\bar{a}^3(\tau)} + \Omega_{\Lambda 0}\,, \tag{6.11}$$

and the second Friedmann equation (6.9) in terms of τ

$$\frac{1}{\bar{a}(\tau)}\,\frac{d^2\bar{a}(\tau)}{d\tau^2} = -\frac{\Omega_{m0}}{2\,\bar{a}^3(\tau)} + \Omega_{\Lambda 0}\,. \tag{6.12}$$

We have used Eq. (1.26), the chain rule $\frac{d}{dt} = \frac{1}{t_0}\frac{d}{d\tau} \approx H_0\,\frac{d}{d\tau}$, and the usual relations for the cosmological density parameters Ω_{m0} and $\Omega_{\Lambda 0}$.

The Friedmann equation (6.11) admits an analytical solution in the late Universe, that is the background scale factor in terms of τ:

$$\bar{a}(\tau) = \left(\frac{\Omega_{m0}}{\Omega_{\Lambda 0}}\right)^{1/3} \left\{\sinh\left[\frac{3}{2}\sqrt{\Omega_{\Lambda 0}}\;(\tau - 1) + \operatorname{arcsinh}\left(\sqrt{\frac{\Omega_{\Lambda 0}}{\Omega_{m0}}}\right)\right]\right\}^{2/3}\,. \tag{6.13}$$

Note also from Eq. (6.13) that the deceleration parameter $\bar{q}(\tau) \equiv -\ddot{\bar{a}}\,\bar{a}^{-1}\,H^{-2} \to -1$ for $\tau \to +\infty$, as it should be in a dark energy fully dominated Universe. We here stress that the solution (6.13) applies only in the late Universe, otherwise we need to solve numerically the field equations, if we also consider the radiation contribution. Nevertheless, we are interested in the evolution of local inhomogeneities at late times.

It should be noted that in the limit

$$\underset{\Omega_\Lambda \to 0}{lim}\quad \bar{a}(\tau) \sim (\tau - 1)^{2/3}\,, \tag{6.14}$$

we recover the well-known relation (1.29) for the background scale factor $\bar{a}$ satisfied in the matter-dominated Universe.

Concerning the evolution of the background energy density $\bar{\rho}$, we start from the continuity equation (2.11) in the LTB metric. We verify that this equation at the zeroth order becomes simply

$$\dot{\bar{\rho}} + 3\,H\,\bar{\rho} = 0\,, \tag{6.15}$$

which admits the well-known background solution (1.26) for the matter component.

Finally, we focus on the relation between the redshift z and the dimensionless parameter τ, defined in Eq. (6.10), to understand to what extent of τ values the background solution (6.13) can be applied in the late Universe. To be more accurate in this computation, we also include the radiation contribution to write τ as

$$\tau\,(z) = 1 + \int_1^{1/1+z} \frac{dx}{x\,\sqrt{\Omega_{m0}\,x^{-3} + \Omega_{r0}\,x^{-4} + \Omega_{\Lambda 0}}}\,, \tag{6.16}$$

where we have adopted the same approach of Sect. 1.1.4 and we have used the definition of τ (6.10). The quantity $\tau\,(z)$ can be computed numerically for a given redshift z, after specifying the cosmological parameters: $\Omega_{m0} = 0.3111$, $\Omega_{\Lambda 0} = 0.6889$, and $\Omega_{r0} = 9.138 \cdot 10^{-5}$ from Table 2 (last column) in [40]. For instance, we can compute: $\tau\,(z_{\rm eq}) = 0.046$ at the redshift of the matter-radiation equality $z_{\rm eq} = 3403.5$; $\tau\,(z_{\rm DE}) = 0.75$ at the matter-dark energy equality $z_{\rm DE} = 0.303$; $\tau\,(z_{\rm 100eq}) = 0.052$ when the energy density of the matter component was one hundred times more than the radiation contribution at $z_{\rm 100eq} = 33.045$. In particular, considering this latter value of τ, you can see in Fig. 6.1 the behavior of the background scale factor $\bar{a}\,(\tau)$ and the deceleration parameter $\bar{q}\,(\tau)$ in the range $\tau_{\rm 100eq} < \tau < 5$, when relativistic species are negligible.

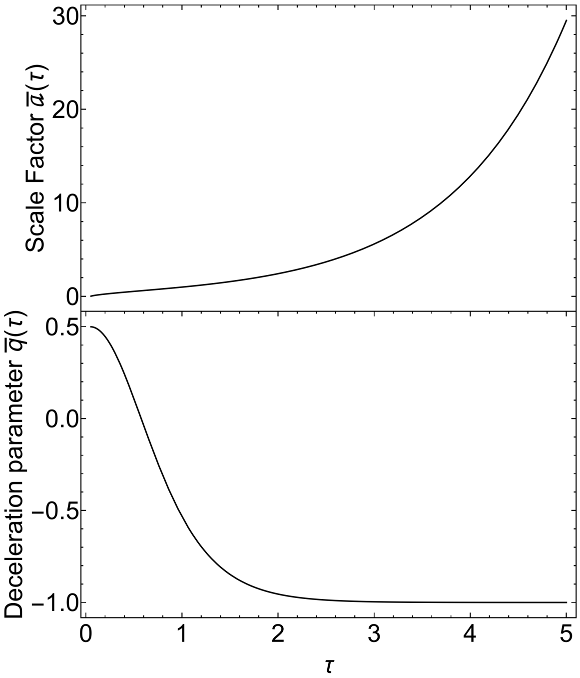

Figure 6.1: Evolution of the background scale factor $\bar{a}\,(\tau)$ (top panel) and the respective deceleration parameter $\bar{q}\,(\tau)$ (bottom panel) in terms of the time dimensionless parameter τ, defined in Eq. (6.10), for a flat ΛCDM model in the range $\tau_{\rm 100eq} < \tau < 5$, according to the solution given in Eq. (6.13). These panels are plotted in [TS 4].

6.2.2 Linearly perturbed solutions in an inhomogeneous Universe

We analyze the impact of local inhomogeneities in the cosmological dynamics. The linearized field equations allow us to investigate the evolution of spherically symmetric perturbations.

If we include local inhomogeneities in the first-order perturbation theory, the Eqs. (2.9a) and (2.9b) become

$$\begin{aligned}\left[\bar{a}^2\,(\chi\,\bar{\rho}+\Lambda)-\dot{\bar{a}}^2\right]\,(3\,\delta a+r\,\delta a')+\chi\,\delta\rho\,\bar{a}^3 &= \\ 2\,\bar{a}\,\dot{\bar{a}}\,(3\,\delta\dot{a}+r\,\delta\dot{a}')+3\,\bar{a}\,K^2+2\,\bar{a}\,r\,K\,K'\,, &\qquad (6.17\text{a})\\ \delta\ddot{a}+\frac{\dot{\bar{a}}}{\bar{a}}\,\delta\dot{a}-\left(\frac{\ddot{\bar{a}}}{\bar{a}}+\frac{\dot{\bar{a}}^2}{\bar{a}^2}\right)\,\delta a+\frac{K^2}{2\,\bar{a}}=0\,, &\qquad (6.17\text{b})\end{aligned}$$

respectively.

Furthermore, we rewrite the continuity equation (2.11) at linear order:

$$\delta\dot{\rho}+3\,\frac{\dot{\bar{a}}}{\bar{a}}\,\delta\rho+\frac{\bar{\rho}}{\bar{a}^2}\,\left[\bar{a}\,(3\,\delta\dot{a}+r\,\delta\dot{a}')-\dot{\bar{a}}\,(3\,\delta a+r\,\delta a')\right]=0\,. \qquad (6.18)$$

To study separately the evolution of local inhomogeneities in time and space, we adopt the separation of variables method to solve analytically the first-order perturbation equations. Hence, we define time and radial functions for all linear perturbations:

$$\delta a\,(t,r)\equiv \mathrm{a}_p\,(t)\;\mathfrak{a}_p\,(r) \qquad\qquad \delta\rho\,(t,r)\equiv R_p\,(t)\;\varrho_p\,(r)\;. \qquad (6.19)$$

The quantities $\mathrm{a}_p\,(t)$ and $\mathfrak{a}_p\,(r)$ are both dimensionless. We assume, without loss of generality, that $R_p\,(t)$ has the physical dimensions of an energy density as $\bar{\rho}$ and $\delta\rho$, while we treat $\varrho_p\,(r)$ like a dimensionless quantity. We also recall that the curvature perturbation $K^2\,(r)$ in the LTB metric depends only on the radial coordinate.

We stress that if we would also include non-linear terms, then the separation of variables could not lead to a general solution. However, the linearization procedure adopted for the dynamics allows us to use a separation of variables characterized by the factorization (6.19) of the time and space dependences in the linear perturbation theory.

Using the factorization (6.19), Eq. (6.17b) can be split into two parts. By setting the radial dependence as

$$K^2\,(r)=\mathfrak{a}_p\,(r)\;, \qquad (6.20)$$

we obtain an ordinary differential equation for the time evolution:

$$\ddot{\mathrm{a}}_p+\frac{\dot{\bar{a}}}{\bar{a}}\,\dot{\mathrm{a}}_p-\left[\frac{\ddot{\bar{a}}}{\bar{a}}+\left(\frac{\dot{\bar{a}}}{\bar{a}}\right)^2\right]\,\mathrm{a}_p=0\,, \qquad (6.21)$$

in which we have also considered that $\bar{a}\ll\mathrm{a}_p$. We would emphasize that the assumption given in Eq. (6.20) is suggested by the form of Eq. (6.17b), once we used the separation of variables from Eq. (6.19). Nevertheless, we have still two metric perturbations given by the quantities $\mathrm{a}_p\,(t)$ and $\mathfrak{a}_p\,(r)$.

Then, we proceed similarly for the first-order perturbation continuity equation (6.18). After straightforward calculations, by using again the factorization (6.19) in Eq. (6.18), we separate terms that depend only on t from those related to r. In particular, the time evolution is provided by

$$\dot{R}_p+3\,\frac{\dot{\bar{a}}}{\bar{a}}\,R_p=X\,\frac{\bar{\rho}}{\bar{a}}\,\left(\frac{\dot{\bar{a}}}{\bar{a}}\,\mathrm{a}_p-\dot{\mathrm{a}}_p\right)\;, \qquad (6.22)$$

while we obtain the following radial dependence

$$\varrho_p = \frac{1}{X}\left(3\,\mathfrak{a}_p + r\,\mathfrak{a}_p'\right)\,. \tag{6.23}$$

The constant X is introduced by the separation of variables method. We recall that the background solutions for $\bar{a}$ and $\bar{\rho}$ are provided by Eqs. (6.13) and (1.26), respectively.

We rewrite the first-order perturbation Eq. (6.17a), by employing Eq. (6.19) and dividing both sides of the equation by $\bar{a}^2\,\mathrm{a}_p\,\mathfrak{a}_p$, as

$$\left[\chi\,\bar{\rho} + \Lambda - \left(\frac{\dot{\bar{a}}}{\bar{a}}\right)^2 - 2\,\frac{\dot{\bar{a}}}{\bar{a}}\,\frac{\dot{\mathrm{a}}_p}{\mathrm{a}_p}\right]\left(3 + r\,\frac{\mathfrak{a}_p'}{\mathfrak{a}_p}\right) = \frac{3}{\bar{a}\,\mathrm{a}_p}\,\frac{K^2}{\mathfrak{a}_p} + \frac{2}{\bar{a}\,\mathrm{a}_p}\,\frac{r\,K\,K'}{\mathfrak{a}_p} - \chi\,\bar{a}\,\frac{R_p}{\mathrm{a}_p}\,\frac{\varrho_p}{\mathfrak{a}_p}\,. \tag{6.24}$$

We observe the presence of several mixed terms depending both on t and r. However, we can reduce the number of these mixed terms, by using Eqs. (6.20), (6.23), and (6.7), to rewrite Eq. (6.24) as

$$\left[2\,\frac{\dot{\bar{a}}}{\bar{a}}\left(\frac{\dot{\bar{a}}}{\bar{a}}\,\mathrm{a}_p - \dot{\mathrm{a}}_p\right) + \frac{\chi}{X}\,\bar{a}\,R_p\right]\frac{\varrho_p}{\mathfrak{a}_p} = 0\,. \tag{6.25}$$

Since we want to avoid trivial solutions, we should have $\varrho_p \neq 0$ and $\mathfrak{a}_p \neq 0$. Then, we obtain a single ordinary differential equation in the time domain:

$$2\,\frac{\dot{\bar{a}}}{\bar{a}}\left(\frac{\dot{\bar{a}}}{\bar{a}}\,\mathrm{a}_p - \dot{\mathrm{a}}_p\right) + \frac{\chi}{X}\,\bar{a}\,R_p = 0\,. \tag{6.26}$$

It is straightforward to check the compatibility between Eqs. (6.21), (6.22), and (6.26). Indeed, by combining the time derivative of Eq. (6.26) with Eq. (6.22), the background field equations (6.7), and (6.9), it is easy to build exactly Eq. (6.21).

Then, we rewrite the term in the brackets on the right-hand side of Eq. (6.22) by using Eq. (6.26), and we get an ordinary differential equation with a single variable $R_p\,(t)$, that is

$$\dot{R}_p + \left(3\,\frac{\dot{\bar{a}}}{\bar{a}} + \frac{\chi\,\bar{\rho}}{2}\,\frac{\bar{a}}{\dot{\bar{a}}}\right)R_p = 0\,. \tag{6.27}$$

Therefore, focusing on the time domain, we can obtain numerical solutions for the unknown quantities a_p and R_p from the linearized equations (6.21) and (6.27). In particular, Eq. (6.21) shows exactly the same behavior in terms of t and τ, as it can be checked by using the definition of τ (6.10) and replacing $\frac{d}{dt} \approx H_0\,\frac{d}{d\tau}$. Recalling the expression (6.13) of the background scale factor in GR, Eq. (6.21) can be solved numerically. We set the initial conditions at $\tau = 1$ today: $\mathrm{a}_p\,(1) = 10^{-5}$ and $\dot{\mathrm{a}}_p\,(1) = 0$. Moreover, we fixed the same values for Ω_{m0} and $\Omega_{\Lambda 0}$ adopted in Sect. 6.2.1. In the upper panel of Fig. 6.2, you can see the numerical results for $1 \leq \tau \leq 5$. Note that the perturbed scale factor a_p increases as τ grows, and this fact may be a problem if perturbations become unstable. However, the evolution of a_p is dominated by the background term $\bar{a}$ at any time τ. Indeed, the ratio[1] between the perturbation and background terms with $\eta\,(\tau) \equiv |\mathrm{a}_p/\bar{a}| \ll 1$ for any τ, as it is shown in the middle panel of Fig. 6.2. In other words, perturbations of the scale factor due to local inhomogeneities will remain small over time.

Concerning the time evolution of the perturbed energy density of the matter component R_p, we rewrite

---

[1] In this chapter, $\eta\,(\tau)$ is defined as the ratio between the linear perturbation and bckground scale factor, it is not the conformal time.

Eq. (6.27) in terms of τ as

$$\frac{dO_p}{d\tau}+3\left[\frac{1}{\bar{a}}\frac{d\bar{a}}{d\tau}+\frac{\Omega_{m0}}{2\,\bar{a}^2}\left(\frac{d\bar{a}}{d\tau}\right)^{-1}\right]O_p=0\,, \tag{6.28}$$

in which we have defined the dimensionless quantity $O_p \equiv R_p/\bar{\rho}_{c0}$, and we have used Eq. (1.26). We solve numerically Eq. (6.28) with the initial condition $O_p\left(1\right)=10^{-5}$ for $\tau=1$. The results are shown in the bottom panel of Fig. 6.2. Note that $O_p\left(\tau\right)\ll 1$ for $1\leq\tau\leq 5$.

Finally, after obtaining numerical solutions for the time domain, we focus on the radial part of perturbations. We recall that $K^2\left(r\right)=\mathfrak{a}_p\left(r\right)$ from Eq. (6.20). Moreover, we assume for simplicity a proportionality between radial perturbations, i.e. $\varrho_p = C\,\mathfrak{a}_p$ with a constant C. Then, we solve the ordinary differential equation (6.23) in r, and we obtain a power-law behavior for the radial correction of the perturbed scale factor in GR:

$$\mathfrak{a}_p\left(r\right)\propto r^{-y}\,, \tag{6.29}$$

for which $y\equiv 3-C\,X$. More in detail, we need to impose the condition $y>0$ to ensure that inhomogeneities decay on large scales, according to the cosmological principle.

6.3 Perturbation approach for the Lemaître-Tolman-Bondi model in the Jordan Frame of $f\left(R\right)$ gravity

In this section, we compare and discuss the evolution of inhomogeneous perturbations in GR and in the Jordan frame of $f\left(R\right)$ gravity, considering again a cosmological dust ($p=0$) in the LTB geometry. A complete general solution in linear perturbation theory within the metric $f\left(R\right)$ gravity was developed in [101, 102, 257]. Instead of proceeding with a fourth-order cosmological dynamics, here we work in the equivalent Jordan frame $f\left(R\right)$ gravity. Furthermore, as a particular case, we focus on spherically symmetric perturbations, following the same perturbation approach developed in Sect. 6.2 by using the metric decomposition in Eq. (6.4). Hence, we split the metric functions α and β, the energy density ρ, and the scalar field ϕ into background terms plus linear corrections as

$$\begin{aligned}&\alpha\left(t,r\right)=\bar{\alpha}\left(t\right)+\delta\alpha\left(t,r\right)\,,\quad \beta\left(t,r\right)=\bar{\beta}\left(t,r\right)+\delta\beta\left(t,r\right)\\&\rho\left(t,r\right)=\bar{\rho}\left(t\right)+\delta\rho\left(t,r\right)\,,\quad \phi\left(t,r\right)=\bar{\phi}\left(t\right)+\delta\phi\left(t,r\right)\,.\end{aligned} \tag{6.30}$$

We also require again that inhomogeneities are much smaller than respective background terms.

It should be stressed that, in the Jordan frame, we can not use the LTB metric in the simpler form (2.7), but we refer to the original LTB line element (2.1). Thus, the two degrees of freedom of the perturbed metric are given by $\alpha\left(t,r\right)$ and $\beta\left(t,r\right)$; we no longer refer to $a\left(t,r\right)$ and $K^2\left(r\right)$, as in the GR scenario.

Note that the background quantities $\bar{\alpha}$ and $\bar{\beta}$ are related to the scale factor $\bar{a}$, since we want to reproduce a flat FLRW geometry at the zeroth-order perturbation. Then, comparing a flat FLRW metric with the LTB line element in the form given by Eq. (2.1), it is straightforward to show that

$$\bar{\alpha}\left(t\right)=\ln\left(\bar{a}\left(t\right)\right)\,, \tag{6.31a}$$

$$\bar{\beta}\left(t,r\right)=\ln\left(\bar{a}\left(t\right)\,r\right)\,. \tag{6.31b}$$

In particular, note that $\dot{\bar{\alpha}}=H=\dot{\bar{\beta}}$, and also $\bar{\beta}'=1/r$.

As a consequence, the metric tensor component g_{rr} in the LTB metric can be approximated for

$\delta\alpha \ll 1/2$ as

$$g_{rr} = e^{2\alpha} = e^{2(\bar{\alpha}+\delta\alpha)} \approx \bar{a}^2\,(t)\,\left(1 + 2\,\delta\alpha\right)\,, \tag{6.32}$$

in which it is possible to recognize the respective metric tensor component g_{rr} in a flat FLRW metric as background term. We can follow the same reasoning for the other metric tensor components involving β with the assumption $\delta\beta \ll 1/2$.

Also, we need to expand the scalar field potential $V\,(\phi)$, defined in Eq. (1.111), which appears in the field equations (6.1b), (6.1c), (6.2) in the Jordan frame of $f\,(R)$ gravity. Therefore, including local inhomogeneities, we obtain

$$V\left[\phi\,(t,r)\right] = V\left[\bar{\phi}\,(t) + \delta\phi\,(t,r)\right] \approx V\left[\bar{\phi}\,(t)\right] + \left.\frac{dV}{d\phi}\right|_{\phi=\bar{\phi}} \delta\phi\,(t,r) + O\left(\delta\phi^2\right) \tag{6.33}$$

for the first-order perturbation theory. Similarly, we rewrite the derivative of $V\,(\phi)$ as

$$\begin{aligned}\frac{dV}{d\phi}\left[\phi\,(t,r)\right] = \frac{dV}{d\phi}\left[\bar{\phi}\,(t) + \delta\phi\,(t,r)\right] \approx \\ \approx \left.\frac{dV}{d\phi}\right|_{\phi=\bar{\phi}} + \left.\frac{d^2V}{d\phi^2}\right|_{\phi=\bar{\phi}} \delta\phi\,(t,r) + O\left(\delta\phi^2\right)\,.\end{aligned} \tag{6.34}$$

As we have proceeded to study the gravitational field equations in GR in Sect. 6.2 to find background and linear solutions, now we analyze the dynamics of $f\,(R)$ gravity in the Jordan frame, provided by the field equations (6.1), and (6.2) in the LTB metric. It should be stressed that, in the Jordan frame, we can not use the LTB metric in the simpler form (2.7), but we refer to the original LTB line element (2.1).

6.3.1 Background solution

If we consider all background quantities, we do not include spherically symmetric perturbations and Eqs. (6.1b), (6.1c), and (6.2) provide field equations in the Jordan frame of $f\,(R)$ gravity in a flat FLRW geometry: Eqs. (1.117a), (1.117b), and (1.117c). Note that Eq. (6.1a) vanishes at the background level in the synchronous gauge, and it becomes a trivial identity.

Then, we focus on the $f\,(R)$ HS model in the Jordan frame, which has been introduced in Sect. Sect. 1.3.2. Recalling the form of the scalar field potential $V\left(\bar{\phi}\right)$ in Eq. (1.124), we observe that the field equations (1.117) do not admit any analytical solutions, and we have to solve it numerically. In this regard, we rewrite the full set of equations (1.117) in terms of the dimensionless parameter τ, defined in Eq. (6.10), and we obtain, respectively:

$$\left[\frac{1}{\bar{a}\,(\tau)}\,\frac{d\bar{a}\,(\tau)}{d\tau}\right]^2 = \frac{\Omega_{m0}}{\bar{\phi}\,(\tau)\;\bar{a}^3\,(\tau)} + \frac{\Omega_{m0}}{6\,\bar{\phi}\,(\tau)}\,\frac{V\left(\bar{\phi}\right)}{m^2} - \frac{1}{\bar{a}\,(\tau)\;\bar{\phi}\,(\tau)}\,\frac{d\bar{a}\,(\tau)}{d\tau}\,\frac{d\bar{\phi}\,(\tau)}{d\tau}\,, \tag{6.35a}$$

$$\begin{aligned}\frac{1}{\bar{a}\,(\tau)}\,\frac{d^2\bar{a}\,(\tau)}{d\tau^2} &= -\frac{\Omega_{m0}}{\bar{\phi}\,(\tau)\;\bar{a}^3\,(\tau)} - \frac{\Omega_{m0}}{6\,\bar{\phi}\,(\tau)}\,\frac{V\left(\bar{\phi}\right)}{m^2} + \frac{1}{6}\,\frac{\Omega_{m0}}{m^2}\,\frac{dV\left(\bar{\phi}\right)}{d\bar{\phi}} + \\ &\quad + \frac{1}{\bar{a}\,(\tau)\;\bar{\phi}\,(\tau)}\,\frac{d\bar{a}\,(\tau)}{d\tau}\,\frac{d\bar{\phi}\,(\tau)}{d\tau}\,,\end{aligned} \tag{6.35b}$$

$$\frac{3}{\bar{\phi}\,(\tau)}\,\frac{d^2\bar{\phi}\,(\tau)}{d\tau^2} - 2\,\frac{\Omega_{m0}}{\bar{\phi}\,(\tau)}\,\frac{V\left(\bar{\phi}\right)}{m^2} + \frac{\Omega_{m0}}{m^2}\,\frac{dV\left(\bar{\phi}\right)}{d\bar{\phi}} + \frac{9}{\bar{a}\,(\tau)\;\bar{\phi}\,(\tau)}\,\frac{d\bar{a}\,(\tau)}{d\tau}\,\frac{d\bar{\phi}\,(\tau)}{d\tau} = \frac{3\,\Omega_{m0}}{\bar{\phi}\,(\tau)\;\bar{a}^3\,(\tau)}\,. \tag{6.35c}$$

We used the usual relation for the cosmological density parameter Ω_{m0}, and we recall that $m^2 = \chi\,\bar{\rho}_{m0}/3$. In particular, Eqs. (6.35a) and (6.35c) allow us to obtain numerical solutions for $\bar{a}\,(\tau)$ and $\bar{\phi}\,(\tau)$, while Eq. (6.35b) is useful to estimate numerically the deceleration parameter $\bar{q}\,(\tau)$.

We choose the parameters of the model in such a way that the background modified gravity scenario is almost equivalent to the ΛCDM cosmological model with the aim of focusing later on the differences between the linear perturbation solutions in the two models. More precisely, we fix $\Omega_{m0} = 0.3111$, the same value adopted in Sect. 6.2.1, and we set the value $|F_{R0}| = 1.0 \cdot 10^{-7}$ at the present cosmic time (redshift $z = 0$ or $\tau = 1$), which provides information about the deviation from the GR scenario, according to Eq. (1.123). As a consequence, we constrain the HS dimensionless parameters: $c_1 = 2.0 \cdot 10^6$ and $c_2 = 1.5 \cdot 10^5$, as developed in Sect. 1.3.2. We recall that the profile of the background quantity $V\left(\bar{\phi}\right)/m^2$ is plotted in Fig. 1.3.

To guarantee a nearly frozen evolution of the scalar field $\bar{\phi}$ for increasing τ, we impose the following condition: $\frac{d\bar{\phi}}{d\tau}\left(\tau = 1\right) = 0$. Finally, we solve numerically Eqs. (6.35a) and (6.35c) for $0.2 < \tau < 5$, when the relativistic components remain negligible as compared with the matter, to obtain the evolution of $\bar{a}\left(\tau\right)$ and $\bar{\phi}\left(\tau\right)$. The numerical results are shown in Fig. 6.3. By comparing it with Fig. 6.3, it should be emphasized that $\bar{a}\left(\tau\right)$ and $\bar{q}\left(\tau\right)$ exhibit almost the same behavior in GR and in Jordan frame of $f\left(R\right)$ gravity, as desired according to the choice of model parameters abovementioned. In particular, in the bottom panel of Fig. 6.3, we plot the quantity $\left|1 - \bar{\phi}\left(\tau\right)\right|$ to evaluate the deviation from GR ($\bar{\phi} = 1$): we observe more relevant deviations in the late Universe for $\tau > 1$, but nevertheless the background modified gravity dynamics still remains almost undistinguishable from the ΛCDM scenario. Hence, we can shift the attention towards the first-order perturbation solutions in the Jordan frame of $f\left(R\right)$ gravity.

6.3.2 Linearly perturbed solutions in an inhomogeneous Universe

We focus on the first-order perturbed equations to study the evolution of spherically symmetric perturbations. Considering the split between background terms and linear perturbations according to Eq. (6.30), the set of field equations (6.1) becomes

$$\delta\dot{\beta}' = \frac{1}{r}\left(\delta\dot{\alpha} - \delta\dot{\beta}\right) - \frac{1}{2\,\bar{\phi}}\left(\delta\dot{\phi}' - \frac{\dot{\bar{a}}}{\bar{a}}\,\delta\phi'\right)\,, \tag{6.36a}$$

$$\begin{aligned}&\frac{2}{\bar{a}^2}\left[\frac{1}{r^2}\left(\delta\alpha - \delta\beta\right) - \delta\beta'' - \frac{3}{r}\,\delta\beta' + \frac{1}{r}\,\delta\alpha'\right] + \\ &\quad + \left(2\,\frac{\dot{\bar{a}}}{\bar{a}} + \frac{\dot{\bar{\phi}}}{\bar{\phi}}\right)\left(\delta\dot{\alpha} + 2\,\delta\dot{\beta}\right) = \frac{\chi}{\bar{\phi}}\,\delta\rho - 3\,\frac{\dot{\bar{a}}}{\bar{a}}\,\frac{\delta\dot{\phi}}{\bar{\phi}} + \\ &\quad + \left(\frac{1}{2}\,\frac{dV}{d\phi}\bigg|_{\phi=\bar{\phi}} - \frac{1}{2}\,\frac{V\left(\bar{\phi}\right)}{\bar{\phi}} - \frac{\chi\,\bar{\rho}}{\bar{\phi}} + 3\,\frac{\dot{\bar{a}}}{\bar{a}}\,\frac{\dot{\bar{\phi}}}{\bar{\phi}}\right)\frac{\delta\phi}{\bar{\phi}} + \frac{1}{\bar{a}^2\,\bar{\phi}}\left(\delta\phi'' + \frac{2}{r}\,\delta\phi'\right)\,,\end{aligned} \tag{6.36b}$$

$$\begin{aligned}&\delta\ddot{\beta} + 3\,\frac{\dot{\bar{a}}}{\bar{a}}\,\delta\dot{\beta} + \frac{1}{\bar{a}^2\,r^2}\left(\delta\alpha - \delta\beta - r\,\delta\beta'\right) = \\ &\quad \left(\frac{1}{2}\,\frac{dV}{d\phi}\bigg|_{\phi=\bar{\phi}} - \frac{1}{2}\,\frac{V\left(\bar{\phi}\right)}{\bar{\phi}} + \frac{\ddot{\bar{\phi}}}{\bar{\phi}} + 2\,\frac{\dot{\bar{a}}}{\bar{a}}\,\frac{\dot{\bar{\phi}}}{\bar{\phi}}\right)\frac{\delta\phi}{2\,\bar{\phi}} + \\ &\quad - \frac{1}{2\,\bar{\phi}}\left(\delta\ddot{\phi} + 2\,\frac{\dot{\bar{a}}}{\bar{a}}\,\delta\dot{\phi} + 2\,\dot{\bar{\phi}}\,\delta\dot{\beta} - \frac{2}{\bar{a}^2\,r}\,\delta\phi'\right)\,.\end{aligned} \tag{6.36c}$$

Similarly, starting from Eq. (6.2), the linearized scalar field equation is given by

$$\begin{aligned}&\delta\ddot{\phi} + 3\,\frac{\dot{\bar{a}}}{\bar{a}}\,\delta\dot{\phi} + \left(\delta\dot{\alpha} + 2\,\delta\dot{\beta}\right)\dot{\bar{\phi}} - \frac{1}{\bar{a}^2}\left(\delta\phi'' + \frac{2}{r}\,\delta\phi'\right) + \\ &\quad + \frac{1}{3}\left(\bar{\phi}\,\frac{d^2V}{d\phi^2}\bigg|_{\phi=\bar{\phi}} - \frac{dV}{d\phi}\bigg|_{\phi=\bar{\phi}}\right)\delta\phi = \frac{1}{3}\,\chi\,\delta\rho\,.\end{aligned} \tag{6.37}$$

Moreover, the continuity equation (2.10) rewrites as

$$\delta\dot{\rho} + 3\,\frac{\dot{\bar{a}}}{\bar{a}}\,\delta\rho + \left(\delta\dot{\alpha} + 2\,\delta\dot{\beta}\right)\,\bar{\rho} = 0 \tag{6.38}$$

at the linear perturbation order. We have used Eq. (6.31) to rewrite $\bar{\alpha}$ and $\bar{\beta}$ in terms of $\bar{a}$.

Following the same approach we adopted in GR in Sect. 6.2, we use a separation of variables method to study separately the evolution of inhomogeneities in time and space. Hence, we factorize the linear perturbations as:

$$\begin{aligned} \delta\alpha\,(t,r) &\equiv A_p\,(t)\;\mathcal{A}_p\,(r)\ , \qquad & \delta\beta\,(t,r) &\equiv B_p\,(t)\;\mathcal{B}_p\,(r)\ , \\ \delta\rho\,(t,r) &\equiv P_p\,(t)\;\varrho_p\,(r)\ , \qquad & \delta\phi\,(t,r) &\equiv \Phi_p\,(t)\;\varphi_p\,(r)\ . \end{aligned} \tag{6.39}$$

Assuming this factorization, we can rewrite Eqs. (6.36), (6.37), and (6.38). However, we notice the presence of several mixed terms depending both on t and r, which do not allow us to solve the equations using the separation of variables in a standard way, unless we rely on reasonable and simplifying assumptions (further details on explicit calculations are in the Appendix on page 133). For instance, we are able to use the separation of variables method for all field equations, if we require the two following conditions:

$$A_p = \lambda_1\,B_p\,, \tag{6.40a}$$

$$\varrho_p = \lambda_2\,\varphi_p\,, \tag{6.40b}$$

where λ_1 and λ_2 are two proportionality constants. These conditions allow us to simplify the equation system and easily separate time and radial dependences: we obtain a set of differential equations describing the radial profiles of perturbations and another equation system concerning only the time evolution.

Hence, starting from Eqs. (6.36), (6.37), and (6.38), after long but straightforward calculations (see the Appendix on page 133), we obtain a set of equations for the radial part:

$$\mathcal{A}_p = \frac{1}{\lambda_1}\,\left[\mathcal{B}_p + r\,\left(\mathcal{B}_p' + \mu_1\,\varphi_p'\right)\right]\ , \tag{6.41a}$$

$$\mathcal{B}_p = \frac{2}{\mu_4\,r}\,\varphi_p' - \mu_1\,\varphi_p\,, \tag{6.41b}$$

$$\varphi_p'' + \frac{2}{r}\,\varphi_p' - \mu_3^2\,\varphi_p = 0\,, \tag{6.41c}$$

$$\varrho_p = \frac{1}{\mu_2}\,\left(\lambda_1\,\mathcal{A}_p + 2\,\mathcal{B}_p\right)\ , \tag{6.41d}$$

where μ_1, μ_2, μ_3, and μ_4 are constants arising from the separation of variables. We have four unknown quantities ($\mathcal{A}_p$, $\mathcal{B}_p$, ϱ_p, and φ_p), which are related through the condition given by Eq. (6.40b), the perturbed 0-1 component of field equations (6.41a), the perturbed 1-1 component (6.41b), the linearized scalar field equation (6.41c), and in addition the perturbed continuity equation (6.41d). In particular, note that μ_3 has dimensions of reciprocal length, i.e. $[\mu_3] = L^{-1}$, as you can see from Eq. (6.41c).

Similarly, in the Appendix on page 133, we write an equation system for the time evolution of perturbations:

$$\dot{B}_p = \frac{1}{2\,\bar{\phi}\,\mu_1}\,\left(\dot{\Phi}_p - \frac{\dot{\bar{a}}}{\bar{a}}\,\Phi_p\right)\ , \tag{6.42a}$$

$$\frac{\mu_2\,\lambda_2}{2\,\mu_1}\,\left(2\frac{\dot{\bar{a}}}{\bar{a}} + \frac{\dot{\bar{\phi}}}{\bar{\phi}}\right)\left(\frac{\dot{\Phi}_p}{\Phi_p} - \frac{\dot{\bar{a}}}{\bar{a}}\right) + \frac{\chi\,\bar{\rho}}{\bar{\phi}} - \frac{1}{2}\,\frac{dV}{d\phi}\bigg|_{\phi=\bar{\phi}} + \frac{V\left(\bar{\phi}\right)}{2\,\bar{\phi}}$$

$$+\,3\frac{\dot{\bar{a}}}{\bar{a}}\left(\frac{\dot{\Phi}_p}{\Phi_p}-\frac{\dot{\bar{\phi}}}{\bar{\phi}}\right)-\chi\lambda_2\frac{P_p}{\Phi_p}+2\mu_1\mu_3^2\frac{\bar{\phi}\,B_p}{\bar{a}^2\,\Phi_p}=\frac{\mu_3^2}{\bar{a}^2}\,, \tag{6.42b}$$

$$\ddot{B}_p+\dot{B}_p\left(3\,\frac{\dot{\bar{a}}}{\bar{a}}+\frac{\dot{\bar{\phi}}}{\bar{\phi}}\right)=\frac{\mu_4}{2\,\bar{a}^2}\left(\frac{\Phi_p}{\bar{\phi}}-\mu_1\,B_p\right)\,, \tag{6.42c}$$

$$\frac{\ddot{\Phi}_p}{\Phi_p}+3\,\frac{\dot{\bar{a}}}{\bar{a}}\,\frac{\dot{\Phi}_p}{\Phi_p}-\frac{1}{3}\,\left.\frac{dV}{d\phi}\right|_{\phi=\bar{\phi}}+\frac{1}{3}\,\bar{\phi}\,\left.\frac{d^2V}{d\phi^2}\right|_{\phi=\bar{\phi}}+$$

$$+\,\mu_2\,\lambda_2\,\dot{\bar{\phi}}\,\frac{\dot{B}_p}{\Phi_p}-\frac{\chi\,\lambda_2}{3}\,\frac{P_p}{\Phi_p}=\frac{\mu_3^2}{\bar{a}^2}\,, \tag{6.42d}$$

$$\dot{P}_p+3\,\frac{\dot{\bar{a}}}{\bar{a}}\,P_p+\mu_2\,\bar{\rho}\,\dot{B}_p=0\,. \tag{6.42e}$$

We have four unknown quantities (A_p, B_p, P_p, and Φ_p) for the time evolution of inhomogeneities, which are fully described by the assumption (6.40a), the perturbed 0-1, 0-0, 1-1 components of field equations given by Eqs. (6.42a), (6.42b), (6.42c), respectively, the linearized scalar field equation (6.42d), and the perturbed continuity equation (6.42e). Note that two equations of the latter list are redundant since the scalar field and continuity equations are not independent of the other field equations.

It should be stressed that the potential $V\,(\phi)$ affects only the time evolution. As a consequence, since the scalar field potential is related to a specific modified $f\,(R)$ model, the time evolution strongly depends on the particular modified gravity model considered, while the radial part of the linearized equations is completely model free. This is a crucial point to identify a peculiar feature of the inhomogeneities evolution in the Jordan frame of $f\,(R)$ gravity through analysis of the radial profiles of perturbations.

Once we have split all field equations in time and radial contributions, we seek linear order solutions separately.

6.3.2.1 Radial profiles

If we focus on the radial evolution of perturbations, we can solve the respective equation system analytically. More specifically, in solving the differential equation (6.41c), we obtain the Yukawa behavior for the radial solution of the linearly perturbed scalar field:

$$\varphi_p\,(r)=\frac{\gamma}{r}\,e^{-\mu_3\,r}\,. \tag{6.43}$$

We have set perturbations to vanish at infinity according to the cosmological principle, hence we have only one integration constant γ. We recall that $[\mu_3]=L^{-1}$, as it can be checked also from Eq. (6.43). Note that $\varrho_p\,(r)$ has the same radial dependence, i.e.

$$\varrho_p\,(r)=\frac{\lambda_2\,\gamma}{r}\,e^{-\mu_3\,r}\,, \tag{6.44}$$

in which we considered the assumption given by Eq. (6.40b).

Consequently, from Eq. (6.41b), we also get

$$\mathcal{B}_p\,(r)=-\frac{\gamma}{\mu_4}\,\exp\left(-\mu_3\,r\right)\left(\frac{\mu_4\,\mu_1}{r}+\frac{2\,\mu_3^2}{r^2}+\frac{2}{r^3}\right)\,, \tag{6.45}$$

where we used the solution (6.43). Finally, we combine Eqs. (6.41a), (6.43), and (6.45) to obtain the scalar perturbation

$$\mathcal{A}_p\,(r)=\frac{\gamma}{\lambda_1}\,\exp\left(-\mu_3\,r\right)\left(\frac{2\,\mu_1+\mu_2\,\lambda_2}{r}+\frac{4\,\mu_3^2}{\mu_4\,r^2}+\frac{4}{\mu_4 r^3}\right)\,. \tag{6.46}$$

It should be noted that, in order to satisfy the compatibility between Eqs. (6.41a), (6.40b), (6.41c), (6.41b), and (6.41d), we require the following relation

$$\mu_4 = \frac{2\,\mu_3^2}{3\,\mu_1 + \mu_2\,\lambda_2} \tag{6.47}$$

between the constants involved in the set of equations. More specifically, to write this compatibility condition, we have started from Eqs. (6.41a), (6.41d), and then we have replaced ϱ_p and $\mathcal{B}_p$ with φ_p and φ_p' by using Eqs. (6.40b) and (6.41b), respectively; finally, the resulting equation is compared with Eq. (6.41c) to set the above relation (6.47) between the constants. In particular, note that $[\mu_4] = L^{-2}$, since μ_3 has the dimension of inverse length, and the other constants are dimensionless.

It should be pointed out that the $f\,(R)$ gravity establishes a typical radial scale, $r_c \equiv \mu_3^{-1}$, such that local inhomogeneities vanish for $r \gg r_c$ more rapidly than the respective perturbations in the ΛLTB model. For instance, this fact can be shown by comparing the behavior of the perturbed scale factor given in Eq. (6.29) with the radial profiles of the LTB metric functions in Eqs. (6.45) and (6.46). It is important to stress that our result is completely independent of the choice of scalar field potential $V\left(\bar{\phi}\right)$. Hence these radial solutions apply to any $f(R)$ extended model, providing a remarkable feature of the radial evolution within the Jordan frame of the $f\,(R)$ gravity if compared to GR.

6.3.2.2 Time evolution

Now we focus on the time evolution of perturbations in the Jordan frame. Clearly, the choice of the background $f\,(R)$ modified gravity model affects the time dependence of inhomogeneities since $V\left(\bar{\phi}\right)$ appears in almost all equations regarding the time part. Our main result concerns the peculiarity of the radial profiles of perturbations in the Jordan frame, which does not depend on a specific modified gravity model. Here, we merely want to prove the existence of at least one stable time solution.

To solve numerically the equation system given by Eqs. (6.40a), (6.42a), (6.42e), (6.42d), (6.42b), (6.42c), we rewrite it in terms of the dimensionless parameter τ, defined in Eq. (6.10). We also recall that $d/dt \approx H_0\, d/d\tau$.

In particular, Eqs. (6.40a) and (6.42a) maintain the same form if we write them in terms of τ as

$$A_p\,(\tau) = \lambda_1\, B_p\,(\tau) \tag{6.48}$$

$$\frac{dB_p}{d\tau} = \frac{1}{2\,\bar{\phi}\,(\tau)\,\mu_1}\left(\frac{d\Phi_p}{d\tau} - \frac{1}{\bar{a}}\frac{d\bar{a}}{d\tau}\,\Phi_p\,(\tau)\right)\,, \tag{6.49}$$

respectively.

Furthermore, the linearized scalar field equation (6.42d) becomes

$$\frac{1}{\Phi_p\,(\tau)}\frac{d^2\Phi_p}{d\tau^2} + 3\,\frac{1}{\bar{a}\,(\tau)}\frac{d\bar{a}}{d\tau}\,\frac{1}{\Phi_p\,(\tau)}\frac{d\Phi_p}{d\tau} - \frac{1}{3}\,\frac{\Omega_{m0}}{m^2}\left.\frac{dV}{d\phi}\right|_{\phi=\bar{\phi}(\tau)} + \frac{1}{3}\,\bar{\phi}\,(\tau)\,\frac{\Omega_{m0}}{m^2}\left.\frac{d^2V}{d\phi^2}\right|_{\phi=\bar{\phi}(\tau)} + \\ + \mu_2\,\lambda_2\,\frac{d\bar{\phi}}{d\tau}\,\frac{1}{\Phi_p\,(\tau)}\frac{dB_p}{d\tau} - \frac{\lambda_2\,\Omega_{m0}\,\Xi\,(\tau)}{\bar{a}^3\,(\tau)\,\Phi_p\,(\tau)} = \frac{\tilde{\mu}_3^2}{\bar{a}^2\,(\tau)}\,. \tag{6.50}$$

We have defined the density contrast $\Xi\,(\tau) \equiv P_p\,(\tau)\,/\bar{\rho}\,(\tau)$ for linear perturbations. Note also that the quantity $\tilde{\mu}_3 \equiv \mu_3/H_0$ is dimensionless in natural units.

Similarly, Eq. (6.42b) in terms of τ rewrites as

$$\frac{\mu_2\,\lambda_2}{2\,\mu_1}\left(\frac{2}{\bar{a}\,(\tau)}\frac{d\bar{a}}{d\tau} + \frac{1}{\bar{\phi}\,(\tau)}\frac{d\bar{\phi}}{d\tau}\right)\left(\frac{1}{\Phi_p\,(\tau)}\frac{d\Phi_p}{d\tau} - \frac{1}{\bar{a}\,(\tau)}\frac{d\bar{a}}{d\tau}\right) +$$

$$+\frac{3\,\Omega_{m0}}{\bar{\phi}\left(\tau\right)\,\bar{a}^3\left(\tau\right)}-\frac{\Omega_{m0}}{2\,m^2}\,\left.\frac{dV}{d\phi}\right|_{\phi=\bar{\phi}(\tau)}+\frac{\Omega_{m0}\,V\left(\bar{\phi}\right)}{2\,m^2\,\bar{\phi}\left(\tau\right)}+$$

$$+\frac{3}{\bar{a}\left(\tau\right)}\,\frac{d\bar{a}}{d\tau}\left(\frac{1}{\Phi_p\left(\tau\right)}\,\frac{d\Phi_p}{d\tau}-\frac{1}{\bar{\phi}\left(\tau\right)}\,\frac{d\bar{\phi}}{d\tau}\right)-\frac{3\,\lambda_2\,\Omega_{m0}\,\Xi\left(\tau\right)}{\Phi_p\left(\tau\right)\,\bar{a}^3\left(\tau\right)}+2\mu_1\tilde{\mu}_3^2\,\frac{B_p\left(\tau\right)}{\Phi_p\left(\tau\right)}\,\frac{\bar{\phi}\left(\tau\right)}{\bar{a}^2\left(\tau\right)}=\frac{\tilde{\mu}_3^2}{\bar{a}^2\left(\tau\right)}\,, \qquad (6.51)$$

and Eq. (6.42c) turns into:

$$\frac{d^2B_p}{d\tau^2}+\frac{dB_p}{d\tau}\left(\frac{3}{\bar{a}\left(\tau\right)}\,\frac{d\bar{a}}{d\tau}+\frac{1}{\bar{\phi}\left(\tau\right)}\,\frac{d\bar{\phi}}{d\tau}\right)=\frac{\tilde{\mu}_4}{2\,\bar{a}^2\left(\tau\right)}\,\left(\frac{\Phi_p\left(\tau\right)}{\bar{\phi}\left(\tau\right)}-\mu_1\,B_p\left(\tau\right)\right)\,. \qquad (6.52)$$

In the latter equation, we have introduced the dimensionless quantity $\tilde{\mu}_4 \equiv \mu_4/H_0^2$ in natural units.

Finally, considering the definition of the density contrast $\Xi\left(\tau\right)$ and the background equation (6.15), it is straightforward to show that the linearly perturbed continuity equation (6.42e) simply rewrites in terms of τ as

$$\frac{d\Xi}{d\tau}+\mu_2\,\frac{dB_p}{d\tau}=0\,. \qquad (6.53)$$

Note that we can replace $dB_p/d\tau$ with $d\Xi/d\tau$, or vice versa, in the other field equations (6.50) to reduce the number of unknown quantities.

Now we want to solve numerically Eqs. (6.49) and (6.50) to obtain $\Xi\left(\tau\right)$ and $\Phi_p\left(\tau\right)$. In this regard, we fix the values of constants for simplicity $\mu_1 = 1$, $\mu_2 = 10^2$, $\lambda_2 = 5$, $\tilde{\mu}_3 = 1$ and set initial conditions at $\tau = 1$ for inhomogeneities: $\Xi\left(1\right) = 10^{-5}$, $\Phi_p\left(1\right) = 10^{-12}$, and $d\Phi_p/d\tau\left(1\right) = 0$. These values have been chosen to have weak and slowly varying perturbations and guarantee the existence of a stable numerical solution. Moreover, we use the background numerical solutions for $\bar{a}\left(\tau\right)$ and $\bar{\phi}\left(\tau\right)$, and the scalar field potential $V\left(\bar{\phi}\right)$ for the HS model discussed in Sect. 6.3.1.

Then, we obtain numerical solutions for $\Xi\left(\tau\right)$ and $\Phi_p\left(\tau\right)$, which are plotted in Fig. 6.4. It should be noted that these solutions are stable in time, since inhomogeneous perturbations are dominated by background terms for any τ.

Once we have obtained Ξ and Φ_p numerically, the remaining perturbed quantities A_p and B_p can be easily found by using Eqs. (6.48) and (6.53).

We conclude this chapter by summarizing briefly our results. Adopting the LTB metric (2.1), we solved perturbatively the system of field equations both in the ΛLTB model and in inhomogeneous cosmological model based on the $f\left(R\right)$ gravity. In particular, we used the method of separation of variables for the linear order. We integrated analytically the radial profiles of local perturbations, while their time evolution required a numerical approach. The main result of the analysis concerns the different radial profiles of local inhomogeneities in the two cosmological scenarios: the radial perturbations follow a power-law in the ΛLTB model (Sect. 6.2), while Yukawa-like contributions appear in the $f\left(R\right)$ theory (Sect. 6.3). Interestingly, this latter peculiar behavior of radial profiles is not affected by the choice of the $f\left(R\right)$ functional form. The numerical solution of time-dependent perturbations exhibits a non-diverging profile. Our method outlined a possible way to investigate the differences between GR and modified gravity theories by studying the evolution of radial perturbations in inhomogeneous cosmologies. The most relevant signature we fixed about the possibility to adopt the $f\left(R\right)$ modified gravity scenario is to describe the accelerating late Universe via spherically symmetric perturbations over a homogeneous background.

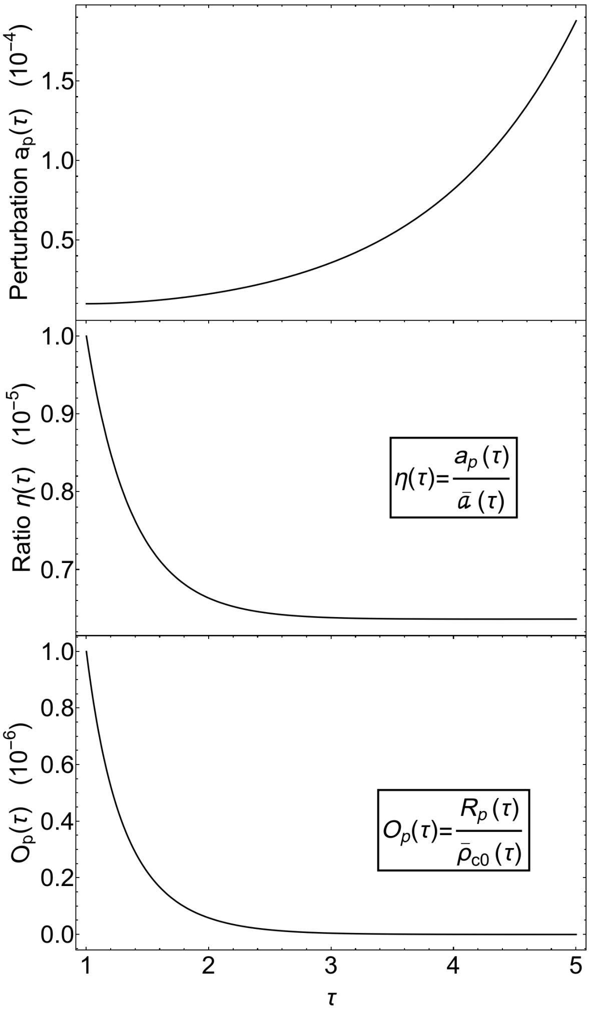

Figure 6.2: Top panel: time evolution of the linear perturbation of the scale factor $\mathrm{a}_p\,(\tau)$ in units of 10^{-4} and in terms of the time dimensionless parameter τ, defined in Eq. (6.10), as a numerical solution of Eq. (6.21). Middle panel: the ratio between the first-order perturbation term and background scale factor, $\eta\,(\tau) \equiv |a_p/\bar{a}|$, versus τ in units of 10^{-5}. Bottom panel: evolution of the dimensionless linear perturbation of the energy density $O_p\,(\tau) \equiv R_p/\bar{\rho}_{c0}$ for the matter component in units of 10^{-6}. Note that all perturbed contributions are smaller than respective background terms for $1 \leq \tau \leq 5$. These panels are extracted from [TS 4].

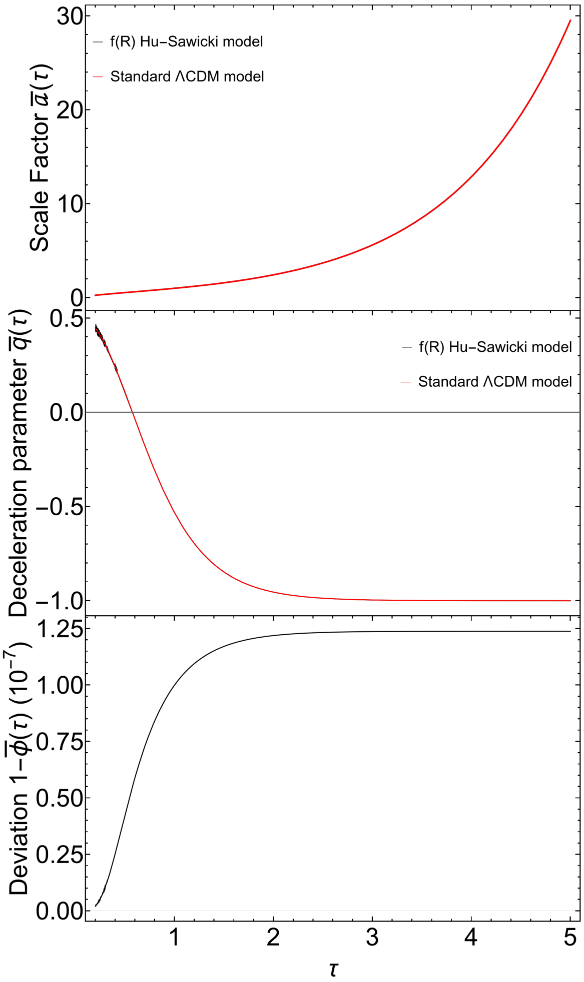

Figure 6.3: Numerical background solutions, considering a flat FLRW geometry, for the $f(R)$ HS model in the Jordan frame. Top panel: evolution of the scale factor $\bar{a}$ in terms of the dimensionless time parameter τ. Middle panel: behavior of the deceleration parameter $\bar{q}(\tau)$. Bottom panel: the deviation from the GR scenario ($\bar{\phi} = 1$) with units of 10^{-7} for the vertical axis. These panels are reported from [TS 4].

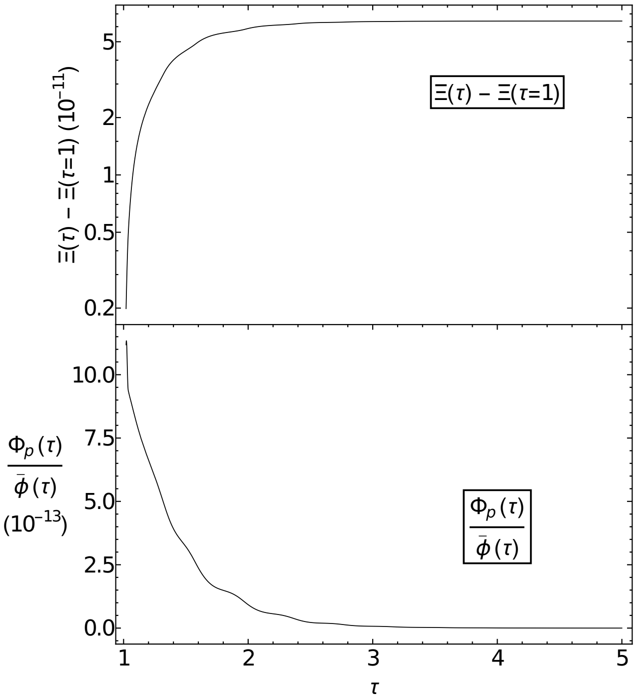

Figure 6.4: Numerical solutions for the evolution of linear perturbations in the Jordan frame of $f(R)$ gravity in terms of the time dimensionless parameter $\tau = t/t_0$. Top panel: the difference between the density contrast Ξ evaluated at a generic τ and $\tau = 1$ represented in units of 10^{-11} and logarithmic scale. Bottom panel: evolution of the ratio between the linearly perturbed scalar field $\Phi_p(\tau)$ and the respective background scalar field $\bar{\phi}(\tau)$ in units of 10^{-13}. This figure is extracted from [TS 4].

Chapter 7

Skewness of the distance-redshift relation in the concordance model

Luminosity-distance relations have been crucial in establishing the accelerating Universe and the standard ΛCDM cosmological model, but it should be considered that light propagation occurs in a clumpy Universe. Therefore, a robust theoretical framework is essential to describe local effects and statistical properties of observed cosmic structures, including their stochastic origin. To investigate the impact of local inhomogeneities of the Universe on cosmological observables, we adopt the averaging formalism in cosmology (see the covariant and gauge-invariant prescription on the past-light cone in Sect. 2.2). While in Chapter 6 we admit a deviation from spatial homogeneity directly in the metric, in the present chapter we build the theoretical framework to evaluate the higher-order moments for the PDF of a given cosmological observable, such as the luminosity distance, within the framework of the concordance model ΛCDM. It should be emphasized that non-Gaussianities in the matter distribution may imply non-Gaussian features in the distance-redshift relation, which are related to non-vanishing higher moments. In this regard, we are interested in computing analytically the skewness of the PDF of the luminosity distance at the leading order in the cosmological perturbative expansion of the gravitational potential, focusing on perturbations of the luminosity distance due to gravitational lensing. Our studies are motivated by the results presented in [166] and based on numerical relativistic simulations of cosmic structure formation by using the code *gevolution* [139], which provide evidence of non-Gaussianities in the Hubble-Lemaître diagram. We show how the late-time matter bispectrum plays a crucial role in determining the skewness in the Hubble-Lemaître diagram. Finally, we discuss our analytical results compared with the numerical simulations mentioned above. The method developed in this chapter is presented in the original work [TS 5].

7.1 Leading-order terms review: average and dispersion

In this section, we present a method to estimate the moments associated with the PDF of a generic observable $\mathcal{S}$. The particular choice of the integration measure used for their evaluation will be addressed later. Specifically, we adopt the covariant averaging prescriptions over the past light-cone of an observer presented in Sect. 2.2.

The average of $\mathcal{S}$ over a specific region of space-time can be written in general as

$$\langle \mathcal{S} \rangle = \frac{\int d\mu \, \mathcal{S}}{\int d\mu} \, , \tag{7.1}$$

in which μ denotes the measure that determines the weight in the averaging procedure. The measure contains a window function to select a specific region of space-time and to ensure the gauge invariance (see, for instance, averages on the past-light cone in Sect. 2.2). Our method is general, we do not adopt a specific averaging prescritpion, but we only require that $\mathcal{S}$ transforms as a scalar field under a generic coordinate transformation. We recall that the average denoted by $\langle \ldots \rangle$ represents a geometric procedure that accounts for the smoothing of an arbitrary inhomogeneous manifold, whereas the stochastic properties of the inhomogeneities are determined by a further ensamble average, as mentioned in Sect. 2.2.

The definition of average given in Eq. (7.1) is an exact expression, but we work in a perturbed FLRW metric. For scalar perturbations at the second order, we have

$$ds^2 = a^2(\eta)\left[-\left(1+2\Phi\right)d\eta^2 + \left(1-2\Psi\right)\left(dr^2 + r^2(d\theta^2 + \sin^2\theta d\varphi^2)\right)\right] \tag{7.2}$$

where the perturbations of the gravitational potentials are given by $\Phi \equiv \sum_i \phi^{(i)}$ and $\Psi \equiv \sum_i \psi^{(i)}$ and i refers to the order of the perturbative expansion[1].

We expand Eq. (7.1) up to second order such that

$$\begin{aligned} \mathcal{S} \simeq & \quad \mathcal{S}^{(0)}\left(1+\sigma^{(1)}+\sigma^{(2)}\right)\,, \\ d\mu \simeq & \quad d\mu^{(0)}\left(1+\mu^{(1)}+\mu^{(2)}\right)\,, \end{aligned} \tag{7.3}$$

Following the same procedure, we can also compute the average of the observable $\mathcal{S}$ with respect to its background value[2] $\mathcal{S}^{(0)}$ by applying Eq. (7.1) to $\mathcal{S}/\mathcal{S}^{(0)}$ instead of $\mathcal{S}$. This choice is motivated by three main reasons. Firstly, the result obtained from numerical simulation (see Fig. 7.1) exhibit the distribution of the ratio between the observed luminosity distance and its value in the background Universe. Secondly, previous estimations in literature [142–144] are consistent with the choice of a rescaled scalar observable to its background value. Thirdly, this choice simplifies our calculations significantly. Actually, we are interested in evaluating the average of the α-th power of $\mathcal{S}/\mathcal{S}^{(0)}$, which will be useful in order to compute the α-th moment of the distribution. Thus, for a generic scalar field $\mathcal{S}$, we can write:

$$\begin{aligned} \left\langle \left(\frac{\mathcal{S}}{\mathcal{S}^{(0)}}\right)^{\alpha} \right\rangle \simeq & \quad \frac{\int d\mu^{(0)}\left[1+\mu^{(1)}+\alpha\,\sigma^{(1)}+\mu^{(2)}+\alpha\,\mu^{(1)}\sigma^{(1)}+\frac{\alpha}{2}\left(2\,\sigma^{(2)}+(\alpha-1)\,{\sigma^{(1)}}^2\right)\right]}{\int d\mu^{(0)}\left(1+\mu^{(1)}+\mu^{(2)}\right)} \\ \simeq & \quad 1+\alpha\, I[\sigma^{(1)}] \\ & +\alpha\, I[\mu^{(1)}\,\sigma^{(1)}]+\alpha\, I[\sigma^{(2)}]+\frac{\alpha\,(\alpha-1)}{2}\, I\left[{\sigma^{(1)}}^2\right]-\alpha\, I[\mu^{(1)}]\, I[\sigma^{(1)}]\,, \end{aligned} \tag{7.4}$$

in which we have defined the average with the background measure

$$I\left[f\right] \equiv \frac{\int d\mu^{(0)} f}{\int d\mu^{(0)}}\,. \tag{7.5}$$

Considering that our perturbations will be sourced by the fluctuations of the gravitational potentials Φ and Ψ, we assume that the ensamble average of the linear gravitational potentials is zero, i.e., $\overline{\phi} = \overline{\psi} = 0$,

---

[1] We work with the conformal time η and we use capital Greek letters for the full non-linear gravitational potentials, while each perturbative term is indicated by lowercase Greek letters. For the sake of simplicity, we will omit the index $^{(1)}$ for linear perturbations of the gravitational potentials, and the superscript $^{(2)}$ is used only for the purely second-order perturbations. Moreover, we will assume that there is no anisotropic stress at linear order, i.e. $\phi = \psi$.

[2] In this chapter, to avoid ambiguity with the ensamble average $\overline{\cdots}$, we refer to background quantities by using the superscript $^{(0)}$, differently from the previous chapter.

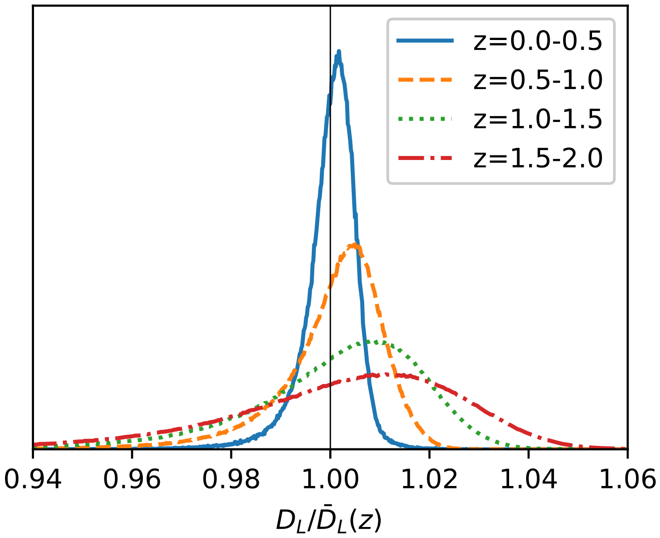

Figure 7.1: PDF of the ratio between the observed luminosity distance and the respective quantity in a pure homogeneous scenario. This figure, reported from [166], is obtained from N-body numerical relativistic simulations by using the code *gevolution* [139] in different redshift bins of size $\Delta z = 0.5$. Note the presence of deviations from Gaussianity at high redshifts.

and allow higher-order powers of Φ and Ψ to have a non-vanishining ensemble average. We then get

$$\overline{\left\langle \left(\frac{\mathcal{S}}{\mathcal{S}^{(0)}} \right)^{\alpha} \right\rangle} = 1 + \alpha\, \overline{I[\mu^{(1)}\, \sigma^{(1)}]} + \alpha\, \overline{I[\sigma^{(2)}]} + \frac{\alpha\,(\alpha-1)}{2}\, \overline{I\left[{\sigma^{(1)}}^2 \right]} - \alpha\, \overline{I[\mu^{(1)}]\, I[\sigma^{(1)}]}\,, \tag{7.6}$$

where we used the abovementioned properties that the ensemble average of linear perturbations vanishes.

In particular, if $\alpha = 1$, it is immediate to evaluate the average of $\mathcal{S}/\mathcal{S}^{(0)}$ by using Eq. (7.6). Indeed, we have:

$$m \equiv \overline{\left\langle \frac{\mathcal{S}}{\mathcal{S}^{(0)}} \right\rangle} = 1 + \overline{I[\mu^{(1)}\, \sigma^{(1)}]} + \overline{I[\sigma^{(2)}]} - \overline{I[\mu^{(1)}]\, I[\sigma^{(1)}]}\,. \tag{7.7}$$

This result allow us to evaluate the generic α-th moment μ_α of the distribution of $\mathcal{S}$, which is written as

$$\begin{aligned} \mu_\alpha \equiv& \overline{\left\langle \left(\frac{\mathcal{S}}{\mathcal{S}^{(0)}} - m \right)^{\alpha} \right\rangle} = \sum_{k=0}^{\alpha} (-1)^{\alpha-k} \binom{\alpha}{k} m^{\alpha-k} \overline{\left\langle \left(\frac{\mathcal{S}}{\mathcal{S}^{(0)}} \right)^{k} \right\rangle} \\ =& \sum_{k=0}^{\alpha} (-1)^{\alpha-k} \binom{\alpha}{k} \Big\{ 1 + \alpha\, \overline{I[\mu^{(1)}\, \sigma^{(1)}]} \\ &+ \alpha\, \overline{I[\sigma^{(2)}]} - \alpha\, \overline{I[\mu^{(1)}]\, I[\sigma^{(1)}]} + \frac{k\,(k-1)}{2}\, \overline{I[{\sigma^{(1)}}^2]} \Big\}\,. \end{aligned} \tag{7.8}$$

The variance of the distribution of $\mathcal{S}$ can be easily evaluated from Eq. (7.8) with $\sigma^2 \equiv \mu_2$. Then, we have

$$\sigma^2 = \overline{I[{\sigma^{(1)}}^2]}\,. \tag{7.9}$$

However, since in this section we have limited our non-linearities to be at most second-order perturbations, all the higher moments μ_α with $\alpha > 2$ vanish. In the next section, we will evaluate the effects of the next-to-leading order terms on the analytic estimation of higher-order multipoles.

7.2 Next-to-leading order term: skewness

In this section, we present the analytical evaluation for the skewness of a generic observable $\mathcal{S}$. We recall that we have eliminated the background contribution to the observable by studying the ratio $\mathcal{S}/\mathcal{S}^{(0)}$ instead of just $\mathcal{S}$. The standardized moments κ_α of the distribution are defined as

$$\kappa_\alpha \equiv \frac{\mu_\alpha}{\left(\sigma^2\right)^{\alpha/2}} = \frac{1}{\left(\sigma^2\right)^{\alpha/2}} \overline{\left\langle \left(\frac{\mathcal{S}}{\mathcal{S}^{(0)}} - m \right)^{\alpha} \right\rangle} . \tag{7.10}$$

However, as mentioned in the previous section, second-order corrections are insufficient to estimate higher-order moments. It might be expected that, naively, each μ_α requires α-th order perturbations to obtain the leading term. This estimation is accurate for even moments. However, for odd moments, the leading terms are of order $\alpha+1$ in perturbation theory (for instance, this applies to the average and dispersion). This peculiar hierarchy arises because the leading term for each moment μ_α is $\overline{I[\sigma^{(1)\,\alpha}]}$. Consequently, since $\sigma^{(1)} \sim \psi^{(1)}$, we have that the α-th order term of μ_α is related to the α-point correlation function of $\psi^{(1)}$, which is non-zero only for even α, as a consequence of Wick's theorem by assuming Gaussian initial conditions.

Based on the discussion so far, evaluating higher-order moments requires perturbations for both the measure μ and the observable $\mathcal{S}$ beyond the second order, at least for the leading terms. However, these quantities are not available in the literature, and determining them poses a non-trivial task, which in itself would be an interesting result. Fortunately, it can be demonstrated that the expansion presented in Eqs. (7.3) captures all terms for the third and fourth moments at leading order, even when perturbations of $\mathcal{S}$ and μ up to the fourth order are consistently taken into account. The derivation of this result is lengthy but straightforward, and interested readers can refer to Appendix on page 139 for a detailed proof. Thus, we obtain

$$\begin{aligned} \mu_3 &= \overline{I[\sigma^{(1)\,3}]} + \overline{I[\sigma^{(1)\,3}\mu^{(1)}]} - \overline{I[\sigma^{(1)\,3}]I[\mu^{(1)}]} + 3\overline{I[\sigma^{(1)\,2}\sigma^{(2)}]} \\ &\quad +3\,\overline{I[\sigma^{(1)\,2}]}\;\overline{I[\mu^{(1)}]\,I[\sigma^{(1)}]} - 3\overline{I[\sigma^{(1)\,2}]}\;\overline{I[\mu^{(1)}\,\sigma^{(1)}]} - 3\overline{I[\sigma^{(1)\,2}]}\;\overline{I[\sigma^{(2)}]} \\ &= \overline{I[\sigma^{(1)\,3}\mu^{(1)}]} + 3\overline{I[\sigma^{(1)\,2}\sigma^{(2)}]} - \overline{I[\sigma^{(1)\,3}]I[\mu^{(1)}]} - 3\,\sigma^2\,(m-1)\;. \end{aligned} \tag{7.11}$$

where m and σ^2 are given by Eqs. (7.7) and (7.9), respectively. Note that the third-order contribution $\overline{I[\sigma^{(1)\,3}]}$ vanishes as a consequence of Wick theorem, as mentioned above.

The results obtained so far are completely general in regard of the kind of observable $\mathcal{S}$ and the chosen prescription of the spatial average μ. In the next section, we will apply them to the specific cases of the distance-redshift relations.

7.3 Higher-order moments for the distance-redshift relations

We consider the luminosity distance-redshift relation $d_L(z)$ as the scalar field $\mathcal{S}$, and we apply the formalism developed in previous sections. The interest in the rescaled luminosity distance distribution arises from recent results by using numerical simulations [166], which show the occurence of non-Gaussianities for the PDF of $d_L(z)$. Our objective is to investigate the extent to which this behavior can be captured within perturbation theory.

Linear and non-linear perturbations for the distance-redshift relations have been discussed in [143, 145, 258–260]. For the purposes of this chapter, we refer to the leading lensing terms as given in Eqs. (B.1) and (B.2) of [148].

Then, we can express the luminosity distance to second order in perturbation theory as follows[3]

$$d_L\left(z\right) \simeq d_L^{(0)}\left(z\right)\left(1+\sigma^{(1)}+\sigma^{(2)}\right)\,, \tag{7.12}$$

in which the linear and second-order perturbations for the luminosity distance-redshift relation are given by

$$\begin{aligned} \sigma^{(1)} &= \int_0^{r_s} dr \frac{r-r_s}{r r_s}\Delta_2\psi\left(r\right)\,, \\ \sigma^{(2)} &= \frac{1}{2}\sigma^{(1)\,2}+\Sigma^{(2)}+\sigma^{(2)}_{LSS}\,, \end{aligned} \tag{7.13}$$

where $d_L^{(0)}\left(z\right)$ is the luminosity distance in a FLRW background, r_s is the comoving distance to the source, Δ_2 is the dimensionless angular Laplacian on the 2-sphere, and $\psi(r)=\psi(\eta_o-r,r)$. We have also introduced[4]

$$\begin{aligned} \sigma^{(2)}_{LSS} &\equiv \frac{1}{2}\int_0^{r_s} dr \frac{r-r_s}{r r_s}\Delta_2\left[\psi^{(2)}+\phi^{(2)}\right](r)\,, \\ \Sigma^{(2)} &\equiv 2\int_0^{r_s} dr \frac{r-r_s}{r r_s}\partial_b\left[\Delta_2\psi(r)\right]\int_0^{r_s} dr\,\frac{r-r_s}{r r_s}\bar{\gamma}_0^{ab}\partial_a\psi(r) \\ &\quad +2\int_0^{r_s} dr\left\{\gamma_0^{ab}\partial_b\left[\int_0^r dr'\,\psi(r')\right]\int_0^r dr'\,\frac{r'-r}{r r'}\partial_a\Delta_2\psi(r')\right\} \\ &\quad +\int_0^{r_s} dr\,\frac{r-r_s}{r r_s}\Delta_2\left[\gamma_0^{ab}\partial_a\left(\int_0^r dr'\,\psi(r')\right)\partial_b\left(\int_0^r dr'\,\psi(r')\right)\right]\,, \end{aligned} \tag{7.14}$$

where $\bar{\gamma}_0^{ab}=\mathrm{diag}(1,\sin^{-2}\theta)$ and $\gamma_0^{ab}=r^{-2}\bar{\gamma}_0^{ab}$.

According to Eq. (7.11), we also need to specify which kind of measure we are adopting for the evaluation of the average and the skewness. Several possibilities have been discussed in [174] for measures which are general covariant and gauge invariant. We decide to adopt the galaxy number count weighted measure for the averages. This kind of weight have been discussed for the backreaction of stochastic inhomogeneities to the mean value of the Hubble diagram in the limit case of small width of the redshift bin [149, 173, 174]. However, it can be applied directly also for the case of finite redshift bin, preserving the property of general covariance [174].

Concerning the comparison with numerical simulations, the adoption of the average weighted with galaxy number count appears to be the most appropriate choice since it naturally weights more the regions where the density contrast is higher. The background term in the measure is then given by

$$d\mu^{(0)} = -\left[\frac{\rho(z)\,d_A^2(z)}{(1+z)H(z)}\right]^{(0)} dz\,d\Omega = \mathcal{W}(z)dzd\Omega\,, \tag{7.15}$$

where $d\Omega$ is the infinitesimal solid angle, $d_A^{(0)}$ is the background angular distance (see Sect. 22), $\rho^{(0)}$ is the background density, the denominator comes from the background expansion of the number count and we have defined

$$\mathcal{W}(z) \equiv -\left[\frac{\rho(z)\,d_A^2(z)}{(1+z)\;H(z)}\right]^{(0)}\,.$$

We are then left with reporting the linear order galaxy number counts [129–131, 261]. The leading terms

---

[3] From now on, unless otherwise specified, $\sigma^{(1)}$ and $\sigma^{(2)}$ refer to the perturbations of the luminosity distance-redshift relation.

[4] As a remark, here we have followed the same convention for the second order gravitational potential as [152], differently from [148], where $\Phi \equiv \phi + \frac{1}{2}\phi^{(2)}$ and $\Psi \equiv \psi + \frac{1}{2}\psi^{(2)}$. This will lead to a difference in the prefactor of $\sigma^{(2)}_{LSS}$ later on.

in the weak field expansion are given by [135]

$$\mu^{(1)} = \delta + \mathcal{H}^{-1}\partial_r v_\parallel + 2\int_0^{r_s} dr \frac{r - r_s}{r r_s}\Delta_2\psi(r) = \delta + \mathcal{H}^{-1}\partial_r v_\parallel + 2\,\sigma^{(1)}\,, \tag{7.16}$$

where we recall that δ is the linear fluctuation in the matter fluid (with the galaxy bias set to $b_1 = 1$), and $\mathcal{H}^{-1}\partial_r v_\parallel$ accounts for the redshift-space distortion.

Eqs. (7.15) and (7.16) provide all the conditions that we need to compute μ_3. Indeed, from Eq. (7.11), we explicitly get

$$\begin{aligned}\mu_3 \;\; = \;\; & \frac{7}{2}\,\overline{I[\sigma^{(1)\,4}]} + 3\overline{I\left[\sigma^{(1)\,2}\sigma^{(2)}_{LSS}\right]} + 3\overline{I[\sigma^{(1)\,2}\Sigma^{(2)}]} \\ & + \overline{I[\sigma^{(1)\,3}\delta]} + \overline{I\left[\frac{\sigma^{(1)\,3}\partial_r v_\parallel}{\mathcal{H}}\right]} - 3\,\sigma^2\,(m-1)\,,\end{aligned} \tag{7.17}$$

where leading order term for σ^2 is given by Eq. (7.9), and the average is written as

$$m - 1 = \overline{I[\sigma^{(1)}\delta]} + \overline{I\left[\frac{\sigma^{(1)}\partial_r v_\parallel}{\mathcal{H}}\right]} + \frac{5}{2}\,\overline{I[\sigma^{(1)\,2}]} + \overline{I[\Sigma^{(2)}]}\,. \tag{7.18}$$

In the derivation of Eq. (7.17) we made use of $I\left[\sigma^{(1)}\right] = 0$. This is because we have considered only lensing terms in Eqs. (7.13) and terms sourced by a Laplacian vanish when averaged over spatial directions. The same result holds also in the derivation of Eq. (7.18) in regard of the term $I\left[\sigma^{(2)}_{LSS}\right]$. In a similar manner, also terms as $\overline{I\left[\sigma^{(1)\,3}\right]I[\delta]}$ and $\overline{I\left[\sigma^{(1)\,3}\right]I\left[\frac{\partial_r v_\parallel}{\mathcal{H}}\right]}$ do not contribute to Eq. (7.17). This is because the ensemble average for these terms always correlates the monopole of δ or $\mathcal{H}^{-1}\partial_r v_\parallel$ with the Laplacian of $\sigma^{(1)}$, selecting then its null eigenvalue. Sub-leading relativistic corrections to the distance-redshift relation, such as Doppler effect, can contribute with a non-vanishing monopole, especially if sources at small redshifts are taken into account. However, for the purposes of this pioneering work presented in this chapter, we have not considered them, even thought they can be of interest for the analysis of close sources.

7.3.1 Infinitesimal redshift bin

Before concluding this section, some comments about the integration domain are in order. The integration over the solid angle $d\Omega$ in Eq. (7.15) covers the entire solid angle. For the integration over the redshift, we adopt a redshift bin of width Δz such that all the needed averages are evaluated within a certain redshift range $[z_s, z_s + \Delta z]$. In case of large value of the redshift bin width, all the redshift dependent terms in Eq. (7.15) needs to be integrated. However, in the limit when Δz becomes small enough to be considered infinitesimal[5], i.e. $\Delta z \to \delta z$, the measure in Eq. (7.15) simplifies to

$$d\mu^{(0)} \simeq -\left[\rho(z_s)\,d_A^2(z_s)\right]^{(0)} \frac{\delta z\, d\Omega}{(1+z_s)H(z_s)}\,, \tag{7.19}$$

and then the integrals in the definition of $I[f]$ in Eq. (7.5) reduce to simple angular integrals. Morevoer, within this limit, all the redshift dependent quantities and δz itself factorize out of the integrals and cancel out in the ratio with the unconnected diagram in Eq. (7.5), returning then[6]

$$\lim_{\Delta z \to \delta z} I[f] = \frac{1}{4\pi}\int d\Omega f(z_s, \vec{n})\,. \tag{7.20}$$

---

[5] This limit has been originally proposed in [149] and its covariance has been then proved in [174].

[6] In this chapter, three-dimensional vectors are written in bold.

In this limit, the non purely second order terms in first equality of Eq. (7.11) cancel. To this end, we anticipate in the limit of Eq. (7.20) that

$$\begin{aligned}\overline{I[\sigma^{(1)\,3}\mu^{(1)}]} &= 3\,I\left[\overline{\sigma^{(1)\,2}}\,\overline{\mu^{(1)}\sigma^{(1)}}\right] = 3\,\overline{\sigma^{(1)\,2}}\,\overline{\mu^{(1)}\sigma^{(1)}} \\ &= 3\,\overline{I[\sigma^{(1)2}]}\,\overline{I[\mu^{(1)}\sigma^{(1)}]} = 3\,\sigma^2\,\overline{I[\mu^{(1)}\sigma^{(1)}]}\,, \qquad (7.21)\end{aligned}$$

where we have used Eq. (7.9) and the fact that the ensemble average can not have any preferred direction due to statistical isotropy. This terms exactly cancels the counterpart coming from Eq. (7.7) in Eq. (7.17). Here, we make the first interesting remark that the weight for the measure is irrelevant in the infinitesimal bin limit for the leading order terms of the skewness for the luminosity distance-redshift case study. Moreover, in this limit, the skewness reduces to the simpler expression

$$\mu_3 = \mu_3^Q + \mu_3^{PB} + \mu_3^{LSS}\,, \qquad (7.22)$$

where we have defined

$$\begin{aligned}\mu_3^Q &\equiv \frac{7}{2}\,\overline{I[\sigma^{(1)\,4}]} - \frac{15}{2}\left(\sigma^2\right)^2\,, \\ \mu_3^{PB} &\equiv 3\left\{\overline{I[\sigma^{(1)\,2}\Sigma^{(2)}]} - \sigma^2\,\overline{I[\Sigma^{(2)}]}\right\}\,, \\ \mu_3^{LSS} &\equiv 3\,\overline{I\left[\sigma^{(1)\,2}\sigma^{(2)}_{LSS}\right]}\,. \qquad (7.23)\end{aligned}$$

We have combined Eqs. (7.17) and (7.18), adapted for an infinitesimal redshift bin by using Eq. (7.21), to cancel out terms like $\overline{I[\sigma^{(1)\,3}\delta]}$ and $\overline{I\left[\frac{\sigma^{(1)\,3}\partial_r v_\parallel}{\mathcal{H}}\right]}$, as previously mentioned.

Eq. (7.22) is entirely sourced by pure non-linear terms in the expression of the distance-redshift relation. Indeed, when considering Gaussian initial conditions, linearly evolved perturbations preserve their PDF. Consequently, they do not generate any non-Gaussianity in the limit of infinitesimally narrow bins, where the hypersurfaces for the averages are evaluated at constant redshift.

Hence, the terms in Eq. (7.22) are sourced by pure non-Gaussian effects and their labels follow accordingly: in Eqs. (7.23) Q, PB ans LSS respectively stand for *Quadratic*, *Post-Born* and *Large-Scale-Structure* since

- μ_3^Q takes into account the non-Gaussianity coming from the quadratic term $\sigma^{(1)\,2}/2$ in Eq. (7.13),
- μ_3^{PB} contains all the relevant terms due to the Post-Born corrections to the $d_L(z)$, such as multi-lens effects,
- μ_3^{LSS} catches the non-Gaussianities arising from the bispectrum of $\overline{\delta^{(2)}\delta^{(1)}\delta^{(1)}}$.

Understanding how much the finite bin effect may mimic non-Gaussian behavior beyond the fundamental non-linearities is of interest *per se*. For the rest of this chapter, we will explicitly compute and numerically evaluate the amplitude of the expected skewness in the infinitesimal redshift bin case, where the only relevant effect is the one due to intrinsic non-Gaussianities in the inhomogeneities.

7.4 Analytic expressions

We provide the explicit expression for the leading order terms of the skewness in the infinitesimal redshift bin. First let us remark that our derivation so far is completely geometrical without any assumption on the underlying theory of gravity, with the only assumption that light propagates along null geodesics. At this point, we need to use GR to relate metric and matter perturbations. We first provide some general preliminaries needed to follow our derivations. Technical details are reported in the Appendix on page 141. In order to compute the different contribution to the third moment defined in Eqs. (7.23), it is convenient to introduce the generalized Hankel transform of the matter power spectrum at two given conformal times η_1 and η_2, namely $P\left(k,\eta_1,\eta_2\right) \equiv P(k)D_1(\eta_1)D_1(\eta_2)$, as

$$J_\ell^n\left(\eta_1,\eta_2\right) = \int \frac{dk}{2\pi^2} k^2 P\left(k,\eta_1,\eta_2\right) \frac{j_\ell\left(k|r_1-r_2|\right)}{\left(k|r_1-r_2|\right)^n}\,, \tag{7.24}$$

where $r_i \equiv r(\eta_i) = \eta_0 - \eta_i$ and $j_\ell(x)$ is the ℓ-th order spherical Bessel function. We also recall that D_1 is the growth function normalized to unity today. The reason why we decide to adopt the definition (7.24) for the Hankel transform is that it can be easily generalized to the science case of non-linear matter power spectrum, as we will discuss in Sect. 7.5.

In evaluating Eqs. (7.23), we encounter the following terms

$$\begin{aligned}
\overline{\Delta_2\psi\left(r_1,\vec{n}\right)\Delta_2\psi\left(r_2,\vec{n}\right)} &= \frac{9\,r_1r_2\,\mathcal{H}_0^4\,\Omega_{m0}^2}{a(r_1)a(r_2)}\left[2r_1r_2J_2^2\left(\eta_1,\eta_2\right)\right.\\
&\quad\left.+J_1^3\left(\eta_1,\eta_2\right)\left(r_1-r_2\right)^2\right] \equiv \mathcal{L}\left(r_1,r_2\right)\,,\\
\overline{\bar{\gamma}_0^{ab}\partial_b\Delta_2\psi\left(r_1,\vec{n}\right)\partial_a\psi\left(r_2,\vec{n}\right)} &= -\mathcal{L}\left(r_1,r_2\right)\,,\\
\overline{\Delta_2\left(\bar{\gamma}_0^{ab}\partial_a\psi\left(r_1,\vec{n}\right)\partial_b\psi\left(r_2,\vec{n}\right)\right)} &= 0\,,\\
\overline{\Delta_2\psi\left(r_1,\vec{n}\right)\partial_a\psi\left(r_2,\vec{n}\right)} &= \overline{\psi\left(r_1,\vec{n}\right)\partial_a\Delta_2\psi\left(r_2,\vec{n}\right)} = 0\,.
\end{aligned} \tag{7.25}$$

We remark that

$$\overline{\Delta_2\psi\left(r_1,\vec{n}\right)\Delta_2\psi\left(r_2,\vec{n}\right)} + \overline{\bar{\gamma}_0^{ab}\partial_b\Delta_2\psi\left(r_1,\vec{n}\right)\partial_a\psi\left(r_2,\vec{n}\right)} = 0\,, \tag{7.26}$$

whereas second last of Eqs. (7.25) vanishes since

$$\overline{\Delta_2\left(\bar{\gamma}_0^{ab}\partial_a\psi\left(r_1,\vec{n}\right)\partial_b\psi\left(r_2,\vec{n}\right)\right)} = \Delta_2\overline{\left(\bar{\gamma}_0^{ab}\partial_a\psi\left(r_1,\vec{n}\right)\partial_b\psi\left(r_2,\vec{n}\right)\right)} \tag{7.27}$$

and $\overline{\left(\bar{\gamma}_0^{ab}\partial_a\psi\left(r_1,\vec{n}\right)\partial_b\psi\left(r_2,\vec{n}\right)\right)}$ can not depend on the direction $\vec{n}$ due to statistical isotropy. For the same reason

$$\overline{\Delta_2\psi^{(2)}} \propto \overline{\Delta_2\psi^2} = \Delta_2\overline{\psi^2} = 0\,. \tag{7.28}$$

Last equality in Eq. (7.25) can be understood in the following way: they always involve an odd number of angular derivatives and hence they vanish due to statistical isotropy, since they naturally introduce a preferred direction, which returns to 0 when the ensemble average acts.

The 2-point correlation functions in Eqs. (7.25) are enough also to evaluate the 4-point correlation functions of interest for us. With the aim of Wick theorem, indeed, we can write

$$\begin{aligned}
&\overline{\Delta_2\psi(r_1,\mathbf{n})\Delta_2\psi(r_2,\mathbf{n})\Delta_2\psi\left(r_3,\vec{n}\right)\Delta_2\psi\left(r_4,\vec{n}\right)}\\
=\;&\mathcal{L}\left(r_1,r_2\right)\mathcal{L}\left(r_3,r_4\right)+\mathcal{L}\left(r_1,r_3\right)\mathcal{L}\left(r_2,r_4\right)+\mathcal{L}\left(r_1,r_4\right)\mathcal{L}\left(r_3,r_2\right)\,.
\end{aligned} \tag{7.29}$$

For the sake of completeness, we report in Appendix on page 141 the derivation of Eq. (7.29). In a similar manner, we obtain also that

$$\begin{aligned}
&\overline{\Delta_2\psi(r_1,\mathbf{n})\Delta_2\psi(r_2,\mathbf{n})\Delta_2\left(\bar{\gamma}_0^{ab}\partial_a\psi\left(r_3,\vec{n}\right)\partial_b\psi\left(r_4,\vec{n}\right)\right)}\\
=\;&\mathcal{L}\left(r_1,r_3\right)\mathcal{L}\left(r_2,r_4\right)+\mathcal{L}\left(r_1,r_4\right)\mathcal{L}\left(r_2,r_3\right)\,.
\end{aligned} \tag{7.30}$$

It is interesting to notice that only two permutations survive in Eq. (7.30) as a consequence of the last two equalities in Eqs. (7.25). Looking at the structure of Eq. (7.30), we notice that only the permutations mixing $\Delta_2\psi$ with one of the term of $\Delta_2(\partial\psi)^2$ survive. Finally, last 4-point correlation function of our interest is

$$\begin{aligned} & \overline{\Delta_2\psi(r_1,\mathbf{n})\Delta_2\psi(r_2,\mathbf{n})\bar{\gamma}_0^{ab}\partial_b\Delta_2\psi\left(r_3,\vec{n}\right)\partial_a\psi\left(r_4,\vec{n}\right)} \\ = \ & \overline{\Delta_2\psi(r_1,\mathbf{n})\Delta_2\psi(r_2,\mathbf{n})}\,\overline{\bar{\gamma}_0^{ab}\partial_b\Delta_2\psi\left(r_3,\vec{n}\right)\partial_a\psi\left(r_4,\vec{n}\right)} = -\mathcal{L}\left(r_1,r_2\right)\mathcal{L}\left(r_3,r_4\right)\,. \end{aligned} \tag{7.31}$$

The interesting thing about Eq. (7.31) is that only one permutation survives in the final result and this is again a consequence of last of Eqs. (7.25). The structure of Eq. (7.31) also exhibits a complete factorization of the 2-point correlation function in the form $(\Delta_2\psi)^2$. This situation is opposite to what we have shown for Eq. (7.30), where only mixed terms survive in the final permutations. The impact of these differences in the ultimate evaluation of μ_3 will be to significantly reduce the final number of non-null terms for the skewness, as we will show in Sect. 7.4.2.

These analytic preliminaries are enough to provide the explicit expressions for μ_3^Q, μ_3^{PB} in the infinitesimal bin case. The evaluation of μ_3^{LSS} is more delicate and will be treated in a specific way.

7.4.1 μ_3^Q: quadratic terms

The starting point for the computation of μ_3^Q is its expression in Eqs. (7.23). To our hand, we first evaluate the variance in the small bin limit. By making use of Eqs. (7.9), (7.13), and (7.25), we get that

$$\sigma^2 = \int_0^{r_s} dr_1 \frac{r_1 - r_s}{r_1 r_s} \int_0^{r_s} dr_2 \frac{r_2 - r_s}{r_2 r_s} \mathcal{L}(r_1, r_2)\,. \tag{7.32}$$

In the same way, thanks to Eq. (7.29), we have that

$$\begin{aligned} \overline{I[\sigma^{(1)\,4}]} &= \int_0^{r_s} dr_1 \frac{r_1 - r_s}{r_1 r_s} \int_0^{r_s} dr_2 \frac{r_2 - r_s}{r_2 r_s} \int_0^{r_s} dr_3 \frac{r_3 - r_s}{r_3 r_s} \int_0^{r_s} dr_4 \frac{r_4 - r_s}{r_4 r_s} \\ & \quad \times \left[\mathcal{L}\left(r_1,r_2\right)\mathcal{L}\left(r_3,r_4\right) + \mathcal{L}\left(r_1,r_3\right)\mathcal{L}\left(r_2,r_4\right) + \mathcal{L}\left(r_1,r_4\right)\mathcal{L}\left(r_3,r_2\right)\right] \\ &= 3\left(\sigma^2\right)^2\,. \end{aligned} \tag{7.33}$$

Hence, the combination of Eqs. (7.13), (7.32), and (7.33) leads to the quite simple result

$$\mu_3^Q = 3\left(\sigma^2\right)^2\,. \tag{7.34}$$

It is worth noticing what happens for the leading term of the standardized third moment. For the quadratic terms coming from Eq. (7.34), we get that

$$\kappa_3^Q \equiv \frac{\mu_3^Q}{\left(\sigma^2\right)^{3/2}} = 3\,\sigma\,, \tag{7.35}$$

namely the skewness of the distance-redshift relation due to the quadratic corrections is proportional to the dispersion of $d_L(z)$. This result already allows us to estimate the amplitude of κ_3^Q. Indeed, in [144] the dispersion for the distance-redshift relation has been estimated for the lensing contribution at higher redshift to be $\sim 1\%$. This evaluation takes into account the non-linear power spectrum for the gravitational potential as provided by the HaloFit model [262].

7.4.2 μ_3^{PB}: post-Born corrections

For the evaluation of the post-Born terms μ_3^{PB} in Eq. (7.23), we first look at the expression of $\Sigma^{(2)}$ in Eq. (7.14) and treat its terms separately. We divide

$$\Sigma^{(2)} = \Sigma^{(2)}_{sep} + \Sigma^{(2)}_{mix}\,, \tag{7.36}$$

where we defined

$$\begin{aligned}
\Sigma^{(2)}_{sep} &\equiv 2\int_0^{r_s} dr\frac{r-r_s}{rr_s}\partial_b\left[\Delta_2\psi(r)\right]\int_0^{r_s} dr\,\frac{r-r_s}{rr_s}\bar{\gamma}_0^{ab}\partial_a\psi(r) \\
&\quad +2\int_0^{r_s} dr\left\{\gamma_0^{ab}\partial_b\left[\int_0^{r} dr'\,\psi(r')\right]\int_0^{r} dr'\,\frac{r'-r}{rr'}\partial_a\Delta_2\psi(r')\right\}\,, \\
\Sigma^{(2)}_{mix} &\equiv \int_0^{r_s} dr\,\frac{r-r_s}{rr_s}\Delta_2\left[\gamma_0^{ab}\partial_a\left(\int_0^{r} dr'\,\psi(r')\right)\partial_b\left(\int_0^{r} dr'\,\psi(r')\right)\right]\,,
\end{aligned} \tag{7.37}$$

such the total contribution to μ_3^{PB} is given by

$$\mu^{PB}_{3\,sep} = 3\left\{\overline{I[\sigma^{(1)\,2}\Sigma^{(2)}_{sep}]} - \sigma^2\,\overline{I[\Sigma^{(2)}_{sep}]}\right\}\,, \tag{7.38}$$

and

$$\mu^{PB}_{3\,mix} = 3\left\{\overline{I[\sigma^{(1)\,2}\Sigma^{(2)}_{mix}]} - \sigma^2\,\overline{I[\Sigma^{(2)}_{mix}]}\right\}\,. \tag{7.39}$$

Thanks to Eqs. (7.30) and (7.31), $\mu^{PB}_{3\,sep}$ and $\mu^{PB}_{3\,mix}$ can be readily evaluated. In fact, since the factorization in Eq. (7.31) does not mix any term of $\Sigma^{(2)}_{sep}$ with $\sigma^{(1)}$, we can immediately factorize

$$\overline{I\left[\sigma^{(1)\,2}\Sigma^{(2)}_{sep}\right]} = \overline{I\left[\sigma^{(1)\,2}\right]}\,\overline{I\left[\Sigma^{(2)}_{sep}\right]} \tag{7.40}$$

as well. Then, using Eq. (7.9), this automatically returns

$$\mu^{PB}_{3\,sep} = 0\,. \tag{7.41}$$

For what concerns $\mu^{PB}_{3\,mix}$, we first notice that $\overline{I\left[\Sigma^{(2)}_{mix}\right]} = 0$ as a consequence of Eqs. (7.25). Moreover, from the structure of the 4-point correlation function already discussed after Eq. (7.30), we obtain

$$\mu^{PB}_{3\,mix} = 6\int_0^{r_s} dr_1\frac{r_1-r_s}{r_1r_s}\int_0^{r_s} dr_2\frac{r_2-r_s}{r_2r_s}\int_0^{r_s}\frac{dr}{r^2}\frac{r-r_s}{rr_s}\int_0^{r} dr_3\int_0^{r} dr_4\,\mathcal{L}\left(r_1,r_3\right)\mathcal{L}\left(r_2,r_4\right)\,. \tag{7.42}$$

Hence the total contribution of the post-Born corrections to the third moment is

$$\mu_3^{PB} = \mu^{PB}_{3\,mix}\,, \tag{7.43}$$

and the skewness is

$$\kappa_3^{PB} \equiv \frac{\mu_3^{PB}}{\left(\sigma^2\right)^{3/2}} = \frac{\mu^{PB}_{3\,mix}}{\left(\sigma^2\right)^{3/2}}\,. \tag{7.44}$$

The structure of μ_3^{PB} reveals a sequence of five nested line-of-sight integrals, consistent with our expectations from post-Born corrections. These corrections effectively incorporate the non-linearities arising from multi-lens effects. To address numerical challenges and minimize the number of integrals, we propose an approximation based on the observation that $\mathcal{L}(r_1, r_2)$ exhibits a strong peak near $r_1 \approx r_2$.

Thus, we can approximate $\mathcal{L}(r_1, r_3)$ as $\sim \delta_D(r_1 - r_3)$, simplifying the calculations. We then have

$$\int_0^r dr_3 \mathcal{L}(r_1, r_3) \approx Q(r_1)\Theta(r - r_1)\,, \tag{7.45}$$

where $Q(r_1)$ is a function to be determined in a numerical way and we recall that $\Theta(x)$ is the Heaviside step function. This means that

$$\mu^{PB}_{3\,mix} \approx 6\int_0^{r_s} dr_1 \frac{r_1 - r_s}{r_1 r_s}\int_0^{r_s} dr_2 \frac{r_2 - r_s}{r_2 r_s}\int_0^{r_s} \frac{dr}{r^2}\frac{r - r_s}{r r_s} Q(r_1)\Theta(r - r_1) Q(r_2)\Theta(r - r_2)\,. \tag{7.46}$$

For what concerns $Q(r_1)$, since the latter is not a function of r and the integrand $\mathcal{L}$ contributes to the integral in Eq. (7.45) only around $r_3 \approx r_1$, we have that integral (7.45) is independent of the value of r as long as $r > r_1$. To this end, then, we can evaluate the function Q once for all by choosing an r equal or larger than a given comoving distance r^* well-beyond the highest redshift that we investigate. For our purposes, we have chosen $r^* = r(z = 4)$ but the final results are clearly independent of this choice. In this way, we have that

$$Q(r_1) = \int_0^{r^*} dr_3 \mathcal{L}(r_1, r_3)\,. \tag{7.47}$$

Numerical results within this approximation will be discussed in Sect. 7.5.

7.4.3 μ_3^{LSS}: the role of the bispectrum

The evaluation of μ_3^{LSS} is the more interesting and demanding, since involves the 3-point function

$$\overline{\Delta_2 \psi\left(r_1, \vec{n}\right) \Delta_2 \psi\left(r_2, \vec{n}\right) \Delta_2 \Psi^{(2)}\left(r_3, \vec{n}\right)}\,, \tag{7.48}$$

where we have defined

$$\Psi^{(2)} \equiv \frac{1}{2}\left(\psi^{(2)} + \phi^{(2)}\right)\,. \tag{7.49}$$

Indeed, the expression of μ_3^{LSS} in Eq. (7.23) can be easily rewritten as

$$\mu_3^{LSS} = 3\int_0^{r_s} dr_1 \frac{r_1 - r_s}{r_1\, r_s}\int_0^{r_s} dr_2 \frac{r_2 - r_s}{r_2\, r_s}\int_0^{r_s} dr_3 \frac{r_3 - r_s}{r_3\, r_s}\overline{\Delta_2 \psi\left(r_1, \vec{n}\right) \Delta_2 \psi\left(r_2, \vec{n}\right) \Delta_2 \Psi^{(2)}\left(r_3, \vec{n}\right)}\,, \tag{7.50}$$

in which we used Eqs. (7.13), (7.14), and (7.49).

Now we focus on the computation of the 3-point function (7.48). To this end, first of all we use again the Poisson equation to relate $\Psi^{(2)}$ to the second order matter fluctuations, which can be express in perturbation theory [263, 264] as

$$\delta^{(2)}(\eta, \vec{k}) = \int \frac{d^3k_1 d^3k_2}{(2\pi)^3}\delta_D\left(\vec{k} - \vec{k}_1 - \vec{k}_2\right) F_2\left(\vec{k}_1, \vec{k}_2\right)\delta\left(\eta, \vec{k}_1\right)\delta\left(\eta, \vec{k}_2\right)\,, \tag{7.51}$$

with

$$F_2\left(\vec{k}_1, \vec{k}_2\right) = \frac{5}{7} + \frac{1}{2}\frac{\vec{k}_1 \cdot \vec{k}_2}{k_1 k_2}\left(\frac{k_1}{k_2} + \frac{k_2}{k_1}\right) + \frac{2}{7}\left(\frac{\vec{k}_1 \cdot \vec{k}_2}{k_1 k_2}\right)^2\,. \tag{7.52}$$

From Eq. (7.51) we see directly that the stochastic average of $\delta^{(2)}$ vanishes. Indeed, we have that

$$\overline{\delta^{(2)}} \propto \overline{\delta\left(\eta, \vec{k}_1\right)\delta\left(\eta, \vec{k}_2\right)} \sim \delta_D\left(\vec{k}_1 + \vec{k}_2\right)\,. \tag{7.53}$$

Hence, because of the Dirac-delta, this automatically selects only the monopole at $\vec{k} = 0$, with $\vec{k}_1 = -\vec{k}_2$.

However, $F_2\left(\vec{k}_1,-\vec{k}_1\right)=0$. Given these features, we then have that

$$\overline{\Delta_2\psi\left(r_1,\vec{n}\right)\Delta_2\psi\left(r_2,\vec{n}\right)\Delta_2\Psi^{(2)}\left(r_3,\vec{n}\right)}=-2\,C\int\frac{d^3k_1\,d^3k_2\,d^3k_3}{(2\pi)^6}F_2\left(k_1,k_2,k_3\right)$$
$$\times\delta_D\left(\vec{k}_1+\vec{k}_2+\vec{k}_3\right)\frac{P\left(k_1,\eta_1,\eta_3\right)P\left(k_2,\eta_2,\eta_3\right)}{k_1^2k_2^2k_3^2}\Delta_2e^{i\vec{k}_1\cdot\vec{n}r_1}\Delta_2e^{i\vec{k}_2\cdot\vec{n}r_2}\Delta_2e^{i\vec{k}_3\cdot\vec{n}r_3}\,, \tag{7.54}$$

where we have defined[7]

$$C\equiv\frac{27}{8}\frac{\mathcal{H}_0^6\,\Omega_{m0}^3}{a(r_1)a(r_2)a(r_3)}\,, \tag{7.55}$$

and following [135], the kernel F_2 has been rewritten in terms of a third vector $\vec{k}_3$ rather than the angle $\vec{k}_1\cdot\vec{k}_2$ as

$$F_2\left(k_1,k_2,k_3\right)\;=\;-\frac{5\left(k_1^2-k_2^2\right)^2}{28\,k_1^2k_2^2}+\frac{3}{28}\left(\frac{1}{k_1^2}+\frac{1}{k_2^2}\right)k_3^2+\frac{k_3^4}{14\,k_1^2k_2^2}\,. \tag{7.56}$$

At this point, a comment about the factor 2 in Eq. (7.54) is in order. In fact, due to Wick theorem, the stochastic average on the r.h.s. of Eq. (7.54) accounts for all the permuted 2-point functions of the linear matter field and this should contain three different terms. However, since $\overline{\delta^{(2)}}=0$, as discussed after Eq. (7.52), only two permutations survive. Moreover, these two terms are equal due to the symmetry under the exchange $r_1\leftrightarrow r_2$. This, then, leads to the factor 2 mentioned above.

From Eq. (7.54), we can write the 3-point function as

$$\overline{\Delta_2\psi\left(r_1,\vec{n}\right)\Delta_2\psi\left(r_2,\vec{n}\right)\Delta_2\Psi^{(2)}\left(r_3,\vec{n}\right)}=\frac{C(r_1,r_2,r_3)}{\pi^5}\sum_{\ell_1\ell_2\ell_3}\ell_1\left(\ell_1+1\right)\ell_2\left(\ell_2+1\right)\ell_3\left(\ell_3+1\right)$$
$$\times\left(\begin{array}{ccc}\ell_1&\ell_2&\ell_3\\0&0&0\end{array}\right)^2\left(2\ell_1+1\right)\left(2\ell_2+1\right)\left(2\ell_3+1\right)\int dk_1\,dk_2\,dk_3\,dx\,x^2P\left(k_1,\eta_1,\eta_3\right)P\left(k_2,\eta_2,\eta_3\right)$$
$$\times F_2\left(k_1,k_2,k_3\right)j_{\ell_1}\left(k_1r_1\right)j_{\ell_1}\left(k_1x\right)j_{\ell_2}\left(k_2r_2\right)j_{\ell_2}\left(k_2x\right)j_{\ell_3}\left(k_3r_3\right)j_{\ell_3}\left(k_3x\right)\,, \tag{7.57}$$

where

$$\left(\begin{array}{ccc}\ell_1&\ell_2&\ell_3\\m_1&m_2&m_3\end{array}\right)\,, \tag{7.58}$$

denotes the so-called 3-j Wigner symbol, which is non-null only when $m_1+m_2+m_3=0$ and (ℓ_1,ℓ_2,ℓ_3) satisfy the triangular inequality. The presence of these symbols selects only specific shapes for the sums in ℓ-space. The detailed derivation of Eq. (7.57) can be found in Appendix on page 141. Here, we directly report the results that are useful for us to discuss the underlying physics. Despite its compact form, Eq. (7.57) is still quite demanding for our scopes. Indeed, we still need to evaluate the contribution to the third moment as given in Eq. (7.23). This implies that three line-of-sight integrals must be performed over Eq. (7.57). In total, then, we have to numerically compute seven integrals for each non-null set of (ℓ_1,ℓ_2,ℓ_3), and this is quite unpractical from the numerical viewpoint.

In order to face the dramatic need for reducing the number of integrals, we invoke the Limber approximation for each integral in k-space in Eq. (7.57). Thanks to it, in fact, we can make the following approximation [265–267]

$$\frac{2}{\pi}\int dkk^2g(k)j_\ell(kr)j_\ell(ks)\approx\frac{\delta_D\left(r-s\right)}{r^2}g\left(\frac{\ell+1/2}{r}\right)\,, \tag{7.59}$$

---

[7] This factor follows from the fact that the transfer function for $\delta^{(2)}$ is linked to the transfer function of $\Psi^{(2)}$ by the Poisson equation, which preserves the form as the linear one reported in (1.78) or Eq. (D.10).

whenever the function g does not vary too much rapidly. In this way, the approximation (7.59) can be used three times to get rid of the k-space integrals. This reduces the number of remaining integrations to four. Hence, Eq. (7.57) becomes

$$\overline{\Delta_2\psi\left(r_1,\vec{n}\right)\Delta_2\psi\left(r_2,\vec{n}\right)\Delta_2\Psi^{(2)}\left(r_3,\vec{n}\right)} \approx \frac{C}{8\pi^2}\sum_{\ell_1\ell_2\ell_3}\ell_1\left(\ell_1+1\right)\ell_2\left(\ell_2+1\right)\ell_3\left(\ell_3+1\right)$$
$$\times\begin{pmatrix}\ell_1 & \ell_2 & \ell_3\\ 0 & 0 & 0\end{pmatrix}^2\left(2\ell_1+1\right)\left(2\ell_2+1\right)\left(2\ell_3+1\right)\int\frac{dx\,x^2}{r_1^2r_2^2r_3^2}\delta_D\left(x-r_1\right)\delta_D\left(x-r_2\right)\delta_D\left(x-r_3\right)$$
$$\times\frac{P\left(\widetilde{k_1},\eta_1,\eta_3\right)P\left(\widetilde{k_2},\eta_2,\eta_3\right)}{\widetilde{k_1}^2\widetilde{k_2}^2\widetilde{k_3}^2}F_2\left(\widetilde{k_1},\widetilde{k_2},\widetilde{k_3}\right)\,, \tag{7.60}$$

where $\widetilde{k_i}\equiv\frac{\ell_i+1/2}{r_i}$. The three delta Dirac distributions in Eq. (7.60) simplify the three line-of-sight integrals in Eq. (7.50), leading to the final expression for the LSS contribution to the third moment

$$\mu_3^{LSS} = 6\sum_{\ell_1\ell_2\ell_3}\ell_1\left(\ell_1+1\right)\ell_2\left(\ell_2+1\right)\ell_3\left(\ell_3+1\right)\begin{pmatrix}\ell_1 & \ell_2 & \ell_3\\ 0 & 0 & 0\end{pmatrix}^2\frac{\left(2\ell_1+1\right)\left(2\ell_2+1\right)\left(2\ell_3+1\right)}{\left(4\pi\right)^2}$$
$$\times\int_0^{r_s}dx\,\frac{C(x,x,x)}{x^4}\left(\frac{x-r_s}{x\,r_s}\right)^3\frac{P\left(\widetilde{k_1},\eta_x,\eta_x\right)P\left(\widetilde{k_2},\eta_x,\eta_x\right)}{\widetilde{k_1}^2\widetilde{k_2}^2\widetilde{k_3}^2}F_2\left(\widetilde{k_1},\widetilde{k_2},\widetilde{k_3}\right)\,, \tag{7.61}$$

where we defined now $\widetilde{k_i}=\frac{\ell_i+1/2}{x}$ and $\eta_x\equiv\eta_0-x$.

Finally, we can write the skewness

$$\kappa_3^{LSS}=\frac{\mu_3^{LSS}}{\left(\sigma^2\right)^{3/2}}\,, \tag{7.62}$$

which is related to the bispectrum and non-linear structures.

7.5 Numerical results

In this section, we discuss the numerical integrations of the analytical results for the skewness given by Eqs. (7.35), (7.44), and (7.62). We work with the fiducial cosmology given by the ΛCDM parameters: cold dark matter density $\Omega_c=0.2638$, baryon density $\Omega_b=0.04827$, reduced Hubble constant $h=0.67556$, primordial power-spectrum amplitude $A_s=2.215\times10^{-9}$ and spectral index $n_s=0.9619$ in accordance with [166].

All figures reported in this chapter are extracted from [TS 5].

7.5.1 The smoothing scale

The evaluation of the skewness, or any other 1-point function, is strongly sensitive to the non-linear nature of structure formation. However, by working in perturbation theory, we know that our prediction will fail beyond the mildly non-linear scale. Therefore, our prediction can be compared to real observations only when the non-linear effects are filtered out, by introducing a smearing scale in real space of size ρ. In this regard, we use a spherical top-hat window function in real space, see Eq. (1.82) in Chapter 1. This procedure introduces a window function $W(k,\rho)$ in Fourier space given by Eq. (1.81), which we recall to be

$$W(k,\rho)=3\,\frac{j_1\left(k\rho\right)}{k\rho}\,. \tag{7.63}$$

As a consequence, the window function affects the power spectrum as

$$P(k,\eta_1,\eta_2) \to P_\rho(k,\eta_1,\eta_2) \equiv P(k,\eta_1,\eta_2) W^2(k,\rho)\,. \tag{7.64}$$

In the following, we will investigate how suitable choices for ρ can be made: we will consider the cases of ρ equal to 5, 10 and 20 Mpc/h.

With such smoothing scale, all the integrals over the momentum k converge quickly, and the choice of $k_{\rm max}$ become numerically irrelevant. Since the time required to evaluate μ_3^{LSS} scales with $k_{\rm max}^3$, we set $k_{\rm max}$ to achieve the percent level precision.

7.5.2 Quadratic and Post-Born terms

We start our numerical investigation by looking at the contributions to the skewness arising from the linear gravitational potential, derived in Sect. 7.4.1 and 7.4.2. For this discussion, we will use the cutoff in real space on small scales as prescribed by Eq. (7.64). Results are shown in Fig. 7.2 for the choices of $\rho = 5$, 10, 20 Mpc/h, respectively. For each case, we consider linear matter power spectrum (left panels) and HaloFit model for the matter power spectrum (right panels).

With these results, we can spot common features among the different cases. First of all, we notice that quadratic terms in κ_3^Q (blue solid lines in Fig. 7.2) are always positive and lead to an increasing skewness with redshift. The order of magnitude of this term reaches about 10^{-2}. In this regard, the positive sign was already expected just by looking at the structure of κ_3^Q in Eq. (7.35), since it is just proportional to the dispersion of the $d_L(z)$ distribution. We have also checked that our framework is in a good agreement with [144] when we push the coarse-graining scale up to 0.3 Mpc/h, roughly corresponding to the UV cutoff $k_{UV} = 10$ h/Mpc used in [144].

For what concerns the post-Born contribution to the skewness, namely κ_3^{PB} in Eq. (7.44), blue dashed lines in Fig. 7.2 show two important features. First of all, the post-Born contribution to the skewness is always negative. This is important to be addressed since κ_3^{PB} in Eq. (7.44) does not show any manifest sign, contrary to κ_3^Q. As a second matter of fact, post-Born corrections contribute to the skewness with the same order of magnitude of κ_3^Q. This is somehow in line with the structure of κ_3^Q and κ_3^{PB}, since they just involve different the line-of-sight integrals of the same kernels $\mathcal{L}(r,r')$. Hence, these two features lead to a competitive effect between κ_3^Q and κ_3^{PB}. Indeed, we have a neat effect for the linear gravitational potential skewness, which is still positive but attenuated (solid red lines in Fig. 7.2). We remark that all the features are shared regardless the value of ρ and whether linear or non-linear matter power spectrum is considered.

The actual contribution of the non-linear scales to the sum $\kappa_3^Q + \kappa_3^{PB}$ is quantified in Fig. 7.3. Indeed, here we show the relative difference

$$\Delta\kappa_3 \equiv 1 - \frac{\left(\kappa_3^Q + \kappa_3^{PB}\right)_{\rm linear}}{\left(\kappa_3^Q + \kappa_3^{PB}\right)_{\rm Halo}}\,, \tag{7.65}$$

as for different smoothing scales ρ. For a value of $\rho = 20$ Mpc/h, the non-linearities in $P_\rho(k)$ marginally contribute to the total effect with a relative correction of $\sim 0.1\%$. The non-linear scales happen to be more relevant when ρ decreases, namely with a few percent and almost 10% relative correction respectively with a coarse-graining radius of 10 Mpc/h and $\rho = 5$ Mpc/h. The impact of non-linearities in the matter power spectrum also decreases by going to higher redshifts. Let us remark that, in principle, replacing the linear power spectrum in the perturbative expansion with HaloFit is not self-consistent. However this can give us a rough estimation of the expected accuracy of our prediction based on perturbation theory

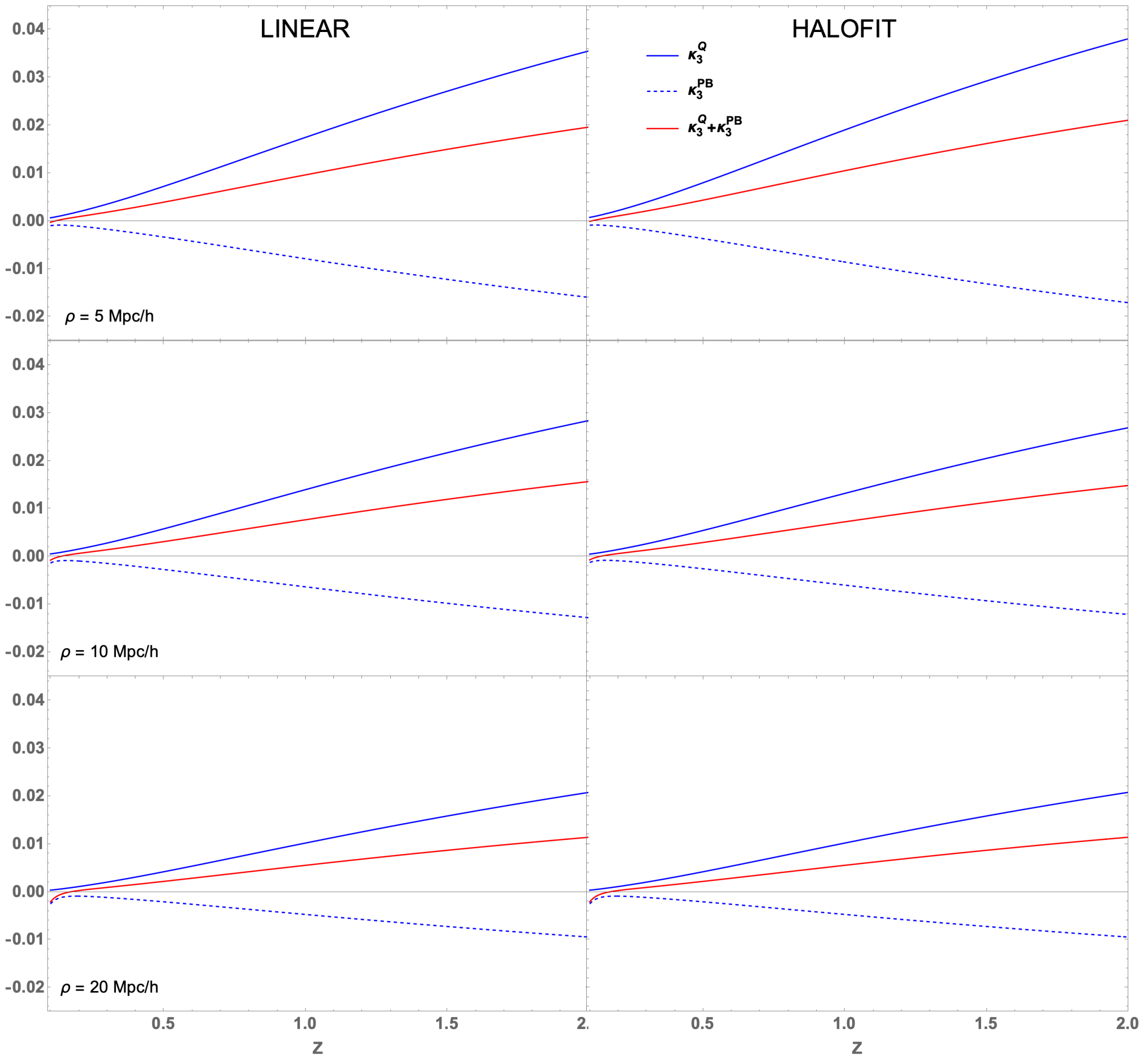

Figure 7.2: Quadratic (blue), post-Born (blue dashed) terms and their sum (red) for the skewness, evaluated at with a coarse-graining scale $\rho = 5$ Mpc$/h$ (top), $\rho = 10$ Mpc$/h$ (center) and $\rho = 20$ Mpc$/h$ (bottom). Left panels are obtained with linear power spectrum, whereas right panels consider HaloFit model for the matter power spectrum.

for different smoothing scales.

7.5.3 Bispectrum

The numerical evaluation of the κ_3^{LSS} from Eq. (7.62) requires some subtleties to be accounted for. In fact, from Eq. (7.61), we have to specify the value of $\ell_{\max}$ to effectively compute the contribution of the bispectrum to the skewness. Since the physical cutoff is determined by the smoothing scale ρ, we only need to ensure that $\ell_{\max} \gtrsim r_s/\rho$, where the specific value is chosen to guarantee a percent precision.

Once again, we perform numerical investigations by using linear matter power spectrum and HaloFit model. For different values of the coarse-graining scale ρ, the numerical results are reported in Fig. 7.4, where we have adopted linear power spectrum in the left panel and HaloFit model in the right one.

At first sight, a general feature is that the absolute value of κ_3^{LSS} is decreasing with the redshift. In particular, whereas the values at $z \sim 1$ are of order 0.1, the skewness at lower redshifts varies more and

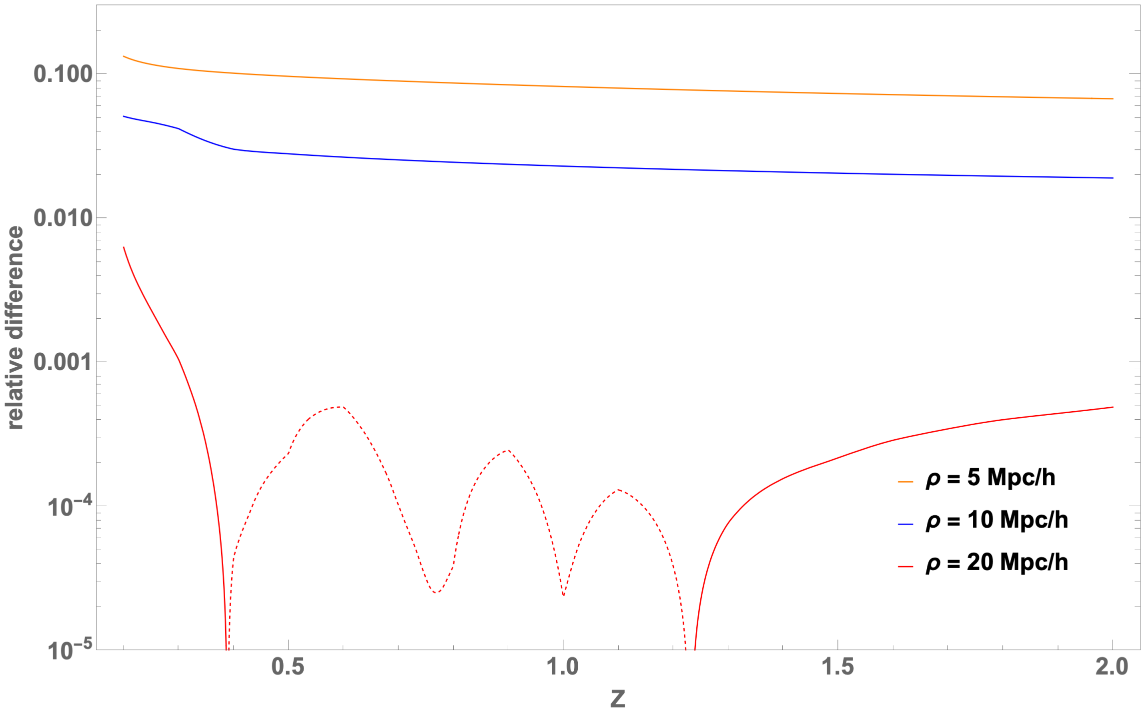

Figure 7.3: Relative difference between the linear and non-linear matter power spectrum for the sum $\kappa_3^Q + \kappa_3^{PB}$. We consider different coarse-graining scales: $\rho = 5$ Mpc$/h$ (orange), $\rho = 10$ Mpc$/h$ (blue) and $\rho = 20$ Mpc$/h$ (red). Dashed curve refers to negative values.

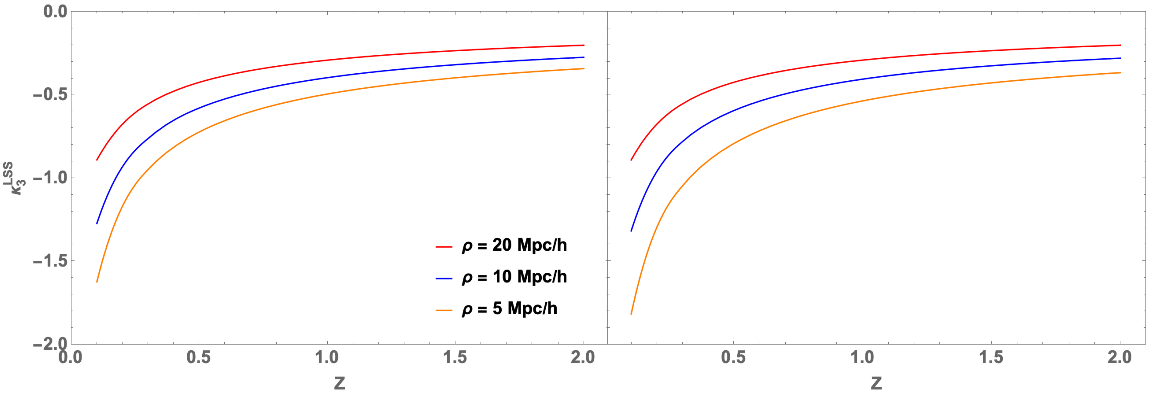

Figure 7.4: Contribution to the skewness given by the the bispectrum for the linear (left panel) and HaloFit (right panel) power spectrum for a coarse-graining scale of $\rho = 20$ Mpc$/h$ (red), $\rho = 10$ Mpc$/h$ (blue) and $\rho = 5$ Mpc$/h$ (orange).

becomes $\mathcal{O}(1)$ when ρ becomes smaller. Moreover, the value is quite insensitive of the kind of spectrum adopted for $\rho = 20$ Mpc$/h$. This last feature is in line with the fact that the involved scales still evolve almost linearly for this case.

A similar behavior occurs also for the case $\rho = 10$ Mpc$/h$. Even in this case, the value of ρ is still such that non-linear features in the power spectrum are marginally relevant, and then the HaloFit model returns results that are almost alongside the ones obtained by the linear power spectrum. However, we notice that the overall amplitude increases quite a lot when we lower the coarse-graining scale from 20 to 10 Mpc$/h$. As a quantitative instance, the comparison between red and blue curves in Fig. 7.4 at

$z = 0.1$ exhibits an increasing in the absolute value of the skewness that is of $\sim 40\%$. This confirms that a significant amount of information is encoded in the skewness within the scales of 10 to 20 Mpc$/h$. However, as the prediction from linear theory does not deviate significantly from the estimation using HaloFit, we are still within a regime where perturbation theory has not yet failed.

Finally, with orange curves in Fig. 7.4 we report the numerical results for $\rho = 5$ Mpc$/h$. For this case study, we have new emerging features. First of all, we start to appreciate a more prominent difference between the linear power spectrum and the non-linear one, and this difference is more evident at smaller redshifts. In fact, here we have an enhancement when the HaloFit model is considered of $\sim 10\%$, as can be appreciated also in Fig. 7.5, where we show the analogous of Fig. 7.3 but only for κ_3^{LSS}. This increasing of κ_3^{LSS}, as given by Eq. (7.62), follows the separate increasing of the two quantities in its ratio, namely μ_3^{LSS} in Eq. (7.61) and σ^3 as derived from Eq. (7.32). Given that, we have that the numerator and the denominator of this ratio separately increase when we decrease ρ from 20 to 5 Mpc$/h$. Hence, by considering the discrepancy between the linear power spectrum and HaloFit as an indicator of the validity range of perturbation theory, we observe that for $\rho = 5$ Mpc$/h$, the accuracy of perturbation theory cannot be trusted beyond approximately 10%. We also remark that at those redshifts our results are only indicative of the order of magnitude, since other relativistic effects here neglected, such as the Doppler correction might significantly alter the result. This is indeed the case for the dispersion, as shown in Fig. 8 of [144]. We plan to investigate more in details the contribution of other relativistic effects on small redshift in a forthcoming paper. On the other hand, we also point out that the result is quite stable for $z > 0.4$ when we decrease the value of ρ.

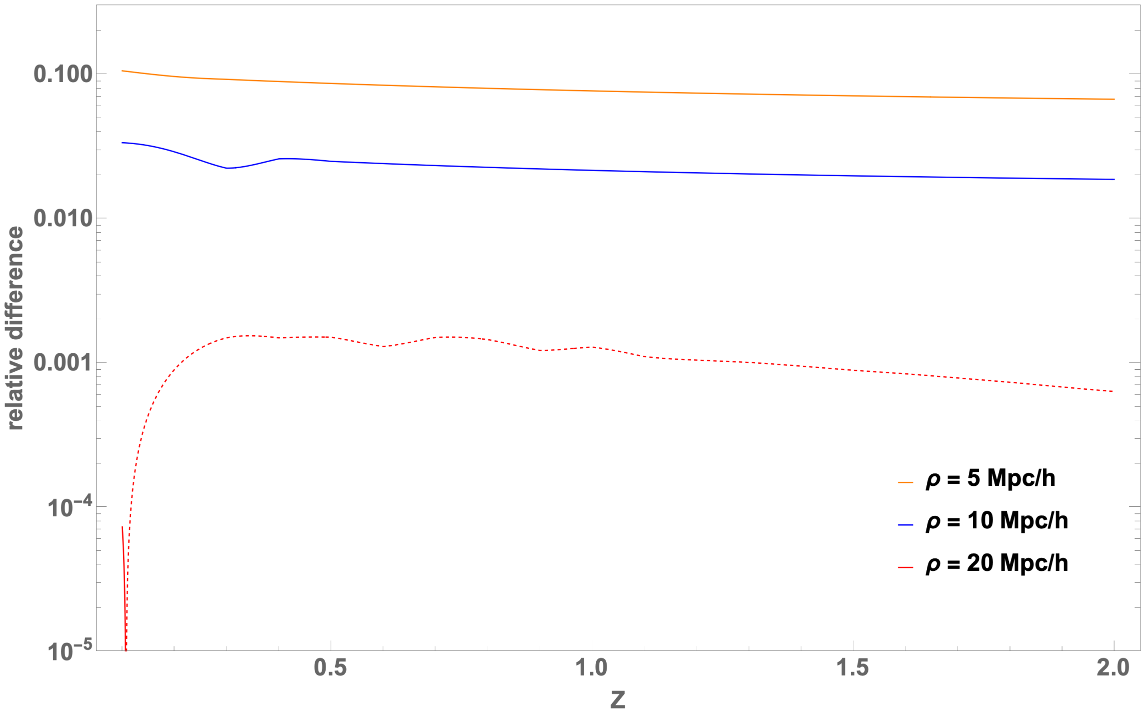

Figure 7.5: Relative difference between the linear and non-linear matter power spectrum for the sum κ_3^{LSS}. We consider different coarse-graining scales: $\rho = 5$ Mpc$/h$ (orange), $\rho = 10$ Mpc$/h$ (blue) and $\rho = 20$ Mpc$/h$ (red). Dashed curve refers to negative values.

Two final comments are in order before concluding the discussion devoted to κ_3^{LSS}. First of all, we recall that our derivation is based on the Limber approximation for the lensing terms. This gave us an appreciable speed-up of the numerical evaluation, since it reduces the number of numerical integrations to one line-of-sight integral, as given in Eq. (7.61). On the other hand, for smaller redshift, the accuracy of this result might be somehow limited, especially because the discrete sum is limited to larger angular scales, when the Limber approximation shows some issues. The second comment is about the use of the HaloFit model to account for the non-linearities in the matter power spectrum. This is clearly a limitation, again on smaller redshifts, when the role of non-linearities in the LSS is more prominent. Both these shortcomings are less serious at higher scales since i) we weight more the smaller angular scales, where the Limber approximation is more accurate, and ii) we move the peak of the lensing kernel to higher redshifts, where the impact of non-linearities is still relevant but attenuated.

Besides all the numerical limitations due to the usage of approximations, a take-home message that emerges from this chapter is that κ_3^{LSS} is always dominant with respect to κ_3^{Q} and κ_3^{PB}, regardless of the choice of the smoothing scale ρ and the use of linear or non-linear matter power spectrum, as one can see from a direct comparison of Figs. 7.2 and 7.4. Hence, the overall sign of the skewness in the investigated range of redshift due to the lensing is always negative, in accordance with the indication of the numerical simulation of [166]. However, a deeper discussion about how to compare our results with [166] is in order. This is the topic of the next section.

7.6 Comparison with numerical simulations

In this section, we will address the challenges that arise when attempting to compare our results with those obtained from ray-tracing across the numerical simulation presented in [166]. We will also outline the recommended approach to ensure a valid and meaningful comparison. To begin, we provide a brief overview of the key elements employed in [166]. The ray-tracing of light-like geodesic in [166] has been performed through a relativistic Universe simulated with *gevolution* [139], with the following cosmological parameters: $h = 0.67556$, $\Omega_c = 0.2638$, and $\Omega_b = 0.048275$. Furthermore, the radiation density that includes massless neutrinos with $N_{\rm eff} = 3.046$ and linear initial conditions are computed with the Cosmic Linear Anisotropy Solving System (CLASS) [268–271] at redshift $z_{\rm ini} = 127$, assuming a primordial power spectrum with amplitude $A_s = 2.215 \times 10^{-9}$ (at the pivot scale 0.05 Mpc^{-1}) and spectral index $n_s = 0.9619$. In this regards, the skewness has been obtained with the following remarks:

1. all the ray-traced light-like geodesics start from a point where a local overdensity has created an Halo;
2. structures evolve in a box with size 2.4 Gpc/h whose grid space is 312.5 kpc/h. Hence, we expect that structures can be investigated roughly up to a scale in Fourier space of 3 h/Mpc;
3. the distribution of the obtained distance-redshift relation is binned in four bins of width 0.5, ranging from $z = 0$ until $z = 2$.

For the sake of completeness, we also report that the ray-tracing in [166] is performed through a light-cone with a partial covering of the observed sky of 450 deg^2. Moreover, the simulations in [166] link the density contrast to the gravitational potential beyond the Newtonian approximation through the second-order Hamiltonian constraint (see Eq. (2.19) of [272]).

With this in mind, we have then extrapolated from Fig. 2 in [166] the values for the skewness in the four bins shown in Table 7.1. The results of Table 7.1 seem quite in disagreement with what we have obtained in Sect. 7.5 for the first two bins, whereas they match better at higher redshifts. However, we have to keep in mind the previous bullet points to understand how our results should (or better, could) be interpreted against [166].

First of all, bullet point 1 states that only regions in the simulated Universe where the overdensity is high enough to have created Halos are spanned by the ray-traced distance-redshift distribution. This

Bin	Redshift Range	Skewness κ_3 from [166]
1	0 - 0.5	-2.27
2	0.5 - 1	-1.44
3	1 - 1.5	-0.72
4	1.5 - 2	-0.44

Table 7.1: Values of the skewness for the distance-redshift relation distribution obtained in [166] from the ray-tracing of photons across a ΛCDM Universe simulated with *gevolution*. Results have been obtained by binning the dataset in four redshift bins from 0 to 2 with bin width of 0.5.

motivates well the adoption of a number-count weighted prescriptions for the averages in Eq. (7.16) since this naturally weights more regions where structures are more likely to have been created.

Moving forward with the discussion, bullet point 2 tells that no smoothing-scale procedure has been introduced in [166], beyond the grid space of the numerical simulation. Moreover, this implies that the expected results can probe scales up to the deeply non-linear regime, and this is somehow problematic for the analytic investigations, since the validity of our perturbative scheme is at least questionable on those scales. However, this point could be easily overcame, since a smoothing scale procedure could be applied as well to the simulated Universe.

Finally, for what concerns bullet point 3, the bin width adopted in [166] is quite large when compared to our infinitesimal bin formalism and this can introduce spurious contamination to the extrapolated skewness in two regards: first, by introducing background effects that are not at all related to the LSS and, secondly, by introducing a plethora of other relativistic effects, such as the contamination due to cross correlations with density fluctuations and redshift-space-distortion in Eq. (7.16), which could complicate the actual analysis. This point can be treated either by slicing the redshift space with more narrow bins or by developing our analytic formalism to the finite bin case. We plan to achieve the latter task in a forthcoming work.

Given all the assumptions and the intrinsic differences that are present between our analytical findings and the numerical ones of [166], we believe that it is quite remarkable that the two results share the same signature and differ only by an order unity factor. In our opinion, our results open an interesting window to resolve the previous bullet points and provide an ultimate comparison.

Conclusions

In this thesis we discussed the robustness of the two pillars of the ΛCDM model, namely General Relativity and the cosmological principle. We explored different scenarios in modified gravity and inhomogeneous cosmologies.

In Chapter 3, we performed a redshift binned analysis of the Pantheon dataset of SNe Ia [176], dividing the sample into equally populated redshift bins. We pointed out a slow evolution of the Hubble constant H_0 with the redshift z, described by the function $H_0^{\rm fit}(z)$ in Eq. (3.4) with a parameter α that is consistent with zero (no evolution) between 1.2 σ and 2.0 σ (see Table 3.1). The evolutionary behavior of $H_0^{\rm fit}(z)$ occurs regardless of the binning division both in the ΛCDM and $w_0 w_a$CDM models. It seems that the Hubble constant tension also emerges locally within the narrow redshift range $0 < z < 2.26$ of the Pantheon sample of SNe Ia.

Then, extrapolating the fit function of $H_0^{\rm fit}(z)$ (3.4) at higher redshifts, we obtain values of H_0 that are remarkably consistent within 1 σ with the CMB measurements by Planck [40]. Our results could point out an intrinsic trend of the Hubble constant with the redshift, which might imply the mismatch between independent measurements of the Hubble constant referred to probes at different redshifts in the early and late Universe.

We remark that we performed a one-dimensional analysis to obtain constraints only on H_0. Actually, in Chapter 4, we extended the analysis and obtain similar results, including BAOs and considering more than one variable in the MCMC methods, for instance H_0 and Ω_{m0}.

Our analysis could suggest the presence of a hidden astrophysical effect, which is the reason for the evolution of $H_0^{\rm fit}(z)$ and has not been taken into account so far. Alternatively, the observed effect may point out that we need a cosmology beyond the ΛCDM paradigm. We discussed the $f(R)$ modified gravity theories in Chapter 4 and proposed a possible form for the scalar field potential (4.10) in the Jordan frame and the respective $f(R)$ function (4.12), inferred from the results of previous abovementioned analysis. Furthermore, we suggested that a new binned analysis of the Pantheon sample, adopting the modified version of the luminosity distance within the framework of $f(R)$ gravity, could be worthwhile to test new physics.

In Chapter 5, we presented a method to interpret an effective Hubble constant $H_0^{\rm eff}(z)$ that runs with the redshift within the $f(R)$ gravity in the Jordan frame. Indeed, we pointed out that the extra d.o.f., i.e., the scalar field dynamics, in such a theoretical scheme might lead to a redefinition of the Hubble constant, as indicated in Eq. (5.5). Motivated from the previous results shown in Chapters 3 and 4, we built a new $f(R)$ model. Our study is able to simultaneously address two key points: on one hand, we obtained a modified gravity model as a suitable candidate alternative to the dark energy component; on the other hand, we provided a natural interpretation for the profile of $H_0^{\rm fit}(z)$ obtained in Chapters 3 and 4. In particular, our results gave us a new perspective to address the Hubble constant tension through a binning approach, thus we foster investigations on the astrophysical parameters of SNe Ia and further theoretical discussions.

To explore the possible evolution of cosmological parameters, it could be very useful in the future to include in our analysis also probes at higher redshifts, such as quasars and GRBs, which in principle could allow to enlarge the redshift range of the actual Hubble diagram [7, 202, 203, 273–277] . We based our analysis on the Pantheon sample of SNe Ia, which datasets was public during the development of this thesis. At the present, the Pantheon+ data [71] are also available, and we might repeat this kind of analysis in the future to check a possible trend of H_0. Moreover, as a future perspective, it could be interesting to investigate together both the H_0 and S_8 tensions (Sect. 1.1.7). Indeed, we should bear in mind that these tensions may be correlated, hence if we try to alleviate one of them, we have to check that the other one does not become worse.

Concerning the inhomogeneous cosmology, we followed firstly a metric approach, considering the LTB line element. In Chapter 6, we analyzed the LTB spherically symmetric solution, linearized over a flat FLRW background, comparing its morphology in GR and $f(R)$ modified gravity theories, as viewed in the Jordan frame. In the former case, we referred to the ΛLTB model, including a matter fluid and a cosmological constant; in the latter model, we considered the $f(R)$ HS formulation (Sect. 1.3.2).

We studied the dynamics in both cosmological scenarios to highlight the peculiarities of these models. To describe spherically symmetric deviations from homogeneity in the late Universe, we used the separation of variables method to address the partial differential equations system for the first-order perturbation. Then, the radial components of such a reduction procedure were analytically integrated, while the-time dependent part required a numerical treatment.

The key difference between the two cosmological models studied in Chapter 6 is the different form of the 0-1 component of the gravitational field equations. Indeed, in the ΛLTB model, Eq. (2.2a) can be easily solved by removing one of the two free metric functions of the problem, hence the LTB metric takes the well-known simplified form in Eq. (2.7). On the other hand, within the framework of the $f(R)$ gravity in the Jordan frame, the presence of a non-minimally coupled scalar field prevents the simplification above in the 0-1 component (6.1a), and we had to deal with two distinct metric functions $\alpha(t,r)$ and $\beta(t,r)$ in the LTB metric given by Eq. (2.1).

As a consequence, our results might be considered as specific markers of the evolution of matter distribution in different theoretical models. Indeed, GR provides only a natural decay of the radial perturbations for large r values, following a power law, as it emerged from Eq. (6.29). Differently, in the $f(R)$ modified gravity formulation, we obtained the Yukawa-like decaying for the radial perturbations of the scalar functions given by Eqs. (6.43), (6.44), (6.45), and (6.46). Furthermore, we employed the $f(R)$ HS model to describe the background Universe for comparison with the ΛCDM model, but we could have considered other viable $f(R)$ modified gravity models. Indeed, we stress that our main result regarding the Yukawa-like radial perturbations does not depend on the $f(R)$ functional form.

It should be noted that Yukawa-like radial profiles are recurring in $f(R)$ theories, as evidenced, for instance, in other studies [278–281] by the presence of Yukawa-like corrections in the Newton potential with consequent implications for the dark matter problem and the flat rotation curves of galaxies. Furthermore, the different morphology of the radial solutions between the ΛLTB model and inhomogeneous $f(R)$ cosmology obtained in Chapter 6 may be possible hints of a theory beyond GR.

For what concerned the time evolution of inhomogeneous perturbations both in the ΛLTB model and in the LTB solution as emerging from the $f(R)$ gravity in the Jordan frame, the numerical analysis outlined that it is always possible to obtain a non-divergent amplitude of the perturbations as time goes by, according to the reliable idea of a stable homogeneous and isotropic Universe in the near future.

Nevertheless, we are aware that our result has one limitation: the obtained radial solutions clearly diverge in the center of the LTB symmetry, where the observer (i.e. human location) is intended to be set. This feature simply suggests that our solution has a non-perturbative extension from a given large enough radial coordinate up to $r = 0$, which is an important task for future investigations in the late Universe. The present analysis fosters further studies about inhomogeneous cosmology when regarded as a local (non-linear) deformation of the FLRW geometry, as it may be also possibly pointed out by local measurements of the Hubble constant. The method presented in Chapter 6 through the investigation of spatial inhomogeneities may become a powerful tool to test the robustness of the cosmological concordance model.

To explore the impact of local inhomogeneities on cosmological observables like the luminosity distance-redshift relation, we presented in Chapter 7 a general method by applying the covariant and gauge-invariant formalism for the light-cone averages detailed in [174]. We discussed the role of non-linearities in the corrections of the Hubble-Lemaître diagram and provided for the first time an analytic evaluation of the skewness for the distance-redshift distribution in the ΛCDM model. We developed the theoretical framework to compare and understand the analogous results of non-Gaussian features [166] obtained from N-body numerical fully relativistic simulations of cosmic structure formation based on *gevolution* [139].

Within our perturbative approach, we included lensing contribution and noted that the second-order corrections of the luminosity distance are enough to determine the leading-order terms of the skewness. In particular, we recall that we made the assumption of an infinitesimal bin width to perform averages for the redshift distribution. We obtained three different terms in the final formula (7.23) of the skewness, due to quadratic, Post-Born corrections and higher-order correlators. The latter are related to the matter bispectrum, integrated along the line of sight. From our numerical investigation, it has emerged that the bispectrum contribution play a dominant role, while quadratic and Post-Born terms exhibit a competitive effect. Despite the number of approximations in the method presented in Chapter 7, our analytical estimation provided remarkably an amplitude of the skewness, which is negative and of the same order of magnitude as the one resulted from to the numerical simulations in [166] (see Sect. 7.6 for a detailed discussion).

We also recall that, in order to have a result indendent of the UV behavior, we introduced a smoothing or coarse-graining scale in real space and determined its impact on the final amplitude of the skewness. To this end, our results pointed out that varying the smoothing scale from 20 to 10 Mpc$/h$ leads to a 40% increasing of the skewness at small redshift ($z \sim 0.1$), although the dependence on the coarse-graining scale is less severe for distant sources ($z \sim 1$). This is quite remarkable, since it seems to suggest that there is room for better agreement with the numerical simulations [166], in which smaller scales than ours had been probed (see again Sect. 7.6).

Our method is also interesting to understand better if a perturbative approach is still valid and at which level to take into account local inhomogeneities. In this regard, it could be worthwhile in the future to generalize the method developed in Chapter 7 also for the case of a small finite redshift bin of size $\Delta z \sim 0.5$, since this was adopted in the abovementioned simulations. Furthermore, including other general relativistic effects, such as the Doppler effect, in the fluctuations of the luminosity distance and the choice of the smoothing scale as in the analysis of the simulated data might be important elements at smaller redshifts.

To conclude this thesis, we would like to stress again that if cosmological tensions still persist in the next few decades, we should be aware that we might be less conservative in developing the theoretical framework to describe our Universe. In this regard, we have to investigate wheter GR and the cosmological principle are the real solid pillars of our concordance cosmological model through several independent methods. In addition to theoretical attempts, the analysis developed in this thesis may have a relevant impact on the observations of the LSS of the Universe, when forthcoming missions [60–66]detect the clumpy galaxy distribution with greater accuracy.

A – Testing the spatial isotropy in the LTB metric in the Jordan frame

We want to check that the spatial isotropy in the LTB geometry is also preserved by the field equations in the Jordan frame of $f\left(R\right)$ modified gravity. In particular, we prove that the 2-2 component of gravitational field equations depends on the other ones. Moreover, it can be easily checked that the 2-2 and 3-3 components are exactly the same.

It should be noted that the isotropy in GR can be shown in field equations by employing Eq. (2.3). However, within the framework of the Jordan frame of $f\left(R\right)$ gravity, this simple relation no longer applies, because of the presence of the non-minimal coupling between the scalar field ϕ and the metric. Then, we need a careful analysis of field equations to verify the isotropy in the LTB metric. In this regard, we rewrite the gravitational field equations (1.113a) in the Jordan frame as $G_{\mu\nu} = S_{\mu\nu}$, where

$$S_{\mu\nu} = \frac{\chi}{\phi}\, T_{\mu\nu} - \frac{1}{2\,\phi}\, g_{\mu\nu}\, V\left(\phi\right) + \frac{1}{\phi}\, \left(\nabla_\mu \nabla_\nu \phi - g_{\mu\nu}\, \Box\, \phi\right) \tag{A.1}$$

denotes all the source elements in a compact way.

Considering a pressure-less dust, the 2-2 component of Eqs. (1.113a) in the Jordan frame in the LTB metric (2.1), i.e. $G^2_{\ 2} = S^2_{\ 2}$, is written as

$$\begin{aligned}
&\ddot{\alpha} + \ddot{\beta} + \dot{\alpha}^2 + \dot{\beta}\, \left(\dot{\alpha} + \dot{\beta}\right) + \\
&\quad - e^{-2\,\alpha}\, \left[\beta'' - \beta'\, \left(\alpha' - \beta'\right)\right] = \frac{V\left(\phi\right)}{2\,\phi} + \\
&\quad - \frac{1}{\phi}\, \left\{\ddot{\phi} + \left(\dot{\alpha} + \dot{\beta}\right)\, \dot{\phi} - e^{-2\,\alpha}\, \left[\phi'' - \phi'\, \left(\alpha' - \beta'\right)\right]\right\}\,.
\end{aligned} \tag{A.2}$$

For the sake of convenience, we also rewrite here the 1-1 component $G^1_{\ 1} = S^1_{\ 1}$, that is Eq. (6.1c):

$$\begin{aligned}
&2\,\ddot{\beta} + 3\,\dot{\beta}^2 + e^{-2\,\beta} - e^{-2\,\alpha}\, \left(\beta'\right)^2 = \frac{V\left(\phi\right)}{2\,\phi} + \\
&\quad - \frac{1}{\phi}\, \left[\ddot{\phi} + 2\,\dot{\beta}\,\dot{\phi} - 2\,e^{-2\,\alpha}\,\beta'\,\phi'\right]\,.
\end{aligned} \tag{A.3}$$

To verify the isotropy, we start from Eq. (A.3) and search for a proper relation to obtain Eq. (A.2). Trying to generalize the relation (2.3) valid in GR, we can write

$$G^1_{\ 1} + \frac{1}{2\,\beta'}\, \left(G^1_{\ 1}\right)' = S^1_{\ 1} + \frac{1}{2\,\beta'}\, \left(S^1_{\ 1}\right)'\,, \tag{A.4}$$

which is equivalent to

$$\begin{aligned}
&\ddot{\alpha} + \ddot{\beta} + \dot{\alpha}^2 + \dot{\beta}\,\left(\dot{\alpha} + \dot{\beta}\right) - e^{-2\,\alpha}\,\left[\beta'' - \beta'\,\left(\alpha' - \beta'\right)\right] \\
&- \frac{\phi'}{2\,\phi\,\beta'}\,G_{\text{extra}} = \frac{V\left(\phi\right)}{2\,\phi} - \frac{\phi'}{2\,\phi\,\beta'}\,S_{\text{extra}} + \\
&- \frac{1}{\phi}\,\left\{\ddot{\phi} + \left(\dot{\alpha} + \dot{\beta}\right)\,\dot{\phi} - e^{-2\,\alpha}\,\left[\phi'' - \phi'\,\left(\alpha' - \beta'\right)\right]\right\}\,.
\end{aligned} \tag{A.5}$$

We have considered geometric G^1_1 and source S^1_1 contributions in Eq. (A.3) and their derivatives with respect to r, and we have defined

$$G_{\text{extra}} = \frac{\ddot{\phi}'}{\phi'} - \ddot{\alpha} - \dot{\alpha}^2 + \left(\frac{\dot{\phi}}{\phi} - 2\,\dot{\beta}\right)\,\left(\dot{\alpha} - \frac{\dot{\phi}'}{\phi'}\right) \tag{A.6}$$

$$\begin{aligned}
S_{\text{extra}} = {} & \frac{\ddot{\phi}'}{\phi'} - \frac{\ddot{\phi}}{\phi} + \frac{\dot{\phi}}{\phi}\,\left(\dot{\alpha} - 2\,\dot{\beta} - \frac{\dot{\phi}'}{\phi'}\right) + 2\,\dot{\beta}\,\frac{\dot{\phi}'}{\phi'} + \frac{V\left(\phi\right)}{2\,\phi} \\
& - \frac{1}{2}\,\frac{dV}{d\phi} + 2\,e^{-2\,\alpha}\,\left(\alpha'\,\beta' - \beta'^2 - \beta'' + \beta'\,\frac{\phi'}{\phi}\right)\,.
\end{aligned} \tag{A.7}$$

Then, comparing Eqs. (A.2) and (A.5), it is quite immediate to recognize that the latter equation becomes

$$G^2_2 = S^2_2 + \frac{\phi'}{2\,\phi\,\beta'}\,\left(G_{\text{extra}} - S_{\text{extra}}\right)\,. \tag{A.8}$$

Note that, as we previously said, the relation (2.3) is no longer valid in the Jordan frame since now we have

$$G^2_2 = G^1_1 + \frac{1}{2\,\beta'}\,\left(G^1_1\right)' + \frac{\phi'}{2\,\phi\,\beta'}\,G_{\text{extra}}\,, \tag{A.9}$$

which is due to an extra term containing the non-minimal coupled scalar field ϕ.

As a last point, we show that the bracket in Eq. (A.8) vanishes. Indeed, it is straightforward to identify the difference $\left(G_{\text{extra}} - S_{\text{extra}}\right) = 0$, since it exactly coincides with the supplementary Eq. (6.3b) given by the effective stress-energy tensor $T^{[\phi]}_{\mu\nu}$ for $\mu = 1$, which is just originated from the gravitational field equations.

Hence, we have proved that the 2-2 component (A.2) of the field equations in the Jordan frame depends on the 1-1 component (A.3) and the additional Eq. (6.3b). As a consequence, despite the presence of extra coupling terms between the scalar field and the metric, the field equations in the Jordan frame of $f\left(R\right)$ gravity implemented at the LTB metric preserve the spatial isotropy, as it must be for a spherically symmetric solution.

B - Separation of variables for the linearly perturbed field equations in the Jordan frame of $f\,(R)$ gravity

In this appendix, we want to rewrite the equation system given by the linearly perturbed field equations (6.36), (6.37), and (6.38) to study separately time and space evolutions of perturbations through the separation of variables method. The final aim is to show explicit calculations to obtain the two sets of equations (6.41) and (6.42), which have been reported in Sect. 6.3.2.

We adopt the factorization (6.39) for all linear perturbations, which we rewrite here for convenience:

$$\begin{aligned} &\delta\alpha\,(t,r) \equiv A_p\,(t)\;\mathcal{A}_p\,(r)\;, \qquad \delta\beta\,(t,r) \equiv B_p\,(t)\;\mathcal{B}_p\,(r)\;, \\ &\delta\rho\,(t,r) \equiv P_p\,(t)\;\varrho_p\,(r)\;, \qquad \delta\phi\,(t,r) \equiv \Phi_p\,(t)\;\varphi_p\,(r)\;. \end{aligned} \tag{B.1}$$

We have split time and radial dependences for each scalar function.

Then, considering the factorization (B.1), the equation system (6.36) becomes:

$$\frac{\mathcal{B}'_p}{\varphi'_p} + \frac{1}{r}\,\frac{\mathcal{B}_p}{\varphi'_p} = \frac{1}{r}\,\frac{\mathcal{A}_p}{\varphi'_p}\,\frac{\dot{A}_p}{\dot{B}_p} - \frac{1}{2\,\bar{\phi}\,\dot{B}_p}\,\left(\dot{\Phi}_p - \frac{\dot{\bar{a}}}{\bar{a}}\,\Phi_p\right)\,, \tag{B.2a}$$

$$\begin{aligned} &\frac{2}{\bar{a}^2}\,\left[\frac{A_p}{r}\,\left(\frac{\mathcal{A}_p}{r} + \mathcal{A}'_p\right) - B_p\,\left(\mathcal{B}''_p + \frac{3}{r}\,\mathcal{B}'_p + \frac{\mathcal{B}_p}{r^2}\right)\right] + \\ &\quad + \left(2\,\frac{\dot{\bar{a}}}{\bar{a}} + \frac{\dot{\bar{\phi}}}{\bar{\phi}}\right)\,\left(\dot{A}_p\,\mathcal{A}_p + 2\,\dot{B}_p\,\mathcal{B}_p\right) = \frac{\chi}{\bar{\phi}}\,P_p\,\varrho_p + \\ &\quad + \left(\frac{1}{2}\,\left.\frac{dV}{d\phi}\right|_{\phi=\bar{\phi}} - \frac{1}{2}\,\frac{V\,(\bar{\phi})}{\bar{\phi}} - \frac{\chi\,\bar{\rho}}{\bar{\phi}} + 3\,\frac{\dot{\bar{a}}}{\bar{a}}\,\frac{\dot{\bar{\phi}}}{\bar{\phi}}\right)\,\frac{\Phi_p\,\varphi_p}{\bar{\phi}} + \\ &\quad + \frac{1}{\bar{a}^2\,\bar{\phi}}\,\left(\Phi_p\,\varphi''_p + \frac{2}{r}\,\Phi_p\,\varphi'_p\right) - 3\,\frac{\dot{\bar{a}}}{\bar{a}}\,\frac{\dot{\Phi}_p\,\varphi_p}{\bar{\phi}}\,, \end{aligned} \tag{B.2b}$$

$$\begin{aligned} &\left(\ddot{B}_p + 3\,\frac{\dot{\bar{a}}}{\bar{a}}\,\dot{B}_p\right)\,\mathcal{B}_p + \frac{1}{\bar{a}^2\,r^2}\,\left[A_p\,\mathcal{A}_p - B_p\,\left(\mathcal{B}_p + r\,\mathcal{B}'_p\right)\right] = \\ &\quad \left(\frac{1}{2}\,\left.\frac{dV}{d\phi}\right|_{\phi=\bar{\phi}} - \frac{V\,(\bar{\phi})}{2\,\bar{\phi}} + \frac{\ddot{\bar{\phi}}}{\bar{\phi}} + 2\,\frac{\dot{\bar{a}}}{\bar{a}}\,\frac{\dot{\bar{\phi}}}{\bar{\phi}}\right)\,\frac{\Phi_p\,\varphi_p}{2\,\bar{\phi}} + \\ &\quad - \frac{1}{\bar{\phi}}\,\left(\frac{1}{2}\,\ddot{\Phi}_p\,\varphi_p + \frac{\dot{\bar{a}}}{\bar{a}}\,\dot{\Phi}_p\,\varphi_p + \dot{\bar{\phi}}\,\dot{B}_p\,\mathcal{B}_p - \frac{\Phi_p\,\varphi'_p}{\bar{a}^2\,r}\right)\,. \end{aligned} \tag{B.2c}$$

We have tried to separate time-dependent and radial terms. However, this equations system exhibits a complicated structure, since it should be noted the occurrence of several mixed terms depending both on t and r. For instance, focusing on Eq. (B.2a), terms on the left-hand side depend only on r, a mixed term is the first contribution on the right side, while the second contribution is only time-dependent.

Using again Eq. (B.1), the linearized scalar field equation (6.37) rewrites as

$$\begin{aligned} &\bar{a}^2 \left[\frac{\ddot{\Phi}_p}{\Phi_p} + 3\, \frac{\dot{\bar{a}}}{\bar{a}}\, \frac{\dot{\Phi}_p}{\Phi_p} + \left(\frac{\dot{A}_p}{\Phi_p}\, \frac{\mathcal{A}_p}{\varphi_p} + 2\, \frac{\dot{B}_p}{\Phi_p}\, \frac{\mathcal{B}_p}{\varphi_p} \right) \dot{\bar{\phi}} + \right. \\ &\left. -\frac{1}{3}\, \frac{dV}{d\phi}\bigg|_{\phi=\bar{\phi}} + \frac{1}{3}\, \bar{\phi}\, \frac{d^2V}{d\phi^2}\bigg|_{\phi=\bar{\phi}} - \frac{\chi}{3}\, \frac{P_p}{\Phi_p}\, \frac{\varrho_p}{\varphi_p} \right] = \\ &\frac{\varphi_p''}{\varphi_p} + \frac{2}{r}\, \frac{\varphi_p'}{\varphi_p}\,, \end{aligned} \tag{B.3}$$

while the linearized continuity equation (6.38) becomes

$$\frac{1}{\bar{\rho}\, \dot{B}_p} \left(\dot{P}_p + 3\, \frac{\dot{\bar{a}}}{\bar{a}}\, P_p \right) + \frac{\dot{A}_p}{\dot{B}_p}\, \frac{\mathcal{A}_p}{\varrho_p} + 2\, \frac{\mathcal{B}_p}{\varrho_p} = 0\,. \tag{B.4}$$

We noticed again the presence of mixed terms depending on t and r, which do not allow us to solve the equations using the separation of variables unless we rely on some simplifying assumptions. For instance, focusing on Eqs. (B.2a) and (B.4), if we require that the perturbations A_p and B_p follow a similar time evolution, i.e.

$$\dot{A}_p = \lambda_1\, \dot{B}_p\,, \tag{B.5}$$

where λ_1 is a constant, then we are able to solve these two equations through the separation of variables method. Actually, we also write equivalently

$$A_p = \lambda_1\, B_p\,, \tag{B.6}$$

which is just Eq. (6.40a), since we can adjust constant term in the first-order perturbation theory.

Then, if we impose the assumption (B.6) in Eq. (B.2a), we obtain two equations, one in the variable t and the other one in r:

$$\dot{B}_p = \frac{1}{2\, \bar{\phi}\, \mu_1} \left(\dot{\Phi}_p - \frac{\dot{\bar{a}}}{\bar{a}}\, \Phi_p \right)\,, \tag{B.7a}$$

$$\mathcal{A}_p = \frac{1}{\lambda_1} \left[\mathcal{B}_p + r\, \left(\mathcal{B}_p' + \mu_1\, \varphi_p' \right) \right]\,, \tag{B.7b}$$

which are just Eqs. (6.42a) and (6.41a), respectively.

In the same way, we can split Eq. (B.4) into Eqs. (6.42e) and (6.41d)

$$\dot{P}_p + 3\, \frac{\dot{\bar{a}}}{\bar{a}}\, P_p + \mu_2\, \bar{\rho}\, \dot{B}_p = 0\,, \tag{B.8a}$$

$$\varrho_p = \frac{1}{\mu_2} \left(\lambda_1\, \mathcal{A}_p + 2\, \mathcal{B}_p \right)\,, \tag{B.8b}$$

respectively, where μ_1 and μ_2 are constants originating from the separation of variables.

Concerning the linearized scalar field equation (B.3), using Eqs. (B.6) and (B.8b), we end up in

$$\bar{a}^2 \left[\frac{\ddot{\Phi}_p}{\Phi_p} + 3\, \frac{\dot{\bar{a}}}{\bar{a}}\, \frac{\dot{\Phi}_p}{\Phi_p} - \frac{1}{3}\, \frac{dV}{d\phi}\bigg|_{\phi=\bar{\phi}} + \frac{1}{3}\, \bar{\phi}\, \frac{d^2V}{d\phi^2}\bigg|_{\phi=\bar{\phi}} + \right.$$

$$+\left(\mu_2\,\dot{\bar{\phi}}\,\frac{\dot{B}_p}{\Phi_p}-\frac{\chi}{3}\,\frac{P_p}{\Phi_p}\right)\,\frac{\varrho_p}{\varphi_p}\Bigg]=\frac{\varphi_p''}{\varphi_p}+\frac{2}{r}\,\frac{\varphi_p'}{\varphi_p}\,. \tag{B.9}$$

At this point, noting a mixed term in the last contribution of the left-hand side, to proceed analytically with the separation of variables, we require an additional simplifying assumption, that is the proportionality between the radial evolution of the matter and scalar field perturbations:

$$\varrho_p=\lambda_2\,\varphi_p\,, \tag{B.10}$$

i.e. Eq. (6.40b), where λ_2 is the proportionality constant.

Hence, we can easily separate time and radial evolutions in Eq. (B.9) to write the two differential equations (6.42d) and (6.41c), respectively:

$$\begin{aligned}&\frac{\ddot{\Phi}_p}{\Phi_p}+3\,\frac{\dot{\bar{a}}}{\bar{a}}\,\frac{\dot{\Phi}_p}{\Phi_p}-\frac{1}{3}\,\frac{dV}{d\phi}\bigg|_{\phi=\bar{\phi}}+\frac{1}{3}\,\bar{\phi}\,\frac{d^2V}{d\phi^2}\bigg|_{\phi=\bar{\phi}}+\\&\quad+\mu_2\,\lambda_2\,\dot{\bar{\phi}}\,\frac{\dot{B}_p}{\Phi_p}-\frac{\chi\,\lambda_2}{3}\,\frac{P_p}{\Phi_p}=\frac{\mu_3^2}{\bar{a}^2}\,, \qquad\qquad \text{(B.11a)}\\&\varphi_p''+\frac{2}{r}\,\varphi_p'-\mu_3^2\,\varphi_p=0\,, \qquad\qquad \text{(B.11b)}\end{aligned}$$

where μ_3 is a constant.

If we focus on Eq. (B.2b), by simplifying mixed terms with Eqs. (B.6), (B.7a), (B.7b), (B.10), and (B.8b), it is straightforward to show that, after long calculations, we encompass the radial part through Eq. (B.11b), and we obtain a single equation in t:

$$\begin{aligned}&\frac{\mu_2\lambda_2}{2\,\mu_1}\left(2\frac{\dot{\bar{a}}}{\bar{a}}+\frac{\dot{\bar{\phi}}}{\bar{\phi}}\right)\left(\frac{\dot{\Phi}_p}{\Phi_p}-\frac{\dot{\bar{a}}}{\bar{a}}\right)+\frac{\chi\,\bar{\rho}}{\bar{\phi}}-\frac{1}{2}\,\frac{dV}{d\phi}\bigg|_{\phi=\bar{\phi}}+\frac{V\left(\bar{\phi}\right)}{2\,\bar{\phi}}\\&+3\frac{\dot{\bar{a}}}{\bar{a}}\left(\frac{\dot{\Phi}_p}{\Phi_p}-\frac{\dot{\bar{\phi}}}{\bar{\phi}}\right)-\chi\lambda_2\frac{P_p}{\Phi_p}+2\mu_1\mu_3^2\frac{\bar{\phi}}{\bar{a}^2}\,\frac{B_p}{\Phi_p}=\frac{\mu_3^2}{\bar{a}^2}\,,\end{aligned} \tag{B.12}$$

which is just Eq. (6.42b).

Finally, regarding the last equation of the system (B.2) to be rewritten with the separation of variables, that is Eq. (B.2c), if we combine it with Eqs. (B.6), (B.7a), (B.7b), we obtain

$$\ddot{B}_p+\dot{B}_p\,\left(3\,\frac{\dot{\bar{a}}}{\bar{a}}+\frac{\dot{\bar{\phi}}}{\bar{\phi}}\right)=\frac{\mu_4}{2\,\bar{a}^2}\,\left(\frac{\Phi_p}{\bar{\phi}}-\mu_1\,B_p\right)\,, \tag{B.13a}$$

$$\mathcal{B}_p=\frac{2}{\mu_4\,r}\,\varphi_p'-\mu_1\,\varphi_p\,, \tag{B.13b}$$

which are exactly Eqs. (6.42c) and (6.41b), respectively, where μ_4 is a constant.

In conclusion, in this appendix, we have shown how the two simplifying assumptions (B.6) and (B.10) are suggested from the analysis of the equation system given by Eqs. (6.36), (6.37), and (6.38) to use the separation of variables. Finally, we have obtained separately two sets of equations (6.41) and (6.42) for the radial and time evolution of linear perturbations, which have been reported in Sect. 6.3.2. Once we have split all field equations into time and space components, we can solve them to obtain linear order perturbations separately in Sect. 6.3.2.1 and Sect. 6.3.2.2.

C - Fourth-order perturbations for the skewness

In this appendix, we prove that Eqs. (7.11) can be equivalently computed holds also when third and fourth order perturbations in the observable and the measure are considered. Hence, it is consistent to consider only second-order perturbations to evaluate the leading order skewness.

We then follow the same approach as the one adopted in Sect. 7.1 and expand

$$\begin{aligned} \frac{\mathcal{S}}{\mathcal{S}^{(0)}} &= 1+\sigma^{(1)}+\sigma^{(2)}+\sigma^{(3)}+\sigma^{(4)}\,, \\ d\mu &= d\mu^{(0)}\left(1+\mu^{(1)}+\mu^{(2)}+\mu^{(3)}+\mu^{(4)}\right)\,. \end{aligned} \tag{C.1}$$

Hence, we obtain for the average m

$$\begin{aligned} m \equiv \overline{\left\langle \frac{\mathcal{S}}{\mathcal{S}^{(0)}} \right\rangle} &= 1+\left\{\overline{I[\sigma^{(2)}]}+\overline{I[\sigma^{(1)}\,\mu^{(1)}]}-\overline{I[\sigma^{(1)}]\,I[\mu^{(1)}]}\right\} \\ &+\left\{\overline{I[\sigma^{(4)}]}+\overline{I[\sigma^{(3)}\,\mu^{(1)}]}+\overline{I[\sigma^{(2)}\,\mu^{(2)}]}+\overline{I[\sigma^{(1)}\,\mu^{(3)}]}-\overline{I[\sigma^{(3)}]\,I[\mu^{(1)}]}\right. \\ &-\overline{I[\sigma^{(2)}\,\mu^{(1)}]\,I[\mu^{(1)}]}-\overline{I[\sigma^{(1)}\,\mu^{(2)}]\,I[\mu^{(1)}]}-\overline{I[\sigma^{(2)}]\,I[\mu^{(2)}]}+\overline{I[\sigma^{(2)}]\,I[\mu^{(1)}]^2} \\ &-\overline{I[\sigma^{(1)}\,\mu^{(1)}]\,I[\mu^{(2)}]}+\overline{I[\sigma^{(1)}\,\mu^{(1)}]\,I[\mu^{(1)}]^2}-\overline{I[\sigma^{(1)}]\,I[\mu^{(3)}]} \\ &\left.+2\overline{I[\sigma^{(1)}]\,I[\mu^{(1)}]\,I[\mu^{(2)}]}-\overline{I[\sigma^{(1)}]\,I[\mu^{(1)}]^3}-\overline{I[\mu^{(4)}]}\right\}\,. \end{aligned} \tag{C.2}$$

First line manifestly reproduces Eq. (7.7), whereas the other lines take into account the next-to-leading order corrections. With Eq. (C.2), we evaluate the α-th order moment of the distribution of $\mathcal{S}/\mathcal{S}^{(0)}$ up to the fourth order as

$$\overline{\left\langle\left(\frac{\mathcal{S}}{\mathcal{S}^{(0)}}-m\right)^{\alpha}\right\rangle}=\sum_{k=0}^{\alpha}(-1)^{\alpha-k}\binom{\alpha}{k}\left(1+A_k^{(2)}+B_k^{(4)}\right)\,, \tag{C.3}$$

where we have defined

$$A_k^{(2)} \equiv \alpha\left\{\overline{I[\sigma^{(2)}]}+\overline{I[\sigma^{(1)}\,\mu^{(1)}]}-\overline{I[\sigma^{(1)}]\,I[\mu^{(1)}]}\right\}+\frac{k}{2}\,(k-1)\,\overline{I[\sigma^{(1)2}]}\,, \tag{C.4}$$

and

$$\begin{aligned} B_k^{(4)} &= \alpha\left\{\overline{I[\sigma^{(4)}]}+\overline{I[\sigma^{(3)}\,\mu^{(1)}]}+\overline{I[\sigma^{(2)}\,\mu^{(2)}]}+\overline{I[\sigma^{(1)}\,\mu^{(3)}]}-\overline{I[\sigma^{(3)}]\,I[\mu^{(1)}]}\right. \\ &-\overline{I[\sigma^{(2)}\,\mu^{(1)}]\,I[\mu^{(1)}]}-\overline{I[\sigma^{(1)}\,\mu^{(2)}]\,I[\mu^{(1)}]}-\overline{I[\sigma^{(2)}]\,I[\mu^{(2)}]}+\overline{I[\sigma^{(2)}]\,I[\mu^{(1)}]^2} \\ &-\overline{I[\sigma^{(1)}\,\mu^{(1)}]\,I[\mu^{(2)}]}-\overline{I[\sigma^{(1)}\,\mu^{(1)}]\,I[\mu^{(1)}]^2}-\overline{I[\sigma^{(1)}]\,I[\mu^{(3)}]} \\ &\left.+2\overline{I[\sigma^{(1)}]\,I[\mu^{(1)}]\,I[\mu^{(2)}]}-\overline{I[\sigma^{(1)}]\,I[\mu^{(1)}]^3}\right\} \end{aligned}$$

$$
\begin{aligned}
&+k\,(k-1)\;\overline{I[\sigma^{(1)}\,\sigma^{(3)}]}+\frac{k}{2}\,(k-1)\;\overline{I[\sigma^{(2)2}]}+\frac{k}{2}\,(k-1)\,(k-2)\,\overline{I[\sigma^{(1)2}\,\sigma^{(2)}]}\\
&+\frac{k}{4!}\,(k-1)\,(k-2)\,(k-3)\;\overline{I[\sigma^{(1)4}]}+\frac{k}{6}\,(k-1)\,(k-2)\;\overline{I[\sigma^{(1)3}\,\mu^{(1)}]}\\
&-\frac{k}{2}\,(k-1)\;\overline{I[\sigma^{(1)2}\,\mu^{(1)}]\,I[\mu^{(1)}]}+k\,(k-1)\;\overline{I[\sigma^{(1)}\,\sigma^{(2)}\,\mu^{(1)}]}+\frac{k}{2}\,(k-1)\;\overline{I[\sigma^{(1)2}\,\mu^{(2)}]}\\
&-k\,(k-1)\;\overline{I[\sigma^{(1)}\,\sigma^{(2)}]\,I[\mu^{(1)}]}-\frac{k}{6}\,(k-1)\,(k-2)\;\overline{I[\sigma^{(1)3}]\,I[\mu^{(1)}]}\\
&-\frac{k}{2}\,(k-1)\;\overline{I[\sigma^{(1)2}]\,I[\mu^{(2)}]}+\frac{k}{2}\,(k-1)\;\overline{I[\sigma^{(1)2}]\,I[\mu^{(1)}]^2}+(k-1-\alpha)\;\overline{I[\mu^{(4)}]}\\
&+\left[\frac{\alpha}{2}\,(\alpha-k-1)+k\,(\alpha-k)\right]\;\left\{\overline{I[\sigma^{(2)}]}+\overline{I[\sigma^{(1)}\,\mu^{(1)}]}-\overline{I[\sigma^{(1)}]\,I[\mu^{(1)}]}\right\}^2\\
&+\frac{k}{2}\,(\alpha-k)\,(k-1)\;\overline{I[\sigma^{(1)2}]}\;\left\{\overline{I[\sigma^{(2)}]}+\overline{I[\sigma^{(1)}\,\mu^{(1)}]}-\overline{I[\sigma^{(1)}]\,I[\mu^{(1)}]}\right\}\,. \qquad \text{(C.5)}
\end{aligned}
$$

Again, the second-order correction $A_k^{(2)}$ is consistent with Eq. (7.8), whereas $B_k^{(4)}$ are the potential next-to-leading order corrections.

Now, we make use of the following relations for the sum of the Newton binomial

$$
\begin{aligned}
&\sum_{k=0}^{\alpha}(-1)^{\alpha-k}\binom{\alpha}{k}=0\,,\\
&\sum_{k=0}^{\alpha}(-1)^{\alpha-k}\binom{\alpha}{k}k=\delta_{\alpha 1}\,,\\
&\sum_{k=0}^{\alpha}(-1)^{\alpha-k}\binom{\alpha}{k}k^2=\delta_{\alpha 1}+2\,\delta_{\alpha 2}\,,\\
&\sum_{k=0}^{\alpha}(-1)^{\alpha-k}\binom{\alpha}{k}k^3=\delta_{\alpha 1}+6\,\delta_{\alpha 2}+6\,\delta_{\alpha 3}\,,\\
&\sum_{k=0}^{\alpha}(-1)^{\alpha-k}\binom{\alpha}{k}k^4=\delta_{\alpha 1}+14\,\delta_{\alpha 2}+36\,\delta_{\alpha 3}+24\,\delta_{\alpha 4}\,, \qquad \text{(C.6)}
\end{aligned}
$$

which tell us that for the skewness ($\alpha = 3$), only the third and fourth power of the index k in the sum in Eq. (C.3) survive. It is already evident from Eq. (C.5) that terms with k^3 and k^4 only contain linear and second order perturbations. An explicit evaluations with the use of Eqs. (C.6) for $\alpha = 3$ returns Eqs. (7.11).

To conclude, this proves that we need only corrections up to second-order for the observable and linear in the measure perturbation to compute the high-order moments. We remark that this is not ensured for the moments of $\mathcal{S}$, since the quantity $\mathcal{S}^{(0)} - m^{(0)}$ does not vanish on the background, and then the generic moment of the distribution of $\mathcal{S}$ includes high-order corrections for the observable and the measure.

D - Analytic proofs for the skewness in Fourier space

In this appendix, we provide the detailed derivations of $\mathcal{L}(r_1, r_2)$ in Eq. (7.25) and μ_3^{LSS} in Eq. (7.57).

$\mathcal{L}(r_1, r_2)$

We start from the Fourier modes of the linear gravitational potential $\psi(\eta, \vec{k})$ and assume that $\psi(\eta, \vec{k})$ is a stochastic field such that

$$\overline{\psi(\eta, \vec{k})} = 0 \qquad \text{and} \qquad \overline{\psi(\eta_1, \vec{k}_1)\psi(\eta_2, \vec{k}_2)} = (2\pi)^3 \delta_D\left(\mathbf{k}_1 + \mathbf{k}_2\right) P_\psi(k_1, \eta_1, \eta_2)\,. \tag{D.1}$$

In this way, the 2-point function of a 2-D Laplacian in real space Δ_2 is given by

$$\overline{\Delta_2\psi(r_1, \vec{n})\Delta_2\psi(r_2, \vec{n})} = \int \frac{d^3k_1}{(2\pi)^3} P_\psi(k_1, \eta_1, \eta_2) \Delta_2 e^{-i\vec{k}_1\cdot\vec{n}\,r_1} \Delta_2 e^{i\vec{k}_1\cdot\vec{n}\,r_2}\,, \tag{D.2}$$

At this point, we expand the exponentials in the Fourier transforms in terms of the spherical harmonics as

$$e^{-i\vec{k}\cdot\vec{n}r} = 4\pi \sum_{\ell m} (-i)^\ell j_\ell(kr) Y_{\ell m}(\hat{\vec{k}}) Y^*_{\ell m}(\vec{n})\,, \tag{D.3}$$

and keep in mind, for later uses, the following orthogonal relations

$$\begin{aligned} \sum_m Y_{\ell m}(\vec{n}) Y^*_{\ell m}(\vec{n}) &= \frac{2\ell+1}{4\pi}\,, \\ \int d^3\vec{n}\, Y_{\ell_1 m_1}(\vec{n}) Y^*_{\ell_2 m_2}(\vec{n}) &= \delta_{\ell_1\ell_2}\delta_{m_1 m_2}\,. \end{aligned} \tag{D.4}$$

In this way, Eq. (D.2) becomes

$$\begin{aligned} \overline{\Delta_2\psi(r_1, \vec{n})\Delta_2\psi(r_2, \vec{n})} &= (4\pi)^2 \int \frac{d^3k_1}{(2\pi)^3} P_\psi(k_1, \eta_1, \eta_2) \sum i^{\ell_1+\ell_2} (-1)^{\ell_1} \ell_1(\ell_1+1)\ell_2(\ell_2+1) \\ &\quad \times j_{\ell_1}(k_1 r_1) Y_{\ell_1 m_1}(\hat{\vec{k}}_1) Y^*_{\ell_1 m_1}(\vec{n}) j_{\ell_2}(k_1 r_2) Y^*_{\ell_2 m_2}(\hat{\vec{k}}_1) Y_{\ell_2 m_2}(\vec{n}) \\ &= (4\pi)^2 \int \frac{k_1^2 dk_1}{(2\pi)^3} P_\psi(k_1, \eta_1, \eta_2) \sum \ell_1^2(\ell_1+1)^2 \\ &\quad \times j_{\ell_1}(k_1 r_1) j_{\ell_1}(k_1 r_2) Y^*_{\ell_1 m_1}(\vec{n}) Y_{\ell_1 m_1}(\vec{n}) \\ &= 4\pi \int \frac{k_1^2 dk_1}{(2\pi)^3} P_\psi(k_1, \eta_1, \eta_2) \sum_{\ell_1} \ell_1^2(\ell_1+1)^2(2\ell_1+1) \\ &\quad \times j_{\ell_1}(k_1 r_1) j_{\ell_1}(k_1 r_2)\,. \end{aligned} \tag{D.5}$$

It is now worth to focus on the sum over ℓ_1 appearing into Eq. (D.5). To this end, we recall that the Legendre polynomials $P_\ell(\cos\theta)$ are eigenfunctions of the 2-D Laplacian with eigenvalues $-\ell(\ell+1)$ and that $P_\ell(1)=1$. Hence, we have

$$\begin{aligned}
&\sum_{\ell_1}(2\ell_1+1)\ell_1^2(\ell_1+1)^2 j_{\ell_1}(k_1r_1)j_{\ell_1}(k_1r_2)\\
=&\left[\Delta_2^2\sum_{\ell_1}(2\ell_1+1)j_{\ell_1}(k_1r_1)j_{\ell_1}(k_1r_2)P_{\ell_1}(\cos\theta)\right]_{\theta=0}\\
=&\left[\Delta_2^2 j_0\left(k_1\sqrt{r_1^2+r_2^2-2r_1r_2\cos\theta}\right)\right]_{\theta=0}\,, \qquad (D.6)
\end{aligned}$$

where last equality holds since the 0-th order spherical Bessel functions can be written as

$$j_0\left(k_1\sqrt{r_1^2+r_2^2-2r_1r_2\cos\theta}\right)=\sum_{\ell_1}(2\ell_1+1)j_{\ell_1}(k_1r_1)j_{\ell_1}(k_1r_2)P_{\ell_1}(\cos\theta)\,. \qquad (D.7)$$

Then, the explicit act of the 2-D Laplacians over j_0 returns

$$\begin{aligned}
&\left[\Delta_2^2 j_0\left(k_1\sqrt{r_1^2+r_2^2-2r_1r_2\cos\theta}\right)\right]_{\theta=0}\\
=&\;4\,r_1r_2\left[r_1^2+r_2^2+4\,r_1r_2-2\,k_1^2\,r_1r_2\,(r_1-r_2)^2\right]\frac{\sin\left[k_1\,(r_1-r_2)\right]}{k_1\,(r_1-r_2)^5}\\
&-4\,r_1r_2\left(r_1^2+r_2^2+4\,r_1r_2\right)\frac{\cos\left[k_1\,(r_1-r_2)\right]}{(r_1-r_2)^4}\\
=&\;4k_1^4r_1r_2\left\{\frac{2r_1r_2\,j_2\left[k_1(r_1-r_2)\right]}{k_1^2(r_1-r_2)^2}+\frac{(r_1-r_2)^2\,j_1\left[k_1(r_1-r_2)\right]}{k_1^3(r_1-r_2)^3}\right\}. \qquad (D.8)
\end{aligned}$$

Now, thanks to the definition of the generalized Hankel transforms (7.24), we can insert Eq. (D.8) into (D.5) and prove then first of Eqs. (7.25). To this end, we relate the power spectrum of the gravitational potential $P_\psi(k,\eta_1,\eta_2)$ to the matter one $P(k,\eta_1,\eta_2)$ as

$$P_\psi(k,\eta_1,\eta_2)=\frac{9}{4k^4}\frac{\mathcal{H}_0^4}{a(\eta_1)a(\eta_2)}\Omega_{m0}^2P(k,\eta_1,\eta_2)\,, \qquad (D.9)$$

where we have used the Poisson equation to link the growth factor of the gravitational potential D_ψ to the growth factor D_1 of the matter perturbations

$$D_\psi=-\frac{3}{2k^2}\frac{\mathcal{H}_0^2}{a}\Omega_{m0}D_1\,, \qquad (D.10)$$

as prescribed by the general dictionary provided in [154] for the relations among the different cosmological transfer functions.

μ_3^{LSS}

In this appendix, we want to provide the detailed evaluation of Eq. (7.57). To this end, we start by writing the Dirac delta over the triangular shapes in Fourier space as

$$\delta_D\left(\vec{k}_1+\vec{k}_2+\vec{k}_3\right) \;=\; 8\sum(-i)^{\ell_1+\ell_2+\ell_3}\,\mathcal{G}_{\ell_1\ell_2\ell_3}^{m_1m_2m_3}Y_{\ell_1m_1}^*\left(\hat{\vec{k}}_1\right)Y_{\ell_2m_2}^*\left(\hat{\vec{k}}_2\right)Y_{\ell_3m_3}^*\left(\hat{\vec{k}}_3\right)$$

$$\times \int dx\, x^2 j_{\ell_1}\left(k_1 x\right) j_{\ell_2}\left(k_2 x\right) j_{\ell_3}\left(k_3 x\right)\,, \tag{D.11}$$

where the integral over the auxiliary variable x runs from 0 to ∞, and the sums are over the indexes ℓ_i and m_i with $i = 1, 2, 3$. We recall the definition of the Gaunt integral

$$\begin{aligned} \mathcal{G}^{m_1 m_2 m_3}_{\ell_1 \ell_2 \ell_3} &\equiv \int d\Omega\, Y_{\ell_1 m_1}\left(\vec{n}\right) Y_{\ell_2 m_2}\left(\vec{n}\right) Y_{\ell_3 m_3}\left(\vec{n}\right) \\ &= \begin{pmatrix} \ell_1 & \ell_2 & \ell_3 \\ 0 & 0 & 0 \end{pmatrix} \begin{pmatrix} \ell_1 & \ell_2 & \ell_3 \\ m_1 & m_2 & m_3 \end{pmatrix} \sqrt{\frac{\left(2l_1+1\right)\left(2l_2+1\right)\left(2l_3+1\right)}{4\pi}}\,. \end{aligned} \tag{D.12}$$

We remark that the integral over x automatically satisfies the triangle inequality over k_1, k_2, and k_3. Then, there is no need to explicitly write any triangular condition. We compute the integrals over the angular directions $\vec{k}_i$ in Eq. (7.54). By making use of Eq. (D.11), we then have

$$\begin{aligned} &\int d\Omega_{\hat{k}_1} d\Omega_{\hat{k}_2} d\Omega_{\hat{k}_3} \delta_D\left(\vec{k}_1 + \vec{k}_2 + \vec{k}_3\right) \Delta_2 e^{i\vec{k}_1\cdot\vec{n}r_1} \Delta_2 e^{i\vec{k}_2\cdot\vec{n}r_2} \Delta_2 e^{i\vec{k}_3\cdot\vec{n}r_3} \\ = &\ -8\left(4\pi\right)^3 \sum \ell_1\left(\ell_1+1\right)\ell_2\left(\ell_2+1\right)\ell_3\left(\ell_3+1\right) j_{\ell_1}\left(k_1 r_1\right) j_{\ell_2}\left(k_2 r_2\right) j_{\ell_3}\left(k_3 r_3\right) \\ &\times Y^*_{\ell_1 m_1}\left(\vec{n}\right) Y^*_{\ell_2 m_2}\left(\vec{n}\right) Y^*_{\ell_3 m_3}\left(\vec{n}\right) \mathcal{G}^{m_1 m_2 m_3}_{\ell_1 \ell_2 \ell_3} \int dx\, x^2 j_{\ell_1}\left(k_1 x\right) j_{\ell_2}\left(k_2 x\right) j_{\ell_3}\left(k_3 x\right)\,, \end{aligned} \tag{D.13}$$

where we made use of the orthonormality of spherical harmonics in Eqs. (D.4). In order to move on with the evaluation, we notice that the we can get rid of the sum over m_i's, since the following relation for the Gaunt integral holds

$$\sum_{m_1 m_2 m_3} \mathcal{G}^{m_1 m_2 m_3}_{\ell_1 \ell_2 \ell_3} Y^*_{\ell_1 m_1}\left(\vec{n}\right) Y^*_{\ell_2 m_2}\left(\vec{n}\right) Y^*_{\ell_3 m_3}\left(\vec{n}\right) = \begin{pmatrix} \ell_1 & \ell_2 & \ell_3 \\ 0 & 0 & 0 \end{pmatrix}^2 \frac{\left(2\ell_1+1\right)\left(2\ell_2+1\right)\left(2\ell_3+1\right)}{\left(4\pi\right)^2}\,, \tag{D.14}$$

thanks to the following properties

$$\begin{aligned} \sum_{m_1 m_2} \mathcal{G}^{m_1 m_2 m_3}_{\ell_1 \ell_2 \ell_3} \mathcal{G}^{M m_1 m_2}_{L \ell_1 \ell_2} &= \begin{pmatrix} \ell_1 & \ell_2 & \ell_3 \\ 0 & 0 & 0 \end{pmatrix}^2 \frac{\left(2\ell_1+1\right)\left(2\ell_2+1\right)}{4\pi} \delta_{\ell_3 L} \delta_{m_3 M}\,, \\ Y_{\ell_1 m_1}\left(\vec{n}\right) Y_{\ell_2 m_2}\left(\vec{n}\right) &= \sum_{LM} \mathcal{G}^{m_1 m_2 M}_{\ell_1 \ell_2 L} Y^*_{LM}\left(\vec{n}\right)\,. \end{aligned} \tag{D.15}$$

Hence, by inserting Eq. (D.14) into Eq. (D.13), we have

$$\begin{aligned} &\int d\Omega_{\hat{k}_1} d\Omega_{\hat{k}_2} d\Omega_{\hat{k}_3} \delta_D\left(\vec{k}_1 + \vec{k}_2 + \vec{k}_3\right) \Delta_2 e^{i\vec{k}_1\cdot\vec{n}r_1} \Delta_2 e^{i\vec{k}_2\cdot\vec{n}r_2} \Delta_2 e^{i\vec{k}_3\cdot\vec{n}r_3} \\ = &\ -8\left(4\pi\right)^3 \sum \ell_1\left(\ell_1+1\right)\ell_2\left(\ell_2+1\right)\ell_3\left(\ell_3+1\right) j_{\ell_1}\left(k_1 r_1\right) j_{\ell_2}\left(k_2 r_2\right) j_{\ell_3}\left(k_3 r_3\right) \\ &\begin{pmatrix} \ell_1 & \ell_2 & \ell_3 \\ 0 & 0 & 0 \end{pmatrix}^2 \frac{\left(2\ell_1+1\right)\left(2\ell_2+1\right)\left(2\ell_3+1\right)}{\left(4\pi\right)^2} \int dx\, x^2 j_{\ell_1}\left(k_1 x\right) j_{\ell_2}\left(k_2 x\right) j_{\ell_3}\left(k_3 x\right)\,. \end{aligned} \tag{D.16}$$

Then, by using this last equation into Eq. (7.54), we finally obtain the desired result of Eq. (7.57).

Bibliography

[1] T. Schiavone, G. Montani, and F. Bombacigno, Mon. Not. Roy. Astron. Soc. **522**, L72 (2023), arXiv:2211.16737 [gr-qc] .

[2] M. G. Dainotti, B. De Simone, T. Schiavone, G. Montani, E. Rinaldi, G. Lambiase, M. Bogdan, and S. Ugale, Galaxies **10**, 24 (2022), arXiv:2201.09848 [astro-ph.CO] .

[3] M. G. Dainotti, B. De Simone, T. Schiavone, G. Montani, E. Rinaldi, and G. Lambiase, ApJ **912**, 150 (2021), arXiv:2103.02117 [astro-ph.CO] .

[4] T. Schiavone and G. Montani, "*Signature of $f(R)$ gravity via Lemaitre-Tolman-Bondi inhomogeneous perturbations*," (2023), submitted for publication to Phys. Rev. D, arXiv:2301.09768 [gr-qc] .

[5] T. Schiavone, E. Di Dio, and G. Fanizza, "*The skewness of the distance-redshift relation in ΛCDM*," (2023), submitted for publication to JCAP, arXiv:2307.13455 [astro-ph.CO] .

[6] I. Albuquerque and o. including Tiziano Schiavone, "*A SHOT IN THE DARK: New Challenges in Cosmology 2022*," (2022), white Paper as the outcome of the workshop A SHOT IN THE DARK: New Challenges in Cosmology 2022 (Leiden), in preparation.

[7] M. Dainotti, B. De Simone, G. Montani, T. Schiavone, and G. Lambiase, in *CORFU2022: 22th Hellenic School and Workshops on Elementary Particle Physics and Gravity* (2023) arXiv:2301.10572 [astro-ph.CO] .

[8] T. Schiavone, G. Montani, M. G. Dainotti, B. De Simone, E. Rinaldi, and G. Lambiase, in *17th Italian-Korean Symposium on Relativistic Astrophysics* (2022) arXiv:2205.07033 [astro-ph.CO] .

[9] T. Schiavone and G. Montani, in *16th Marcel Grossmann Meeting on Recent Developments in Theoretical and Experimental General Relativity, Astrophysics and Relativistic Field Theories* (2021) arXiv:2111.03197 [astro-ph.CO] .

[10] A. Einstein, Annalen Phys. **49**, 769 (1916).

[11] A. Einstein, Jahrbuch der Radioaktivität und Elektronik **4**, 411 (1907).

[12] A. Einstein, Sitzungsber. Preuss. Akad. Wiss. Berlin (Math. Phys.) **1915**, 844 (1915).

[13] A. Einstein, Sitzungsber. Preuss. Akad. Wiss. Berlin (Math. Phys.) **1916**, 1111 (1916).

[14] C. W. Misner, K. S. Thorne, and J. A. Wheeler, *Gravitation* (W. H. Freeman, San Francisco, 1973).

[15] F. W. Dyson, A. S. Eddington, and C. Davidson, Phil. Trans. Roy. Soc. Lond. A **220**, 291 (1920).

[16] A. Einstein, Annalen Phys. **35**, 898 (1911).

[17] A. Einstein, Sitzungsber. Preuss. Akad. Wiss. Berlin (Math. Phys.) **1915**, 831 (1915).

[18] U. J. Le Verrier, Annales de l'Observatoire de Paris **5**, 1 (1859).

[19] A. Einstein, Sitzungsber. Preuss. Akad. Wiss. Berlin (Math. Phys.) **1916**, 688 (1916).

[20] A. Einstein, Sitzungsber. Preuss. Akad. Wiss. Berlin (Math. Phys.) **1918**, 154 (1918).

[21] A. Einstein and N. Rosen, J. Franklin Inst. **223**, 43 (1937).

[22] B. P. Abbott *et al.* (LIGO Scientific, Virgo), Phys. Rev. Lett. **116**, 061102 (2016), arXiv:1602.03837 [gr-qc] .

[23] A. Einstein, Sitzungsber. Preuss. Akad. Wiss. Berlin (Math. Phys.) **1917**, 142 (1917).

[24] G. Lemaitre, Annales Soc. Sci. Bruxelles A **47**, 49 (1927).

[25] V. M. Slipher, Proc. Am. Phil. Soc. **56**, 403 (1917).

[26] E. Hubble, Proc. Nat. Acad. Sci. **15**, 168 (1929).

[27] K. Maguire, "Type ia supernovae," in *Handbook of Supernovae*, edited by A. W. Alsabti and P. Murdin (Springer International Publishing, Cham, 2017) pp. 293–316.

[28] M. M. Phillips and C. R. Burns, "The peak luminosity–decline rate relationship for type ia supernovae," in *Handbook of Supernovae*, edited by A. W. Alsabti and P. Murdin (Springer International Publishing, Cham, 2017) pp. 2543–2561.

[29] G. Gamow, R. A. Alpher, and R. Herman, Physics Today **24**, 51 (1971), https://pubs.aip.org/physicstoday/article-pdf/24/3/51/11138254/51_1_online.pdf .

[30] W. de Sitter, Mon. Not. Roy. Astron. Soc. **78**, 3 (1917).

[31] A. Friedmann, Zeitschrift für Physik <Berlin> **10**, 377 (2008).

[32] A. Friedmann, Z. Phys. **21**, 326 (1924).

[33] H. P. Robertson, Astrophys. J. **82**, 284 (1935).

[34] A. G. Walker, Proceedings of the London Mathematical Society **s2-42**, 90 (1937), https://londmathsoc.onlinelibrary.wiley.com/doi/pdf/10.1112/plms/s2-42.1.90 .

[35] S. Weinberg, *Cosmology* (Oxford University Press, 2008).

[36] S. Perlmutter *et al.* (Supernova Cosmology Project), ApJ **517**, 565 (1999), arXiv:astro-ph/9812133 .

[37] A. G. Riess *et al.* (Supernova Search Team), AJ **116**, 1009 (1998), arXiv:astro-ph/9805201 .

[38] J. Yoo and Y. Watanabe, Int. J. Mod. Phys. D **21**, 1230002 (2012), arXiv:1212.4726 [astro-ph.CO] .

[39] L. Amendola and S. Tsujikawa, *Dark Energy: Theory and Observations* (Cambridge University Press, 2015).

[40] N. Aghanim *et al.* (Planck), A&A **641**, A6 (2020), [Erratum: Astron.Astrophys. 652, C4 (2021)], arXiv:1807.06209 [astro-ph.CO] .

[41] V. Trimble, Ann. Rev. Astron. Astrophys. **25**, 425 (1987).

[42] T. Marrodán Undagoitia and L. Rauch, J. Phys. G **43**, 013001 (2016), arXiv:1509.08767 [physics.ins-det] .

[43] J. M. Gaskins, Contemporary Physics **57**, 496 (2016).

[44] O. Buchmueller, C. Doglioni, and L. T. Wang, Nature Phys. **13**, 217 (2017), arXiv:1912.12739 [hep-ex] .

[45] G. Arcadi, M. Dutra, P. Ghosh, M. Lindner, Y. Mambrini, M. Pierre, S. Profumo, and F. S. Queiroz, Eur. Phys. J. C **78**, 203 (2018), arXiv:1703.07364 [hep-ph] .

[46] J. L. Feng, Ann. Rev. Astron. Astrophys. **48**, 495 (2010), arXiv:1003.0904 [astro-ph.CO] .

[47] D. J. E. Marsh, Phys. Rept. **643**, 1 (2016), arXiv:1510.07633 [astro-ph.CO] .

[48] J. Yadav, S. Bharadwaj, B. Pandey, and T. R. Seshadri, Mon. Not. Roy. Astron. Soc. **364**, 601 (2005), arXiv:astro-ph/0504315 .

[49] P. Sarkar, J. Yadav, B. Pandey, and S. Bharadwaj, Mon. Not. Roy. Astron. Soc. **399**, L128 (2009), arXiv:0906.3431 [astro-ph.CO] .

[50] D. J. Schwarz, C. J. Copi, D. Huterer, and G. D. Starkman, Class. Quant. Grav. **33**, 184001 (2016), arXiv:1510.07929 [astro-ph.CO] .

[51] S. Weinberg, Rev. Mod. Phys. **61**, 1 (1989).

[52] P. J. E. Peebles and B. Ratra, Rev. Mod. Phys. **75**, 559 (2003), arXiv:astro-ph/0207347 .

[53] M. Chevallier and D. Polarski, Int. J. Mod. Phys. D **10**, 213 (2001), arXiv:gr-qc/0009008 .

[54] E. V. Linder, Phys. Rev. Lett. **90**, 091301 (2003), arXiv:astro-ph/0208512 .

[55] R. R. Caldwell and E. V. Linder, Phys. Rev. Lett. **95**, 141301 (2005), arXiv:astro-ph/0505494 .

[56] E. Di Valentino, A. Melchiorri, O. Mena, and S. Vagnozzi, Phys. Dark Univ. **30**, 100666 (2020), arXiv:1908.04281 [astro-ph.CO] .

[57] M. Lucca, Phys. Rev. D **104**, 083510 (2021), arXiv:2106.15196 [astro-ph.CO] .

[58] S. Alam *et al.* (BOSS), Mon. Not. Roy. Astron. Soc. **470**, 2617 (2017), arXiv:1607.03155 [astro-ph.CO] .

[59] T. M. C. Abbott *et al.* (DES), Phys. Rev. D **105**, 023520 (2022), arXiv:2105.13549 [astro-ph.CO] .

[60] R. Laureijs *et al.* (EUCLID), (2011), arXiv:1110.3193 [astro-ph.CO] .

[61] P. A. Abell *et al.* (LSST Science, LSST Project), (2009), arXiv:0912.0201 [astro-ph.IM] .

[62] O. Doré *et al.*, (2014), arXiv:1412.4872 [astro-ph.CO] .

[63] A. Aghamousa *et al.* (DESI), (2016), arXiv:1611.00036 [astro-ph.IM] .

[64] L. Amendola *et al.*, Living Rev. Rel. **21**, 2 (2018), arXiv:1606.00180 [astro-ph.CO] .

[65] P. Ade *et al.* (Simons Observatory), JCAP **02**, 056 (2019), arXiv:1808.07445 [astro-ph.CO] .

[66] K. Abazajian *et al.*, (2019), arXiv:1907.04473 [astro-ph.IM] .

[67] E. Di Valentino *et al.*, Astropart. Phys. **131**, 102605 (2021), arXiv:2008.11284 [astro-ph.CO] .

[68] E. Di Valentino, O. Mena, S. Pan, L. Visinelli, W. Yang, A. Melchiorri, D. F. Mota, A. G. Riess, and J. Silk, Class. Quant. Grav. **38**, 153001 (2021), arXiv:2103.01183 [astro-ph.CO] .

[69] E. Abdalla *et al.*, JHEAp **34**, 49 (2022), arXiv:2203.06142 [astro-ph.CO] .

[70] L. Perivolaropoulos and F. Skara, New Astron. Rev. **95**, 101659 (2022), arXiv:2105.05208 [astro-ph.CO] .

[71] A. G. Riess *et al.*, ApJ **934**, L7 (2022), arXiv:2112.04510 [astro-ph.CO] .

[72] S. Dodelson, *Modern Cosmology* (Academic Press, Amsterdam, 2003).

[73] B. A. Bassett and R. Hlozek, (2009), arXiv:0910.5224 [astro-ph.CO] .

[74] Z. Li, Y. P. Jing, P. Zhang, and D. Cheng, Astrophys. J. **833**, 287 (2016), arXiv:1609.03697 [astro-ph.CO] .

[75] H. Gil-Marín, W. J. Percival, L. Verde, J. R. Brownstein, C.-H. Chuang, F.-S. Kitaura, S. A. Rodríguez-Torres, and M. D. Olmstead, Mon. Not. Roy. Astron. Soc. **465**, 1757 (2017), arXiv:1606.00439 [astro-ph.CO] .

[76] E. Di Valentino *et al.*, Astropart. Phys. **131**, 102604 (2021), arXiv:2008.11285 [astro-ph.CO] .

[77] G. J. Olmo, Phys. Rev. D **72**, 083505 (2005), arXiv:gr-qc/0505135 .

[78] G. J. Olmo, Phys. Rev. Lett. **95**, 261102 (2005), arXiv:gr-qc/0505101 .

[79] S. Nojiri and S. D. Odintsov, eConf **C0602061**, 06 (2006), arXiv:hep-th/0601213 .

[80] G. J. Olmo, Phys. Rev. D **75**, 023511 (2007), arXiv:gr-qc/0612047 .

[81] T. P. Sotiriou and V. Faraoni, Rev. Mod. Phys. **82**, 451 (2010), arXiv:0805.1726 [gr-qc] .

[82] S. Nojiri and S. D. Odintsov, Phys. Rept. **505**, 59 (2011), arXiv:1011.0544 [gr-qc] .

[83] V. Faraoni and S. Capozziello, *Beyond Einstein Gravity: A Survey of Gravitational Theories for Cosmology and Astrophysics* (Springer, Dordrecht, 2011).

[84] S. Capozziello and M. De Laurentis, Phys. Rept. **509**, 167 (2011), arXiv:1108.6266 [gr-qc] .

[85] S. Nojiri, S. D. Odintsov, and V. K. Oikonomou, Phys. Rept. **692**, 1 (2017), arXiv:1705.11098 [gr-qc] .

[86] S. Tsujikawa, Lect. Notes Phys. **800**, 99 (2010), arXiv:1101.0191 [gr-qc] .

[87] C. Brans and R. H. Dicke, Phys. Rev. **124**, 925 (1961).

[88] K. Nordtvedt, Jr., Astrophys. J. **161**, 1059 (1970).

[89] J. O'Hanlon, Phys. Rev. Lett. **29**, 137 (1972).

[90] G. Magnano and L. M. Sokolowski, Phys. Rev. D **50**, 5039 (1994), arXiv:gr-qc/9312008 .

[91] S. Capozziello, R. de Ritis, and A. A. Marino, Class. Quant. Grav. **14**, 3243 (1997), arXiv:gr-qc/9612053 .

[92] S. Capozziello, S. Nojiri, S. D. Odintsov, and A. Troisi, Phys. Lett. B **639**, 135 (2006), arXiv:astro-ph/0604431 .

[93] S. Capozziello, F. S. N. Lobo, and J. P. Mimoso, Phys. Rev. D **91**, 124019 (2015), arXiv:1407.7293 [gr-qc] .

[94] S. Bahamonde, S. D. Odintsov, V. K. Oikonomou, and M. Wright, Annals Phys. **373**, 96 (2016), arXiv:1603.05113 [gr-qc] .

[95] S. Carloni, E. Elizalde, and S. Odintsov, Gen. Rel. Grav. **42**, 1667 (2010), arXiv:0907.3941 [gr-qc] .

[96] S. Bahamonde, S. D. Odintsov, V. K. Oikonomou, and P. V. Tretyakov, Phys. Lett. B **766**, 225 (2017), arXiv:1701.02381 [gr-qc] .

[97] D. Saez-Gomez, (2008), arXiv:0812.1980 [hep-th] .

[98] Y. Bisabr, Grav. Cosmol. **24**, 201 (2018), arXiv:1504.05648 [hep-th] .

[99] D. K. Çiftci and V. Faraoni, Annals Phys. **391**, 65 (2018), arXiv:1711.04026 [gr-qc] .

[100] V. Faraoni, A. Giusti, and B. H. Fahim, Phys. Rept. **925**, 1 (2021), arXiv:2101.00266 [gr-qc] .

[101] W. Hu and I. Sawicki, Phys. Rev. D **76**, 064004 (2007), arXiv:0705.1158 [astro-ph] .

[102] Y.-S. Song, W. Hu, and I. Sawicki, Phys. Rev. D **75**, 044004 (2007), arXiv:astro-ph/0610532 .

[103] A. A. Starobinsky, JETP Lett. **86**, 157 (2007), arXiv:0706.2041 [astro-ph] .

[104] S. Tsujikawa, Phys. Rev. D **77**, 023507 (2008), arXiv:0709.1391 [astro-ph] .

[105] S. D. Odintsov, D. Sáez-Chillón Gómez, and G. S. Sharov, Nucl. Phys. B **966**, 115377 (2021), arXiv:2011.03957 [gr-qc] .

[106] S. Nojiri, S. D. Odintsov, and V. K. Oikonomou, Nucl. Phys. B **980**, 115850 (2022), arXiv:2205.11681 [gr-qc] .

[107] C. Burrage and J. Sakstein, Living Rev. Rel. **21**, 1 (2018), arXiv:1709.09071 [astro-ph.CO] .

[108] F. S. Labini, Class. Quant. Grav. **28**, 164003 (2011), arXiv:1103.5974 [astro-ph.CO] .

[109] P. K. Aluri *et al.*, Class. Quant. Grav. **40**, 094001 (2023), arXiv:2207.05765 [astro-ph.CO] .

[110] R. C. Tolman, Proc. Nat. Acad. Sci. **20**, 169 (1934).

[111] H. Bondi, Mon. Not. Roy. Astron. Soc. **107**, 410 (1947).

[112] P. J. E. Peebles, *Principles of physical cosmology* (Princeton University Press, 1994).

[113] G. Montani, M. V. Battisti, R. Benini, and G. Imponente, *Primordial cosmology* (World Scientific, Singapore, 2009).

[114] I. Zehavi, A. G. Riess, R. P. Kirshner, and A. Dekel, Astrophys. J. **503**, 483 (1998), arXiv:astro-ph/9802252 .

[115] J. Garcia-Bellido and T. Haugboelle, JCAP **04**, 003 (2008), arXiv:0802.1523 [astro-ph] .

[116] B. Sinclair, T. M. Davis, and T. Haugbolle, Astrophys. J. **718**, 1445 (2010), arXiv:1006.0911 [astro-ph.CO] .

[117] A. Moss, J. P. Zibin, and D. Scott, Phys. Rev. D **83**, 103515 (2011), arXiv:1007.3725 [astro-ph.CO] .

[118] L. Cosmai, G. Fanizza, F. Sylos Labini, L. Pietronero, and L. Tedesco, Class. Quant. Grav. **36**, 045007 (2019), arXiv:1810.06318 [astro-ph.CO] .

[119] V. V. Luković, B. S. Haridasu, and N. Vittorio, Mon. Not. Roy. Astron. Soc. **491**, 2075 (2020), arXiv:1907.11219 [astro-ph.CO] .

[120] D. Camarena, V. Marra, Z. Sakr, and C. Clarkson, Mon. Not. Roy. Astron. Soc. **509**, 1291 (2021), arXiv:2107.02296 [astro-ph.CO] .

[121] W. D. Kenworthy, D. Scolnic, and A. Riess, Astrophys. J. **875**, 145 (2019), arXiv:1901.08681 [astro-ph.CO] .

[122] Q. Ding, T. Nakama, and Y. Wang, Sci. China Phys. Mech. Astron. **63**, 290403 (2020), arXiv:1912.12600 [astro-ph.CO] .

[123] R.-G. Cai, J.-F. Ding, Z.-K. Guo, S.-J. Wang, and W.-W. Yu, Phys. Rev. D **103**, 123539 (2021), arXiv:2012.08292 [astro-ph.CO] .

[124] S. Castello, M. Hogras, and E. Mortsell, JCAP **07**, 003 (2022), [Erratum: JCAP 09, E01 (2022)], arXiv:2110.04226 [astro-ph.CO] .

[125] D. Camarena, V. Marra, Z. Sakr, and C. Clarkson, Class. Quant. Grav. **39**, 184001 (2022), arXiv:2205.05422 [astro-ph.CO] .

[126] R. C. Keenan, A. J. Barger, and L. L. Cowie, Astrophys. J. **775**, 62 (2013), arXiv:1304.2884 [astro-ph.CO] .

[127] M. Haslbauer, I. Banik, and P. Kroupa, Mon. Not. Roy. Astron. Soc. **499**, 2845 (2020), arXiv:2009.11292 [astro-ph.CO] .

[128] J. H. W. Wong, T. Shanks, N. Metcalfe, and J. R. Whitbourn, Mon. Not. Roy. Astron. Soc. **511**, 5742 (2022), arXiv:2107.08505 [astro-ph.CO] .

[129] J. Yoo, A. L. Fitzpatrick, and M. Zaldarriaga, Phys. Rev. D **80**, 083514 (2009), arXiv:0907.0707 [astro-ph.CO] .

[130] A. Challinor and A. Lewis, Phys. Rev. D **84**, 043516 (2011), arXiv:1105.5292 [astro-ph.CO] .

[131] C. Bonvin and R. Durrer, Phys. Rev. D **84**, 063505 (2011), arXiv:1105.5280 [astro-ph.CO] .

[132] D. Jeong, F. Schmidt, and C. M. Hirata, Phys. Rev. D **85**, 023504 (2012), arXiv:1107.5427 [astro-ph.CO] .

[133] J. Yoo and M. Zaldarriaga, Phys. Rev. D **90**, 023513 (2014), arXiv:1406.4140 [astro-ph.CO] .

[134] D. Bertacca, R. Maartens, and C. Clarkson, JCAP **09**, 037 (2014), arXiv:1405.4403 [astro-ph.CO] .

[135] E. Di Dio, R. Durrer, G. Marozzi, and F. Montanari, JCAP **12**, 017 (2014), [Erratum: JCAP 06, E01 (2015)], arXiv:1407.0376 [astro-ph.CO] .

[136] E. Di Dio and U. Seljak, JCAP **04**, 050 (2019), arXiv:1811.03054 [astro-ph.CO] .

[137] E. Di Dio and F. Beutler, JCAP **09**, 058 (2020), arXiv:2004.07916 [astro-ph.CO] .

[138] M. Magi and J. Yoo, JCAP **09**, 071 (2022), arXiv:2204.01751 [astro-ph.CO] .

[139] J. Adamek, D. Daverio, R. Durrer, and M. Kunz, Nature Phys. **12**, 346 (2016), arXiv:1509.01699 [astro-ph.CO] .

[140] N. E. Chisari and M. Zaldarriaga, Phys. Rev. D **83**, 123505 (2011), [Erratum: Phys.Rev.D 84, 089901 (2011)], arXiv:1101.3555 [astro-ph.CO] .

[141] C. Fidler, C. Rampf, T. Tram, R. Crittenden, K. Koyama, and D. Wands, Phys. Rev. D **92**, 123517 (2015), arXiv:1505.04756 [astro-ph.CO] .

[142] I. Ben-Dayan, M. Gasperini, G. Marozzi, F. Nugier, and G. Veneziano, JCAP **04**, 036 (2012), arXiv:1202.1247 [astro-ph.CO] .

[143] I. Ben-Dayan, G. Marozzi, F. Nugier, and G. Veneziano, JCAP **11**, 045 (2012), arXiv:1209.4326 [astro-ph.CO] .

[144] I. Ben-Dayan, M. Gasperini, G. Marozzi, F. Nugier, and G. Veneziano, JCAP **06**, 002 (2013), arXiv:1302.0740 [astro-ph.CO] .

[145] O. Umeh, C. Clarkson, and R. Maartens, Class. Quant. Grav. **31**, 205001 (2014), arXiv:1402.1933 [astro-ph.CO] .

[146] I. Ben-Dayan, R. Durrer, G. Marozzi, and D. J. Schwarz, Phys. Rev. Lett. **112**, 221301 (2014), arXiv:1401.7973 [astro-ph.CO] .

[147] C. Bonvin, C. Clarkson, R. Durrer, R. Maartens, and O. Umeh, JCAP **07**, 040 (2015), arXiv:1504.01676 [astro-ph.CO] .

[148] G. Fanizza, M. Gasperini, G. Marozzi, and G. Veneziano, JCAP **08**, 020 (2015), arXiv:1506.02003 [astro-ph.CO] .

[149] P. Fleury, C. Clarkson, and R. Maartens, JCAP **03**, 062 (2017), arXiv:1612.03726 [astro-ph.CO] .

[150] I. Odderskov, S. M. Koksbang, and S. Hannestad, JCAP **02**, 001 (2016), arXiv:1601.07356 [astro-ph.CO] .

[151] G. Fanizza, B. Fiorini, and G. Marozzi, Phys. Rev. D **104**, 083506 (2021), arXiv:2102.12419 [astro-ph.CO] .

[152] E. Di Dio, R. Durrer, G. Marozzi, and F. Montanari, JCAP **01**, 016 (2016), arXiv:1510.04202 [astro-ph.CO] .

[153] E. Di Dio, R. Durrer, R. Maartens, F. Montanari, and O. Umeh, JCAP **04**, 053 (2019), arXiv:1812.09297 [astro-ph.CO] .

[154] E. Castorina and E. di Dio, JCAP **01**, 061 (2022), arXiv:2106.08857 [astro-ph.CO] .

[155] G. Pratten and A. Lewis, JCAP **08**, 047 (2016), arXiv:1605.05662 [astro-ph.CO] .

[156] G. Marozzi, G. Fanizza, E. Di Dio, and R. Durrer, JCAP **09**, 028 (2016), arXiv:1605.08761 [astro-ph.CO] .

[157] A. Lewis and G. Pratten, JCAP **12**, 003 (2016), arXiv:1608.01263 [astro-ph.CO] .

[158] J. Liu, J. C. Hill, B. D. Sherwin, A. Petri, V. Böhm, and Z. Haiman, Phys. Rev. D **94**, 103501 (2016), arXiv:1608.03169 [astro-ph.CO] .

[159] G. Marozzi, G. Fanizza, E. Di Dio, and R. Durrer, Phys. Rev. Lett. **118**, 211301 (2017), arXiv:1612.07650 [astro-ph.CO] .

[160] G. Marozzi, G. Fanizza, E. Di Dio, and R. Durrer, Phys. Rev. D **98**, 023535 (2018), arXiv:1612.07263 [astro-ph.CO] .

[161] G. Fabbian, M. Calabrese, and C. Carbone, JCAP **02**, 050 (2018), arXiv:1702.03317 [astro-ph.CO] .

[162] P. Schneider, L. van Waerbeke, B. Jain, and G. Kruse, Mon. Not. Roy. Astron. Soc. **296**, 873 (1998), arXiv:astro-ph/9708143 .

[163] S. Dodelson and P. Zhang, Phys. Rev. D **72**, 083001 (2005), arXiv:astro-ph/0501063 .

[164] A. Petri, Z. Haiman, and M. May, Phys. Rev. D **95**, 123503 (2017), arXiv:1612.00852 [astro-ph.CO] .

[165] V. Böhm, C. Modi, and E. Castorina, JCAP **03**, 045 (2020), arXiv:1910.06722 [astro-ph.CO] .

[166] J. Adamek, C. Clarkson, L. Coates, R. Durrer, and M. Kunz, Phys. Rev. D **100**, 021301 (2019), arXiv:1812.04336 [astro-ph.CO] .

[167] T. Buchert, Gen. Rel. Grav. **32**, 105 (2000), arXiv:gr-qc/9906015 .

[168] T. Buchert, Gen. Rel. Grav. **33**, 1381 (2001), arXiv:gr-qc/0102049 .

[169] T. Buchert and S. Räsänen, Ann. Rev. Nucl. Part. Sci. **62**, 57 (2012), arXiv:1112.5335 [astro-ph.CO] .

[170] M. Gasperini, G. Marozzi, and G. Veneziano, JCAP **03**, 011 (2009), arXiv:0901.1303 [gr-qc] .

[171] M. Gasperini, G. Marozzi, and G. Veneziano, JCAP **02**, 009 (2010), arXiv:0912.3244 [gr-qc] .

[172] M. Gasperini, G. Marozzi, F. Nugier, and G. Veneziano, JCAP **07**, 008 (2011), arXiv:1104.1167 [astro-ph.CO] .

[173] J. Yoo and R. Durrer, JCAP **09**, 016 (2017), arXiv:1705.05839 [astro-ph.CO] .

[174] G. Fanizza, M. Gasperini, G. Marozzi, and G. Veneziano, JCAP **02**, 017 (2020), arXiv:1911.09469 [gr-qc] .

[175] T. Buchert, H. van Elst, and A. Heinesen, Gen. Rel. Grav. **55**, 7 (2023), arXiv:2202.10798 [gr-qc] .

[176] D. M. Scolnic *et al.* (Pan-STARRS1), ApJ **859**, 101 (2018), arXiv:1710.00845 [astro-ph.CO] .

[177] C. Krishnan, E. O. Colgáin, Ruchika, A. A. Sen, M. M. Sheikh-Jabbari, and T. Yang, Phys. Rev. D **102**, 103525 (2020), arXiv:2002.06044 [astro-ph.CO] .

[178] L. Kazantzidis and L. Perivolaropoulos, Phys. Rev. D **102**, 023520 (2020), arXiv:2004.02155 [astro-ph.CO] .

[179] C. Krishnan, E. O. Colgáin, M. M. Sheikh-Jabbari, and T. Yang, Phys. Rev. D **103**, 103509 (2021), arXiv:2011.02858 [astro-ph.CO] .

[180] H. Mo, F. C. van den Bosch, and S. White, *Galaxy Formation and Evolution* (2010).

[181] E. W. Kolb and M. S. Turner, *The Early Universe*, Vol. 69 (1990).

[182] T. Padmanabhan, *Structure Formation in the Universe* (1993).

[183] J. Guy *et al.* (SNLS), Astron. Astrophys. **466**, 11 (2007), arXiv:astro-ph/0701828 .

[184] M. Tegmark *et al.* (SDSS), Astrophys. J. **606**, 702 (2004), arXiv:astro-ph/0310725 .

[185] D. J. Eisenstein *et al.* (SDSS), Astrophys. J. **633**, 560 (2005), arXiv:astro-ph/0501171 .

[186] G. S. Sharov and V. O. Vasiliev, Math. Model. Geom. **6**, 1 (2018), arXiv:1807.07323 [gr-qc] .

[187] G. S. Sharov, JCAP **06**, 023 (2016), arXiv:1506.05246 [gr-qc] .

[188] A. Lewis, A. Challinor, and A. Lasenby, Astrophys. J. **538**, 473 (2000), arXiv:astro-ph/9911177 .

[189] A. Cuceu, J. Farr, P. Lemos, and A. Font-Ribera, JCAP **10**, 044 (2019), arXiv:1906.11628 [astro-ph.CO] .

[190] E. Aubourg *et al.*, Phys. Rev. D **92**, 123516 (2015), arXiv:1411.1074 [astro-ph.CO] .

[191] V. F. Mukhanov, H. A. Feldman, and R. H. Brandenberger, Phys. Rept. **215**, 203 (1992).

[192] A. Riotto, ICTP Lect. Notes Ser. **14**, 317 (2003), arXiv:hep-ph/0210162 [hep-ph] .

[193] D. Baumann, in *Theoretical Advanced Study Institute in Elementary Particle Physics: Physics of the Large and the Small* (2011) pp. 523–686, arXiv:0907.5424 [hep-th] .

[194] J. H. Jeans, Phil. Trans. A. Math. Phys. Eng. Sci. **199**, 1 (1902).

[195] P. Meszaros, Astron. Astrophys. **37**, 225 (1974).

[196] A. G. Riess, S. Casertano, W. Yuan, L. M. Macri, and D. Scolnic, Astrophys. J. **876**, 85 (2019), arXiv:1903.07603 [astro-ph.CO] .

[197] Gaia Collaboration, Brown, A. G. A., *et al.*, A&A **649**, A1 (2021).

[198] K. C. Wong *et al.*, Mon. Not. Roy. Astron. Soc. **498**, 1420 (2020), arXiv:1907.04869 [astro-ph.CO] .

[199] A. Gómez-Valent and L. Amendola, JCAP **04**, 051 (2018), arXiv:1802.01505 [astro-ph.CO] .

[200] W. L. Freedman *et al.*, Astrophys. J. **882**, 34 (2019), arXiv:1907.05922 [astro-ph.CO] .

[201] G. Risaliti and E. Lusso, Nature Astron. **3**, 272 (2019), arXiv:1811.02590 [astro-ph.CO] .

[202] V. F. Cardone, S. Capozziello, and M. G. Dainotti, Mon. Not. Roy. Astron. Soc. **400**, 775 (2009), arXiv:0901.3194 [astro-ph.CO] .

[203] V. F. Cardone, M. G. Dainotti, S. Capozziello, and R. Willingale, Mon. Not. Roy. Astron. Soc. **408**, 1181 (2010), arXiv:1005.0122 [astro-ph.CO] .

[204] M. G. Dainotti, V. F. Cardone, E. Piedipalumbo, and S. Capozziello, Mon. Not. Roy. Astron. Soc. **436**, 82 (2013), arXiv:1308.1918 [astro-ph.HE] .

[205] A. Ingram *et al.*, Mon. Not. Roy. Astron. Soc. **509**, 619 (2021), arXiv:2110.15651 [astro-ph.HE] .

[206] R. Abbott *et al.* (LIGO Scientific, Virgo,, KAGRA, VIRGO), Astrophys. J. **949**, 76 (2023), arXiv:2111.03604 [astro-ph.CO] .

[207] H. Hildebrandt *et al.*, Mon. Not. Roy. Astron. Soc. **465**, 1454 (2017), arXiv:1606.05338 [astro-ph.CO] .

[208] C. Hikage *et al.* (HSC), Publ. Astron. Soc. Jap. **71**, 43 (2019), arXiv:1809.09148 [astro-ph.CO] .

[209] M. A. Troxel *et al.* (DES), Phys. Rev. D **98**, 043528 (2018), arXiv:1708.01538 [astro-ph.CO] .

[210] D. I. Santiago and A. S. Silbergleit, Gen. Rel. Grav. **32**, 565 (2000), arXiv:gr-qc/9904003 .

[211] D. F. Torres, Phys. Rev. D **66**, 043522 (2002), arXiv:astro-ph/0204504 .

[212] V. Faraoni, *Cosmology in scalar tensor gravity* (Springer, 2004).

[213] T. Koivisto, Class. Quant. Grav. **23**, 4289 (2006), arXiv:gr-qc/0505128 .

[214] D. Saez-Gomez, Class. Quant. Grav. **30**, 095008 (2013), arXiv:1207.5472 [gr-qc] .

[215] A. de la Cruz-Dombriz, P. K. S. Dunsby, S. Kandhai, and D. Sáez-Gómez, Phys. Rev. D **93**, 084016 (2016), arXiv:1511.00102 [gr-qc] .

[216] L. Lombriser, Annalen Phys. **526**, 259 (2014), arXiv:1403.4268 [astro-ph.CO] .

[217] T. L. Smith, (2009), arXiv:0907.4829 [astro-ph.CO] .

[218] L. Lombriser, F. Schmidt, T. Baldauf, R. Mandelbaum, U. Seljak, and R. E. Smith, Phys. Rev. D **85**, 102001 (2012), arXiv:1111.2020 [astro-ph.CO] .

[219] M. A. Mitchell, C. Arnold, and B. Li, Mon. Not. Roy. Astron. Soc. **508**, 4157 (2021), arXiv:2107.14224 [astro-ph.CO] .

[220] Y.-S. Song, H. Peiris, and W. Hu, Phys. Rev. D **76**, 063517 (2007), arXiv:0706.2399 [astro-ph] .

[221] J. Dossett, B. Hu, and D. Parkinson, JCAP **03**, 046 (2014), arXiv:1401.3980 [astro-ph.CO] .

[222] M. Raveri, B. Hu, N. Frusciante, and A. Silvestri, Phys. Rev. D **90**, 043513 (2014), arXiv:1405.1022 [astro-ph.CO] .

[223] M. Cataneo, D. Rapetti, F. Schmidt, A. B. Mantz, S. W. Allen, D. E. Applegate, P. L. Kelly, A. von der Linden, and R. G. Morris, Phys. Rev. D **92**, 044009 (2015), arXiv:1412.0133 [astro-ph.CO] .

[224] L. Xu, Phys. Rev. D **91**, 063008 (2015), arXiv:1411.4353 [astro-ph.CO] .

[225] T. Liu, X. Zhang, and W. Zhao, Phys. Lett. B **777**, 286 (2018), arXiv:1711.08991 [astro-ph.CO] .

[226] K. Enqvist and T. Mattsson, JCAP **02**, 019 (2007), arXiv:astro-ph/0609120 .

[227] G. Ellis, S. Nel, R. Maartens, W. Stoeger, and A. Whitman, Physics Reports **124**, 315 (1985).

[228] R. Arnowitt, S. Deser, and C. W. Misner, Phys. Rev. **116**, 1322 (1959).

[229] R. M. Wald, *General Relativity* (Chicago Univ. Pr., Chicago, USA, 1984).

[230] R. Zalaletdinov, Gen. Rel. Grav. **25**, 673 (1993).

[231] C. Krishnan and R. Mondol, (2022), arXiv:2201.13384 [astro-ph.CO] .

[232] E. O. Colgáin, M. M. Sheikh-Jabbari, R. Solomon, M. G. Dainotti, and D. Stojkovic, (2022), arXiv:2206.11447 [astro-ph.CO] .

[233] E. O. Colgáin, M. M. Sheikh-Jabbari, and R. Solomon, Phys. Dark Univ. **40**, 101216 (2023), arXiv:2211.02129 [astro-ph.CO] .

[234] X. D. Jia, J. P. Hu, and F. Y. Wang, Astron. Astrophys. **674**, A45 (2023), arXiv:2212.00238 [astro-ph.CO] .

[235] S. A. Rodney, A. G. Riess, D. M. Scolnic, D. O. Jones, S. Hemmati, A. Molino, C. McCully, B. Mobasher, L.-G. Strolger, O. Graur, and et al., The Astronomical Journal **151**, 47 (2016).

[236] J. Torrado and A. Lewis, JCAP **05**, 057 (2021), arXiv:2005.05290 [astro-ph.IM] .

[237] P. A. Oesch *et al.*, The Astrophysical Journal **819**, 129 (2016).

[238] S. Postnikov, M. G. Dainotti, X. Hernandez, and S. Capozziello, **783**, 126 (2014).

[239] M. J. Childress *et al.*, Astrophys. J. **770**, 107 (2013), arXiv:1304.4719 [astro-ph.CO] .

[240] M. Sullivan *et al.* (SNLS), Mon. Not. Roy. Astron. Soc. **406**, 782 (2010), arXiv:1003.5119 [astro-ph.CO] .

[241] P. L. Kelly, M. Hicken, D. L. Burke, K. S. Mandel, and R. P. Kirshner, Astrophys. J. **715**, 743 (2010), arXiv:0912.0929 [astro-ph.CO] .

[242] H. Lampeitl *et al.* (SDSS), Astrophys. J. **722**, 566 (2010), arXiv:1005.4687 [astro-ph.CO] .

[243] R. Kessler and D. Scolnic, Astrophys. J. **836**, 56 (2017), arXiv:1610.04677 [astro-ph.CO] .

[244] I. Tutusaus, B. Lamine, A. Dupays, and A. Blanchard, Astron. Astrophys. **602**, A73 (2017), arXiv:1706.05036 [astro-ph.CO] .

[245] N. Nicolas, M. Rigault, Y. Copin, R. Graziani, G. Aldering, M. Briday, Y. L. Kim, J. Nordin, S. Perlmutter, and M. Smith, Astron. Astrophys. **649**, A74 (2021), arXiv:2005.09441 [astro-ph.CO] .

[246] G. K. Malmquist, Meddelanden fran Lunds Astronomiska Observatorium Serie II **22**, 3 (1920).

[247] A. D. Linde, Physics Letters B **129**, 177 (1983).

[248] S. Nojiri, S. D. Odintsov, and D. Saez-Gomez, Phys. Lett. B **681**, 74 (2009), arXiv:0908.1269 [hep-th] .

[249] F. Moretti, F. Bombacigno, and G. Montani, Phys. Rev. D **100**, 084014 (2019), arXiv:1906.01899 [gr-qc] .

[250] P. Brax, C. van de Bruck, A.-C. Davis, and D. J. Shaw, Phys. Rev. D **78**, 104021 (2008), arXiv:0806.3415 [astro-ph] .

[251] A. A. Starobinsky, Phys. Lett. B **91**, 99 (1980).

[252] L. Cosmai, G. Fanizza, and L. Tedesco, Int. J. Theor. Phys. **55**, 754 (2016), arXiv:1311.7281 [astro-ph.CO] .

[253] G. Fanizza, G. Franchini, M. Gasperini, and L. Tedesco, Gen. Rel. Grav. **52**, 111 (2020), arXiv:2010.06569 [gr-qc] .

[254] P. Marcoccia and G. Montani, (2018), arXiv:1808.01489 [gr-qc] .

[255] H. van Elst and G. F. R. Ellis, Class. Quant. Grav. **13**, 1099 (1996), arXiv:gr-qc/9510044 .

[256] R. A. Sussman, (2010), arXiv:1001.0904 [gr-qc] .

[257] W. Hu and I. Sawicki, Phys. Rev. D **76**, 104043 (2007), arXiv:0708.1190 [astro-ph] .

[258] M. Sasaki, Mon. Not. Roy. Astron. Soc. **228**, 653 (1987).

[259] C. Bonvin, R. Durrer, and M. A. Gasparini, Phys. Rev. D **73**, 023523 (2006), [Erratum: Phys.Rev.D 85, 029901 (2012)], arXiv:astro-ph/0511183 .

[260] S. G. Biern and J. Yoo, JCAP **04**, 045 (2017), arXiv:1606.01910 [astro-ph.CO] .

[261] J. Yoo, Phys. Rev. D **82**, 083508 (2010), arXiv:1009.3021 [astro-ph.CO] .

[262] R. Takahashi, M. Sato, T. Nishimichi, A. Taruya, and M. Oguri, Astrophys. J. **761**, 152 (2012), arXiv:1208.2701 [astro-ph.CO] .

[263] M. H. Goroff, B. Grinstein, S. J. Rey, and M. B. Wise, Astrophys. J. **311**, 6 (1986).

[264] F. Bernardeau, S. Colombi, E. Gaztanaga, and R. Scoccimarro, Phys. Rept. **367**, 1 (2002), arXiv:astro-ph/0112551 .

[265] D. N. Limber, ApJ **117**, 134 (1953).

[266] D. N. Limber, Astrophys. J. **119**, 655 (1954).

[267] M. LoVerde and N. Afshordi, Phys. Rev. D **78**, 123506 (2008), arXiv:0809.5112 [astro-ph] .

[268] J. Lesgourgues, (2011), arXiv:1104.2932 [astro-ph.IM] .

[269] D. Blas, J. Lesgourgues, and T. Tram, JCAP **07**, 034 (2011), arXiv:1104.2933 [astro-ph.CO] .

[270] J. Lesgourgues, (2011), arXiv:1104.2934 [astro-ph.CO] .

[271] J. Lesgourgues and T. Tram, JCAP **09**, 032 (2011), arXiv:1104.2935 [astro-ph.CO] .

[272] J. Adamek, J. Calles, T. Montandon, J. Noreña, and C. Stahl, JCAP **04**, 001 (2022), arXiv:2110.11249 [astro-ph.CO] .

[273] A. L. Lenart, G. Bargiacchi, M. G. Dainotti, S. Nagataki, and S. Capozziello, Astrophys. J. Suppl. **264**, 46 (2023), arXiv:2211.10785 [astro-ph.CO] .

[274] G. Bargiacchi, M. G. Dainotti, S. Nagataki, and S. Capozziello, MNRAS **521**, 3909 (2023), arXiv:2303.07076 [astro-ph.CO] .

[275] M. G. Dainotti, G. Bargiacchi, S. Nagataki, M. Bogdan, and S. Capozziello, arXiv e-prints , arXiv:2303.06974 (2023), arXiv:2303.06974 [astro-ph.CO] .

[276] M. G. Dainotti, G. Bargiacchi, M. Bogdan, A. L. Lenart, K. Iwasaki, S. Capozziello, B. Zhang, and N. Fraija, Astrophys. J. **951**, 63 (2023), arXiv:2305.10030 [astro-ph.CO] .

[277] G. Bargiacchi, M. G. Dainotti, and S. Capozziello, (2023), arXiv:2307.15359 [astro-ph.CO] .

[278] R. H. Sanders, A&A **136**, L21 (1984).

[279] S. Capozziello and M. De Laurentis, Annalen Phys. **524**, 545 (2012).

[280] A. Stabile and S. Capozziello, Phys. Rev. D **87**, 064002 (2013), arXiv:1302.1760 [gr-qc] .

[281] A. O. F. de Almeida, L. Amendola, and V. Niro, JCAP **08**, 012 (2018), arXiv:1805.11067 [astro-ph.GA] .